

UNIVERSITÄT
BAYREUTH

Fakultät für Biologie, Chemie und Geowissenschaften

**Biochemical and structural characterization of the regulation
of human Sirtuin 1 by small molecules and proteins**

DISSERTATION

zur Erlangung des akademischen Grades einer Doktorin der
Naturwissenschaften (Dr. rer. nat.) an der Fakultät für Biologie, Chemie und
Geowissenschaften der Universität Bayreuth

vorgelegt von

M. Sc. Biochemikerin

Ramona Sabine Adolph

aus Rosenheim

Bayreuth, 2020



Die vorliegende Arbeit wurde in der Zeit von Februar 2014 bis Juli 2020 in Bayreuth am Lehrstuhl für Biochemie unter Betreuung von Herrn Professor Dr. Clemens Steegborn angefertigt.

Vollständiger Abdruck der von der Fakultät für Biologie, Chemie und Geowissenschaften der Universität Bayreuth genehmigten Dissertation zur Erlangung des akademischen Grades einer Doktorin der Naturwissenschaften (Dr. rer. nat.).

Dissertation eingereicht am: 16.12.2019

Zulassung durch die Prüfungskommission: 08.01.2020

Wissenschaftliches Kolloquium: 15.07.2020

Amtierender Dekan: Prof. Dr. Matthias Breuning

Prüfungsausschuss:

Prof. Dr. Clemens Steegborn (Gutachter)

Prof. Dr. Birte Höcker (Gutachterin)

Prof. Dr. Birgitta Wöhrl (Vorsitz)

Prof. Dr. Matthias Breuning

Published figures within this dissertation were reprinted with the permission of the respective copyright holders.

Table of contents

Table of contents.....	V
List of abbreviations.....	IX
Summary	XII
Zusammenfassung.....	XIII
1. Introduction	1
1.1 Role of post-translational protein modifications for cell signaling	1
1.2 Significance of lysine acetylation and acylation.....	1
1.3 Deacylase class III - the sirtuin family	2
1.4 Physiological relevance of sirtuin deacylases	4
1.4.1 Caloric restriction and lifespan extension	4
1.4.2 Role of sirtuins on cell signaling pathways.....	4
1.5 Structure and enzymatic mechanism of mammalian sirtuins	6
1.5.1 Structure of mammalian sirtuins	6
1.5.2 Role of extended termini in Sirtuin1	9
1.5.3 Enzymatic mechanism of sirtuin-catalyzed deacylation	10
1.6 Modulation of sirtuin activity by small molecules	11
1.6.1 Regulation of sirtuin activity by metabolites and precursor enzymes	12
1.6.2 Inhibition of sirtuins by small molecules	13
1.6.3 Activation of sirtuins by STACs	14
1.7 Modulation of Sirt1 activity by other proteins.....	16
1.7.1 Regulation of Sirt1 activity by AROS	17
1.7.2 Inhibition of Sirt1 by DBC1.....	18
1.7.3 Modulation of Sirt1 activity by Hic1	19
1.7.4 Inhibition of Sirt1 by HIV1-Tat	21
2. Objectives of this work.....	25
2.1 Modulation of Sirt1 activity by small molecules.....	25
2.2 Regulation of Sirt1 activity by hAROS	25
2.3 Characterization of the interaction of Sirt1 with Hic1-BTB.....	25
2.4 Biochemical and structural characterization of Sirt1-inhibition by HIV1-Tat.....	26
3. Materials and methods.....	27
3.1. Materials	27
3.1.1 Chemicals, enzymes, standards	27
3.1.2 Bacterial strains	27
3.1.3 Growth media and antibiotics	28
3.1.4 Plasmids and oligonucleotides.....	29
3.1.5 Buffers and solutions	29

3.1.6 Equipment.....	32
3.1.7 Consumables.....	33
3.2 Molecular biological methods	34
3.2.1 Polymerase chain reaction (PCR).....	34
3.2.2 Purification of PCR products and restricted vectors.....	36
3.2.3 Preparation of plasmid DNA	36
3.2.4 Agarose gel electrophoresis	36
3.2.5 DNA restriction digest	37
3.2.6 DNA ligation	37
3.2.7 Transformation of ligation reactions into chemically competent cells.....	38
3.2.8 Identification of positive clones by colony and analytical PCR.....	38
3.2.9 DNA sequencing.....	38
3.3 Microbiological methods	39
3.3.1 Sterilization.....	39
3.3.2 Transformation of chemically competent cells.....	39
3.3.3 <i>E. coli</i> cultivation and heterologous overexpression of recombinant proteins.....	39
3.3.4 Cell harvest and disruption	40
3.4 Purification of recombinant proteins after heterologous expression in <i>E. coli</i>	41
3.4.1 Overview of purification protocols.....	41
3.4.2 Affinity chromatography	42
3.4.3 Refolding of hAROS <i>on-column</i>	43
3.4.4 Dialysis and proteolytic cleavage of the His ₆ -tag.....	44
3.4.5 Ion exchange chromatography.....	44
3.4.6 Size exclusion chromatography	45
3.5 Biochemical methods.....	45
3.5.1 SDS-Polyacrylamide gel electrophoresis	45
3.5.2 Concentration of proteins by centrifugation	46
3.5.3 Photometric determination of concentrations	46
3.5.4 Thermal shift denaturation assay	46
3.5.5 Continuous coupled enzymatic deacylation activity assay.....	47
3.5.6 <i>Fluor de Lys</i> deacylation activity assay.....	49
3.5.7 Mass spectrometric deacylation activity assay	50
3.5.8 Statistical analyses	50
3.6 Interaction analysis methods.....	51
3.6.1 Pulldown.....	51
3.6.2 <i>Blue Native</i> PAGE	51
3.6.3 <i>In vitro</i> -phosphorylation	52

3.6.4 Crosslinking	52
3.6.5 Nuclear magnetic resonance spectroscopy	53
3.6.6 Microscale thermophoresis	53
3.7 Bioanalytical methods.....	55
3.7.1 Circular dichroism spectroscopy	55
3.7.2 Intact mass spectrometric analysis of proteins	56
3.7.3 Tryptic digest of proteins for mass spectrometric analysis	56
3.7.4 Limited proteolysis.....	57
3.7.5 Analysis of mass spectrometric data	57
3.8 Crystallographic methods	58
3.8.1 Screening for initial crystallization conditions	58
3.8.2 Optimization of initial crystallization conditions	58
3.8.3 Cryoprotection of protein crystals	59
3.8.4 X-ray structure analysis and data collection	59
3.8.5 Data processing, model building, and structure refinement	60
3.8.6 Crystallization conditions and structure solution of obtained complexes.....	61
3.9 Bioinformatical methods.....	63
4. Results.....	64
4.1 Characterization of human Sirtuin 1 and its intrinsic and extrinsic activity modulation by small molecules.....	64
4.1.1 Recombinant expression, purification, and characterization of fl-hSirt1	64
4.1.2 Recombinant expression, purification, and characterization of human mini-Sirt1 ..	66
4.1.3 Relevance of the ESA/CTR region for the intrinsic hSirt1 activity	71
4.1.4 Stimulation of hSirt1 activity by small molecules.....	72
4.1.5 Inhibition of hSirt1 by tranilast.....	75
4.2 Modulation of hSirt1 activity by hAROS	77
4.2.1 Recombinant expression and purification of His ₆ -hAROS	77
4.2.2 Regulation of hSirt1 activity by recombinant refolded hAROS.....	79
4.3 Elucidation of the mechanism of Sirt1 activity modulation by Hic1-BTB	83
4.3.1 Recombinant expression, purification, and characterization of human Hic1-BTB. 83	
4.3.2 Biochemical characterization of the interaction between Sirt1 and Hic1-BTB.....	86
4.3.3 Structural characterization of Hic1-BTB	92
4.4 Biochemical and structural characterization of hSirt1-inhibition by HIV1-Tat	96
4.4.1 Bioanalytical characterization of HIV1-Tat Cys ⁻	96
4.4.2 Modulation of hSirt1 activity by Tat Cys ⁻	97
4.4.3 Specificity of Tat-mediated inhibition of human sirtuin isoforms.....	98
4.4.4 Mapping of general sirtuin-interacting regions on Tat Cys ⁻	100

4.4.5 Biochemical and structural characterization of the HIV1-Tat region necessary for inhibition of human Sirt1-3	107
4.4.6 Elucidation of the inhibitory mechanism of HIV1-Tat on hSirt1-3	121
5. Discussion	127
5.1 Characterization of recombinant human Sirtuin 1	127
5.1.1 Human fl-Sirt1 and truncated variants	127
5.1.2 Mini-Sirt1 as a model for mimicking fl-hSirt1	128
5.2 Modulation of hSirt1 activity by small molecules	130
5.2.1 Importance of the Sirt1-specific ESA/CTR region for hSirt1 activity.....	130
5.2.2 Stimulation of hSirt1 activity by dehydroabiatic acid.....	131
5.2.3 Biochemical and structural studies of tranilast and hSirt1	132
5.3 Modulation of hSirt1 activity by hAROS	133
5.3.1 Characterization of refolded His ₆ -hAROS	133
5.3.2 Interaction between hSirt1 and hAROS	135
5.4 Interaction of the BTB domain of Hic1 with Sirt1	136
5.4.1 Expression and purification of Hic1-BTB	136
5.4.2 Oligomerization state of the BTB domain of Hic1 in solution	136
5.4.3 Analysis of the interaction of Hic1-BTB with hSirt1	138
5.4.4 Structural characterization of Hic1-BTB and putative interaction sites with hSirt1	140
5.5 Biochemical and structural characterization of hSirt1 inhibition by HIV1-Tat	143
5.5.1 Characterization of HIV1-Tat Cys ⁻	143
5.5.2 Inhibition of human sirtuin isoforms by HIV1-Tat Cys ⁻	144
5.5.3 Sirtuin activity-modulating potential of HIV1-Tat Lys50	146
5.5.4 Mapping of the sirtuin-inhibiting region on HIV1-Tat	147
5.5.5 Mechanism of inhibition of hSirt1-3 by HIV1-Tat	148
6. References.....	154
7. Supplementary	167
7.1 Additional materials.....	167
7.2 Additional results	171
7.2.1 Purification of human mini-Sirt1 variants.....	171
7.2.2 Regulation of hSirt1 activity by small molecules and AROS.....	176
7.2.3 Interaction between Hic1-BTB and hSirt1	179
7.2.4 Inhibition of hSirt1 by HIV1-Tat	182
Danksagung.....	190
(Eidesstattliche) Versicherungen und Erklärungen.....	192

List of abbreviations

A ₂₈₀	absorbance at 280 nm
AADPr	2'- <i>O</i> -acyl adenosine diphosphate ribose
AC	affinity chromatography
AceCS2	acetyl-CoA synthetase 2
ADPr	adenosine diphosphate ribose
AFU	arbitrary fluorescence units
AIDS	acquired immunodeficiency syndrome
Amp	ampicillin
APS	ammonium persulfate
AROS	<i>Active regulator of Sirt1</i>
ATM	ataxia telangiectasia-mutated kinase
ATP	adenosine triphosphate
ATR	ataxia telangiectasia and Rad3-related kinase
BCL-6	B-cell lymphoma 6
β-ME	β-Mercaptoethanol
bp	base pair
BTB	<u>b</u> ric-a-brac, <u>t</u> ramtrack, and <u>b</u> road complex
Cam	chloramphenicol
CCAR2	cell cycle activator and apoptosis regulator 2
CD	circular dichroism
Cdk9	cyclin-dependent kinase 9
CID	collision-induced dissociation
CK2	casein kinase 2
CoA	coenzyme A
CPP	cell-penetrating peptide signal
CPS1	carbamoyl phosphate synthase 1
CR	caloric restriction
CREB	cyclic adenosine monophosphate response element-binding protein
CtBP	C-terminal binding protein
CTR	<i>C-terminal regulatory segment</i> (Sirt1)
CV	column volume
Da	Dalton
DAA	dehydroabiatic acid
DBC1	deleted in breast cancer 1
ddH ₂ O	double-distilled water
DHP	1, 4-dihydropyridine
DMS	dimethyl suberimidate
DMSO	dimethylsulfoxid
DNA	deoxyribonucleic acid
dNTP	2'-desoxyribonucleoside-5'-triphosphate
DR	dietary restriction
Dr.	Doctor
DSS	disuccinimidyl suberate
DSSO	disuccinimidyl sulfoxide
DTT	dithiothreitol
EDTA	ethylenediaminetetraacetic acid
<i>E. coli</i>	<i>Escherichia coli</i>
e.g.	<i>exempli gratia</i> , for example
ESA	<i>Essential for Sirt1 activity</i>
FA	formic acid
FAZF	fanconi anemia zinc finger protein
Fdl	<i>Fluor de Lys</i>
FITC	fluorescein isothiocyanate
fl	full length
FOXO	forkhead box, subgroup O
h	human
GDH	glutamate dehydrogenase
Gent	gentamycin
GmbH	Gesellschaft mit beschränkter Haftung

List of abbreviations

GST	glutathione-S-transferase
HDAC	histone deacetylase
Hic1	hypermethylated in cancer 1
HIPK2	homeodomain interacting protein kinase 2
HiRE	Hic1 responsive element
HIV1	<i>Human immunodeficiency virus type 1</i>
HMGA1	high-mobility group AT-hook 1
hMOF	human MYST acetyltransferase <i>Males absent on the First</i>
HPLC	high performance liquid chromatography
HPSF	high purity salt-free
IC ₅₀	inhibitor concentration for half-maximal activity
IDP	intrinsically disordered protein
IEX	ion exchange chromatography
Instr.	instruments
Int.	international
IR	infrared
ITC	isothermal titration calorimetry
Kan	kanamycin
kb	kilo bases
K _d	dissociation constant
K _m	<i>Michaelis-Menten constant</i>
LB	lysogeny broth
LED	light-emitting diode
LTQ	linear trap quadrupole
LZ	leucine zipper
M	SDS-PAGE marker
MALLS	multi-angle laser light-scattering
Miz1	Myc-interacting zinc finger protein 1
MS	mass spectrometry
MST	microscale thermophoresis
MTA1	metastasis-associated protein 1
MTS	mitochondrial targeting sequence
MW	molecular weight
MWCO	molecular weight cutoff
<i>n</i>	number of individual samples or experiments
<i>n. a.</i>	not available
<i>n. d.</i>	not determined
NAM	nicotinamide
NAMPT	NAM phosphoribosyl transferase
NCS	non-crystallographic symmetry
Neo	neomycin
NES	nuclear export signal
NF-κB	nuclear factor κ-light-chain-enhancer of activated B-cells
NHD	nudix hydrolase domain
NHS	N-hydroxysuccinimide
NMR	nuclear magnetic resonance
NLS	nuclear localization signal
NTA	nitrilotriacetic acid
NuRD	nucleosome remodeling deacetylase
PAGE	polyacrylamide gel electrophoresis
PARP	poly-ADP-ribose polymerase
PBS	phosphate buffered saline
PCAF	p300/CREB-binding protein-associated factor
PCR	polymerase chain reaction
PDB	<i>Protein Data Bank</i>
PEG	polyethylene glycol
PGC-1α	PPARγ coactivator 1α
pI	isoelectric point
PIAS	protein inhibitor of activated STAT, E3 sumo ligase
PLZF	promyeolytic leukemia zinc finger protein
PMSF	phenylmethylsulfonyl fluoride

X

PPAR γ	peroxisome proliferator-activated receptor γ
POZ	<u>p</u> ox virus and <u>z</u> inc finger
Prof.	Professor
P-TEFb	positive transcription elongation factor
PTM	post-translational modification
rcf	relative centrifugal force
Rev	regulator of expression of virion proteins
RMSD	root mean square deviation
RNA	ribonucleic acid
rpm	revolutions per minute
RPS19	ribosomal protein S19
RPS19BP1	RPS19 binding protein 1 (AROS)
SBD	STAC-binding domain (Sirt1)
SD	sample denaturation
SDS	sodium dodecyl sulfate
SEC	size exclusion chromatography
Senp	sentrin-specific protease
Sirt	Sirtuin
SPR	surface plasmon resonance
STAC	<i>Sirtuin-activating compound</i>
Strep	streptavidin
SUMO	small ubiquitin-like modifier
TAR	transactivation responsive element (RNA)
Tat	transactivator of transcription
TB	terrific broth
TCA	tricarboxylic acid (cycle)
TCEP	tris-(2-carboxyethyl)-phosphine
TEMED	tetramethylethylenediamine
Tet	tetracyclin
TEV	tobacco etch virus
TFA	trifluoroacetic acid
TFE	2,2,2-trifluoroethanol
TNF α	tumor necrosis factor α
TSA	thermal shift denaturation assay
T _m	melting temperature
TOF	time-of-flight
U	unit
UV	ultraviolet
WAT	white adipose tissue
ZF	zinc finger

For amino acids, the established one- or three-letter code was used.

Units were used in the metric system.

Countries were abbreviated according to the ISO norm, states in the USA with the known two-letter code.

Summary

Sirtuins are NAD⁺-dependent lysine deacylases, which regulate various cell signaling pathways and are associated with lifespan extension through caloric restriction. The human isoforms Sirt1-7 are linked to diverse age-related diseases such as Alzheimer's, Parkinson's, but also cancer and AIDS. Sirtuins are therefore emerging targets for therapeutic approaches and regulating sirtuin activity contextually is important. While current pharmacological modulation of sirtuin activity is almost exclusively restricted to inhibitors, which often lack isoform-specificity, potency, or bioavailability, the physiological modulation of sirtuin activity by other proteins is incompletely understood. This study covers important and new aspects for the physiological and pharmacological regulation of human Sirtuin 1.

Concerning regulation by small molecules, the activation of hSirt1 by dehydroabietic acid was characterized providing potential for pharmacological modulation with a new nature-derived activator scaffold. In addition, the proposed anti-tumor potential of tranilast was linked to inhibition of hSirt1. Regarding the physiological modulation of hSirt1 activity by other proteins, conflictive results were available for hAROS. Within this thesis, hAROS was validated as hSirt1 inhibitor. Furthermore, a stable core was suggested for the intrinsically disordered protein hAROS, which will be used for future interaction analyses. Conversely, an hSirt1-activity modulating effect for human Hic1 has not been described yet. Focusing on the interaction between hSirt1 and the BTB/POZ domain of Hic1, this study showed that the interaction is limited to the catalytic domain of hSirt1 and does not require phosphorylation of hSirt1, nor the presence of NAD⁺ or sirtuin substrate. Hic1-BTB might even have a dual and concentration-dependent effect on hSirt1 activity, which will be subject to future studies. In addition, the first crystal structure of Hic1 was solved demonstrating a typical BTB fold and offering an analysis of putative interacting regions with hSirt1. Finally, the region of hSirt1 interacting with HIV1-Tat was also identified as the catalytic domain and an additional *in vitro* inhibition of the structurally similar catalytic domains of hSirt2 and hSirt3 was observed. Tat binding to hSirt1-3 was competitive to the sirtuin substrate, but not to NAD⁺. In line with this observation, several complex structures of hSirt3 with Tat peptides could demonstrate that acetylated or deacetylated Tat binds to the sirtuin substrate binding cleft with its basic region. Using structural superpositions and crosslinking, the major contribution to binding was found to be mediated by HIV1-Tat amino acids 49-52, while Tat amino acids 53-59 provide the additional high potency needed for physiological inhibition of hSirt1 through disruption of an important salt bridge between the hSirt1 SBD and catalytic core.

Zusammenfassung

Sirtuine sind NAD⁺-abhängige Lysin-Deacylasen, die diverse zelluläre Prozesse beeinflussen und mit den positiven Effekten der Kalorienlimitierung in Verbindung gebracht werden. Die humanen Isoformen Sirt1-7 sind überdies hinaus an diversen altersbedingten Krankheiten wie Alzheimer und Parkinson, aber auch Krebs und AIDS beteiligt. Daher gewinnt die kontextabhängige Regulation von Sirtuinen zunehmend an Bedeutung für therapeutische Anwendungen. Bisher beschränkt sich die pharmakologische Modulation der Sirtuinaktivität nahezu ausschließlich auf Inhibitoren mit häufig unzureichender Spezifität, Wirkungskraft oder biologischer Verträglichkeit. Die physiologische Sirtuinregulation durch Proteine ist zudem unvollständig erfasst. Diese Studie umfasst nun neue Aspekte der physiologischen und pharmakologischen Regulation von humanem Sirtuin 1.

Im Bereich der Kleinmolekülregulation konnte die Aktivierung von hSirt1 durch Dehydroabietinsäure charakterisiert werden, sodass ein neues, naturnahes Aktivatorgerüst zur Modulation der Spezifität zur Verfügung steht. Weiterhin wurde die tumorhemmende Wirkung von Tranilast auf eine Inhibition von hSirt1 zurückgeführt. Bezüglich der physiologischen Regulation von hSirt1 durch andere Proteine wurden bisher widersprüchliche Ergebnisse zu hAROS veröffentlicht. In dieser Studie konnte nun eine inhibierende Wirkung bestätigt werden. Zudem scheint das intrinsisch ungeordnete Protein hAROS einen stabilen Kern zu besitzen, welcher für zukünftige Interaktionsstudien mit hSirt1 genutzt werden kann. Dagegen wurde bisher noch kein modulierender Effekt der hSirt1-Aktivität durch humanes Hic1 beschrieben. Hier konnte gezeigt werden, dass für die Interaktion der BTB/POZ-Domäne von Hic1 mit hSirt1 nur die katalytische Domäne von hSirt1 benötigt wird und keine Phosphorylierung von hSirt1 oder die Anwesenheit von NAD⁺ oder Substrat erfordert. Hic1-BTB könnte sogar einen dualen und konzentrationsabhängigen Effekt auf die hSirt1-Aktivität haben, was Gegenstand zukünftiger Studien sein wird. Weiterhin wurde die erste Kristallstruktur von Hic1 gelöst, welche eine typische BTB-Faltung zeigt und zur Analyse möglicher Interaktionsbereiche dient. Schließlich konnte auch die mit HIV1-Tat interagierende Region von hSirt1 auf die katalytische Domäne beschränkt werden, wobei eine zusätzliche *in vitro*-Inhibition der strukturell ähnlichen katalytischen Domänen von hSirt2 und hSirt3 beobachtet wurde. Die Bindung von Tat an hSirt1-3 war kompetitiv zum Substrat, aber nicht zu NAD⁺, was durch mehrere Komplexstrukturen von hSirt3 mit Tat-Peptiden bestätigt wurde. Durch Strukturüberlagerungen und Quervernetzung konnte gezeigt werden, dass acetyliertes oder deacetyliertes Tat mittels der Aminosäuren 49-52 seiner basischen Region in

die Sirtuin-Substratbindetasche bindet. Die zusätzliche hohe Wirksamkeit der physiologisch bedeutenden hSirt1-Inhibition wird dabei durch die Aminosäuren 53-59 von Tat vermittelt, welche eine wichtige Salzbrücke zwischen der Sirt1 SBD und der katalischen Domäne aufbrechen.

1. Introduction

1.1 Role of post-translational protein modifications for cell signaling

The complex interaction networks between proteins and biomolecules play an important role for the function and fate of living cells. These networks react dynamically to effectors like the extracellular matrix, growth factors, ligands, cell-cycle checkpoints, DNA damage, and oxygen and nutrient status¹. Regulation of cell-signaling networks is thereby often realized by selective expression of genes including modulation of human gene transcripts through allelic variations, mRNA splicing, and post-translational protein modifications (PTMs)².

More than 200 PTMs have been identified^{2,3}, which modulate protein structure and function². Proteins can not only exhibit single modifications, but also multi-site modifications of different classes of PTMs that cooperate to fine-tune molecular interactions^{1,3}. An example for a multi-site modified protein is the tumor suppressor p53³⁻⁵. PTMs are site-specific², e. g., reversible phosphorylation occurs at serine, threonine, or tyrosine residues via protein kinases^{1,6}. Phosphorylated proteins often undergo a conformational change followed by enzymatic activation¹ or induce effective protein-protein or protein-ligand interactions^{2,6}. In contrast, reversible methylation targets lysine or arginine residues¹ and is important for histone modification and regulating chromatin dynamics and gene activity^{2,7}. Irreversible post-translational modification of proteins can be achieved by glycosylation of asparagine, serine, or threonine³. Protein glycosylations affect cell-cell interactions and often trigger disease outbreaks^{8,9}. A further irreversible PTM is the covalent attachment of ubiquitin or small ubiquitin-like modifier (SUMO) to lysine². Polyubiquitylation prepares proteins for degradation, whereas sumoylation is a response to cell cycle control or viral infections¹⁰.

1.2 Significance of lysine acetylation and acylation

Reversible acetylation of lysines is another abundant PTM² associated with the regulation of protein-protein or protein-ligand interactions¹¹. After discovery of histone acetylation by Allfrey *et al.* in 1964^{11,12}, the first non-histone acetylation targets were found 30 years later and include α -tubulin¹³, p53¹⁴, and human immunodeficiency virus 1 (HIV1) transactivator of transcription (Tat)¹⁵. Acetylation sites are often conserved throughout organisms¹¹ if they occur in structured regions of the protein¹⁶. The mechanism is catalyzed by lysine acetyltransferases (KATs; formerly histone acetyltransferases, HATs) and involves the transfer of the acetyl group from acetyl-Coenzyme A (acetyl-CoA) to the ϵ -amino group of lysines¹⁷ (Figure 1.1A). Lysine acetylation can be reversed by histone deacetylases (HDACs)¹¹.

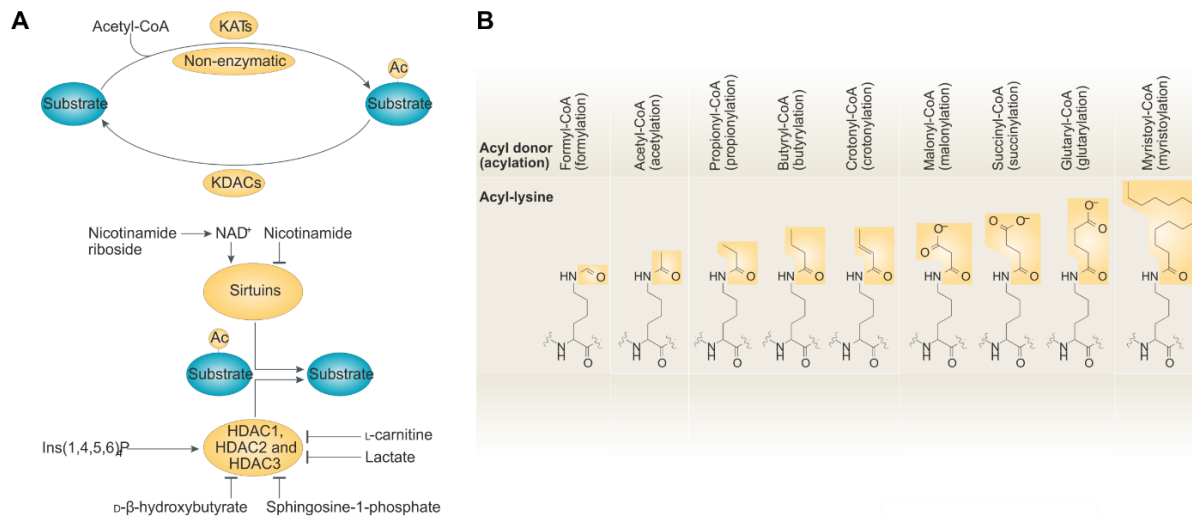


Figure 1.1: Lysine acetyl- and acyl-modification. **A** Reversible mechanism of acetylation catalyzed by lysine acetyltransferases (KATs) and counteracted by lysine deacetylases (KDACs) with a highlight on NAD^+ -dependent deacetylation by sirtuins in contrast to other histone deacetylases (HDACs). **B** Acyl-moieties for lysine modification. (Adapted from Choudhary *et al.* (2014)¹¹ with permission from Springer Nature).

The past ten years have revealed that the ϵ -amino group of lysine can also be modified with other acyl moieties¹¹. The most prominent lysine acyl modifications are formylation¹⁸, propionylation¹⁹, butyrylation²⁰, crotonylation²¹, malonylation^{22,23}, succinylation^{23,24}, glutarylation²⁵, and myristoylation²⁶ (Figure 1.1B). Since formyl, propionyl, and butyryl are just small variations in length with respect to the acetyl moiety and otherwise maintain the chemistry, they can be accommodated by acetyltransferases with a larger pocket for acyl-CoA^{11,27}. Other acyl groups like formyl¹¹, acetyl¹⁷, and succinyl²⁸ might also be conjugated through a non-enzymatic reaction using metabolites¹¹ because a high acylation rate and concentration of metabolites was observed in mitochondria, while the mitochondrial membrane is impervious to acyl-CoA¹¹. With the dependence of acylations on acyl-CoA or metabolites, they have a direct effect on many metabolic pathways like glycolysis, urea cycle, tricarboxylic acid (TCA) cycle, fatty acid metabolism, and amino acid catabolism²⁸. While all acylations remove the positive charge from lysine or even introduce a negative charge as in case of malonylation, succinylation, and glutarylation¹¹ (Figure 1.1B), they often also cause steric hindrance modulating protein-protein interactions or regulating enzymatic activity by altering substrate accessibility or allosteric regulation¹¹. In particular, the class III deacylase family, the sirtuins, were shown to effectively remove other acyl moieties from lysine^{23,26,29}.

1.3 Deacylase class III - the sirtuin family

There are 18 mammalian histone deacetylases (HDACs) that can be divided into five classes according to their structure, enzymatic function, subcellular localization, and expression patterns¹⁷ (Figure 1.2A). Classes I, IIa, and IIb comprise HDAC1-10, which are sensitive to

trichostatin A inhibition, while class IV contains the trichostatin A insensitive HDAC11¹⁷. HDACs1-11 have in common that they use a Zn²⁺ ion for hydrolyzing the acetyl-lysine amide bond³⁰. Class III deacetylases constitute the sirtuin family and differ from the aforementioned classes in the fact that deacetylation depends on the cofactor NAD⁺^{31,32} and can be inhibited by the metabolite nicotinamide (NAM), but not trichostatin A¹⁷. The Zn²⁺ ion in sirtuins does not contribute to the deacetylation reaction³³, but is essential for maintaining the structural integrity³³. In addition, some sirtuins are able to remove other acyl moieties from the ε-amino group of lysine^{23,26,29} and are therefore more accurately described as deacylases.

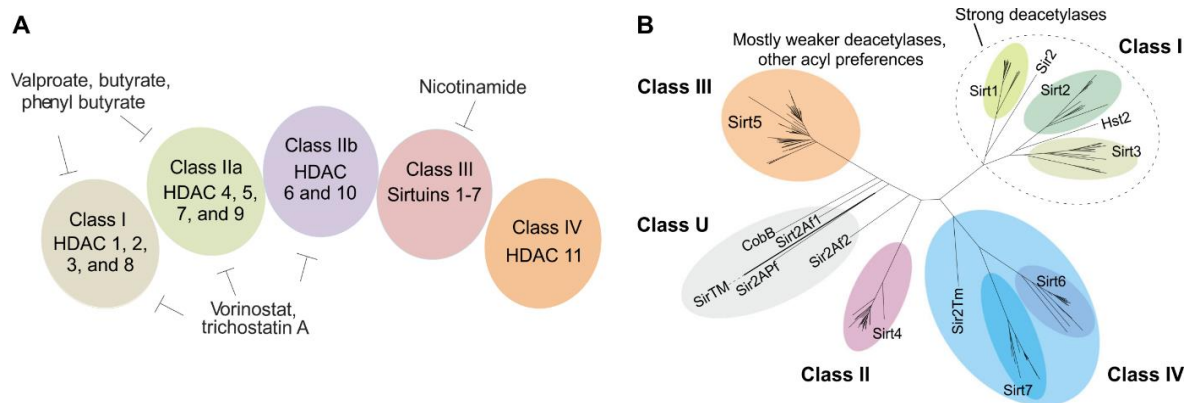


Figure 1.2: Classification of histone deacetylases (HDACs). **A** Mammalian HDACs are grouped into five subclasses and sensitive to different inhibitors as indicated. (Reprinted from Sharma *et al.* (2015)³⁴ with permission from Hindawi Publishing Corporation). **B** Phylogenetic tree of the sirtuin family, generated by a structure-based sirtuin alignment extended by aligning 195 chordate sirtuin sequences²⁹. (Adapted from Pannek *et al.* (2017)²⁹ with permission from Springer Nature).

Sirtuins are named after their first family member, silent information regulator 2 (Sir2) from *Saccharomyces cerevisiae*³⁵, which extends yeast life span³⁶. Mammals feature seven sirtuin isoforms, Sirtuin 1-7 (Sirt1-7), which are classified into five subclasses according to molecular phylogenetic analysis³⁷ (Figure 1.2B). Class I sirtuins consist of Sirt1-3 with a strong deacetylase activity, the Class II subfamily includes Sirt4, Class III Sirt5, Class IV Sirt6 and Sirt7, and Class U covers all undetermined members of the sirtuins³⁷. Importantly, Class II, III, and U sirtuins may have evolved earlier than the other classes, whereas Class I and IV sirtuins only occur in eukaryotes^{29,37}. Therefore, Sirt4 and Sirt5 could be the first eukaryotic sirtuins evolved. The seven mammalian sirtuins are localized in different cellular compartments: Sirt1 is mainly present in the nucleus, but can shuttle to the cytosol³⁷. In contrast, Sirt2 is a mostly cytosolic sirtuin and Sirt3, Sirt4, and Sirt5 are found in mitochondria³⁷. Sirt6 occurs in the nucleus and Sirt7 is the only mammalian sirtuin localized in the nucleolus³⁷.

1.4 Physiological relevance of sirtuin deacylases

1.4.1 Caloric restriction and lifespan extension

Today, the hallmarks of aging are known to encompass a variety of different malfunctions including genomic instability, telomere degradation, mitochondrial dysfunction, and cellular senescence³⁸. Targeting any of these factors for a prolonged life and health span is therefore an interesting endeavor. In 1935, McCay *et al.* showed that caloric restriction (CR, or DR for dietary restriction) results in life span extension in rodents³⁹. CR is the reduction of calories by 30-40% of an *ad libitum* diet without causing malnutrition⁴⁰. The beneficial effects of CR on health and life span include the improvement of metabolic health, the prevention of obesity⁴¹, and the delay or prevention of the onset of age-related diseases⁴⁰.

Interestingly, sirtuins seem to mediate some of these positive results on health span as they are activated under CR conditions⁴⁰. This activation depends on the NAD⁺/NADH ratio⁴² and the concentration of the product inhibitor NAM⁴³. In addition, a yeast Sir2 knockout failed to extend life span in response to CR⁴⁴. The requirement of Sir2-related genes for life span extension under CR conditions was also demonstrated in worms and flies⁴⁰. In line with these results, the overexpression of Sirt1 in mice had beneficial health effects, e.g., improved homeostasis, reduced body weight, and prevention of fatty liver⁴⁵⁻⁴⁷. In some organisms there may be other possibilities for life span extension in response to CR which are not sirtuin-dependent^{36,40}. But the evidence shows that sirtuins are an attractive target for pharmaceutical regulation by small-molecule activators to promote health and prolong life^{47,48}.

1.4.2 Role of sirtuins on cell signaling pathways

Mammalian sirtuins are localized in different subcellular compartments regulating various cell signaling pathways (Figure 1.3A). Sirt2 is present in the cytosol and deacetylates cytoskeletal components like α -tubulin⁴⁹, but can also shuttle to the nucleus for histone deacetylation⁵⁰. Sirt3, Sirt4, and Sirt5, are located exclusively in the mitochondria⁵¹ (Figure 1.3B). Sirt3 activates β -oxidation⁵¹ and influences the TCA cycle by deacetylating succinate dehydrogenase⁵², isocitrate dehydrogenase 2⁵³, acetyl-CoA synthetase 2 (AceCS2)⁵⁴, and glutamate dehydrogenase (GDH)⁵³. Sirt4 does not exhibit a pronounced deacetylation function, but regulates the TCA cycle and insulin secretion by inhibition of GDH through ADP-ribosylation⁵⁵ and repression of pyruvate dehydrogenase by delipoylation⁵⁶. Both Sirt3 and Sirt4 are involved in ATP generation and have a tumor-suppressive role^{29,51}. Sirt5 removes succinyl and malonyl groups from lysines²³ effecting glyceraldehyde 3-phosphate dehydrogenase⁵⁷ and carbamoyl phosphate synthase 1 (CPS1)²³.

Sirt5 also displays a robust deacetylase activity on CPS1 activating the urea cycle⁵⁸. Sirt6 is located in the nucleus and deacetylates histone H3 Lys9 at telomeric chromatin, thereby preventing premature ageing⁵⁹ and influencing base-excision repair (Figure 1.3A)³⁷. Sirt6 can also remove long-chain fatty acids like myristoyl from lysines and thus regulate tumor necrosis factor α (TNF α)²⁶. An additional auto-ADP-ribosylation activity of Sirt6 regulates its own activity⁶⁰. Sirt7 is settled in the nucleolus controlling rDNA transcription via interaction with RNA polymerase I⁶¹. Further functions of Sirt7 are still unknown.

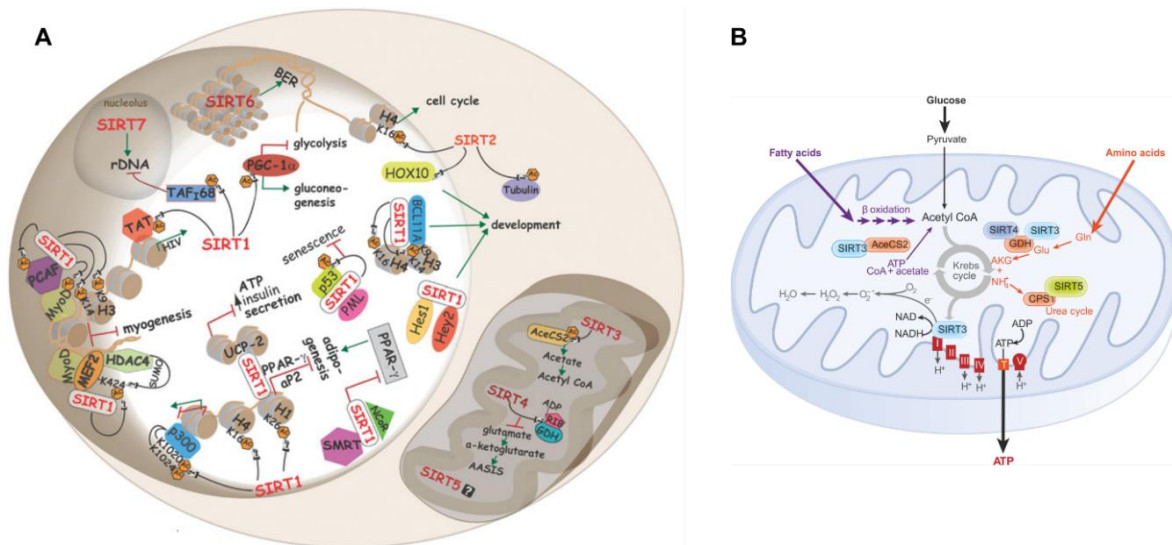


Figure 1.3: Physiological role of sirtuins on cell signaling and metabolism. **A** Relevance of sirtuins in cellular processes like chromatin formation, base excision repair, or repression of adipogenesis and cellular senescence. (Reprinted from Michan and Sinclair (2007)³⁷ with permission from Portland Press Ltd.). **B** Function of the mitochondrial sirtuins Sirt3, 4, and 5 on metabolic pathways including fatty acid oxidation, TCA (or Krebs) cycle, and urea cycle. (Reprinted from Haigis and Sinclair (2010)³⁵ with permission from Annual Reviews).

The best characterized mammalian sirtuin is Sirt1, which is located in the nucleus, but can shuttle to the cytosol³⁵. Sirt1 is a strong deacetylase acting on histones like H1K26⁶² and H4K16^{63,64} for maintaining intact chromatin structure (Figure 1.3A). Sirt1 also associates with CLOCK to control circadian rhythm⁶⁵. In addition, Sirt1 interacts with various transcription factors (Figure 1.4), for example by rescuing cells from senescence through deacetylation of the tumor suppressor p53³⁷. Sirt1 mobilizes fat stored in white adipose tissue through inhibition of the transcription factor peroxisome proliferator-activated receptor γ (PPAR γ)⁶⁶. Activated under low-nutrient conditions, Sirt1 deacetylates PPAR γ coactivator 1 α (PGC-1 α) promoting the switch from glycolysis to gluconeogenesis and to fatty acid oxidation^{67,68}. In response to oxidative stress, Sirt1 interacts with the forkhead box, subgroup O (FOXO) family of transcription factors to shift cells from apoptosis towards stress resistance^{69,70}. Any malfunction of the described sirtuin-substrate interactions can lead to pathologies associated with cell signaling or metabolism (Figure 1.4). Sirtuins are therefore promising targets for the treatment of diverse diseases.

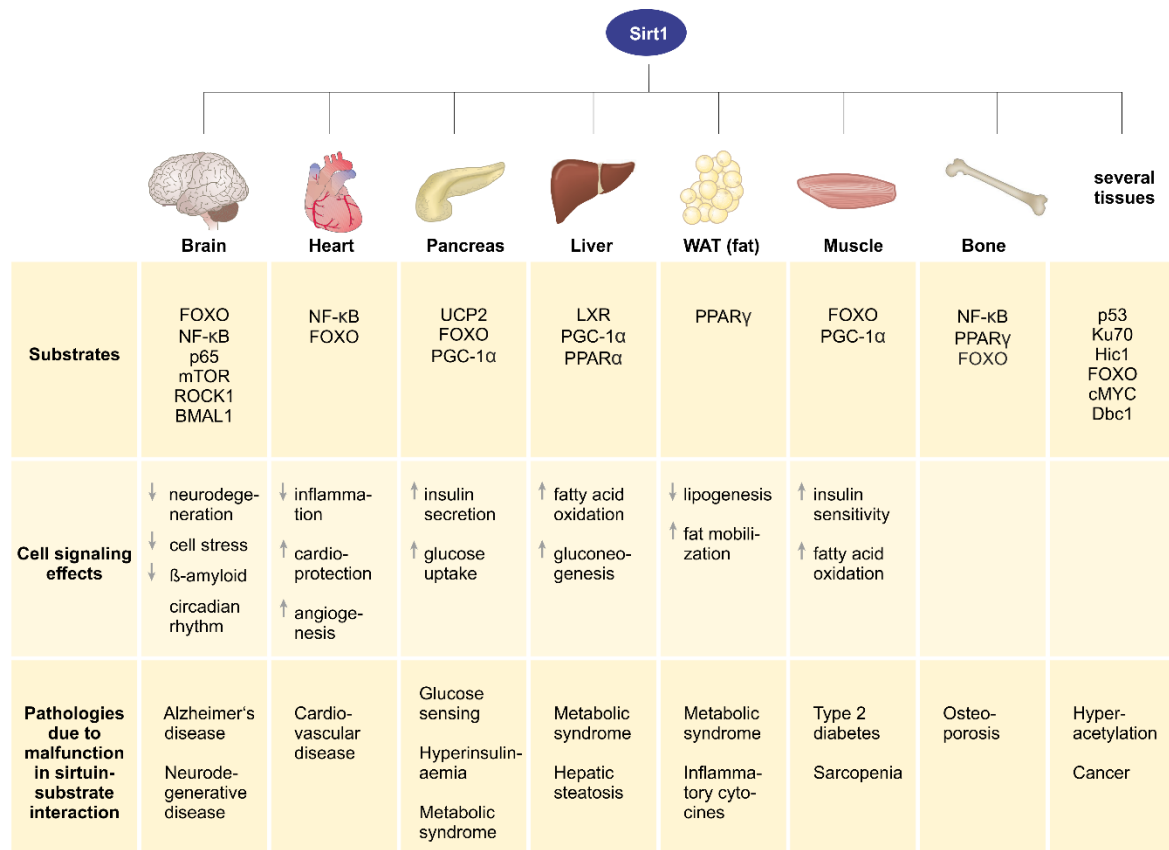


Figure 1.4: Sirt1 substrates and pathologies linked to malfunction of sirtuin-substrate interactions. Overview of the up- or downregulation of cell signaling effects by Sirt1-dependent deacetylation of substrates, together with the associated pathologies due to malfunction. (Created based on Haigis and Sinclair (2010)³⁵, Morris (2013)⁷¹, Bhullar and Hubbard (2015)⁷², and Bonkowski and Sinclair (2016)⁷³).

1.5 Structure and enzymatic mechanism of mammalian sirtuins

1.5.1 Structure of mammalian sirtuins

Sirtuins contain a highly conserved catalytic core domain of about 275 amino acids flanked by N- and C-terminal regions of different lengths^{33,74} (Figure 1.5A). These extensions comprise nuclear localization signals (NLS), nuclear export signals (NES), or mitochondrial targeting sequences (MTS)⁷⁴. Sometimes, the extensions also play a role in enzymatic autoregulation⁷⁵, such as for Sirt1, which has additional regions that are relevant for its activity⁷⁶. To date, more than 100 crystal structures of sirtuins have been solved⁷⁷ including human Sirt1^{78–81}, Sirt2⁸², Sirt3⁸³, Sirt5²³, and Sirt6⁸⁴. They allow for a detailed study of the overall sirtuin structure and distinctive features of some isoforms.

The sirtuin core domain consists of two globular subdomains: the structurally conserved larger NAD⁺-binding domain and the smaller, more variable Zn²⁺-binding domain, which are connected by four loops^{75,85} (Figure 1.5B). The NAD⁺-binding domain adopts a Rossmann fold with a central β-sheet of six β-strands surrounded by several α-helices³³. This Rossmann fold is typical for NAD⁺/NADH-binding proteins⁸⁵. The smaller domain is formed by

connection of two modules inserted between the Rossmann fold sequence⁷⁵: a Zn²⁺-binding motif with the consensus sequence Cys-X₂₋₄-Cys-X₁₅₋₄₀-Cys-X₂₋₄-Cys and an α -helical region, which exhibits the highest diversity among sirtuin isoforms⁷⁵. Although the Zn²⁺ ion does not contribute to the deacetylation reaction, it is essential for maintaining the structural integrity of the catalytic core³³. The active site cleft (Figure 1.5C) is located between the Zn²⁺-binding and the Rossmann fold domain perpendicular to the β -sheet of the NAD⁺-binding domain³³. One of the four connection loops between both domains contains the catalytic histidine³³. Another loop, referred to as the cofactor-binding loop, is essential for binding of NAD⁺³³. This latter loop exhibits a disordered conformation in apo sirtuins and becomes structured upon binding of NAD⁺⁸⁵ (Figure 1.5D). The binding pocket for NAD⁺ is divided into four subpockets (Figure 1.5C)³³: the A pocket for the adenine moiety, the B site for binding the nicotinamide ribose moiety, and the C pocket for the NAM moiety³³. The C-pocket is largely defined by the cofactor-binding loop and NAM forms van-der-Waals interactions with a Gly-Ala-Gly motif and π -stacking interactions with a phenylalanine on the loop³³. When NAD⁺ is not bound, the C-pocket is occupied by this phenylalanine³³. The D pocket was initially assumed to rebind free NAM^{33,86}, which was rebutted in a later study⁸⁷.

The substrate binds to the active site cleft with the acylated lysine inserted into a conserved hydrophobic tunnel^{33,85}. The substrate main chain forms antiparallel β -staple interactions with the β 8- α 9 loop within the Rossmann fold and the β 6- α 8 loop connecting the large and the small sirtuin core domain³³ (Figure 1.5E). Substrate binding causes a rigid body rotation of the Zn²⁺-binding domain and closure of the active site cleft³³. Sirtuin interaction with the substrate is limited to the backbone of the residues surrounding the acylated lysine, but the amino acid directly N-terminal to the acylated lysine can also form side chain interactions³³. Some sirtuins have specific features allowing the recognition of different acyl moieties or the development of substrate-sequence selectivity^{88,89}. While Sirt1, 2 and 3 are strong deacetylases⁹⁰, Sirt4-7 display other primary functions like dehydroxymethyl-glutarylation²⁹ and ADP-ribosylation⁵⁵ for Sirt4, desuccinylation, demalonylation²³, and deglutarylation²⁵ for Sirt5, and demyristoylation²⁶ for Sirt6. Sirt4 contains a loop reaching to the active site (Figure 1.5F), where a small additional channel allows to bind larger acyl moieties like lipoyl²⁹. In contrast, Sirt1-3 have a short hydrophobic tunnel to accommodate an acetylated lysine or a lysine modified with a slightly shorter or longer acyl moiety⁸⁹ (Figure 1.5G). Sirt6 forms a wide hydrophobic pocket to harbor long-chain fatty acyl modifications⁸⁹ (Figure 1.5H) and the Sirt5 acyl lysine tunnel can recognize negatively charged acyl moieties^{23,89} with a Tyr-X-X-Arg motif⁸⁹ (Figure 1.5I).

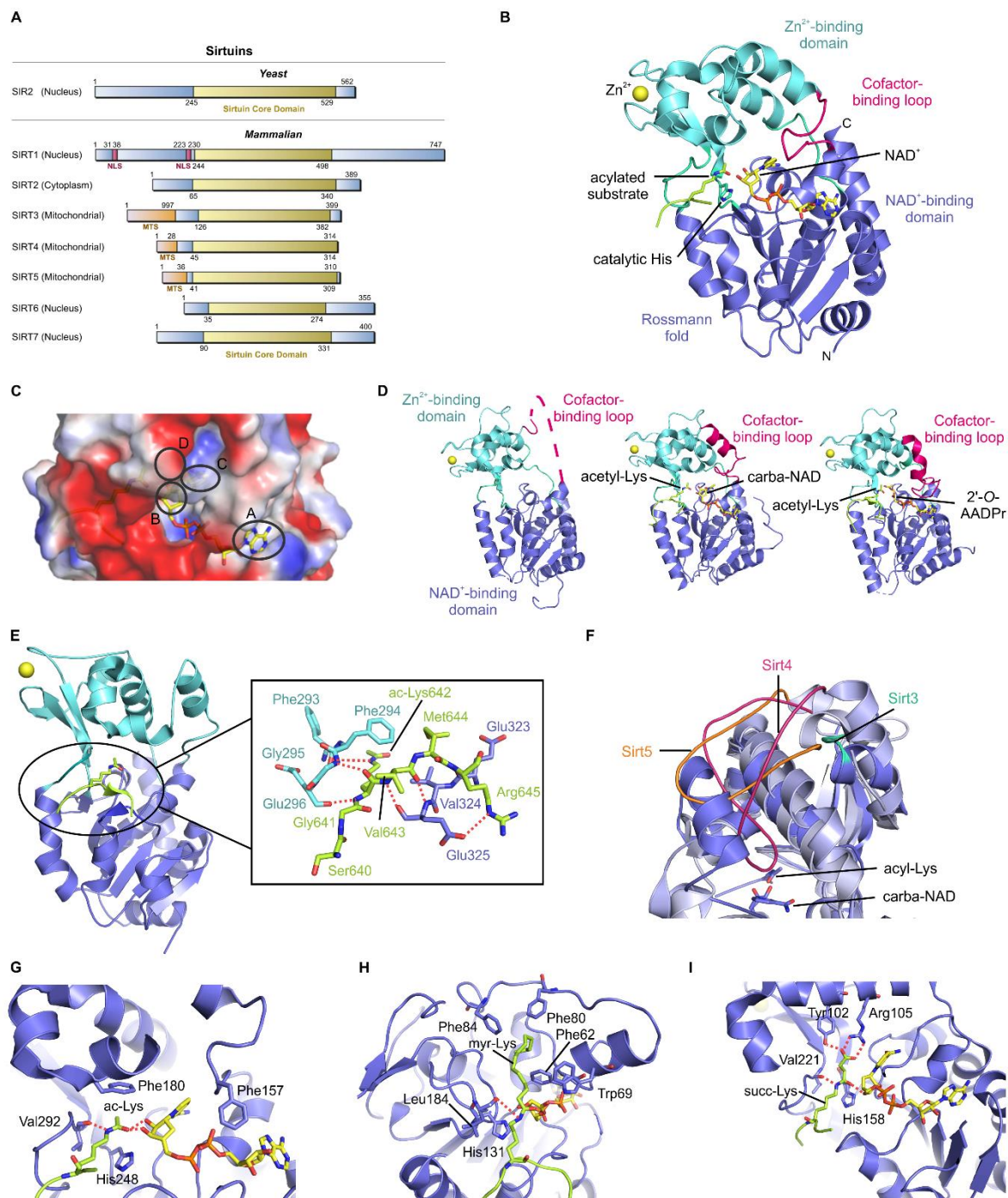


Figure 1.5: Structural characterization of sirtuins. **A** Sirtuins contain a conserved catalytic core (gold) flanked by extensions of different lengths (blue). (Reprinted from Guarente (2013)⁷⁴ with permission from Cold Spring Harbor Laboratory Press). **B** General structure of the sirtuin core with the NAD⁺-binding domain (blue) and the Zn²⁺-binding domain (cyan). The acylated substrate (lime) binds in close proximity of the catalytic His and carba-NAD⁺ (yellow) (PDB: 4FVT). **C** Electrostatic surface representation of the sirtuin active site ranging from -50 (red) to +50 k_BT/e_c (blue). NAD⁺ (yellow) binds at the A, B, and C site (PDB: 4FVT). **D** Conformational change of the cofactor-binding loop (pink) in yeast Hst2 upon binding of the substrate (lime) and NAD⁺ (yellow). The loop changes from a disordered form in apo Hst2 (PDB: 1Q14) to an α -helical open conformation with carba-NAD (PDB: 1SZC) and a closed conformation with ADPr (PDB: 1Q1A). **E** Binding of the acylated substrate (PDB: 3GLR). Interactions are highlighted with red dotted lines. **F** Sirt4 active site loop (pink) from xSirt4 (PDB: 5OJ7, lightblue) overlaid with the Sirt5 (PDB: 4G1C, white) surface loop (orange) and the short turn (green) in Sirt1-3 (PDB: 4FVT, blue). **G** Acetyl-lysine binding site of Sirt1-3 (PDB: 4FVT). **H** Acyl-lysine binding site of Sirt6 (PDB: 3ZG6) for binding of long-chain fatty acids. **I** Acyl-lysine binding site of Sirt5 (PDB: 4G1C) for recognition of negatively charged acyl moieties.

1.5.2 Role of extended termini in Sirtuin1

In contrast to the other mammalian sirtuins, Sirt1 has long N- and C-terminal extensions, which comprise about 200 amino acids in each direction (Figure 1.5A). The Sirt1 catalytic domain has a very low intrinsic deacetylase activity^{76,80}, but extension with adjacent regions leads to a 12-fold potentiation of Sirt1 activity with only the N-terminal part and a 25-fold enhancement of Sirt1 activity with both extensions⁷⁶. In this regard, the N-terminal extension seems to contribute to the catalytic rate⁷⁶ by facilitating substrate interactions via the motifs A (hSirt1 amino acids 1-53) and B (hSirt1 amino acids 171-229)⁹¹ and sometimes via exon 2 of a tissue-specific alternative splicing variant of Sirt1⁹². The C-terminal extension is beneficial for the binding affinity to NAD⁺⁷⁶. Out of these extensions, two Sirt1-specific regions were defined⁸⁰: the globular N-terminal Sirtuin-activating compound (STAC)-binding domain (SDB)⁸⁰ and the C-terminal regulatory region (CTR)⁷⁹. A Sirt1 construct containing both regions and the catalytic core domain proved to be fully functional and as active as full length Sirt1, thus it was called mini-Sirt1⁸⁰ (Figure 1.6A).

The CTR comprises human Sirt1 residues 641-665⁷⁹ and is also referred to as murine *essential for Sirt1 activity* (ESA)⁹³. In murine Sirt1, the ESA region acts as an “on switch” for Sirt1 deacetylase activity by looping back towards the catalytic core⁹³. Addition of the ESA/CTR region to the catalytic core of Sirt1⁸⁰ or to an N-terminally extended SBD-catalytic core variant of Sirt1^{76,93} thereby restores the activity comparable to fl-Sirt1. Interestingly, this activation of Sirt1 activity is revoked by binding of the leucine zipper region⁹³ of the known Sirt1 inhibitor deleted in breast cancer 1 (DBC1)^{94,95}. In a structure of the hSirt1 catalytic domain complexed with the co-expressed CTR region (Figure 1.6B), the N-terminal residues 641-653 of the hSirt1-CTR form a β -hairpin elongating the β -sheet of the NAD⁺-binding domain and covering a large hydrophobic patch⁷⁹. In contrast, the C-terminal residues 654-665 of the hSirt1-CTR are disordered and appear to bind in close proximity of the A pocket within the NAD⁺-binding site, which may result in an inhibitory effect on Sirt1 deacetylase activity⁷⁹. The CTR also contains two serines (Ser659 and Ser661) that are phosphorylated by casein kinase 2 (CK2) after DNA damage, leading to a higher hSirt1 deacetylation rate by increased substrate-binding affinity⁹⁶. Thus, the ESA/CTR motif seems to be essential for the intrinsic Sirt1 deacetylase activity, but also bears a regulatory role.

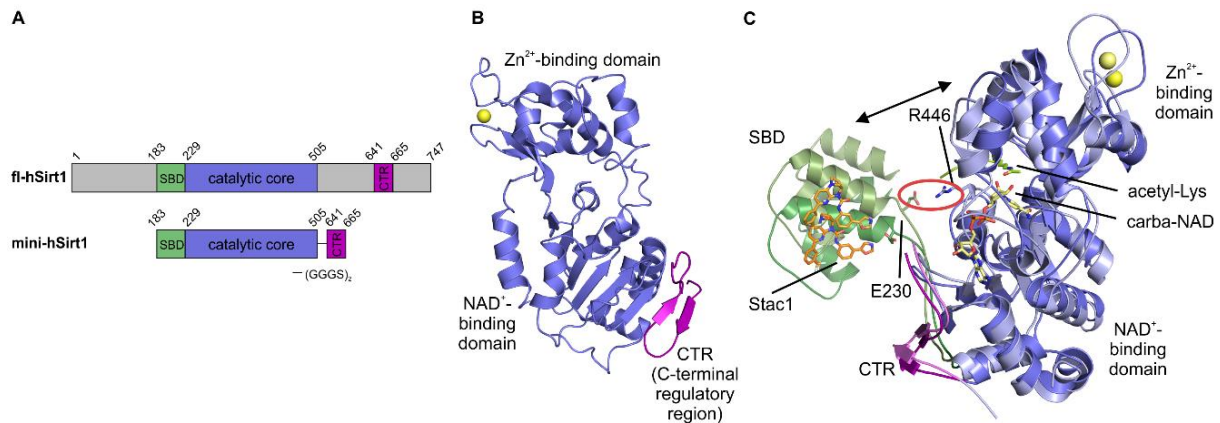


Figure 1.6: Role of Sirt1-specific additional domains. **A** Domain architecture of fl-hSirt1 with the STAC-binding domain (SBD), the catalytic core, and the C-terminal regulatory region (CTR). Mini-hSirt1 comprises those three regions with the CTR linked to the core via a (GGGS)₂-linker⁸⁰. **B** The CTR (purple) folds back towards the Sirt1 catalytic core (blue) elongating the β -sheet in the Rossmann fold domain^{76,79} (PDB: 4IG9). **C** STACs (here Stac1, orange) bind allosterically to the SBD (green)⁸⁰ (PDB: 4ZZH; dark colors). Upon binding of an acetylated substrate (lime) and NAD⁺ (yellow) (PDB: 4ZZJ; bright colors), the SBD attaches with a lever-like loop to the catalytic core forming a salt bridge between Glu230 and Arg446^{80,97} (red circle).

Directly N-terminal to the catalytic domain of Sirt1 lies the STAC-binding domain (SBD) comprising human Sirt1 residues 183-229^{47,80} (Figure 1.6A). The SBD is not essential for the intrinsic activity of Sirt1⁸⁰, but STACs can increase Sirt1 activity by binding to the SBD and lowering the Michaelis-Menten constant for the substrate in an enzyme-substrate complex^{47,80,98}. STAC-mediated activation depends on hydrophobic residues at the (+1) position next to the acetyl-lysine⁹⁷. The SBD is connected to the catalytic core of Sirt1 via a lever-like loop⁷³. Binding of a STAC alone keeps the loop in an extended conformation⁸⁰ (Figure 1.6C). In combination with an acetylated substrate and carba-NAD, STAC-binding leads to a rigid-body rotation of the SBD towards the catalytic core of Sirt1 by bending of the lever-like loop⁸⁰ (Figure 1.6C). A glutamate at the end of this loop plays a crucial role as it establishes a salt bridge between the loop-Glu230 and Arg446 in the catalytic core⁹⁷. Replacing the acetyl-substrate and carba-NAD with an inhibitor blocking both binding sites, the SBD moves even closer to the catalytic core of Sirt1⁸⁰ (Figure 1.6C). Thus, the SBD is a flexible Sirt1 region mediating STAC-dependent activation of Sirt1.

1.5.3 Enzymatic mechanism of sirtuin-catalyzed deacylation

Sirtuins are NAD⁺-dependent deacylases^{31,32}. NAD⁺ is either synthesized from tryptophan (*de novo* pathway), nicotinic acid (Preiss-Halder pathway), or generated via the NAD salvage pathway using NAM phosphoribosyl-transferase (NAMPT) and NAM mononucleotide adenylyl-transferase⁷³. Sirtuins utilize NAD⁺ to transfer the acyl moiety of a lysine under formation of 2'-*O*-acetyl-ADP-ribose (AADPr) and NAM⁹⁹ (Figure 1.7).

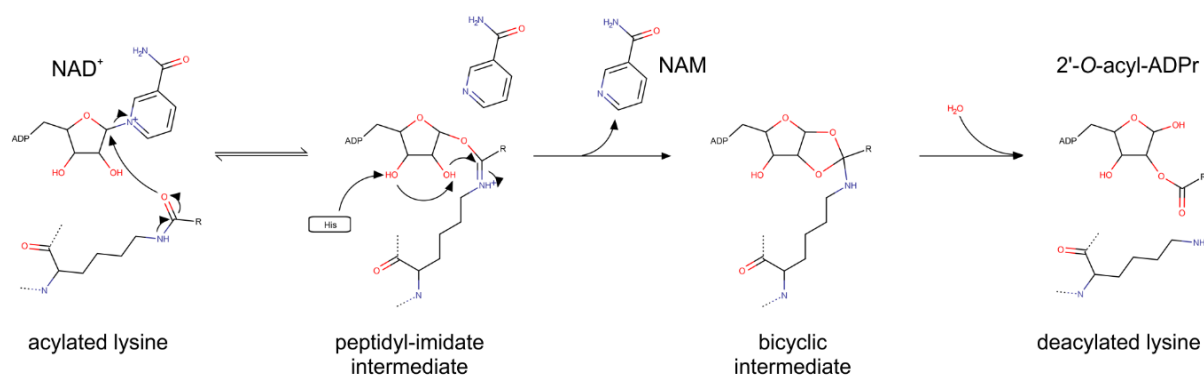


Figure 1.7: Deacylation mechanism of sirtuins. The first reaction step follows a concerted asynchronous S_N2 mechanism, which is driven by NAD^+ -hydrolysis facilitating the nucleophilic addition of the acyl oxygen to the C1' of ADPr¹⁰⁰. The resulting peptidyl-imidate intermediate is reversible¹⁰⁰. A catalytic histidine in the active site mediates a nucleophilic attack of the 2'-OH group of the intermediate affording a bicyclic intermediate⁹⁹. The deacylated lysine is released through an attack of the bicyclic intermediate by a base-activated water molecule leading to the formation of 2'-O-acyl-ADPr⁹⁹.

Several mechanisms have been discussed for the first reaction step¹⁰⁰. The S_N1 mechanism is centered on the formation of an oxonium ion by dissociation of the leaving group¹⁰⁰. In a traditional S_N2 mechanism, the nucleophilic attack occurs first and destabilizes the C-N bond of NAD^+ with simultaneous bond formation and dissociation¹⁰⁰. In an asynchronous S_N2 mechanism, the driving force is the dissociation of the leaving group, which is electrophile-driven and facilitates nucleophile association with asynchronous bond progressions¹⁰⁰. A study using kinetic isotope effects and computational approaches suggests that the first step is a concerted asynchronous S_N2 mechanism^{99,101}. Therefore, NAD^+ hydrolysis is the driving force which mediates nucleophilic addition of the lysine acyl oxygen to the C1' of ADPr resulting in the formation of a C1'-O-alkylamidate intermediate and NAM⁹⁹. As regulatory mechanism, free NAM remains bound in the active site in an equilibrium allowing it to reverse the peptidyl-imidate intermediate to NAD^+ by reacting at the C1'-anomeric carbon¹⁰⁰. In the second reaction step, a conserved catalytic histidine in the active site activates the 2'-hydroxyl group of the peptidyl imidate intermediate and mediates a nucleophilic attack of the lysine acyl carbon resulting in a 1', 2'-cyclic intermediate⁹⁹. In this step, NAM irreversibly leaves the reaction equilibrium¹⁰⁰. Finally, a base-activated water molecule attacks the bicyclic intermediate and releases 2'-O-acyl-ADPr and the deacylated lysine⁹⁹.

1.6 Modulation of sirtuin activity by small molecules

Sirtuin activity can be modulated by a variety of mechanisms including PTMs, transcriptional repression or activation, metabolites, complex formation, or substrate and cofactor availability¹⁰². Abundance or lack of active sirtuins is associated with beneficial or detrimental phenotypes^{103,104}. For example, the overexpression of Sirt1 has cardioprotective effects^{103,105} and shows beneficial effects in Alzheimer's¹⁰⁶ and Huntington's disease¹⁰⁷. In

contrast, Sirt1 knockout leads to p53 hyperacetylation¹⁰⁴, increasing p53 stability¹⁰⁸ and promoting downstream pathways linked to growth arrest, apoptosis, and cell senescence¹⁰⁹. Selective Sirt1 inhibition in cancer cells therefore offers an exceptional anti-cancer strategy since more than 50% of all human cancer types are associated with dysfunctional p53¹⁰⁹. Such selective regulation can be achieved through development of small-molecule effectors that directly target sirtuins or affect the complex formation between sirtuin and an interaction partner. For example, targeting Sirt2 with small-molecule inhibitors seems to be advantageous for the treatment of Parkinson's disease¹¹⁰. Sirt3 stimulation might prevent hepatic steatosis^{103,111}, while Sirt4 activation appears to be beneficial for the treatment of lung cancer¹¹¹ and hyperinsulinaemia¹¹¹. Activation of Sirt6 could also be an anti-cancer approach^{103,112} and stimulation of Sirt7 might prolong a healthy life span by rescuing from inflammatory cardiac hypertrophy^{103,104,113}. Sirtuins are therefore emerging and outstanding targets for small-molecule regulation in the treatment of various age-related diseases.

1.6.1 Regulation of sirtuin activity by metabolites and precursor enzymes

The nature of the NAD⁺-dependent deacylation mechanism makes sirtuins susceptible to the regulation by metabolites. The first reaction step in the deacylation mechanism yields a reversible peptidyl-imidate intermediate¹⁰⁰ (Figure 1.7). The leaving group NAM remains bound in the active site in an equilibrium and can act as a feedback-inhibitor¹⁰⁰. Sirtuins also depend on the availability of the cofactor NAD⁺ linking their activity to the energy state of a cell^{31,102}. At a low-energy state of the cell, NAD⁺ levels are upregulated correlating with increased sirtuin activity¹⁰². Since NAD⁺ is subject to reduction to NADH and the latter is a competitive inhibitor of sirtuins, an elevated NAD⁺/NADH ratio also leads to an increase in sirtuin activity⁴². In addition, NAD⁺ levels in the cell depend on the activity of enzymes involved in NAD⁺ biosynthesis¹⁰². For example, upregulation of NAMPT¹¹⁴ or treatment with the NAD⁺ precursor NAM mononucleotide was shown to enhance sirtuin activity¹¹⁴. Conversely, NAD⁺-consuming enzymes like poly-ADP-ribose polymerases (PARPs)¹¹⁵ compete directly with sirtuins for the same pool of NAD⁺ in the cell¹⁰² and their downregulation might promote sirtuin activity¹¹⁶. However, these natural regulation mechanisms by metabolites or precursor enzymes only provide a general activity modulation of all sirtuin isoforms and isoform-specific modulators are necessary to control selective pathways initiated by specific sirtuin deacylation reactions.

1.6.2 Inhibition of sirtuins by small molecules

Small-molecule inhibitors target the catalytic site of sirtuins¹¹⁷. They can prevent binding of substrate or cofactor by occupying any of the binding pockets like the acyl-lysine channel or the A/B/C pockets for NAD⁺¹⁰⁸. A special case is the neurotoxic suramin (Figure 1.8) which binds unspecifically to all pockets and is able to inhibit two sirtuin molecules¹¹⁸. A number of tumor-suppressive small molecule inhibitors for sirtuins have been proposed such as cambinol^{119,120} (Figure 1.8), which is competitive to the sirtuin substrate¹¹⁹. The related sirtinol¹¹⁸ (Figure 1.8) is beneficial for the treatment of human breast and lung cancer¹¹⁸, but also for parasitic diseases like leishmaniasis¹²¹. Salermide with a similar scaffold (Figure 1.8) is more potent and induces p53-independent apoptosis of cancer cells, but not of normal cells^{118,122}. However, those compounds are often not sirtuin isoform-selective¹¹⁸.

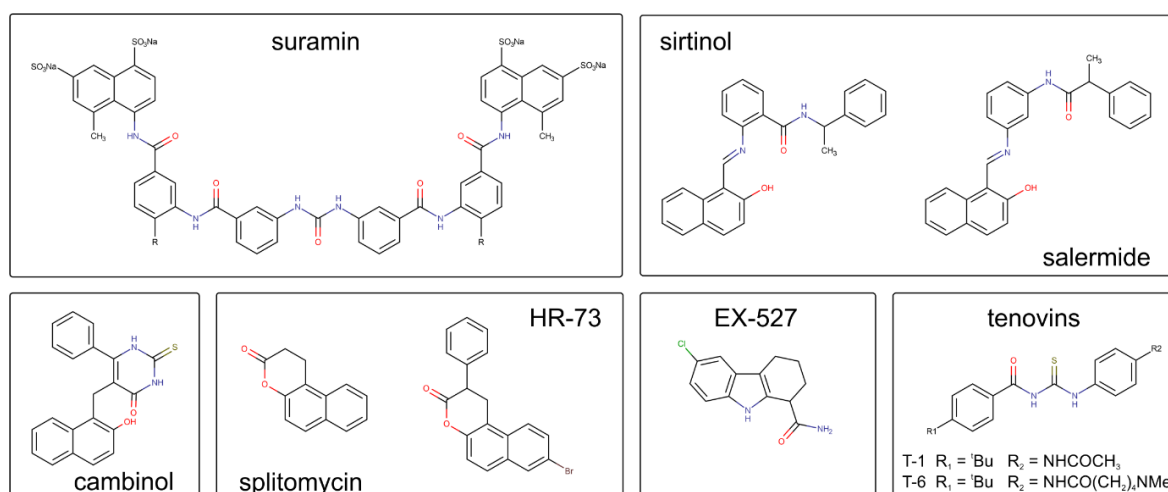


Figure 1.8: Small-molecule inhibitors of sirtuins. Inhibitors bind to the catalytic site of sirtuins. They act either by blocking any of the pockets like the acyl-lysine pocket or the A/B/C pockets for NAD⁺ or by stalling the deacylation mechanism and blocking product release.

In contrast, tenovin-1 and a more water-soluble analog, tenovin-6 (Figure 1.8), inhibit Sirt1 and reduce tumor cell growth *in vitro* and *in vivo*^{108,123}. Furthermore, splitomycin (Figure 1.8) is a selective inhibitor of yeast Sir2p and Hst2¹²⁴, but derivatives show antiproliferative activity in human breast cancer cells¹⁰⁸. The splitomycin derivative HR-73 (Figure 1.8) represses human Sirt1 potently with a negative effect on HIV1-Tat^{108,125}, revealing a new drug scaffold for the treatment of AIDS¹⁰⁸.

Sirtuin inhibitors can also directly impede the deacylation reaction by binding to a sirtuin-cofactor complex in presence or absence of substrate¹²⁶. EX-527 (Figure 1.8), for example, allows NAM cleavage and formation of the peptidyl-imidate intermediate by stabilizing the *closed state*, but represses product release¹²⁶. In turn, binding to a sirtuin-substrate complex as non-convertible cofactor analog is also possible¹⁰⁸. Besides nicotinamide, ADPr also

inhibits the first step of the sirtuin deacylation reaction¹¹⁸ and the non-hydrolyzable carba-NAD is a pharmacological sirtuin inhibitor¹⁰⁸. Such mechanism-based inhibitors, however, are often not sirtuin isoform-selective and may also restrain other NAD⁺-utilizing enzymes possibly reverting the positive effects on the cell¹⁰⁸. In contrast, thioacetyl-lysine peptides, based on known sirtuin substrates like p53, α -tubulin, histone H3, or ACS2^{127,128}, are potent mechanism-based sirtuin inhibitors, often with isoform selectivity¹⁰⁸. They follow the same reaction mechanism, but form stalled thioimidate intermediates^{108,127}.

1.6.3 Activation of sirtuins by STACs

In contrast to inhibitors, the binding site of activators is usually remote from the catalytic site allowing an allosteric but direct activation mechanism¹²⁹. Small-molecule sirtuin activators are summarized under the term of STACs, sirtuin-activating compounds (formerly Sirt1-activating compounds)¹²⁹. The first STACs were plant-based polyphenols (Figure 1.9) which mimic CR effects in yeast⁴⁸. They act by lowering the K_m values for the sirtuin substrate and NAD⁺⁴⁸. Resveratrol, which occurs in grape skin, is most prominent and has been attributed chemoprotective and cardioprotective effects¹³⁰. But resveratrol targets also other cell signaling proteins such as kinases, adenylyl cyclase, or DNA polymerase¹³⁰ suggesting that it may be an indirect activator for sirtuins^{131,132}. Indeed, *in vitro* activation of Sirt1 by resveratrol could only be detected with a substrate containing a C-terminal 7-amino-4-methylcoumarin (AMC) fluorophore^{133,134}. Resveratrol-mediated activation of Sirt1 was later found to be substrate-sequence selective requiring hydrophobic amino acids at the (+1) and (+3) position C-terminal to the acetyl-lysine mimicking the effects of the fluorophore¹³⁵. Structural studies with Sirt1⁸¹, Sirt3, and Sirt5¹³⁶ showed that resveratrol binds close to the acetylated lysine confirming the direct effect on sirtuins. Despite its poor bioavailability and only short-term effects on human health, resveratrol has been used in a variety of drugs like SRT501, resVida, or Longevinex^{®130,137}. Other plant-based polyphenols have an even less potent effect than resveratrol on the activity of selected sirtuin isoforms^{48,136,138,139}. The natural phytochemical dehydroabietic acid (DAA) (Figure 1.9), however, is a non-polyphenolic Sirt1 activator with a 10-fold higher potency than resveratrol¹⁴⁰. DAA occurs in the resin of conifers and was attributed antimicrobial, antiulcer, and cardiovascular activities as well as life span extension in *C. elegans*¹⁴⁰. In a molecular docking study, DAA was proposed to bind directly to Sirt1 in a similar mode as resveratrol, but independently of NAD⁺¹⁴⁰. But those described natural compounds are still weak activators and new synthetic STACs have been developed which deviate from the first generation of STACs⁴⁷.

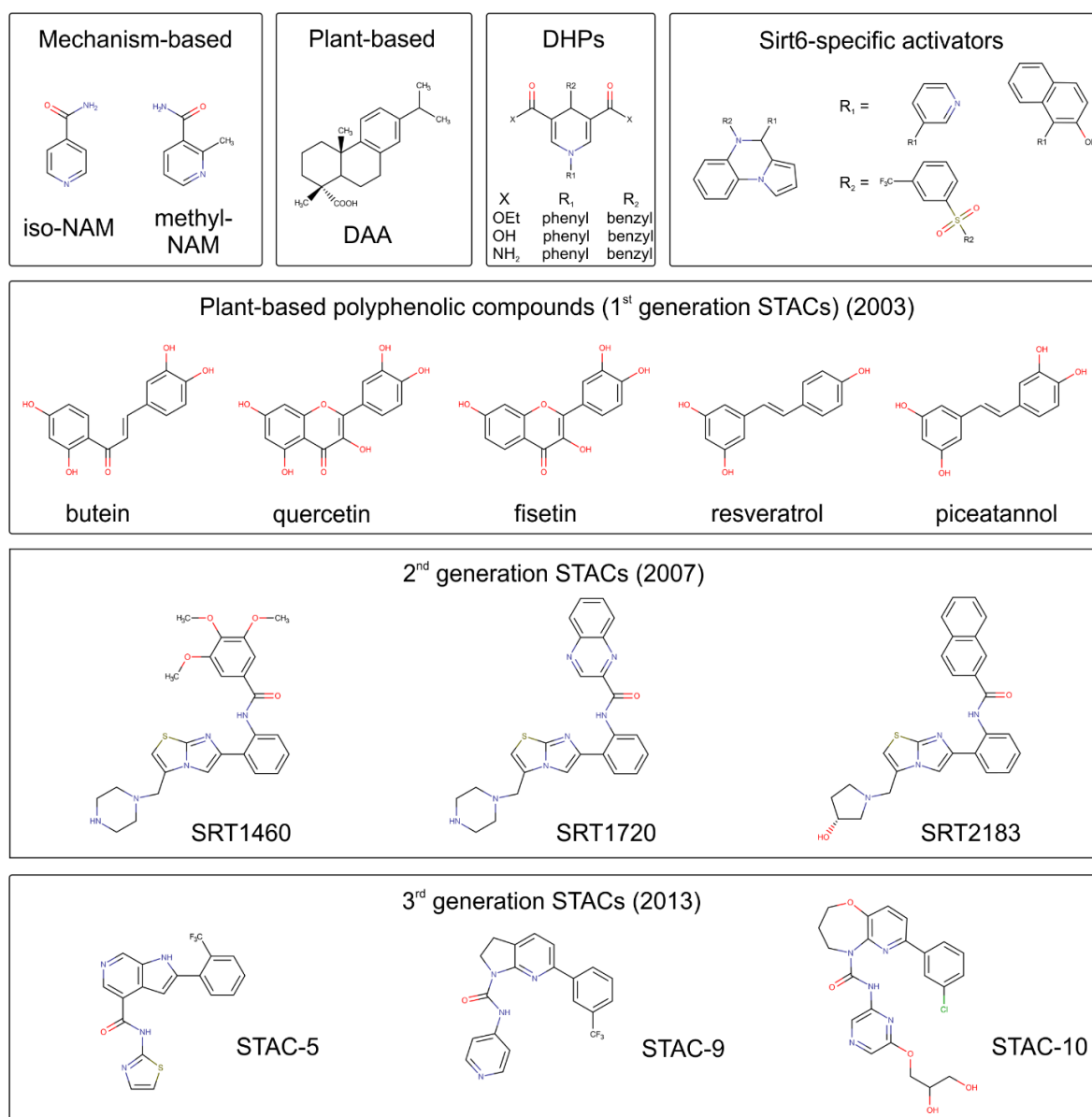


Figure 1.9: Activators of human sirtuins. Activators enhance sirtuin activity in a direct allosteric manner and mostly bind to sites distant from the catalytic core⁴⁸. Resveratrol and piceatannol bind close to the substrate^{81,136}, whereas STACs bind at a Sirt1-specific STAC-binding domain⁸⁰ and the pyrrolo-[1,2-*a*]-quinoxaline activators bind to a specific Sirt6 pocket adjacent to the acyl-binding channel¹⁴¹.

First, mechanism-based synthetic STACs were derived from NAM. Non-reactive analogs like methyl-NAM or iso-NAM (Figure 1.9) bind to the C pocket of the peptidyl-imidate intermediate and act as pan-sirtuin activators by displacing the feedback inhibitor NAM^{142,143}. This scaffold served to create the isoform-specific class of 1,4-dihydropyridine (DHP) activators^{137,144} (Figure 1.9). DHPs have different effects on Sirt1-3 depending on the substituents¹³⁷: compounds with a benzyl moiety on N1 have a stimulating effect on Sirt1-3, while DHPs with an additional phenyl moiety at the C4 position are selective for Sirt1¹⁴⁴.

Second generation STACs involve the compounds SRT1460, SRT1720, and SRT2183⁴⁷ (Figure 1.9) which improve insulin sensitivity⁴⁷ and mimic CR effects¹⁴⁵. SRT compounds

are selective for Sirt1^{47,117} and require the SBD to enhance Sirt1 activity⁴⁷. STAC-mediated Sirt1 activation is thereby facilitated by hydrophobic residues at the (+1) position of the acetylated lysine⁹⁷ and implies binding to an enzyme-substrate complex, which lowers the K_m for the substrate^{47,117}. A structural study showed that STACs bind actually to the SBD and STAC-binding to an enzyme-substrate complex causes the SBD to move towards the Sirt1 catalytic core⁸⁰ (Figure 1.6C). A salt bridge is thereby formed between the crucial Glu230⁹⁷ at the hinge region of the SBD and Arg446 in the catalytic core to keep the SBD at a distance where STACs can stimulate Sirt1^{73,80}. Further sets of STACs with improved water-solubility, potency, and bioavailability were presented by Dai *et al.*¹²⁹, Hubbard *et al.*⁹⁷, and the STAC research company Sirtris¹⁴⁶ comprising the third generation of STACS (Figure 1.9).

Activators for other sirtuin isoforms often lack potency or selectivity. However, a family of pyrrolo-[1, 2-*a*]-quinoxaline derivatives (Figure 1.9) was found as potent Sirt6 activators¹⁴¹. They bind to a Sirt6-specific pocket, which is absent in Sirt1 because the cofactor-binding loop and the helical module cover this area¹⁴¹. On the other hand, Sirt6 would not be able to exploit the direct allosteric activation mechanism described for Sirt1 since its N-terminus blocks the resveratrol binding site¹⁴¹. This demonstrates that different sirtuin isoforms can be activated by different activators which are potent and selective over other sirtuin isoforms.

1.7 Modulation of Sirt1 activity by other proteins

In addition to modulation of sirtuin activity by small molecules, other proteins can regulate Sirt1 activity in the cell¹⁰². Such fine-tuning effects on Sirt1 activity include transcriptional activation, e.g., by FOXO1, FOXO3a, PPAR α , or PPAR β/σ , or transcriptional repression, e.g., by PPAR γ , or hypermethylated in cancer 1 (Hic1)¹⁰². Furthermore, PTM-induced stimulation of Sirt1 activity can be achieved through phosphorylation¹⁴⁷ and sumoylation¹⁴⁸, whereas PTM-induced inhibition of Sirt1 is caused by methylation or nitrosylation¹⁰². A third way to modulate Sirt1 activity is direct association with other proteins¹⁴⁹. Up to now, *Active regulator of Sirt1* (AROS), deleted in breast cancer 1 (DBC1), Hic1, and HIV1-Tat are known for their roles in the activation or inhibition of Sirt1 by complexation^{102,149} (Figure 1.10).

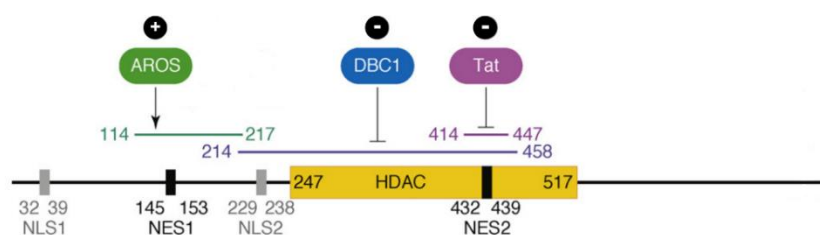


Figure 1.10: Regulation of Sirt1 activity by other proteins and their putative binding sites to human Sirt1. (Adapted from Kwon *et al.* (2008)¹⁴⁹ with permission from Elsevier).

1.7.1 Regulation of Sirt1 activity by AROS

AROS is a nuclear protein of 142 amino acids¹⁵⁰, which engages with ribosomal protein S19 (RPS19)¹⁵¹ to act in ribosome biogenesis¹⁵² and is thus also called RPS19 binding protein 1 (RPS19BP1)¹⁵². AROS also binds to the N-terminal amino acids 114-217 of hSirt1¹⁵⁰ (Figure 1.10) independent of the Sirt1 deacetylase activity¹⁵⁰. The initial study proposed that the deacetylase activity of Sirt1 is enhanced by AROS, thereby repressing the activity of p53 as observed in several cancer cell lines¹⁵⁰. *In vitro*, Sirt1 was also active in absence of AROS and could only be stimulated up to 2-fold by AROS¹⁵⁰. Since the *in vivo* effects exceeded the *in vitro* effects, an additional factor was suggested to be involved in the AROS-Sirt1 interaction^{150,153}. This could be either a Sirt1 inhibitor, which is displaced by AROS, or another activator forming a synergistic Sirt1 activation complex with AROS¹⁵³. However, such a factor has not been identified yet and subsequent studies have also shown contradictory results regarding the AROS-Sirt1 interaction. First, AROS was only able to stimulate Sirt1 in response to cell damaging stress in human cancer cell lines, but not in non-cancerous human cell lines¹⁵⁴. Therefore, AROS was proposed to promote specifically the survival of cancer cells¹⁵⁴. Second, another study observed a weak inhibitory effect on hSirt1 *in vitro* using recombinant and refolded AROS¹⁵⁵. Although the CD spectrum of the refolded AROS suggested distinct secondary structure elements, it could not be excluded that the refolded protein does not exhibit its native form¹⁵⁵. Finally, Kokkola *et al.* confirmed that AROS does not alter Sirt1 activity in non-cancerous human cell lines¹⁵⁶. In different Sirt1 *in vitro* activity assays with recombinant GST-AROS (as for the initial study) and His₆-tagged AROS (as for the refolded protein), AROS inhibited Sirt1 with the degree of inhibition depending on the type of AROS used and the assay conditions¹⁵⁶. A substrate-dependent effect was excluded because various natural and non-natural substrates showed comparable effects¹⁵⁶. However, the hSirt1 region from amino acids 114-217 does not seem to be sufficient for AROS-mediated inhibition¹⁵⁶. In this regard, DNA damage-induced phosphorylation of hSirt1 Ser682 by homeodomain interacting protein kinase 2 (HIPK2) disrupts the complex between Sirt1 and AROS¹⁵⁷ and thus, a C-terminal region of hSirt1 may be required for a stable complex. Furthermore, AROS might stabilize association of the N-terminal Sirt1 motifs A (hSirt1 amino acids 1-53) and B (hSirt1 amino acids 171-229), promoting Sirt1-substrate interaction⁹¹. In turn, AROS peptides from amino acids 1-19, 26-42, 78-99, and 109-126 were still able to inhibit fl-hSirt1 *in vitro* suggesting several binding regions or a competition to the Sirt1 substrate¹⁵⁶. Therefore, these results from several studies indicate that the Sirt1-AROS interaction is complex and highly dependent on the biological context¹⁵⁶.

1.7.2 Inhibition of Sirt1 by DBC1

DBC1 is located at a region of chromosome 8p21 which is homozygously deleted in human breast cancer^{95,158}. Today, it is known that rather a disturbed balance between Sirt1 and DBC1 expression is responsible for human breast cancer and that Sirt1 inhibition might prevent tumorigenesis¹⁵⁹. Other names for DBC1 are also KIAA1967 because of its role as component of the DBIRD complex regulating alternative splicing¹⁶⁰ and CCAR2 due to its sequence homology to cell cycle activator and apoptosis regulator 1 (CCAR1)^{161,162}. DBC1 is a nuclear protein of 923 amino acids comprising several domains¹⁶³ (Figure 1.11A): its N-terminal region hosts an NLS (amino acids 202-219) and a leucine zipper motif (LZ; amino acids 243-265), while the C-terminal region includes an EF hand motif (amino acids 704-748) and a coiled coil region (amino acids 794-918)¹⁶³. In addition, two domains are predicted for DBC1: an RNA-binding domain (amino acids 55-112), presumably involved in formation of the DBIRD complex, and a central putative nudix hydrolase domain (NHD; amino acids 339-462) for hydrolysis of nucleotides¹⁶³. However, the DBC1 NHD sequence lacks some key features rendering it inactive, but able to sense and bind NAD⁺¹⁶⁴, thereby preventing DBC1 from inhibiting PARP1¹⁶⁵.

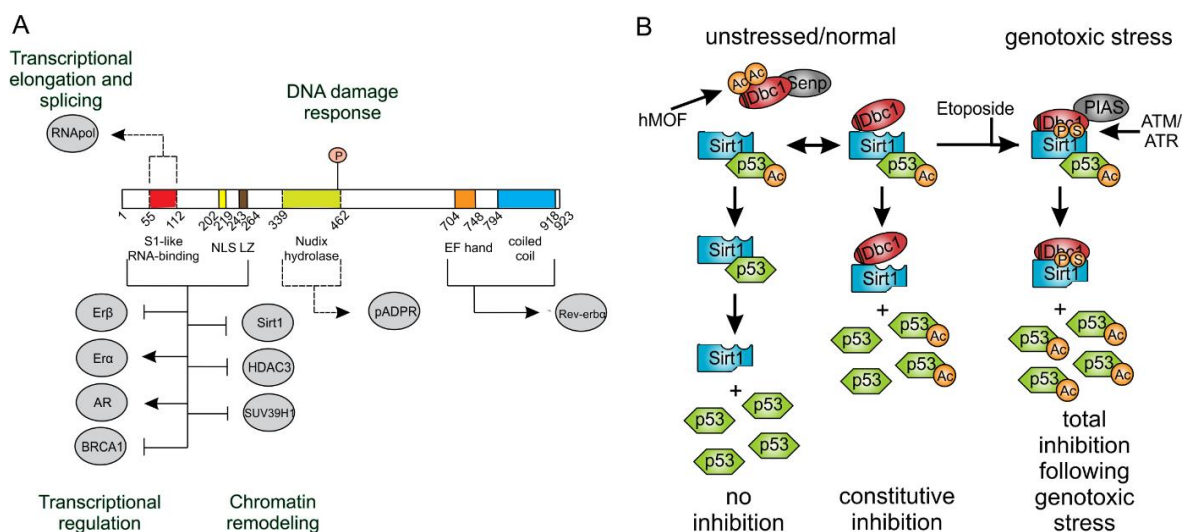


Figure 1.11: Regulation of Sirt1 activity by DBC1. **A** DBC1 domain architecture. Putative binding regions to known interaction partners are indicated. (Reprinted from Joshi *et al.* (2014)¹⁶³ with permission from Longdom Publishing). **B** Revised model of the DBC1-Sirt1 interaction. In unstressed cells, deacetylated DBC1 can inhibit the Sirt1 activity towards p53. Following genotoxic stress, DBC1 is phosphorylated at Thr454 which induces sumoylation of DBC1 Lys591 and creates a second binding site on Sirt1, leading to complete repression of Sirt1. (Created based on studies by Yuan *et al.* (2012)¹⁶⁶, Zannini *et al.* (2012)¹⁶⁷, and Park *et al.* (2014)¹⁶⁸).

DBC1 interacts directly with Sirt1 and inhibits Sirt1-mediated deacetylation of p53 in a dose-dependent manner *in vivo* and *in vitro*^{94,95}. DBC1 does not impair the activity of other human sirtuin isoforms⁹⁵. Different Sirt1 regions were suggested to be sufficient for DBC1 binding and include either the catalytic core of Sirt1^{94,95}, or the B-motif (hSirt1 amino acids 171-

229)⁹¹, or the bottom of the Rossmann fold of the catalytic core where the ESA/CTR interacts with Sirt1⁹³. In favor of the latter, a peptide comprising the DBC1 LZ inhibited Sirt1 activity and had a higher affinity for Sirt1 than the ESA/CTR region⁹³. DBC1 might thus compete with the ESA/CTR for the same binding site and inhibit Sirt1 by preventing ESA/CTR-mediated Sirt1 activation⁹³. The region of DBC1 to which Sirt1 binds is also controversial although all reports agree that the N-terminal part of DBC1 mediates binding to Sirt1^{93-95,169,170} (Figure 1.11A). This could include either DBC1 amino acids 1-265 with the NLS and LZ motifs⁹⁵, or solely the LZ^{93,94}, or DBC1 amino acids 1-240 excluding the LZ^{169,170}.

The DBC1-Sirt1 interaction is complex and involves various factors in the cell (Figure 1.11B). In normal and unstressed cells, Sirt1 deacetylates its target p53 and DBC1 binds to Senp1, an enzyme that desumoylates DBC1¹⁶⁸. A constitutive, yet incomplete inhibition of Sirt1 is achieved when isolated DBC1 binds to Sirt1 with its N-terminal region¹⁶⁶. However, acetylation of isolated or Senp1-bound DBC1 at Lys112 and Lys215 by the histone acetyltransferase hMOF¹⁶¹ prevents the DBC1-Sirt1 association and increases Sirt1 activity¹⁶¹. In turn, DBC1 can be deacetylated at Lys215 by Sirt1 leading to cytoplasmic localization of DBC1, which also obstructs its inhibitory association with Sirt1¹⁷⁰. Upon DNA damage and oxidative stress, acetylation of DBC1 is inhibited through phosphorylation of DBC1 Thr454 by ataxia telangiectasia-mutated (ATM) kinase^{161,166,167} or ataxia telangiectasia and Rad3-related (ATR) kinase¹⁶⁷. This phosphorylation increases the Sirt1-DBC1 interaction by inducing a conformational change of DBC1, which creates a second binding site for Sirt1^{166,167}, and by switching from Senp1 to PIAS3 as binding partner for DBC1¹⁶⁸. PIAS3-bound DBC1 can form a ternary complex with Sirt1 and inhibit Sirt1 more potently than isolated DBC1¹⁶⁸. In addition, phosphorylation at Thr454 facilitates DBC1 sumoylation at Lys591, further strengthening the DBC1-Sirt1 interaction and leading to complete suppression of Sirt1 deacetylase activity¹⁶⁸. A positive feedback loop between Sirt1 and c-Myc, which is overexpressed in the majority of tumors, causes activation of c-Myc through Sirt1-mediated deacetylation¹⁷¹. In turn, c-Myc activates Sirt1 by sequestering DBC1 from Sirt1 and upregulating the NAMPT expression levels¹⁷¹. Thus, inhibition of Sirt1 by DBC1 is highly regulated in cells.

1.7.3 Modulation of Sirt1 activity by Hic1

HIC1 is localized at the chromosome region 17p13.3, which is frequently hypermethylated or deleted in various cancers such as medulloblastoma¹⁷², breast cancer¹⁷³, gastric cancer¹⁷⁴, or lung cancer^{175,176}. Functional Hic1 is therefore a tumor suppressor¹⁷⁷. Hic1 expression is

directly regulated by p53^{178,179}. Due to alternative splicing, *HIC1* encodes for two proteins, a major transcript of 714 amino acids and a minor transcript with 19 additional N-terminal amino acids¹⁸⁰. The nuclear protein acts as transcriptional repressor by binding to the Hic1-responsive element (HiRE) with its C-terminal zinc fingers¹⁷⁷ (Figure 1.12A). Hic1 has three distinct domains which all interact with Sirt1: an N-terminal BTB/POZ (bric-a-brac, tramtrack, and broad complex/pox virus and zinc finger) domain, a central core domain, and a C-terminal domain with five krueppel-like C₂H₂ zinc fingers (ZF)¹⁸¹ (Figure 1.12A).

The BTB/POZ domain is a conserved structural domain with low sequence identity found in many transcription factors¹⁸². BTB-ZF proteins are able to homodimerize, heterodimerize, oligomerize, or interact with other proteins¹⁸². An N-terminal extension of 25 amino acids in BTB-ZF proteins folds into one β -sheet and one α -helix and mediates dimerization of BTB-ZF proteins¹⁸². In contrast to many other BTB domains, the Hic1 BTB/POZ domain acts independently of HDAC1 as transcriptional repressor¹⁸³. Instead, the Hic1 BTB/POZ domain binds directly to Sirt1 and forms a transcriptional repression complex which associates with the *SIRT1* promoter and inhibits Sirt1 transcription¹⁸⁴ (Figure 1.12B). This leads to hyperacetylated p53 and transcription of pro-apoptotic genes in response to DNA damage¹⁸⁴. Acetylated p53 in turn binds to the *HIC1* promoter enforcing its further transcription^{178,179} (Figure 1.12B). During aging, the *HIC1* promoter undergoes hypermethylation, which reduces both Hic1 expression and formation of the transcriptional repression complex with Sirt1, thereby facilitating deacetylation of p53, cell proliferation, and tumorigenesis¹⁸⁴.

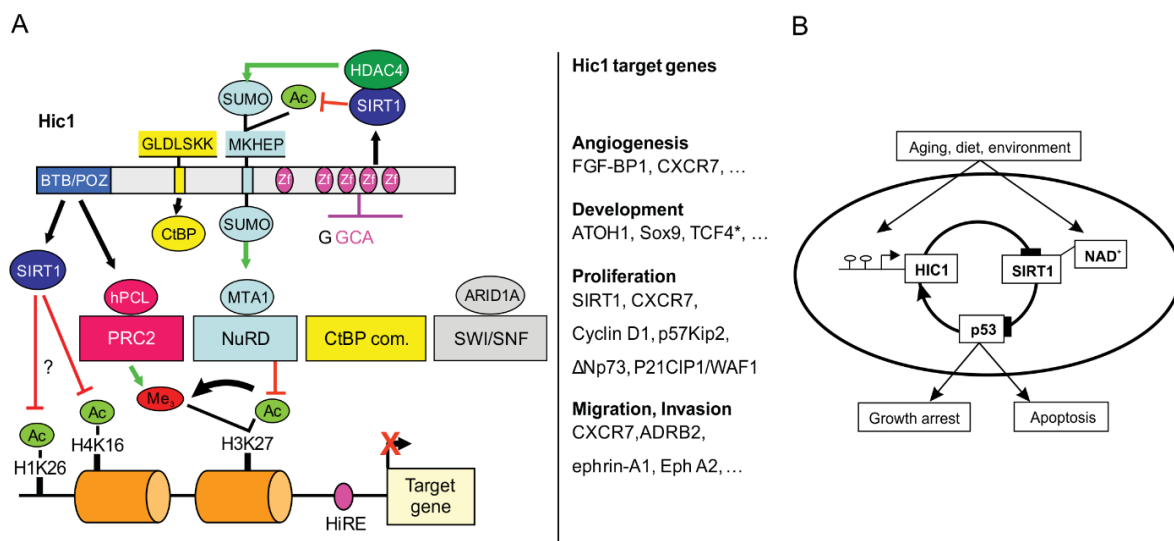


Figure 1.12: Interaction of Sirt1 with hypermethylated in cancer 1 (*Hic1*). **A** Domain architecture of Hic1 with interacting regions for various proteins. The N-terminal BTB/POZ domain¹⁸⁴, the central core domain¹⁸⁵, and the C-terminal ZF cluster^{185,186} of Hic1 interact with Sirt1 in different ways. (Adapted from Rood *et al.* (2013)¹⁸¹ with permission from Taylor and Francis and small modifications based on Dehennaut *et al.* (2012)¹⁸⁵ and Le Douce *et al.* (2016)¹⁸⁶). **B** Feedback-loops in the interaction between p53, Hic1, and Sirt1. (Reprinted from Chen *et al.* (2005)¹⁸⁴ with permission from Elsevier).

In addition to the transcriptional repression via the BTB/POZ domain, Hic1 contains a second autonomous repression domain, the central core domain¹⁸⁷. It comprises a GLDLSKK motif recruiting the co-repressor C-terminal binding protein (CtBP) to suppress transcription in a trichostatin A-sensitive manner¹⁸⁷ (Figure 1.12A). Binding of CtBP depends on dimerization of Hic1 via its BTB/POZ domain, although the N-terminal domain does not associate with CtBP¹⁸⁷. The core domain also contains a MKHEP motif with an acetylation/sumoylation switch¹⁸⁸ (Figure 1.12A). While P300/CBP acetylates Hic1 Lys314¹⁸⁵, Sirt1 recruits HDAC4 upon genotoxic stress and deacetylates Hic1, which in turn promotes sumoylation of the same lysine mediated by HDAC4¹⁸⁸. Sumoylation of Hic1 is required for recruitment of the co-repressor metastasis-associated protein 1 (MTA1) within the NuRD complex and initiation of the pro-apoptotic response to irreparable DNA double-strand breaks^{181,189}.

The C-terminal domain of Hic1 contains five krueppel-like zinc fingers (ZF) with the last four forming a cluster¹⁸¹. This ZF cluster mediates binding to the HiRE DNA for transcriptional repression depending on the BTB/POZ domain¹⁷⁷. In addition, the ZF cluster also recruits Sirt1 for deacetylation of Hic1 Lys314^{185,186} (Figure 1.12A). In this respect, hSirt1 amino acids 610-677 including the ESA/CTR region are essential for interaction with the Hic1-ZF and deacetylation of Hic1 Lys314¹⁸⁵. Following genotoxic stress, casein kinase 2 (CK2) mediates phosphorylation of Ser659 and Ser661 within the Sirt1 ESA region, which is crucial for the interaction of Sirt1 and Hic1¹⁸⁵ and was previously found to increase the Sirt1-substrate binding affinity⁹⁶. However, whether this phosphorylation of Sirt1 is also necessary for the interaction with Hic1 via its BTB/POZ domain or whether both mechanisms act independently of each other is not clear.

1.7.4 Inhibition of Sirt1 by HIV1-Tat

Human immunodeficiency virus type 1 (HIV1) is the cause for acquired immunodeficiency syndrome (AIDS)¹⁹⁰, which affects more than 30 million people¹⁹¹. A combinative highly active antiretroviral therapy is used to treat AIDS patients¹⁹². However, the required lifelong drug adherence often leads to side effects, which eventually cause non-AIDS-related diseases such as cardiopathy, nephropathy, or cancer¹⁹³. Understanding the virus replicative cycle with all factors involved is thus essential for the development of more potent anti-HIV1 drugs with increased bioavailability.

Upon HIV1 infection, mature HIV1 virions attach to CD4⁺ T-cell receptors of host target cells¹⁹³ (Figure 1.13A). The viral envelope fuses with the host cell membrane and releases its content into the cytoplasm, where HIV1 RNA is reversely transcribed¹⁹³. The synthesized

double-stranded DNA forms a pre-integration complex with viral and host proteins, which is imported to the nucleus and integrated into the host cell genome¹⁹³. During the early phase of viral transcription, the rate is driven by host factors generating spliced viral mRNAs, which are exported to the cytoplasm¹⁹³. Subsequent translation of the viral proteins transactivator of transcription (Tat) and regulator of expression of virion proteins (Rev) activates the late phase of viral transcription¹⁹³. Tat and Rev re-enter the nucleus, where Tat recruits the positive transcription elongation factor (P-TEFb) to RNA polymerase II raising the transcriptional rate of unspliced viral RNA¹⁹³. Rev then exports the unspliced RNA to the cytoplasm, where it is packed into new virions containing viral proteins and the viral genome¹⁹³.

The viral protein Tat is encoded by two exons, a major exon 1 with the highly conserved amino acids 1-72 and a subtype-specific exon 2 with variable lengths of amino acids 73-86 or 73-101¹⁹⁴. Tat comprises five functional protein domains¹⁹⁴: the N-terminal acidic/proline rich region, a cysteine rich region, the core region, a basic region, and the C-terminal glutamine rich region¹⁹⁴ (Figure 1.13B). The N-terminal part up to the core acts as activation domain mediating the interaction of Tat with the host cellular machinery¹⁹⁵. The basic region contains lysines and arginines and is responsible for binding of Tat to the transactivation responsive element (TAR) RNA¹⁹⁶. The same region also contains an NLS and cell penetrating peptide (CPP) signal mediating Tat translocation to the nucleus and entering of extracellular Tat into non-infected T-cells, respectively¹⁹⁷. Binding to the nuclear import receptor importin- α seems to be induced by the basic region of Tat as well¹⁹⁷. The amino acids encoded by exon 2 contain a conserved Arg-Gly-Asp (RGD) motif used for integrin-mediated cell adhesion in presence of divalent cations¹⁹⁸. Nuclear magnetic resonance (NMR) studies of HIV1-Tat revealed that the protein is very flexible with part of the N-terminus clamped between the hydrophobic core and the glutamine rich region¹⁹⁹. A recent crystal structure showed that the cysteine rich region of Tat is able to form small helices and bind two zinc ions upon association of Tat with P-TEFb²⁰⁰. Whether this conformational change of Tat is necessary for all interactions with other proteins remains to be clarified.

Tat deacetylation by Sirt1 is required to initiate HIV1 transactivation¹²⁵ (Figure 1.13C). In absence of Tat, NF- κ B binds to the HIV1 promotor and recruits P-TEFb, a complex of cyclin T1 and cyclin-dependent kinase 9 (Cdk9), to the RNA polymerase II^{195,201}. Cdk9 hyper-phosphorylates Ser2 in RNA polymerase II inducing transcription of the viral genome^{125,201} in a rate-limiting first step¹⁹⁵. Upon synthesis of Tat, the protein is phosphorylated at Ser16²⁰² and re-enters the nucleus where it binds to TAR¹²⁵. This allows

Tat to recruit P-TEFb directly accelerating HIV1 transcription¹²⁵. For elongation, acetylation of Tat Lys50 by CBP/p300 is required to release Tat from TAR and to associate with p300/CREB-binding protein-associated factor (PCAF) instead¹²⁵. Upon termination, all factors are released from RNA polymerase II²⁰¹ and Tat Lys50 is deacetylated by Sirt1 allowing Tat to separate from PCAF and to bind again to TAR, initiating a new cycle of HIV1 transcription¹²⁵. Therefore, Sirt1 seems to act as transcriptional coactivator during HIV1 transactivation.

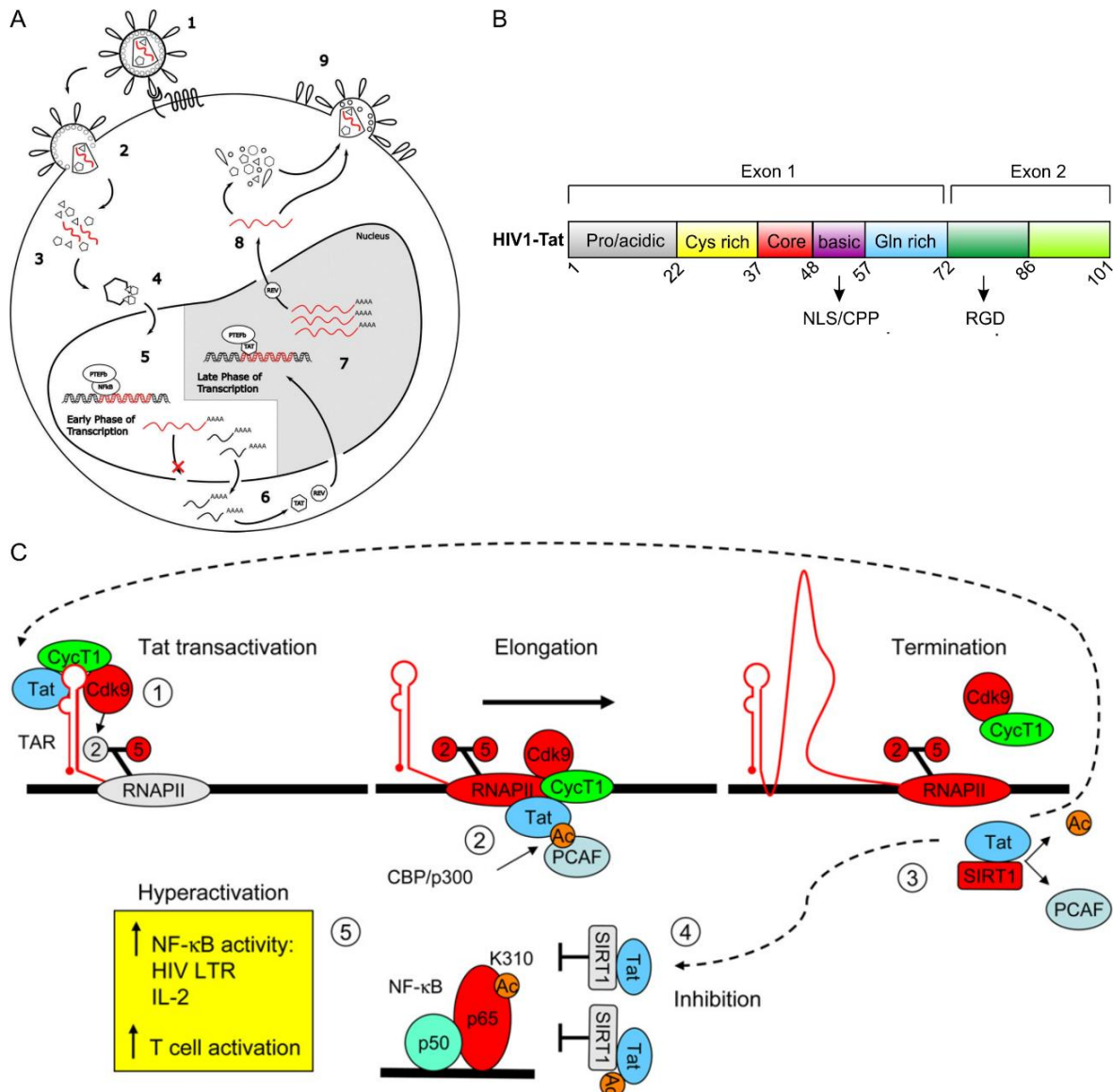


Figure 1.13: Regulation of Sirt1 activity by HIV1 transactivator of transcription (Tat). **A** HIV1 replication cycle. (Reprinted from Le Douce *et al.* (2016)¹⁹³ with permission from Taylor and Francis). **B** Domain architecture of HIV1-Tat²⁰³. **C** Importance of Sirt1 for HIV1 transcription. Deacetylated Tat binds to TAR and requires acetylation upon transcriptional elongation. After termination of HIV1 transcription, Tat is deacetylated by Sirt1 and recycled. In turn, Tat can bind to Sirt1 and inhibit its activity. Active and inactive proteins are shown in colors and grey, respectively. (Reprinted from Blazek *et al.* (2008)²⁰¹ with permission from Elsevier).

In addition, acetylated or deacetylated Tat is able to bind to the catalytic domain of Sirt1 and inhibit its deacetylase activity²⁰⁴. This leads to hyperacetylation of Lys310 in p65, a subunit

of NF- κ B, followed by continuous viral replication²⁰⁴ (Figure 1.13C). Inhibition of Sirt1 by Tat also results in hyperacetylated p53 and activation of the apoptosis response pathway²⁰⁵. In this regard, extracellular Tat can invade non-infected CD4⁺ T-cells²⁰⁶, impede Sirt1 deacetylation activity, and induce apoptosis resulting in a decline of CD4⁺ T-cells, which is a critical hallmark for the development of AIDS²⁰⁵. A mechanism was proposed where Tat acts as a “supersubstrate” for Sirt1 which first mediates its own deacetylation, but then remains bound to the deacetylase thereby inhibiting Sirt1 through blocking access for other substrates²⁰⁴. In contrast, binding of Tat to Sirt1 does not require acetylation of Tat¹²⁵.

A number of further regulation mechanisms involving Sirt1 act upon HIV1 infection. First, Tat indirectly impairs Sirt1 expression by depletion of intracellular NAD⁺ levels causing a decrease in NAD⁺/NADH ratio²⁰⁷ and reduced promotor activity of Sirt1²⁰⁵. Second, the previously described Hic1 is deacetylated by Sirt1, which facilitates its association with the transcription factor high-mobility group AT-hook 1 (HMGA1)¹⁸⁶. HMGA1 binds to TAR and recruits Hic1¹⁸⁶. Hic1 seems to interact directly with Tat forming a repressive complex at RNA polymerase II which inhibits HIV1 transcription¹⁸⁶. Finally, the polyphenol resveratrol was shown to recover Sirt1 activity by attenuating Tat-induced HIV1 transactivation²⁰⁷. This generates possibilities for the development of drugs targeting Sirt1, Tat, or any interacting protein for therapeutic approaches to AIDS.

2. Objectives of this work

2.1 Modulation of Sirt1 activity by small molecules

Since age-related diseases such as Alzheimer's, cardiovascular disease, or cancer are today's major causes of premature death⁴⁰, the search for new and more potent pharmacological modulators of Sirt1 proceeds. This study investigates the biochemical effects of tranilast (*N*-[3', 4'-dimethoxycinnamoyl]-anthranilic acid) and dehydroabiatic acid (DAA)¹⁴⁰. DAA constitutes a new class of natural Sirt1 activators and its mechanism needs to be compared to other Sirt1 activators¹⁴⁰. Tranilast has been used as anti-allergy drug in Japan and South Korea, but has recently gained interest as potential anti-tumor drug²⁰⁸. Research is needed to determine whether this property is conveyed through interaction with Sirt1. Furthermore, Sirt1 has two intrinsic regions which are important for its regulation, the N-terminal SBD and the C-terminal ESA/CTR region^{76,79,80}. In scope of this work, peptides derived from the ESA/CTR region are investigated for their potential to stabilize Sirt1. In addition, it has to be clarified whether ESA/CTR peptides might be used as specific Sirt1 activators.

2.2 Regulation of Sirt1 activity by hAROS

AROS was initially identified as an active regulator of Sirt1 activity¹⁵⁰. However, more recent studies could not reproduce the stimulating effect on Sirt1^{155,156}. AROS appears to have a context-dependent effect on Sirt1 and can only enhance Sirt1 activity in human cancer cell lines following genotoxic stress¹⁵⁶. Our laboratory has previously purified a recombinant and refolded hAROS which showed a weak inhibitory effect on Sirt1¹⁵⁵. The question is whether this refolded hAROS comprises its native structure and is able to interact with Sirt1 *in vitro*. Furthermore, the nature of the activity modulation of Sirt1 by hAROS has to be identified in order to clarify the previously conflicting results.

2.3 Characterization of the interaction of Sirt1 with Hic1-BTB

The BTB/POZ domain of Hic1 binds to Sirt1 and forms a transcriptional repression complex which associates with the *SIRT1* promotor to suppress transcription of Sirt1¹⁸⁴. In addition, following genotoxic stress, a CK2-mediated phosphorylation at Ser659 and Ser661 within the ESA/CTR region of hSirt1 facilitates binding of the hSirt1 amino acids 610-677 to the last four zinc fingers of Hic1¹⁸⁵ leading to deacetylation of Hic1 Lys314 by Sirt1¹⁸⁸. The mechanisms underlying these two different modes of interaction of Sirt1 with Hic1 still need to be unraveled. This study focuses on Hic1-BTB to elucidate whether the Sirt1 ESA/CTR, and specifically the phosphorylation of Ser659/Ser661, is also necessary for the interaction of

Sirt1 with the Hic1 BTB/POZ domain. Furthermore, a direct activity modulation of Sirt1 by Hic1-BTB has to be investigated to resolve whether this is possible or whether the Hic1-BTB domain indirectly represses Sirt1 by associating with Sirt1.

2.4 Biochemical and structural characterization of Sirt1-inhibition by HIV1-Tat

Sirt1 acts as a transcriptional coactivator in the late phase of HIV1 transcription by deacetylating HIV1-Tat Lys50¹²⁵. Acetylated or deacetylated Tat can bind to the Sirt1 catalytic domain and inhibit its deacetylase activity, which is important for progression of HIV1 infection^{204,205}. It is not clear, however, which region of Tat mediates the interaction with Sirt1 and whether the model of Tat as a “supersubstrate” for Sirt1, which remains bound to block access for other substrates, is correct. In addition, a possible contribution of the Sirt1 ESA/CTR and SBD to the repressive complex needs to be clarified to determine whether Tat-mediated inhibition is exclusive to Sirt1 or whether Tat may also act as inhibitor for other human sirtuin isoforms. Finally, structural studies should support the mechanism of interaction between Tat and Sirt1.

3. Materials and methods

3.1. Materials

3.1.1 Chemicals, enzymes, standards

All chemicals were purchased from Sigma-Aldrich, Applichem, Gerbu, Serva, Merck, or Carl Roth unless noted otherwise. DNA-modifying enzymes and DNA standards came from New England Biolabs or Fermentas. Protein standards were bought from Bio-Rad or New England Biolabs. Enzymes for activity assays were purchased from Fermentas, Promega, Sigma, or New England Biolabs. Nicotinamidase, TEV protease, and all Sirtuin isoforms were purified in our laboratory using established protocols. Tat Cys⁻ was kindly provided by Prof. Dr. Birgitta Wöhrle (Department of Biopolymers, University of Bayreuth). Substrate peptides for activity assays as well as peptides derived from HIV1-Tat were synthesized by GL Biochem, China. The synthetic *Fluor de Lys-1 (FdL-1)* peptide comprising a C-terminal aminomethyl-coumarin moiety was produced by the department of Prof. Dr. Mike Schutkowski (University of Halle-Wittenberg). Overlapping peptides derived from the Sirt1 ESA region were kindly provided by Prof. Dr. Antonello Mai (Sapienza University of Rome, Italy). An overview of the sequences, molecular weight, and purity of the peptides can be found in Table 3.1 (Tat peptides) and Table 7.1 (all other peptides).

Table 3.1: Characteristics of peptides derived from HIV1-Tat. Peptides were dissolved in 20 mM Tris with pH adjusted to 7 or in 100% (v/v) DMSO (pH not adjusted) unless stated differently.

Peptide	Sequence (N → C)	MW (g/mol)	Purity (%)	Solvent
Tat_20-30	TASNRAHAKKS	1170.30	95.14	Tris/HCl
Tat_31-49	SYHSQVAFITKGLGISYGR	2084.38	98.46	DMSO
Tat_31-60	SYHSQVAFITKGLGISYGRKKRRQRRRPSQ	3562.14	95.28	DMSO
Tat_34-54	SQVAFITKGLGISYGRKKRRQ	2393.84	90.81	75% DMSO
Tat_34-59	SQVAFITKGLGISYGRKKRRQRRRPS	3046.60	98.59	DMSO
Tat_35-44	LVCFQTKGLG	1065.30	98.92	DMSO
Tat_37-54	AFITKGLGISYGRKKRRQ	2079.50	97.01	DMSO
Tat_37-59	AFITKGLGISYGRKKRRQRRRPS	2732.48	96.89	DMSO
Tat_46-54	SYGRKKRRQ	1178.37	98.14	Tris/HCl
ac-Tat_46-54	SYGR-(<i>acetyl</i> -K)-KRRQ	1220.41	98.07	Tris/HCl
Tat_49-60	RKKRRQRRRPSQ	1651.96	97.80	Tris/HCl

3.1.2 Bacterial strains

Vectors and plasmids were amplified in *E. coli* DH5 α TM, *E. coli* GC5TM, *E. coli* One Shot[®] Top10 or *E. coli* XL1blue. Heterologous overexpression of the recombinant proteins Hic1-BTB (pET15b*mod*), fl-Sirt1 (pET15b), mini-Sirt1, mini-Sirt1- Δ STAC, and mini-Sirt1- Δ ESA

was done in *E. coli* CodonPlus™ (DE3) pLysS. Recombinant hAROS and Hic1-BTB (pET15b) were expressed in *E. coli* Rosetta (DE3) pLysS RARE. For small scale expression further strains like *E. coli* BL21 (DE3), *E. coli* Rosetta 2 (DE3), *E. coli* Tuner (DE3) pREP4 GroESL, or *E. coli* OverExpress™ C43 (DE3) pREP4 were used. All cells were chemically competent. The bacterial strains with their genotype and provider are stated in Table 3.2.

Table 3.2: Genotypes of the *E. coli* strains used. The specific antibiotic resistance is highlighted in bold.

<i>E. coli</i> strain	Genotype (resistance)
DH5α™ (Invitrogen)	<i>fhuA2 Δ(argF-lacZ) U169 phoA glnV44 Φ80 Δ(lacZ)M15 gyrA96 recA1 relA1 endA1 thi-1 hsdR17 (-)</i>
GC5™ (Gene Choice)	<i>F' Φ80lacZΔM15 Δ(lacZYA-argF) U169 recA1 endA1 hsdR17 (r_K⁻, m_K⁺) phoA supE44 λ- thi-1 gyrA96 relA1 (-)</i>
One Shot® Top10 (Invitrogen)	<i>Φ80lacZΔM15 mcrA Δ(mrr-hsdRMS-mcrBC) ΔlacX74 deoR recA1 araD139Δ(ara-leu)7697 galU galK rpsL(SmR) endA1 nupG (Strep^R)</i>
XL1blue (Stratagene)	<i>F' proAB lacIqZΔM15 Tn10 recA1 endA1 gyrA96 thi-1 hsdR17 supE44 relA1 lac (Tet^R)</i>
CodonPlus™ (DE3) pLysS (Agilent Technologies)	<i>F' ompT hsdS(r_B⁻ m_B⁻) dcm⁺ Tetr gal endA Hte [argU ileY leuW] (Cam^R)</i>
Rosetta (DE3) pLysS RARE (Novagen)	<i>F' ompT hsdS_B(r_B⁻ m_B⁻) gal dcm λ(DE3 [lacI lacUV5- T7 gene 1 ind1 sam7 nin5]) pLysS RARE (Cam^R)</i>
BL21 (DE3) (Novagen)	<i>F' dcm ompT hsdS(r_B⁻ m_B⁻) gal λ(DE3) (-)</i>
Rosetta 2 (DE3) (Novagen)	<i>F' ompT hsdS_B(r_B⁻ m_B⁻) gal dcm λ(DE3) pRARE2 (Cam^R)</i>
Tuner (DE3) pREP4 GroESL (Novagen)	<i>F' ompT hsdS(r_B⁻ m_B⁻) gal dcm lacY1(DE3) (Kan^R)</i>
OverExpress™ C43 (DE3) pREP4 (Lucigen)	<i>F' ompT gal dcm hsdS_B(r_B⁻ m_B⁻) pREP4 λ(DE3) (Kan^R)</i>
ArcticExpress™ (DE3) (Agilent)	<i>F' ompT hsdS(r_B⁻ m_B⁻) dcm⁺ Tet^R gal λ(DE3) endA Hte [cpn10 cpn60] (Gent^R)</i>

3.1.3 Growth media and antibiotics

E. coli cells were cultivated in lysogeny broth (LB) or terrific broth medium (TB, only for small scale test expressions). Growth media was prepared with desalted water and sterilized at 121 °C and 2 bar for 20 min immediately after preparation. LB agar plates contained 1% (w/v) tryptone, 0.5% (w/v) yeast extract, 1% (w/v) NaCl, and 1.6% (w/v) agar-agar. LB medium was prepared with 1% (w/v) tryptone, 0.5% (w/v) yeast extract, and 1% (w/v) NaCl. In contrast, TB medium included 1.2% (w/v) tryptone, 2.4% (w/v) yeast extract, 0.4% (v/v) glycerol, 0.017 M KH₂PO₄, and 0.072 M K₂HPO₄, whereby KH₂PO₄ and K₂HPO₄ were prepared as 10x stock solution, sterilized, and added directly before inoculation of the expression culture. Growth media for cultivation of *E. coli* cells were supplemented with the appropriate antibiotics at the following final concentrations: 100 mg/l ampicillin (Amp), 34 mg/l chloramphenicol (Cam), or 30 mg/l kanamycin (Kan).

3.1.4 Plasmids and oligonucleotides

Recombinant human fl-Sirt1 and hAROS were expressed from a pET15b vector. The functional short hSirt1 construct called mini-Sirt1 was described by Dai *et al.*⁸⁰. Our mini-Sirt1 contained hSirt1 amino acids 183-505 linked with a (GGGS)₂ linker to hSirt1 641-665 and was subcloned into a pET19b*mod* vector containing a His₆-tag and a TEV cleavage site. A pcDNA3 vector for expression of recombinant human Hic1 was kindly provided by the Leprince group (University of Lille, Pasteur Institute of Lille, France). The BTB/POZ domain of Hic1 comprising amino acids 20-154 was subcloned into a pET15b vector (thrombin cleavage site) and a pET15b*mod* vector containing a TEV cleavage site. Tat Cys⁻ was kindly provided by the group of Prof. Dr. Birgitta Wöhrle (University of Bayreuth). All other sirtuins (hSirt2(43-356), hSirt2(55-356), hSirt3(93-399), hSirt3(118-399), hSirt5(34-302), hSirt6(1-355)) were expressed in various vectors (Table 3.3). For assays and crystallization, all expression tags were proteolytically cleaved off.

Table 3.3: Characteristics of plasmids used for cloning and expression. The plasmid for HIV1-Tat Cys⁻(1-86) contained amino acid exchanges C22S, C25A, C27A, C30A, C31A, C34S, and C37A.

Vector	Target gene	Resistance	Promotor	Tag	Protease site
pET15b	fl-hSirt1 hAROS Hic1-BTB	Amp	T7	N-terminal His ₆	Thrombin
pET15b <i>mod</i>	Hic1-BTB	Amp	T7	N-terminal His ₆	TEV
pET19b <i>mod</i>	mini-Sirt1 mini-Sirt1-ΔSTAC mini-Sirt1-ΔESA	Amp	T7	N-terminal His ₆	TEV
pcDNA3	fl-Hic1	Amp, Neo/Kan	CMV, T7	N-terminal FLAG	Enterokinase
pET11a	HIV1-Tat Cys ⁻	Amp	T7	N-terminal His ₆ -GB1	TEV
pET19b <i>mod</i> -Sumo	hSirt2-(43-356) hSirt2-(55-356)	Amp	T7	N-terminal His ₆ - Sumo	TEV Senp2
pVFT3S	hSirt3-(118-399)	Kan	T7	N-terminal His ₆ -TrxA	TEV
pET32a <i>mod</i>	hSirt3-(93-399)	Amp	T7	N-terminal TrxA-His ₆	TEV
pET-151/D-TOPO	hSirt5-(34-302)	Amp	T7	N-terminal His ₆ -V5	TEV
pQE80L.1	hSirt6-(1-355)	Amp, Cam	T5	N-terminal His ₆	TEV

Oligonucleotides for cloning were ordered from Sigma (salt-free) or from Eurofins Genomics in HPSF (high purity salt-free) quality. All oligonucleotides (Table 7.2) were solubilized in ddH₂O to reach a stock concentration of 100 μM.

3.1.5 Buffers and solutions

Buffers for electrophoresis (Table 3.4) were prepared with ddH₂O. For tracking of DNA size, the 1 kb ladder (NEB, #N3232S) or the 100 bp ladder (NEB, # N3231S) were used. The protein composition of samples was tracked with either the Protein Test Mixture 6 for SDS-

PAGE (Serva, #39207: phosphorylase B (97.4 kDa), bovine serum albumin (67 kDa), ovalbumin (45 kDa), carbonic anhydrase (29 kDa), soy trypsin inhibitor (21 kDa), cytochrome C (12.5 kDa), bovine lung trypsin inhibitor (6.5 kDa)) or with the SDS-PAGE Broad Range Standard (Bio-Rad, #1610317: myosin (200 kDa), β -galactosidase (116.25 kDa), phosphorylase B (97.4 kDa), bovine serum albumin (66.2 kDa), ovalbumin (45 kDa), carbonic anhydrase (31 kDa), trypsin inhibitor (21.5 kDa), lysozyme (14.4 kDa), aprotinin (6.5 kDa)). The native state of proteins was tracked with a customary composition of the Protein MW Standard for non-denaturing systems (Serva, #39064).

Table 3.4: Buffers and solutions for electrophoresis.

Buffer/solution	Composition
Agarose gel electrophoresis	
Agarose gel	0.5-2% (w/v) agarose, 100 ml 1x TAE buffer, 5 μ l Midori Green per gel (~ 40 ml)
TAE running buffer (1x)	40 mM Tris/HCl, pH 8.0, 20 mM acetic acid, 1 mM EDTA
DNA sample buffer (6x)	30% (v/v) glycerol, 0.25% (w/v) Bromphenol Blue, 0.25% (v/v) Xylene Cyanol FF
SDS-PAGE	
Stacking gel	5% (w/v) 37.5:1 Acrylamide/N,N'-Methylenbisacrylamide, 125 mM Tris/HCl, pH 6.8, 0.1% (w/v) SDS, 0.1% (v/v) TEMED, 0.65% (w/v) APS
Separating gel	15% (w/v) 37.5:1 Acrylamide/N,N'-Methylenbisacrylamide, 375 mM Tris/HCl, pH 8.8, 0.1% (w/v) SDS, 0.1% (v/v) TEMED, 0.6% (w/v) APS
Running buffer (10x)	25 mM Tris/HCl, pH 6.8, 0.1% (w/v) SDS, 192 mM glycine
SDS sample buffer (5x)	250 mM Tris/HCl, pH 6.8, 10% (w/v) SDS, 50% (v/v) glycerol, 0.02% (w/v) Bromphenol Blue, 10% (v/v) β -ME
Staining solution	30% (v/v) ethanol, 10% (v/v) acetic acid, 0.25% (w/v) Coomassie Brilliant Blue G-250
Fast staining solution (1 l)	67 ml ethanol (> 99%), 52 ml phosphoric acid (85%), 115 mg Coomassie Brilliant Blue G-250, 10 g β -Cyclodextrin
Blue Native PAGE	
Glycerol buffer 1	150 mM Bis-tris/HCl, pH 7.0, 600 mM ϵ -aminocaproic acid
Glycerol buffer 2	150 mM Bis-tris/HCl, pH 7.0, 60% (v/v) glycerol, 600 mM ϵ -aminocaproic acid
Cathode buffer	15 mM Bis-tris/HCl, pH 7.0, 50 mM tricine, 0.02% (w/v) Coomassie Brilliant Blue G-250
Anode buffer	50 mM Bis-tris/HCl, pH 7.0

All buffers for purification (Table 3.5) were prepared with ddH₂O and filtered through a 0.45 μ m filter. Buffers used on ÄKTA, ÄKTApurifier, or ITC were degassed prior to use.

Table 3.5: Buffers for purification of recombinant proteins.

Buffer	Composition
Purification of fl-hSirt1	
Lysis buffer	50 mM Tris/HCl, pH 7.5, 300 mM NaCl, 5 mM β -ME
His-tag resin nuclease buffer	50 mM Tris/HCl, pH 7.5, 25 mM NaCl, 5 mM $MgCl_2$, 5 mM β -ME
His-tag resin wash buffer	50 mM Tris/HCl, pH 7.5, 300 mM NaCl, 10 mM imidazole, 5 mM β -ME
His-tag resin elution buffer	50 mM Tris/HCl, pH 7.5, 300 mM NaCl, 250 mM imidazole, 5 mM β -ME
IEX buffer A	25 mM HEPES, pH 7.5, 2 mM DTT
IEX buffer B	25 mM HEPES, pH 7.5, 500 mM NaCl, 2 mM DTT
SEC buffer	25 mM HEPES, pH 7.5, 150 mM NaCl, 2 mM DTT
Purification of mini-Sirt1 and mini-Sirt1 mutants	
Lysis buffer	25 mM HEPES, pH 7.5, 200 mM NaCl, 5% (v/v) glycerol, 5 mM β -ME
His-tag resin equilibration buffer	25 mM HEPES, pH 7.5, 200 mM NaCl, 5% (v/v) glycerol, 20 mM imidazole, 5 mM β -ME
His-tag resin wash buffer	25 mM HEPES, pH 7.5, 200 mM NaCl, 5% (v/v) glycerol, 50 mM imidazole, 5 mM β -ME
His-tag resin elution buffer AC	25 mM HEPES, pH 7.5, 200 mM NaCl, 5% (v/v) glycerol, 250 mM imidazole, 5 mM β -ME
His-tag resin elution buffer reverse AC	25 mM HEPES, pH 7.5, 200 mM NaCl, 5% (v/v) glycerol, 5 mM imidazole, 5 mM β -ME
SEC buffer	20 mM Tris/HCl, pH 8.0, 250 mM NaCl, 5% (v/v) glycerol, 10 mM DTT
Purification of hAROS	
Lysis buffer	50 mM Tris/HCl, pH 7.5, 150 mM NaCl
Solubilization buffer	50 mM Tris/HCl, pH 7.5, 300 mM NaCl, 6 M guanidinium hydrochloride
Refolding buffer 1	50 mM Tris/HCl, pH 7.5, 300 mM NaCl, 8 M urea
Refolding buffer 2	50 mM Tris/HCl, pH 7.5, 300 mM NaCl, 4 M urea
Refolding buffer 3	50 mM Tris/HCl, pH 7.5, 300 mM NaCl, 2 M urea
Refolding buffer 4	50 mM Tris/HCl, pH 7.5, 300 mM NaCl, 1 M urea
Refolding buffer 5	50 mM Tris/HCl, pH 7.5, 300 mM NaCl, 10 mM imidazole
His-tag resin elution buffer	50 mM Tris/HCl, pH 7.5, 300 mM NaCl, 150 mM imidazole
SEC buffer	25 mM HEPES, pH 7.5, 100 mM KCl, 2 mM DTT
Purification of Hic1-BTB (pET15b)	
Lysis buffer	50 mM Tris/HCl, pH 8.0, 250 mM NaCl, 5 mM β -ME
His-tag resin wash buffer	50 mM Tris/HCl, pH 8.0, 250 mM NaCl, 10 mM imidazole, 5 mM β -ME
His-tag resin elution buffer	50 mM Tris/HCl, pH 8.0, 250 mM NaCl, 250 mM imidazole, 5 mM β -ME
SEC buffer	50 mM Tris/HCl, pH 8.0, 150 mM NaCl, (1 mM TCEP)
Purification of Hic1-BTB (pET15b$_{mod}$)	
Lysis buffer/Ni-NTA column buffer A	50 mM Tris/HCl, pH 8.0, 250 mM NaCl, 5% (v/v) glycerol, 0.05% (v/v) Tween [®] 20, 5 mM β -ME
His-tag resin wash buffer	50 mM Tris/HCl, pH 8.0, 250 mM NaCl, 5% (v/v) glycerol, 10 mM imidazole, 0.05% (v/v) Tween [®] 20, 5 mM β -ME
His-tag resin elution buffer/Ni-NTA buffer B	50 mM Tris/HCl, pH 8.0, 250 mM NaCl, 5% (v/v) glycerol, 250 mM imidazole, 0.05% (v/v) Tween [®] 20, 5 mM β -ME
IEX buffer A	50 mM Tris/HCl, pH 8.0, 5% (v/v) glycerol, 0.05% (v/v) Tween [®] 20, 5 mM β -ME
IEX buffer B	50 mM Tris/HCl, pH 8.0, 1 M NaCl, 5% (v/v) glycerol, 0.05% (v/v) Tween [®] 20, 5 mM β -ME
SEC buffer	25 mM HEPES, pH 7.5, 150 mM NaCl, 5% (v/v) glycerol, 0.05% (v/v) Tween [®] 20, 10 mM DTT
Purification of Tat Cys	
SEC buffer	10 mM K_2HPO_4/KH_2PO_4 , pH 6.4, 150 mM NaCl

Buffers for assays (Table 3.6) were either prepared with ddH₂O and filtered through a 0.45 µm filter or contained highest grade stock solutions (MS).

Table 3.6: Buffers and solutions for assays and analytics.

Buffer/Solution	Composition
Assay buffer	
General assay buffer	10 mM K ₂ HPO ₄ /KH ₂ PO ₄ , pH 7.8
Hic1-BTB assay buffer	20 mM Tris/HCl, pH 7.8, 150 mM NaCl, 10 mM MgCl ₂ , 0.05% (v/v) Tween [®] 20
Pulldown	
Loading buffer	20 mM Tris/HCl, pH 7.8, 150 mM NaCl
Wash buffer 1	20 mM Tris/HCl, pH 7.8, 500 mM NaCl
Wash buffer 2	20 mM Tris/HCl, pH 7.8, 150 mM NaCl, 10 mM imidazole
Elution buffer	20 mM Tris/HCl, pH 7.8, 150 mM NaCl, 300 mM imidazole
Crosslinking	
Reaction buffer	25 mM HEPES, pH 7.5, 150 mM NaCl, 5% (v/v) glycerol
Stop solution	1 M Tris/HCl, pH 8.0
Microscale thermophoresis	
Labeling buffer	1x PBS, pH 7.4
Reaction buffer for Tat Cys ⁻	48.7 mM K ₂ HPO ₄ /KH ₂ PO ₄ , pH 7.8, 150 mM NaCl, 10 mM MgCl ₂ , 0.05% (v/v) Tween [®] 20
Reaction buffer for Hic1-BTB, DAA, and peptides	50 mM Tris/HCl, pH 7.8, 150 mM NaCl, 10 mM MgCl ₂ , 0.05% (v/v) Tween [®] 20
Sample denaturation (SD) mix (2x)	4% (w/v) SDS, 40 mM DTT
Mass spectrometry	
Discoloration solution	50 mM NH ₄ HCO ₃ , pH 8.0, 50% (v/v) acetonitrile
Re-hydration solution	25 mM DTT in 25 mM NH ₄ HCO ₃ , pH 8.0
Alkylation solution	55 mM iodoacetamide in 25 mM NH ₄ HCO ₃ , pH 8.0
Dehydration solution	50 mM NH ₄ HCO ₃ , pH 8.0, 50% (v/v) acetonitrile
Digestion solution	200 ng trypsin in 25 mM NH ₄ HCO ₃ , pH 8.0
Elution solution	50% (v/v) acetonitrile, 0.5% (v/v) TFA
MS running buffers for intact protein analysis on a C4 column (TOF)	buffer A: 0.1% (v/v) TFA, 99.9% (v/v) ddH ₂ O; buffer B: 0.1% (v/v) TFA, 99.9% (v/v) acetonitrile; buffer C: 0.1% (v/v) FA, 5% (v/v) acetonitrile
MS running buffers for peptide analysis on a C18 column (TOF/LTQ)	buffer A: 0.1% (v/v) FA, 5% (v/v) acetonitrile; buffer B: 0.1% (v/v) FA, 95% (v/v) acetonitrile; buffer C: 0.1% (v/v) FA, 5% (v/v) acetonitrile

3.1.6 Equipment

Table 3.7: Equipment used in this work and their manufacturers.

Equipment	Manufacturer
ÄKTAprime plus	GE Healthcare, Freiburg (DEU)
ÄKTApurifier	GE Healthcare, Freiburg (DEU)
Autoclave Systec DX-150	Systec, Wettenberg (DEU)
Avanti R centrifuge J-26 XP, rotor: JLA-8.1000	Beckman Coulter, Krefeld (DEU)
Avanti centrifuge J-30I, rotor: JA-30.50	Beckman Coulter, Krefeld (DEU)
Benchmark myFuge™ Mini	Benchmark Scientific, South Plainfield NJ (USA)
Bio-Rad miniProtean Tetra System	Bio-Rad Laboratories, CA (USA)
Bio-Rad mini Sub Cell GT	Bio-Rad Laboratories, CA (USA)
Branson Sonifier 250	Emerson, MO (USA)

Continuation of Table 3.7:

Equipment	Manufacturer
CD spectrophotometer J-715	JASCO Corporation, Tokyo (JPN)
Digital camera E-620	Olympus, Hamburg (DEU)
Ditabis MHR 11 96-well thermoshaker	Ditabis, Pforzheim (DEU)
Epoch 2 microplate spectrophotometer	BioTek Instruments, Vermont (USA)
Eppendorf thermomixer 5436	Eppendorf, Hamburg (DEU)
Eppendorf centrifuge 5417 R, rotor: F45-30-11	Eppendorf, Hamburg (DEU)
EPS 3500 power supply (agarose gels)	Pharmacia Biotech, Uppsala (SWE)
EV243 power supply (SDS-PAGE)	Consort, Cohasset, MA (USA)
FlexCycler	Analytik Jena, Eisfeld (DEU)
FluoDia T70 spectrofluorometer	Photal Technology Int., NJ (USA)
Formulatrix Rock Imager 1000	Formulatrix, MA (USA)
Heraeus Labofuge 400R, rotor: 8179	Thermo Scientific, Braunschweig (DEU)
HLC Micro-PCR thermomixer	Ditabis, Pforzheim (DEU)
HLC cooling thermomixer MKR 13	Ditabis, Pforzheim (DEU)
Ice machine	Ziegra, Isernhagen (DEU)
Infors MT Multitron (Pro)	Infors HT, Leipzig (DEU)
Innova 4200 & 40 incubator shaker	New Brunswick Scientific, NJ (USA)
INTAS gel imaging system	INTAS Science Imaging Instr., Goettingen (DEU)
Intelli-Mixer RM-2S	Elmi Ltd., Riga (LVA)
KMO2 basic magnetic stirrer	IKA-Werke, Staufen (DEU)
LKB 2050 Midget Electrophoresis Unit	LKB Bromma, Stockholm (SWE)
LTQ Mass spectrometer	Thermo Fisher Scientific, Waltham, MA (USA)
Milli-Q water system	Merck Millipore, Billerica, MA (USA)
Monolith™ NT.115	NanoTemper Technologies GmbH, Muenchen (DEU)
MP220 pH detector	Mettler-Toledo, Columbus, OH (USA)
NanoDrop 2000 UV/Vis spectrophotometer	Thermo Scientific, Braunschweig (DEU)
Odyssey Sa infrared imaging system	LI-COR, Lincoln (USA)
Phoenix Liquid Handling System	Art Robbins Instruments, CA (USA)
Plate incubator	Memmert, Nuernber (DEU)
Rotating anode	Bruker, Billerica, MA (USA)
Sorvall RC6 Plus centrifuge, rotor: SS-34	Thermo Scientific, Braunschweig (DEU)
Spectrofluorometer JP-6500	JASCO Corporation, Tokyo (JPN)
Stereo microscope SZX16	Olympus, Tokio (JPN)
System Gold programmable detector module	Beckman Coulter, Krefeld (DEU)
System Gold programmable solvent module	Beckman Coulter, Krefeld (DEU)
Thermoshake incubation shaker	Gerhardt, Koenigswinter (DEU)
Thermoshaker TS100	Peqlab, Erlangen (DEU)
Vakuum concentrator BA-VC 300H	H. Sauer Laborbedarf, Reutlingen (DEU)
Vortex Genie 2	Roth, Karlsruhe (DEU)
VWR ultrasonic cleaner USC-T	VWR International, PA (USA)
x-ray detector MAR 345	MarResearch, Norderstedt (DEU)

3.1.7 Consumables

Consumables for general use were purchased from Bio-Rad, Eppendorf, GE Healthcare, Greiner Bio-One, Hartenstein, Millipore, NanoTemper, Pall Corporation, Promega, Sarstedt, Sartorius, Serva Electrophoresis, or StarLab. Consumables for crystallography were bought from Hampton Research, Jena Bioscience, Molecular Dimensions, Qiagen, or VWR.

3.2 Molecular biological methods

3.2.1 Polymerase chain reaction (PCR)

Polymerase chain reaction (PCR) is used to amplify double-stranded DNA with specific primers. Different strategies were used for cloning of mini-Sirt1, mini-Sirt1 mutagenesis, or cloning of other targets, which will be described in the following.

3.2.1.1 Cloning of mini-Sirt1 with Kapa HiFi[®] polymerase

Mini-Sirt1⁸⁰ was cloned in two steps by amplifying the catalytic domain of fl-hSirt1 and its ESA/CTR region separately with a short, flexible (GGGS)₂ linker and then fusing both domains. The use of Kapa HiFi[®] polymerase (Kapa Biosystems, MA, USA) was crucial as well as addition of DMSO to inhibit secondary structure formation of the template DNA and facilitate amplification of GC-rich regions (Table 3.8). Amplification of the catalytic domain also benefited from addition of MgCl₂. The PCR amplification protocol is listed in Table 3.9.

Table 3.8: PCR reaction mixes for cloning of mini-Sirt1. The mini-Sirt1 construct was fused with the primers Sirt1_5XhoI183 and Sirt1_3BamHI665stop. All individual primers are listed in Table 7.2.

	Catalytic domain	ESA/CTR domain	Mini-Sirt1 fusion
DNA template 1	1 µl fl-hSirt1	1 µl fl-hSirt1	1 µl catalytic domain
DNA template 2	-	-	1 µl ESA/CTR domain
10 µM forward primer	1.5 µl	1.5 µl	1.5 µl
10 µM reverse primer	1.5 µl	1.5 µl	1.5 µl
5x HiFidelity [®] buffer	10 µl	10 µl	10 µl
25 mM MgCl ₂	10 µl	-	-
10 mM 4x dNTPs	1.5 µl	1.5 µl	1.5 µl
100% (v/v) DMSO	0.5 µl	0.5 µl	0.5 µl
ddH ₂ O	23 µl	33 µl	32 µl
Kapa HiFi [®] polymerase	1 µl	1 µl	1 µl

Table 3.9: PCR amplification for mini-Sirt1 cloning with Kapa HiFi[®] polymerase.

	Temperature [°C]	Duration [s]
Initial denaturation	98	120
Cycles	25	
Denaturation	98	20
Annealing	60	20
Elongation	72	20
Final elongation	72	300
End	4	∞

For colony PCR, analytical PCR, and cloning of mini-Sirt1 deletion mutants a standard Vent[®] polymerase (NEB) protocol was used. Mini-Sirt1 phosphomimetic mutants were cloned with a two-step Phusion[®] High-Fidelity (NEB) PCR protocol.

3.2.1.2 Standard cloning with Vent[®] polymerase

Vent[®] DNA polymerase (NEB) was the polymerase of choice for cloning most targets and testing positive ligation results. Table 3.10 lists a general setup of the PCR reaction mixes. For initial amplification of target DNA a 50 µl mix was prepared, for colony or analytical PCR a 10 µl mix was prepared for each clone.

Table 3.10: PCR reaction mixes for cloning with Vent[®] DNA polymerase (NEB). This protocol was used for cloning of Hic1-BTB, mini-Sirt1 deletion mutants, and colony and analytical PCR of most targets if not noted differently. The primers used for cloning are listed in Table 7.2.

	50 µl Reaction	Final concentration
DNA template	1-2.5 µl	100-500 ng
10 µM forward primer	2.5 µl	0.5 µM
10 µM reverse primer	2.5 µl	0.5 µM
10x ThermoPol buffer	5 µl	1x
10 mM 4x dNTPs	1 µl	200 µM
100% (v/v) DMSO	0-1.5 µl	0-3%
ddH ₂ O	to 50 µl	
Vent [®] polymerase	0.5-1 µl	1-2 U

Vent[®] polymerase has a lower denaturation temperature than Kapa HiFi[®] polymerase. For amplification of target DNA, 30 cycles of denaturation, annealing, and extension were used. The annealing temperature was chosen according to the average T_m of the primer pair used, whereas the extension time was dependent on the length of the target DNA (Table 3.11).

Table 3.11: PCR amplification for Vent[®] polymerase. Annealing temperature and extension time were adapted for each primer pair and the length of the target DNA.

	Temperature [°C]	Duration [s]
Initial denaturation	95	300
Cycles	30	
Denaturation	95	30
Annealing	55-65	30
Elongation	72	60 s per kb
Final elongation	72	300
End	4	∞

3.2.1.3 Cloning of mini-Sirt1 phosphomimetic mutants with Phusion[®] polymerase

Phosphomimetic S659D and S661D mutations were introduced into the mini-Sirt1 ESA/CTR region with a two-step PCR protocol using Phusion[®] DNA polymerase (NEB). Since primers were designed to already contain the mutations (Table 7.2), they were longer and had a higher T_m which made them amenable to a combined annealing/elongation step during PCR. Table 3.12 lists the contents of the PCR reaction mixture, whereas Table 3.13 indicates the PCR protocol. Colony and analytic PCR were performed with the same protocol.

Table 3.12: PCR reaction mixes for cloning of mini-Sirt1 phosphomimetic mutants with Phusion® DNA polymerase (NEB). The reverse primers already contained the respective mutations (Table 7.2).

	50 µl Reaction	Final concentration
DNA template	1 µl	100-500 ng
10 µM forward primer	1.5 µl	0.3 µM
10 µM reverse primer	1.5 µl	0.3 µM
5x Phusion® HF buffer	10 µl	1x
10 mM 4x dNTPs	1.5 µl	300 µM
100% (v/v) DMSO	0.5 µl	1%
ddH ₂ O	33.5 µl	
Phusion® polymerase	0.5 µl	1 U

Table 3.13: Two-step PCR for cloning of phosphomimetic mini-Sirt1 mutants with Phusion® polymerase.

	Temperature [°C]	Duration [s]
Initial denaturation	98	120
Cycles	30	
Denaturation	98	20
Annealing/elongation	72	45 (15 s per kb)
Final elongation	72	600
End	4	∞

3.2.2 Purification of PCR products and restricted vectors

PCR products and digested vectors were purified with the FavorPrep™ GEL/PCR Purification Mini Kit (Favorgen® Biotech Corporation, Taiwan) according to the manual. The column was dried at 18,000 rcf for 5 min before elution with 40 µl ddH₂O which was pre-heated to 60 °C. Prior to elution by centrifugation at 18,000 rcf for 1 min, the DNA was allowed to incubate with the warm ddH₂O for 20 min at 20 °C.

3.2.3 Preparation of plasmid DNA

Plasmids were transformed into chemically competent *E. coli* cells for amplification. For cell lysis, extraction, and purification of plasmid DNA, the FavorPrep™ Plasmid Extraction Mini Kit (Favorgen® Biotech Corporation, Taiwan) was used according to the manual. The column was dried at 18,000 rcf for 5 min before elution. Instead of the supplied elution buffer, plasmid DNA was eluted with 50 µl ddH₂O which was pre-heated to 60 °C. To facilitate extraction, the DNA was allowed to incubate with the warm ddH₂O for 20 min at 20 °C before elution by centrifugation at 18,000 rcf for 1 min.

3.2.4 Agarose gel electrophoresis

Agarose gel electrophoresis was used to evaluate the result of a PCR or restriction digest of vectors. Depending on the expected fragment size, gels of 0.5-2% (w/v) agarose were prepared with 1x TAE buffer supplemented with 5 µl Midori Green per 40 ml of gel. After solidification of the gel, 6x DNA sample buffer was added to the DNA and electrophoresis

was performed at 95 V for 30 min. Agarose gels were inspected under UV light with an INTAS gel imaging system. In case of a preparative agarose gel electrophoresis, bands were cut out with a glass slide and prepared for purification with the FavorPrep™ GEL/PCR Purification Mini Kit (Favorgen® Biotech Corporation, Taiwan) as described.

3.2.5 DNA restriction digest

PCR products with overhangs for restriction sites as well as vectors were cut with the specific restriction enzymes from New England Biolabs (NEB) before ligation. Restriction reactions were carried out in a volume of 50 μ l with 20 μ l of the DNA, 23 μ l ddH₂O, 5 μ l of the 10x CutSmart® restriction buffer (NEB), and 1 μ l each of the two restriction enzymes. The reaction mix was incubated at 37 °C for 2 h. Afterwards, restriction enzymes were inactivated by a heat shock at 65 °C for 20 min. Digested PCR products and vectors were allowed to cool on ice for 5 min. Digested vectors were treated with antarctic phosphatase to prevent self-ligation. For this purpose, the inactivated restriction mix was supplemented with 6 μ l 10x antarctic phosphatase buffer (NEB), 1 μ l antarctic phosphatase, and 3 μ l ddH₂O. Dephosphorylation of digested vector ends occurred at 37 °C for 30 min, followed by heat inactivation at 70 °C for 10 min. Success of the restriction digest was monitored by agarose gel electrophoresis. Digested PCR products and vectors were purified with the FavorPrep™ GEL/PCR Purification Mini Kit (Favorgen® Biotech Corporation, Taiwan) before ligation.

3.2.6 DNA ligation

DNA ligations were performed in a 20 μ l reaction mix with 1.25 μ l T4 DNA ligase and 2 μ l 10x T4 DNA ligase buffer (NEB) for 2 h at 16 °C followed by heat inactivation at 65 °C for 20 min. In case of an unsuccessful ligation, the incubation temperature was changed to 4 °C overnight. For the ligation reaction mix, an amount of 100 ng vector was used with a 3-fold or 5-fold excess of insert. The amount of vector or insert was calculated based on the following equations 1 or 2, respectively.

$$V_{vector} (\mu l) = \frac{100 \text{ ng}}{c_{vector} \left(\frac{\text{ng}}{\mu l}\right)} \times 1.25 \quad (1)$$

$$V_{insert} (\mu l) = \frac{100 \text{ ng} \times \frac{bp_{insert}}{bp_{vector}} \times ratio\left(\frac{insert}{vector}\right)}{c_{insert} \left(\frac{\text{ng}}{\mu l}\right)} \times 1.25 \quad (2)$$

with V = volume (μ l), c = concentration (ng/ μ l), bp = number of basepairs.

3.2.7 Transformation of ligation reactions into chemically competent cells

50 µl aliquots of chemically competent *E. coli* One Shot® Top10 (Invitrogen) or *E. coli* XL1blue (Stratagene) cells were carefully thawed on ice for 10 min. Addition of the 20 µl ligation reaction was followed by further 20 min incubation on ice. After a heat shock (45 s, 42 °C), cells were allowed to recover for 2 min on ice. Subsequently, 950 µl LB medium were added and cells were incubated at 37 °C, 600 rpm for 1 h. Cells were then centrifuged at 4500 rcf for 90 s and 900 µl of the supernatant was removed. Transformed cells were resuspended in the residual medium and plated on an LB agar plate supplemented with the appropriate antibiotic for selection of the transformed plasmid. Agar plates were inverted and incubated at 37 °C overnight.

3.2.8 Identification of positive clones by colony and analytical PCR

Colony PCR was used for testing positive clones after transformation of ligation reactions. Single clones were picked with a sterile pipette tip and resuspended in 10 µl ddH₂O. 1 µl of this resuspended colony was used as a template for colony PCR, whereas 9 µl were used to inoculate a 10 ml LB culture supplemented with the appropriate antibiotics if the clone was positive. Colony PCRs were performed in a 10 µl reaction mix using Vent® or Phusion® polymerase. After PCR, the amplified products were analyzed by agarose gel electrophoresis by adding 2 µl of 6x DNA sample buffer. Pre-cultures of positive clones were grown for at least 5 h at 37 °C and 160 rpm. Afterwards, cells were harvested and DNA was isolated using the FavorPrep™ Plasmid Extraction Mini Kit (Favorgen® Biotech Corporation, Taiwan). 1 µl of isolated plasmid DNA was further used as template for analytical PCR to check for successful ligation. For analytical PCR, the insert-specific forward primer was used with the vector-specific reverse primer to exclude false positive clones from colony PCR. Since T7 primers (Table 7.2) have lower melting temperature than the longer insert-specific primers, the annealing temperature had to be carefully adapted using the web-based T_m calculator, version 1.9.12 from New England Biolabs. Results of the analytical PCR were analyzed by agarose gel electrophoresis as described.

3.2.9 DNA sequencing

Plasmid DNA of positive clones was sequenced at Eurofins MWG Operon (Ebersberg, DEU). DNA concentrations had to reach 50-100 ng/µl. Vector-specific primers were added by Eurofins MWG Operon. For one sequencing reaction, 15 µl of plasmid DNA was needed, inserts larger than 800 bp required a forward and reverse sequencing reaction to cover the whole sequence.

3.3 Microbiological methods

3.3.1 Sterilization

All media and buffers for media were sterilized for 15 min at 121 °C and 2 bar, instruments and pipette tips were sterilized for 20 min at 121 °C and 2 bar in a Systec autoclave.

3.3.2 Transformation of chemically competent cells

For amplification of plasmids or empty vectors, *E. coli* DH5 α TM (Invitrogen) or *E. coli* GC5TM (Gene Choice) cells were used. Heterologous overexpression of proteins was carried out in different chemically competent *E. coli* strains as described in chapter 3.1.2.

In general, a 50 μ l aliquot of chemically competent cells was carefully thawed on ice for 10 min and transformed by adding 100-200 ng of circular DNA. The further steps are identical with the transformation of ligation reactions into chemically competent cells (chapter 3.2.7). After 1 h of incubation at 37 °C, cells for heterologous overexpression of proteins were directly used for inoculation of a 50-100 ml LB medium pre-culture supplemented with all antibiotics specific for the bacterial strain and the transformed plasmid. Liquid pre-cultures were incubated at 37 °C, 160 rpm overnight in an Innova 40 or 4200 incubator shaker.

3.3.3 *E. coli* cultivation and heterologous overexpression of recombinant proteins

For test expressions of His₆-hAROS in *E. coli* Rosetta (DE3) pLysS RARE, Tuner (DE3) pREP GroESL, and ArcticExpress (DE3), 100 ml LB medium were inoculated with 0.5 ml of the respective overnight pre-culture and supplemented with the appropriate antibiotics for the bacterial strain and plasmid. Cells were grown at 37 °C, 120 rpm until they reached an optical density of OD₆₀₀ = 0.6, then subjected to a cold shock on ice for 20 min. They were induced with 0.5 mM IPTG to produce His₆-hAROS at OD₆₀₀ = 0.8. While *E. coli* Tuner (DE3) pREP GroESL cells were cooled to 20 °C for expression, *E. coli* Rosetta (DE3) pLysS RARE were kept at 37 °C or cooled to 30 °C. Expression in *E. coli* ArcticExpress (DE3) was performed by growth at 30 °C, followed by expression at 12 °C. Samples (1 ml) were taken before induction with IPTG and 1 h, 2 h, 4 h, and 12-16 h afterwards. These samples were pelleted by centrifugation and removal of the medium. The pellets were then solubilized in 1 x SDS sample buffer and analyzed by SDS PAGE.

Preparative heterologous overexpression of proteins was performed in a total volume of at least 12 times 1 l LB medium in 2 l Erlenmeyer flasks. In case of mini-Sirt1 and Hic1-BTB from pET15bmod, upscaling to 10 l fermenters was possible without harming purity or yield. Heterologous overexpression of the recombinant proteins Hic1-BTB (pET15bmod), fl-hSirt1

(pET15b), mini-Sirt1 (pET19b*mod*), mini-Sirt1- Δ STAC (pET19b*mod*), and mini-Sirt1- Δ E5A (pET19b*mod*) was done in *E. coli* CodonPlusTM (DE3) pLysS. Recombinant hAROS (pET15b) and Hic1-BTB (pET15b) were expressed in *E. coli* Rosetta (DE3) pLysS RARE. Growth media was supplemented with the appropriate antibiotics and inoculated with 4 ml of the pre-culture per 1 l of medium (5 ml for hAROS). Cells were grown at 37 °C, 120 rpm to an OD₆₀₀ = 0.6 followed by a cold shock on ice for 30 min. However, mini-Sirt1 and mutants thereof had to be gently cooled to 16 °C while still shaking at 120 rpm to reach soluble overexpression. After the cold shock, expression cultures were induced with 0.5 mM IPTG at an approximate OD₆₀₀ = 1.1 to produce the protein of interest (0.2 mM IPTG for mini-Sirt1 and its mutants). Heterologous overexpression was performed at 20 °C, 120 rpm for 16-18 h. Mini-Sirt1 and its mutants were overexpressed at 16 °C, hAROS at 12 °C. Fl-hSirt1 was already harvested 5 h after induction with IPTG to prevent degradation of the protein.

3.3.4 Cell harvest and disruption

After overexpression, cells were harvested by centrifugation at 6500 rcf and 12 °C for 10 min in a JLA-8.1000 rotor. If not directly disrupted, cell pellets were snap-frozen in liquid nitrogen and stored at -80 °C. Frozen cells were carefully thawed on ice for 10 min followed by the addition of 4 ml lysis buffer per 1 g cells. To inhibit proteolytic digestion of the overexpressed protein, 0.2 mM PMSF and 1-2 cComplete EDTA-free protease inhibitor tablets (Roche) were added. Cells were resuspended at 4 °C, 100 rpm on a magnetic stirrer for up to 1 h. Cell disruption was performed in a maximal volume of 150 ml at 4 °C on a Branson sonifier using a big tip with 70% output at stage 8 for 6-8 times 1 min. After each interval, cells were allowed to cool on ice for 30 s. Cell debris was then removed by centrifugation in a JA-30.50 rotor at 20,000 rpm, 4 °C, 1 h. For mini-Sirt1 and mutants thereof, a speed of 10,000 rcf was used, fl-hSirt1 and hAROS were centrifuged at 18,000 rpm.

Overnight test expression cultures were also harvested by 10 min centrifugation at 6500 rcf and 12 °C in a SLA-3000 rotor (Sorvall). Cells were resuspended in 10 ml lysis buffer with 0.2 mM PMSF at 4 °C and disrupted using the Branson sonifier equipped with a small tip with 30% output at stage 4 for four times 15 s. Cell debris was removed by centrifugation in a JA-30.50 rotor at 10,000 rcf, 4 °C for 30 min.

3.4 Purification of recombinant proteins after heterologous expression in *E. coli*

3.4.1 Overview of purification protocols

Recombinant overexpressed proteins were purified from the supernatant after centrifugation and removal of cell debris. Apart from that, hAROS was not solubly expressed and had to be purified from inclusion bodies using a stepwise refolding procedure. Figure 3.1 shows an overview of the purification steps for each recombinant protein.

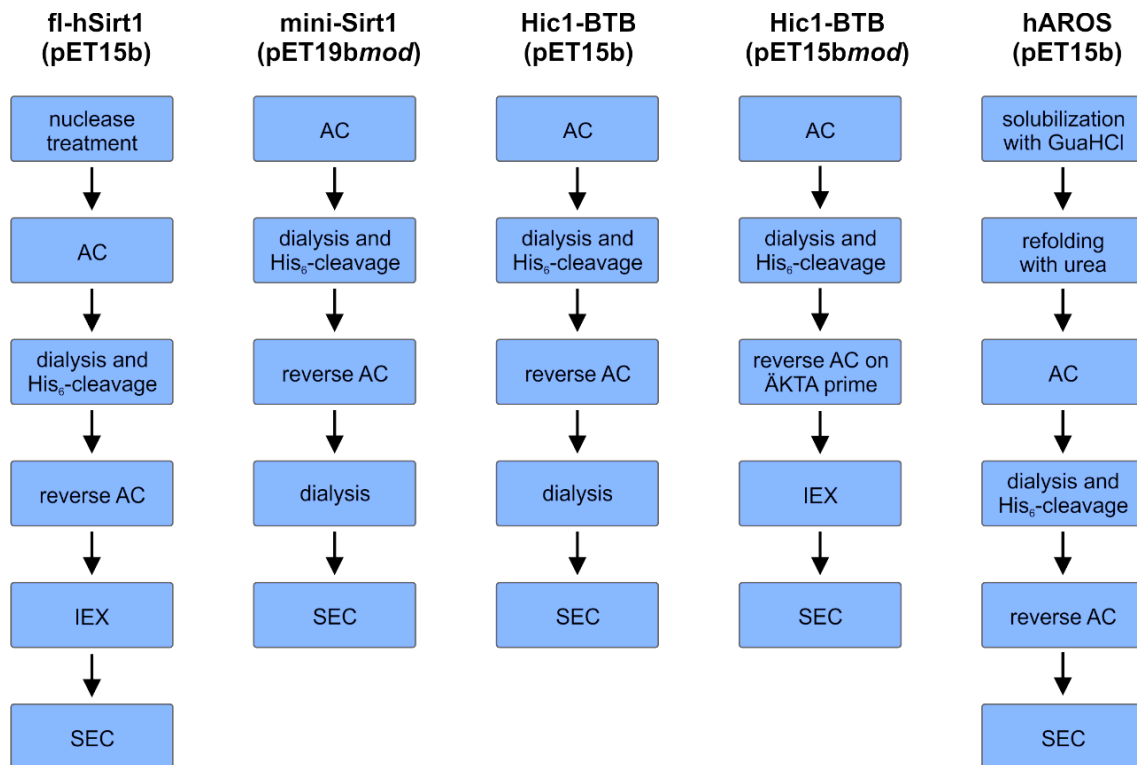


Figure 3.1: Overview of purification steps for fl-hSirt1, mini-Sirt1, Hic1-BTB, and hAROS. Abbreviations: AC - affinity chromatography, IEX - ion exchange chromatography, SEC - size exclusion chromatography.

Tat Cys⁻ was purified by the group of Prof. Dr. Birgitta Wöhrl (Department of Biopolymers, University of Bayreuth). Shortly, HIV1-Tat Cys⁻(1-86) from the HIV1 Zaire 2 *TAT* gene was cloned into pET11a with amino acid exchanges C22S, C25A, C27A, C30A, C31A, C34S, and C37A²⁰⁹. After expression in *E. coli* BL21 (DE3) for 4 h at 37 °C, cell pellets were resuspended in 50 mM Tris/HCl, pH 8, 1 M MgCl₂, 200 mM NaCl, 2 mM PMSF, and ½ cComplete EDTA-free protease inhibitor tablet (Roche), a small amount of benzamidine and DNaseI. Cells were lysed with a microfluidizer (MFTI Corporation, MA, USA), followed by slow pH decrease to pH 3-4 with HCl under stirring for 45 min at 4 °C. After centrifugation at 4 °C and 16,503 rcf, the pH of the supernatant was raised to pH 8 and the protein was precipitated by addition of 0.436 g (NH₄)₂SO₄ per ml of supernatant. The suspension was first stirred for 15 min at 20 °C, then moved to 8 °C for further 2 h of stirring prior to centrifugation at 4 °C and 16,503 rcf for 30 min. The protein pellet was resuspended in

10 mM potassium phosphate, pH 6.4, 200 mM NaCl, and 1 cOmplete EDTA-free protease inhibitor tablet (Roche) and subsequently dialyzed overnight against 20 mM potassium phosphate, pH 6.4, 200 mM NaCl, and 2 mM PMSF. After centrifugation at 4 °C and 19,000 rcf for 20 min, the supernatant was subjected to affinity chromatography on a HiTrap Heparin HP column (GE Healthcare) and eluted with a NaCl gradient. Fractions containing Tat Cys⁻ were pooled, dialyzed against 10 mM potassium phosphate, pH 6.4 and 150 mM NaCl, and concentrated with VivaSpin20 concentrators (Sartorius, MWCO 5 kDa). The protein was aliquoted, snap frozen in liquid nitrogen, and stored at -80 °C.

3.4.2 Affinity chromatography

All overexpressed and soluble proteins were equipped with an N-terminal His₆-tag for separation from *E. coli* proteins in the first purification step by immobilized metal ion affinity chromatography (IMAC/”AC”). Ni-cOmplete beads (Roche) were equilibrated with the appropriate lysis buffer or equilibration buffer using 1 ml of beads per 4 g of cells. The supernatant after removal of cell debris was then incubated with the beads for 1 h at 4 °C under careful stirring. Hic1-BTB from pET15b was treated with 5 mg DNaseI per 100 g of cells during this incubation step to remove DNA. After incubation, the mixture was filtered through a gravity flow column (Bio-Rad), the flowthrough was collected, and beads were washed with 10-20 column volumes (CV) of lysis buffer or equilibration buffer. Fl-hSirt1 was then treated with 10 µg/ml DNaseI and 20 µg/ml RNaseA in a volume of 50 ml nuclease buffer for 45 min, 4 °C, under rolling incubation. Bound proteins were further washed with 10 CV wash buffer collecting fractions of 5-10 ml (mini-Sirt1 started eluting during this step). Soluble His₆-tagged proteins were completely eluted in fractions of 5-10 ml with 10 CV elution buffer. The concentration of collected fractions was measured with a Nanodrop 2000 UV/Vis spectrophotometer using the protein-specific molecular weight and ϵ_{280} (Table 7.3). Purity of the fractions was assessed by SDS-PAGE. Fractions containing the protein of interest were pooled for the next purification step.

The reverse affinity chromatography was used as purification step after cleavage of the His₆-tag to remove the tag and His₆-tagged protease. 1 ml of Ni-cOmplete beads per 15 ml of dialysate was equilibrated with lysis buffer and incubated with the dialysate at 4 °C under careful stirring for 45 min. The cleaved target protein was eluted with the flowthrough from a gravity flow column. For fl-hSirt1, the gravity flow column with Ni-cOmplete beads was connected to a downstream column filled with likewise equilibrated Benzamidine SepharoseTM 4 Fast Flow (High Sub) (GE Healthcare), which binds thrombin efficiently. To

achieve the highest possible yield of recombinant protein, beads were washed with 10-20 CV lysis buffer and fractions of 5 ml were collected. The beads were then washed with 10 CV wash buffer and 10 CV elution buffer to elute the His₆-tag and His₆-tagged protease. The gravity flow columns for purification of fl-hSirt1 were washed similarly using an additional final step for elution of thrombin with 10 mM SPG, pH 4, whereby the eluate was neutralized in 10 mM SPG, pH 9. Hic1-BTB from pET15b stayed bound to the beads until elution with elution buffer, where small fractions of 5 ml were collected.

Only for Hic1-BTB from pET15b*mod*, the reverse affinity chromatography was performed on an ÄKTAprime to separate a potential dimer of Hic1-BTB from TEV protease which has a similar molecular weight. The dialysate was loaded onto an equilibrated 5 ml HisTrap HP column (GE Healthcare) with a flowrate of 2 ml/min and the column was then washed with 5 CV of the degassed lysis buffer. Afterwards, the flowrate was reduced to 1 ml/min and a step to 10% degassed elution buffer was performed and was maintained for 10 CV. In a gradient for the length of 10 CV, imidazole concentration was increased to 50% elution buffer, which was then maintained for 10 CV or until Hic1-BTB completely eluted from the HisTrap column. The column was recovered by a step to 100% elution buffer which was maintained for 10 CV to remove all residual bound proteins.

SDS-PAGE was used to determine which fractions of the reverse affinity chromatography contained the protein of interest. Corresponding fractions were pooled, concentrated, and used for dialysis to rebuffer the recombinant protein (mini-Sirt1, Hic1-BTB from pET15b), for ion exchange chromatography (fl-hSirt1, Hic1-BTB from pET15b*mod*), or for SEC (hAROS).

3.4.3 Refolding of hAROS *on-column*

hAROS could not be expressed as soluble protein in *E. coli* and had to be refolded *on-column*. In contrast to purification of soluble proteins, the pellet after cell disruption and centrifugation was used and incubated with 60 ml of solubilization buffer at 20 °C for 1 h under careful stirring. 6 M guanidinium hydrochloride included in the solubilization buffer acts as a strong chaotrope and completely unfolds the insoluble protein. During 45 min centrifugation in a JA-30.50 rotor at 18,000 rpm and 20 °C, cell debris was removed from the unfolded hAROS. The supernatant containing hAROS was incubated for 1 h at 20 °C under careful stirring with 10 ml of Ni-cOmpete beads (Roche) equilibrated in solubilization buffer. The mixture was then passed through a gravity flow column (Bio-Rad) and the flowthrough was collected. hAROS was slowly refolded *on-column* using 10 CV each of the refolding buffers 1-5, which contained a decreasing concentration of urea. Flowthroughs were collected and the folded

protein was eluted from the beads with 10 CV elution buffer collecting fractions of 5 ml. Purity of the fractions was assessed by SDS-PAGE and concentrations were measured using a Nanodrop 2000 UV/Vis spectrophotometer with the protein-specific molecular weight and extinction coefficient at 280 nm. Fractions containing hAROS were pooled for dialysis.

3.4.4 Dialysis and proteolytic cleavage of the His₆-tag

All recombinant proteins were equipped with an N-terminal His₆-tag, which could be either cleaved off by thrombin (fl-hSirt1, hAROS, Hic1-BTB from pET15b) or TEV protease (mini-Sirt1, Hic1-BTB from pET15b*mod*). Cleavage was performed after the first affinity chromatography during dialysis against 4 l of lysis buffer at 4 °C. TEV protease was used in a molar ratio of 1:10 to the recombinant protein, while 1 U thrombin was sufficient to cleave 2 mg of protein as long as dialysis was performed overnight. In all cases, a dialysis tube with a molecular weight cutoff of 10 kDa was used. The removed His₆-tag and the His₆-tagged protease were separated from the target protein during reverse affinity chromatography.

In the purification procedure of mini-Sirt1 and Hic1-BTB from pET15b, a second dialysis step overnight at 4 °C was added after reverse affinity. Mini-Sirt1 required this step to gently change the buffer system from HEPES to Tris/HCl. In contrast, Hic1-BTB from pET15b bound unspecifically to the Ni²⁺-cOmplete beads even though the His₆-tag was cleaved off and had to be recovered from high imidazole concentrations in the buffer prior to SEC.

3.4.5 Ion exchange chromatography

Fl-hSirt1 and Hic1-BTB from pET15b*mod* were further purified using an ion exchange chromatography (IEX) after reverse affinity chromatography. For fl-hSirt1, a HiTrap Q FF column (GE Healthcare) was used on an ÄKTApurifier with a flowrate of 0.5 ml/min. The column was first equilibrated with 20 CV of degassed IEX buffer A. The concentrated protein was then loaded in a volume of less than 5 ml. For binding of the protein to the column, the amount of NaCl was removed during concentration to a maximum of 50 mM NaCl. After loading, the HiTrap Q FF was washed with 10 CV of IEX buffer A before a linear gradient was applied for the length of 40 CV up to 100% IEX buffer B. Fractions of 1 ml were collected and the column was recovered by washing at 100% IEX buffer B for 5 CV.

For Hic1-BTB from pET15b*mod*, a HiTrap SP FF column (GE Healthcare) was used on an ÄKTAprime with a flowrate of 1 ml/min. The protein was loaded onto the column which was previously equilibrated with 20 CV degassed IEX buffer A. The salt concentration of the injected protein solution had to be reduced to 50 mM for the protein to bind to the IEX

column. After loading, the column was washed with 10 CV IEX buffer A. Hic1-BTB eluted with a linear gradient of 30 CV up to 40% IEX buffer B and maintenance at 40% buffer B for further 20 CV. Fractions of 1 ml were collected during IEX and the column was recovered by maintaining the high-salt concentration of 100% IEX buffer B for 10 CV.

Fractions containing the proteins of interest were analyzed by SDS-PAGE, concentrated, and pooled for SEC.

3.4.6 Size exclusion chromatography

Size exclusion chromatography (SEC) was the final step to assess target protein of highest purity with a homogenous oligomerization state. SEC was performed on ÄKTA purifiers using GE Healthcare columns S200 10/300 GL (fl-hSirt1, Hic1-BTB from pET15b*mod*), S200 16/60 GL (mini-Sirt1, Hic1-BTB from pET15b), or Superose 12 10/300 GL (hAROS). All columns were equilibrated with 1.5 CV of degassed SEC buffer at a flowrate of 0.5 ml/min (S200 10/300 GL, Superose 12 10/300 GL) or 1 ml/min (S200 16/60 GL). Protein was concentrated to a maximum volume of 0.5 ml containing 10 mg of protein for S200 10/300 GL and Superose 12 10/300 GL or to 2-5 ml containing maximal 30 mg of protein for S200 16/60 GL. To remove any aggregates, the concentrated protein was centrifuged at 14,000 rpm, 10 min, 4 °C in a F45-30-11 rotor prior to gel filtration. The loaded protein was eluted with 1.5 CV SEC buffer and fractions of 0.5 ml or 1 ml, respectively, were collected.

Fractions containing the target protein were determined by SDS-PAGE and pooled. Mini-Sirt1 and Hic1-BTB from pET15b were concentrated to 30-40 mg/ml, whereas all other proteins were concentrated to 8-20 mg/ml. Concentrated proteins were aliquoted to 10 µl, snap-frozen in liquid nitrogen, and stored at -80 °C.

3.5 Biochemical methods

3.5.1 SDS-Polyacrylamide gel electrophoresis

Denaturing SDS-polyacrylamide gel electrophoresis (SDS-PAGE) was used for analytical separation of protein mixtures according to their molecular weight in a 15% (w/v) SDS gel. Prior to electrophoresis, samples were mixed with 5x sample buffer and denatured at 95 °C for 5 min. The electrophoresis was carried out at 150 V for 5 min or until samples reached the separating gel, then voltage was increased to 180 V for further 50 min. After SDS-PAGE, gels were washed with desalted water and stained by covering them in staining solution and heating them up in a microwave for 1 min. They were destained in desalted water under slow shaking at 20 °C overnight. In order to create distinct protein bands for further analysis with

mass spectrometry, gels were stained with *Fast* staining solution and covered in this solution for 10-20 min at 20 °C in a closed box. Destaining was done with desalted water as described.

3.5.2 Concentration of proteins by centrifugation

Protein solutions were concentrated by centrifugation to a desired volume or a desired concentration. All proteins were concentrated using PALL Microsep[®] or Macrosep[®] concentrators (PALL Corporation) with molecular weight cutoffs of 10 kDa (hAROS, Hic1-BTB) or 30 kDa (fl-hSirt1, mini-Sirt1). Centrifugation steps were carried out at 4 °C in a Heraeus centrifuge with an 8179 rotor for up to 15 min.

3.5.3 Photometric determination of concentrations

Concentrations of DNA and protein solutions were determined using a NanoDrop 2000 UV/Vis spectrophotometer (Thermo Scientific). DNA concentrations were measured at 260 nm with 1 A_{260} equaling 50 ng/ μ l of double-stranded DNA. For determination of the concentration of protein solutions, the Lambert-Beer law (equation 3) was used with a theoretical molecular weight and extinction coefficient based on the sequence and calculated by the online tool ProtParam (ExPASy²¹⁰). An overview of the calculated molecular weight and extinction coefficients for each protein is given in Table 7.3.

$$c \left(\frac{\text{mol}}{\text{l}} \right) = \frac{A_{280}}{\epsilon_{280} (M^{-1} \text{cm}^{-1}) \times d (\text{cm})} \quad (3)$$

with c = concentration (mol/l), A_{280} = absorbance at 280 nm,
 ϵ_{280} = extinction coefficient at 280 nm, d = path length (cm)

3.5.4 Thermal shift denaturation assay

The thermal shift denaturation assay (TSA) was used to determine the melting temperature (T_m) of proteins²¹¹. In an assay mastermix block of 96 conditions, half of the conditions was used as a pH/buffer screen, whereas the other half of conditions was used in a second step to find additives which enhance the T_m compared to the previously determined buffer. For the pH/buffer TSA screen, 40 μ l of the 1.5-fold mastermix buffer stock were supplemented with 6 μ l protein at a final concentration of 5 μ M, 6 μ l of Sypro[®] Orange (Sigma) at a final concentration of 5-fold, and 8 μ l of ddH₂O. For the additive TSA screen, 40 μ l of the 1.5-fold mastermix additive stock were supplemented with 8 μ l of 7.5-fold buffer determined in the pH/buffer TSA assay, 6 μ l of protein at a final concentration of 5 μ M, and 6 μ l of Sypro[®] Orange (Sigma) at a final concentration of 5-fold. 50 μ l of the reaction mix were transferred to a 96-well black/white hard-shell plate (HSP9665, Bio-Rad) and sealed with 15 μ l of mineral oil to prevent evaporation of heated samples. Thermal denaturation of proteins was

performed in 1 °C-steps in a FluoDia T70 spectrofluorometer (Photal) with an excitation wavelength of 465 nm and an emission wavelength of 580 nm. The T_m was determined in GraFit 7.0.3 (Erithacus Software Limited) using equation 4.

$$y_T = \frac{f + n \times z + (d + u \times z) \times e^{\left(-\frac{H}{R} \times \left(\frac{1}{z} - \frac{1}{T_m}\right) - \frac{C}{R}\right) \times \left(1 - \frac{T_m}{z} + \ln\left(\frac{T_m}{z}\right)\right)}}{1 + e^{\left(-\frac{H}{R} \times \left(\frac{1}{z} - \frac{1}{T_m}\right) - \frac{C}{R}\right) \times \left(1 - \frac{T_m}{z} + \ln\left(\frac{T_m}{z}\right)\right)}} \quad (4)$$

with f = native protein, n = baseline slope of the native protein, z = temperature (°C) + 273.15, d = denatured protein, u = baseline slope of the denatured protein, H = reaction enthalpy, R = gas constant (8.3144 Jmol⁻¹K⁻¹), T_m = melting temperature, c = constant (6000)

3.5.5 Continuous coupled enzymatic deacylation activity assay

Coupled enzymatic deacylation assays²¹² were used to determine Sirtuin activity continuously over a timespan of 1 h. The Sirtuin deacylation reaction releasing deacylated substrate, NAM, and AADPr is coupled to two follow-up reactions. In the first reaction, NAM is hydrolyzed by nicotinamidase to nicotinic acid and ammonia (Figure 3.2). Ammonia is then transferred to α -ketoglutarate by glutamate dehydrogenase (GDH) resulting in glutamate formation under oxidation of NADPH to NADP⁺ (Figure 3.2). Activity was measured in 30 s intervals through NADPH depletion at a wavelength of 340 nm using an Epoch 2 microplate spectrophotometer (BioTek) with transparent half area UV-STAR[®] 96-well microplates (#675801, Greiner Bio-one). A negative reaction without NAD⁺ served as a control for the autohydrolysis rate of NADPH.

In general, a 100 μ l reaction mix consisted of 1 μ M sirtuin, 500 μ M NAD⁺, 100 μ M sirtuin-specific substrate, 2 μ M nicotinamidase, 2 U/ml GDH, 3.5 mM α -ketoglutarate, and 500 μ M NADPH. For K_m determinations of the sirtuin-specific substrate, NAD⁺ was used in excess of 3 mM and the substrate was titrated starting from 1 mM of substrate. For determining the K_m of NAD⁺, the substrate was used in excess of 1 mM. Inhibition of Sirtuins by HIV1-Tat was always measured at the K_m for the sirtuin-specific substrate with 500 μ M NAD⁺. To enhance the solubility of modulating compounds or peptides derived from HIV1-Tat or the Sirt1 ESA region, the reaction mix was supplemented with 5-15% (v/v) DMSO. In the setup, the sirtuin substrate as well as DMSO and the modulator were always put into the microplate first and the reaction was started with 75-90 μ l of an enzyme mastermix containing sirtuin, NAD⁺, and all coupled enzymes and cosubstrates.

Results of the assay were analyzed in Microsoft Excel (Microsoft Corp.) by first determining the linear range of the reaction and calculating its slope. This slope was then corrected for

NADPH autohydrolysis and the relative sirtuin activity (%) was computed. The mean relative sirtuin activity (%) and standard deviation (%) from at least duplicates within each assay were determined likewise. Graphs were plotted in GraFit 7.0.3 (Erithacus Software Limited). For determination of the specific activity ($\text{nmol} \times \text{mg}^{-1} \times \text{min}^{-1}$), equation 5 was used with the sirtuin-specific molecular weight. K_m values were calculated in GraFit 7.0.3 assuming Michaelis-Menten kinetics and a steady-state²¹³ with equation 6 (“enzyme kinetics”). IC_{50} values were determined in GraFit 7.0.3 with the “ IC_{50} full four parameter” function (equation 7).

$$\text{Specific activity} \left(\frac{\text{nmol}}{\text{mg} \times \text{min}} \right) = \frac{\left(\frac{\Delta A_{340} (\text{min}^{-1})}{\epsilon_{\text{NADPH}} (\text{mM}^{-1} \text{cm}^{-1}) \times d (\text{cm})} \right) \times V (\mu\text{l})}{\text{MW} \left(\frac{\text{g}}{\text{mol}} \right) \times m_{\text{Sirt}} (\mu\text{M}) \times 10^{-7}} \quad (5)$$

with $\Delta A_{340} (\text{min}^{-1})$ = slope of the linear range, $\epsilon_{\text{NADPH}} = 6.22 \text{ mM}^{-1} \text{ cm}^{-1}$,
 $d = 0.604 \text{ cm}$ (pathlength for 100 μl sample in half area UV plates), $V =$ sample volume (100 μl),
 $\text{MW} =$ molecular weight of the Sirtuin (g/mol), $m_{\text{Sirt}} =$ amount of Sirtuin used in the assay (μM)

$$v = \frac{v_{\text{max}} \times c_S}{K_m + c_S} \quad (6)$$

with $v =$ reaction rate, $v_{\text{max}} =$ maximum reaction rate,
 $K_m =$ Michaelis-Menten constant, $c_S =$ substrate concentration

$$\text{Relative activity} (\%) = \frac{\text{range} (\%)}{1 + \left(\frac{c_I (\mu\text{M})}{IC_{50} (\mu\text{M})} \right)^s} + \text{background} (\%) \quad (7)$$

with $\text{range} (\%) =$ fitted uninhibited value minus background, $s =$ slope factor,
 $c_I =$ inhibitor concentration (μM), $IC_{50} =$ half-maximal inhibitory concentration (μM).
 The equation assumes that the relative activity (%) falls with increasing $c_I (\mu\text{M})$.

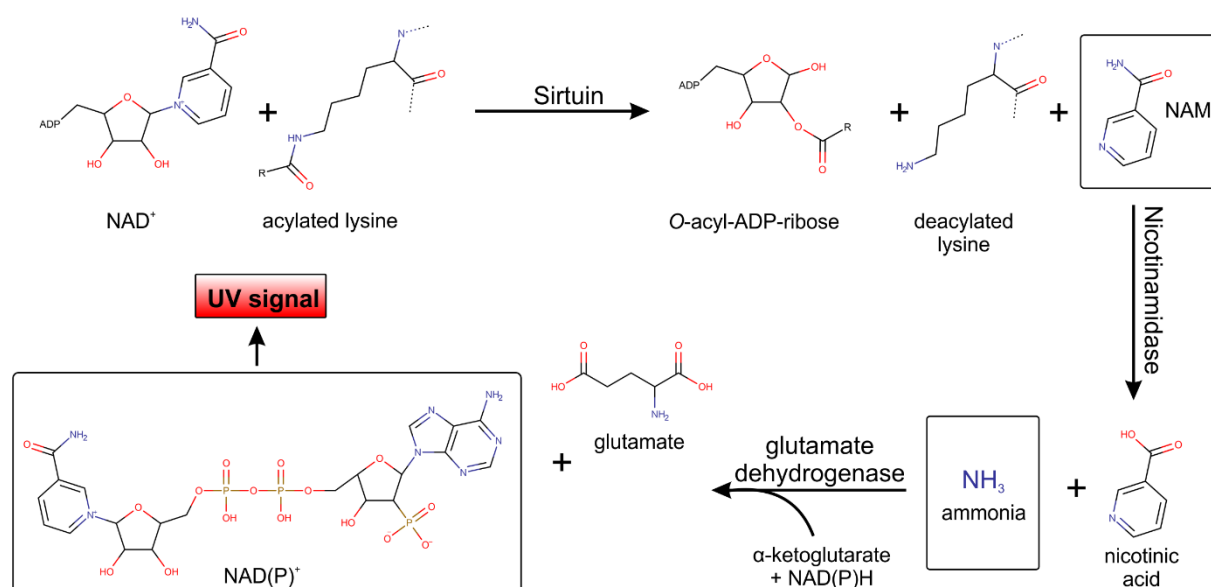


Figure 3.2: Continuous coupled enzymatic deacylation activity assay for sirtuins. The assay couples the sirtuin deacylation reaction to two subsequent enzymatic reactions, whereby NADPH oxidation is monitored at 340 nm in a spectrophotometer²¹⁴.

3.5.6 *Fluor de Lys* deacylation activity assay

The *Fluor de Lys* (FdL) deacylation assay is a sensitive endpoint assay for sirtuin activity⁴⁸, which was used to validate results from the continuous coupled enzymatic deacylation activity assay or in cases where the continuous coupled enzymatic assay was not applicable. The *Fluor de Lys* assay utilizes a substrate derived from human p53 comprising R379-K382 with an acetylated K382 coupled to a C-terminal 7-amino-4-methyl-coumarin group (termed *FdL-1* substrate). The sirtuin deacetylation reaction was stopped after 20 min by addition of a developer consisting of 2 mM NAM and 10 mg/ml Trypsin (Figure 3.3). Deacetylated *FdL-1* substrate makes the fluorophore amenable for tryptic cleavage. The free fluorophore can be reported after incubation at 20 °C for 45 min in a FluoDia T70 spectrofluorometer (Photal) using an excitation wavelength of 365 nm and an emission wavelength of 465 nm.

Reactions were carried out in a volume of 25 μ l at 37 °C in a Ditabis 96-well thermoblock (Ditabis) with 1 μ M Sirtuin, 500 μ M NAD⁺, and *FdL-1* at 100 μ M or at the determined K_m. The stop solution was added at an equal volume of 25 μ l. After 45 min, 45 μ l were transferred to a 96-well black/white hard-shell plate (HSP9665, Bio-Rad). A negative reaction control without sirtuin was included to subtract the background fluorescence of *FdL-1*. To account for false positive artifacts, a control with the modulator added after the developer stop solution was performed. K_m values were measured as described in chapter 3.5.5 with the exception that K_m values for NAD⁺ were determined in presence of 400 μ M *FdL-1*. Results of the assay were first analyzed in Microsoft Excel (Microsoft Corp.) by subtracting the negative background control from all raw fluorescence data. The relative sirtuin activity (%) was then calculated as well as the mean relative sirtuin activity (%) and the standard deviation (%) from at least three individual samples per assay. K_m and IC₅₀ values were assessed in GraFit 7.0.3 as described in chapter 3.5.5 using equations 6 and 7, respectively.

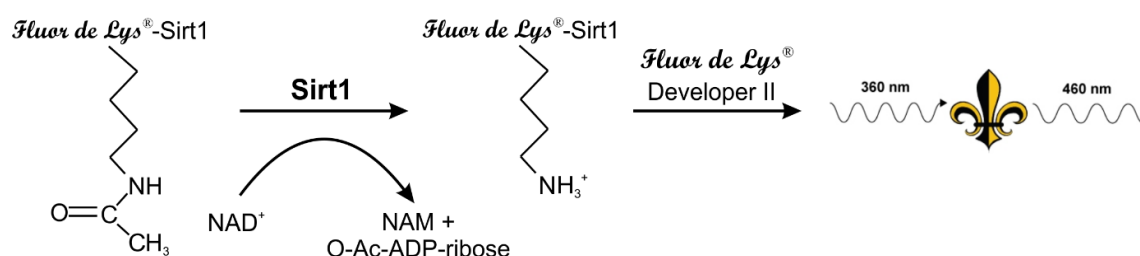


Figure 3.3: *Fluor de Lys*[®] deacylation endpoint assay for sirtuin activity. After stopping the sirtuin reaction, the fluorophore of the deacetylated *FdL-1* substrate can be specifically cleaved off by trypsin, followed by detection in a spectrofluorometer using an excitation wavelength of 365 nm and an emission wavelength of 465 nm. (Adapted from the *Fluor de Lys*[®] User Manual²¹⁵ with permission from Enzo Life Sciences, Inc.).

3.5.7 Mass spectrometric deacylation activity assay

Sirtuin activity can also be directly reported using a mass spectrometry-based deacylation assay²¹⁶ (Figure 3.4). This assay was used when modulators were incompatible with the continuous coupled enzymatic assay or the *Fluor de Lys* assay. A reaction mix in a volume of 70 μl consisting of 0.139 μg hSirt1, 500 μM NAD^+ , and 500 μM substrate was incubated at 37 $^{\circ}\text{C}$ with varying concentrations of the modulator. After six different timepoints between 2.5-60 min, 10 μl of the reaction mix were removed and stopped with 10 μl 0.5% (v/v) trifluoroacetic acid (TFA). Samples were diluted with 0.1% (v/v) formic acid (FA) to attain a final concentration of 1 μM substrate. HSirt1 was removed from the diluted reaction mix by filtration through a 10 kDa cutoff Eppendorf tube filter (VWR). Acetylated and deacetylated substrate peptides in each sample were separated by HPLC on a C18 column followed by subsequent mass spectrometric quantification.

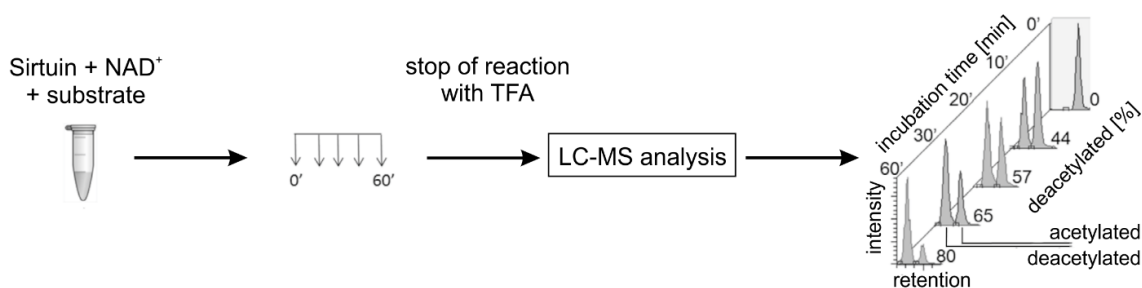


Figure 3.4: Mass-spectrometric direct deacylation sirtuin activity assay. After stopping the sirtuin reaction with TFA, samples are diluted and filtered prior to quantification by HPLC-MS. (Adapted from Fischer *et al.* (2012)²¹⁶ with permission from Public Library of Science).

Results were analyzed using Skyline (MacCross Lab) to determine the area under the peak of acetylated and deacetylated peptide for each sample. Relative hSirt1 activity (%) and standard deviation (%) were calculated in Microsoft Excel (Microsoft Corp.) as already described (chapter 3.5.5) and results were plotted using GraFit 7.0.3 (Erithacus Software Limited).

3.5.8 Statistical analyses

Unless noted otherwise, sirtuin activity for single data points was calculated from the mean of at least two individual samples ($n = 2$) with the respective standard deviation and plotted as a column graph or point graph (without fit). For K_m and IC_{50} determinations, three individual titrations ($n = 3$) were performed and individually fitted. The respective K_m or IC_{50} was then calculated from the mean of those three values with the respective standard deviation. Graphs for K_m or IC_{50} determinations show the mean activity of single data points (with their respective standard deviation) as point graph and a fit of the mean activity for simplification.

3.6 Interaction analysis methods

3.6.1 Pulldown

Pulldowns are a direct method to study the interaction between a known protein and others. But the method is prone to false positives due to interaction with the column material or the tag of the immobilized protein. The interaction between fl-hSirt1 and hAROS was studied with pulldowns by immobilizing 100 µg His₆-hAROS in 100 µl loading buffer to 100 µl of Ni²⁺-cOmplete beads (Roche). The protein-bead mixture was loaded in a MoBiCol[®] spin column (MoBiTec[®] GmbH, DEU) and His₆-hAROS was allowed to bind to the beads during incubation for 1 h at 4 °C on a rolling incubator. Afterwards, 130 µg fl-hSirt1 was added in 50 µl loading buffer followed by further incubation for 45 min at 4 °C on a rolling incubator. Controls were performed with an equal amount of loading buffer. Excess non-bound protein was removed by centrifugation for 5 min at 20 °C and 5,200 rcf in a F45-30-11 rotor (Eppendorf). Beads were washed twice with 400 µl of a high-salt buffer (wash buffer 1) and 400 µl of a buffer containing imidazole (wash buffer 2) to reduce unspecific binding of the untagged protein to the beads. Every wash step was followed by centrifugation as described. The complex was eluted with 100 µl elution buffer by centrifugation at 5,200 rcf and 20 °C for 5 min in a F45-30-11 rotor (Eppendorf). Success of the pulldown was evaluated by SDS-PAGE including a sample with the Ni²⁺-beads after the experiment.

3.6.2 Blue Native PAGE

Blue Native PAGE is used to analyze the native oligomerization state of a protein as well as a putative complex formation between two proteins. Gels for *Blue Native* PAGE contained three layers of 5/12/15% (w/v) Acrylamide/N,N'-Methylenbisacrylamide (37.5:1) with 0/10/20% (v/v) glycerol, respectively (Table 3.14). Solutions for all three layers were prepared at the same time and filled into a gel caster (Bio-Rad) from bottom to top creating a natural gradient through different glycerol concentrations. After polymerization of the gel, (mixed) protein samples were preincubated for 30 min at 4 °C, supplemented with 20% (v/v) glycerol, and applied to the gel pockets. Cathode buffer was filled in the upper chamber of an electrophoresis unit (Hoefer[™] SE250) and anode buffer in the lower chamber. In case of *Clear Native* PAGE of mini-Sirt1 phosphorylation mimicry mutants and Hic1-BTB, the electrophoresis buffers did not contain Coomassie. Electrophoresis was performed for 15 min at 150 V and 4 °C before increasing the voltage to 200 V for at least 2 h or until the running line had reached the end of the gel. *Blue Native* PAGE gels were destained in ddH₂O as described for SDS-PAGE.

Table 3.14: Preparation of three-layer Blue Native PAGE gels.

	5% (Top)	12% (Middle)	15% (Bottom)
ddH ₂ O	1.96 ml	1.04 ml	0.65 ml
Glycerol buffer 1	1.33 ml	0.67 ml	-
Glycerol buffer 2	-	0.67 ml	1.33 ml
Acrylamide/N,N'-Methylenbisacrylamide (37.5:1)	0.67 ml	1.60 ml	2.00 ml
10% (v/v) APS	0.04 ml	0.02 ml	0.01 ml
TEMED	0.004 ml	0.006 ml	0.01 ml

3.6.3 *In vitro*-phosphorylation

For the interaction of mini-Sirt1 and Hic1-BTB, 25 µg mini-Sirt1 were phosphorylated *in vitro* by 1000 U CK2 in presence of 1 mM ATP at 30 °C overnight. A control of mini-Sirt1 was incubated with buffer under the same conditions. Afterwards, 25/50/100 µg Hic1-BTB octamer were added to samples of 5 µg mini-Sirt1, phosphorylated or not, and *Blue Native* PAGE was performed.

3.6.4 Crosslinking

Crosslinking is a direct method to prove the interaction between two known proteins. If coupled to subsequent mass spectrometric analysis, the interaction site on each of the proteins can be determined. For crosslinking experiments, both proteins were first dialyzed separately in Xpress Micro Dialyzer tubes (Serva, MD100 or MD300, MWCO 6-8 kDa) to exchange for the reaction buffer. In a total volume of 60 µl, the proteins (50-70 µM each) were crosslinked at 20 °C with a molar excess of the specific crosslinker. Crosslinkers were solubilized in 100% (v/v) DMSO and pre-diluted to a 10-fold stock in 50% (v/v) DMSO. Four different crosslinkers with different spacer lengths were used to link proteins between the amine groups of lysines (Figure 3.5): disuccinimidyl suberate (DSS) and the cleavable crosslinker disuccinimidyl sulfoxide (DSSO) in a final concentration of 2.82 mM, dimethyl suberimidate (DMS) in a final concentration of 1 mM, and glutaraldehyde in a final concentration of 1.69 mM. Before adding the crosslinker, a sample of 10 µl was removed from the reaction (t = 0 min) and stopped by addition of 1 µl 1 M Tris/HCl, pH 8. The crosslinker was added and after several time-points, 10 µl each of the reaction were stopped in the same manner. Controls contained only one of the two proteins and were treated similarly to exclude self-crosslinks. The stopped reaction samples were supplemented with SDS sample buffer and proteins were separated by SDS-PAGE. Crosslinked bands were subjected to tryptic digest for mass spectrometric analysis (chapter 3.7.3).

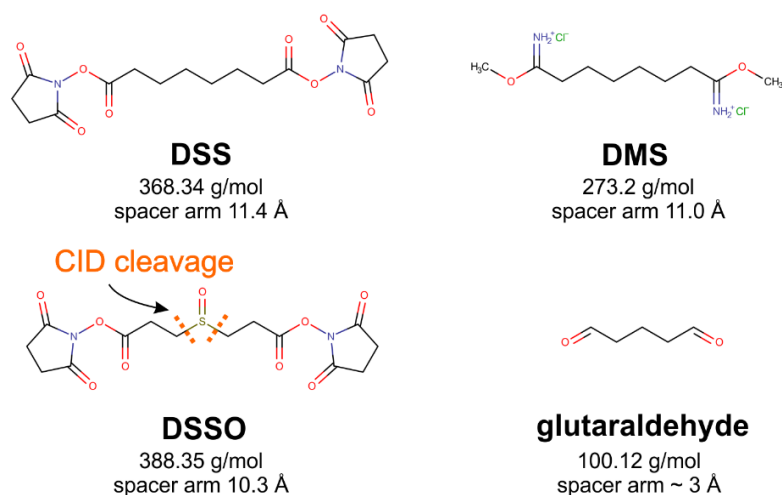


Figure 3.5: Crosslinkers for linking two proteins via the amine group of lysines. DSS (disuccinimidyl suberate), DMS (dimethyl suberimidate), and glutaraldehyde are permanent crosslinkers. DSSO (disuccinimidyl sulfoxide) contains two collision-induced dissociation (CID) sites (dotted lines) ²¹⁷.

3.6.5 Nuclear magnetic resonance spectroscopy

Besides determination of the structure of small proteins below 35 kDa, solution nuclear magnetic resonance (NMR) spectroscopy is widely used to investigate protein-ligand interactions. As part of this work, 2D-NMR spectroscopy was used by the collaborating group of Prof. Dr. Birgitta Wöhrle (Department of Biopolymers, University of Bayreuth) to identify the regions of Tat Cys⁻, which are involved in hSirt1 inhibition. Therefore, mini-Sirt1 in 10 mM potassium phosphate, pH 6.4 and 150 mM NaCl was titrated to ¹⁵N-labeled HIV-Tat Cys⁻(1-86). A control with buffer instead of mini-Sirt1 was included. 2D-(¹H, ¹⁵N)-HSQC NMR spectra were recorded at 298 K on a 700 MHz spectrometer (Bruker) equipped with a cryogen cooling stream and changes in chemical shifts were analyzed after subtracting the control spectrum from the one obtained for the protein-protein interaction.

3.6.6 Microscale thermophoresis

Microscale thermophoresis (MST) is a direct method to determine the affinity between a protein and ligand or between two proteins. The resulting dissociation constant K_d corresponds to the concentration of the titrant at which half of the protein molecules are bound to the titrant and half of them are free (equation 8).

$$K_d = \frac{c_P \times c_T}{c_{PT}} \quad (8)$$

with K_d = dissociation constant (M), c_P = concentration of free protein (M),
 c_T = concentration of free titrant (M), c_{PT} = concentration of the complex (M).

Microscale thermophoresis can be performed with native proteins since the fluorescence of tryptophan and other aromatic amino acids is sufficient to detect changes in the hydration

shell due to binding of the titrant ^{218,219}. In order to study protein-protein interactions this is usually not possible. In this case, one of the binding partners is artificially labeled with a highly sensitive fluorophore. For studying interactions between hSirt1 and other regulating proteins, one protein was labeled with fluorescein isothiocyanate (FITC) in a molar ratio of protein:FITC = 2:1. The labeling reaction was carried out in 200 µl 1x PBS, pH 7.4 for 15 min at 20 °C in the dark. The labeled protein was separated from unlabeled protein and free fluorophore by fractionated elution from an illustra NAP-5 gravity flow column (GE Healthcare). An UV/Vis spectrum of each fraction was recorded on a Nanodrop 2000 UV/Vis spectrophotometer to determine the absorbance at 280 nm and 495 nm using a pathlength of 1 mm. The final concentration of labeled protein and its labeling ratio was calculated by the following equations 9 and 10, respectively.

$$c_{\text{labeled protein}} = \frac{A_{280} - \left(\frac{A_{495}}{r_{\text{FITC}}}\right)}{\epsilon_{280}(\text{protein})} \times f_{\text{cm}} \quad (9)$$

with $c_{\text{labeled protein}}$ = concentration of the labeled protein (M), A_{280} = absorbance at 280 nm, A_{495} = absorbance at 495 nm, $\epsilon_{280}(\text{protein})$ = extinction coefficient of the protein ($\text{M}^{-1} \text{cm}^{-1}$), $r_{\text{FITC}} = A_{495}(\text{free FITC})/A_{280}(\text{free FITC}) = 3.0$, and f_{cm} = pathlength correction factor (10 cm^{-1}).

$$LR_{F/P} = \frac{\frac{A_{495}}{\epsilon_{495}(\text{FITC})}}{c_{\text{labeled protein}}} \times f_{\text{cm}} \quad (10)$$

with $LR_{F/P}$ = labeling ratio of the protein (values between 0.3-1.5), A_{495} = absorbance at 495 nm, $\epsilon_{495}(\text{FITC})$ = extinction coefficient of FITC at pH 7.4 ($70,000 \text{ M}^{-1} \text{cm}^{-1}$), f_{cm} = pathlength correction factor (10 cm^{-1}), $c_{\text{labeled protein}}$ = concentration of the labeled protein (M).

Depending on the labeling ratio, FITC-labeled proteins were used in final concentrations of 5-80 nM to achieve an initial fluorescence between 400-1800 AFU. A 2-fold stock solution of the labeled protein in a volume of 140-180 µl MST buffer was prepared. The titrant was diluted in MST buffer in a 1:1 dilution series with a volume of 10 µl each in 12-16 steps. According to a general recommendation from NanoTemper Technologies Inc., the MST buffer always contained 0.05% (v/v) Tween[®] 20 to prevent labeled proteins from sticking to reaction tubes or capillaries, as well as 150 mM NaCl, and 10 mM MgCl₂ ²²⁰. 10 µl of the 2-fold stock solution of labeled protein was carefully mixed with 10 µl of the diluted titrant and samples were centrifuged for 2 min at 20,000 rcf and 20 °C in an Eppendorf centrifuge prior to thermophoresis. Standard treated capillaries for NT.115 (NanoTemper Technologies Inc.) were filled with the mixed samples and carefully laid on a tray by only touching capillaries at their ends. After a capillary scan, microscale thermophoresis was carried out at 25 °C using the “blue” detector with an excitation wavelength of 470 nm and an emission wavelength of

520 nm. The initial LED laser power was set to 6% (Hic1-BTB) or 12% (Tat Cys⁻, peptides) and three different MST IR laser power intensities (20/30/40%) were used. After 5 s of initial fluorescence detection, the MST IR laser was turned on for 30 s to create temperature-induced movement and then turned off again to allow for back-diffusion. Binding was analyzed using thermophoresis and temperature jump, if the initial fluorescence remained unchanged across all capillaries. In cases of a titrant concentration-dependent change in initial fluorescence (as seen for all measurements with Hic1-BTB or Tat Cys⁻), a sample denaturation test was performed: 10 µl each of the measured samples with the highest and the lowest titrant concentration were mixed with 10 µl of 2-fold SD mix. After denaturation at 95 °C for 5 min, samples were centrifuged at 20,000 rcf and 20 °C for 2 min. Capillaries were loaded with the denatured samples and a capillary scan was performed. If the fluorescence in the denatured samples did not show any titrant concentration-dependent fluorescence change, binding was analyzed from the first 5 s of initial fluorescence. Raw data was exported and fitted in GraFit 7.0.3 (Erithacus Software Limited) using the “1 site with background” function (equation 11).

$$c_{bound} = \frac{capacity \times c_{free}}{K_d + c_{free}} + background \quad (11)$$

with c_{bound} = concentration of bound titrant (M), capacity = maximal percentage of bound titrant molecules, K_d = dissociation constant with 50% of titrant molecules in bound form (M), c_{free} = concentration of free titrant (M), background = minimal percentage of bound titrant molecules.

3.7 Bioanalytical methods

3.7.1 Circular dichroism spectroscopy

Circular dichroism (CD) uses circularly polarized light to examine the secondary structure of proteins²²¹. A mostly α -helical protein exhibits local minima at 208 nm and 222 nm when exposed to circularly polarized light, whereas a protein with wide stretches of β -sheets shows a local minimum at 215 nm²²¹. In contrast, proteins with random coils have a local minimum at 198 nm²²¹. CD spectroscopy was used to examine the secondary structure of fl-hSirt1 and Tat Cys⁻. In all cases, the final CD spectrum was an accumulation of five individual CD spectra of the same sample to reduce noise. CD spectroscopy of 0.2 mg/ml protein was performed in 400 µl of 10 mM potassium phosphate, pH 6.4, 150 mM NaCl at 20 °C. As control, a CD spectrum of 400 µl buffer was recorded similarly.

Since Tat Cys⁻ exhibited no distinct secondary structure in solution, the α -helical propensity of the protein was tested with a trifluoroethanol (TFE) titration^{222,223}. A CD spectrum of 10 µM Tat Cys⁻ in 250 µl 10 mM potassium phosphate, pH 6.4, 150 mM NaCl was measured

at 20 °C. In five steps, the TFE concentration was increased by 10% (v/v) each and CD spectra were recorded. To exclude any effects of TFE on the buffer, a control without protein was treated the same way.

The final protein CD spectra in Θ_{mdeg} were normalized by subtraction of the buffer CD spectrum at the respective temperature, and subsequent application of equation 12 (including the molecular weight of the protein) to reach the mean molar ellipticity per residue.

$$\Theta_{\text{MRE}} = \frac{\Theta_{\text{mdeg}} \times M}{10 \times c \times d \times r} \quad (12)$$

with Θ_{MRE} = mean molar ellipticity per residue; Θ_{mdeg} = ellipticity (mdeg); M = molecular weight (g/mol); c = concentration (mg/ml); d = path length (cm); r = number of residues

3.7.2 Intact mass spectrometric analysis of proteins

Proteins can be analyzed by mass spectrometry in order to determine their exact molecular weight. In a total volume of 20 μl 20-50 μM of purified protein were diluted with 0.1% (v/v) FA and injected onto a C4 column of the TOF mass spectrometer. In the case of Tat Cys⁻, the protein was dialyzed against 10 mM sodium acetate, pH 6 for 1 h in an Xpress Micro Dialyzer tube (Serva, MD100 or MD300, MWCO 6-8 kDa) prior to intact mass spectrometry since 0.1% (v/v) FA and other buffers like HEPES or potassium phosphate turned out to be incompatible with the protein or the method.

3.7.3 Tryptic digest of proteins for mass spectrometric analysis

For identification of proteins or for a detailed analysis of protein sequences by mass spectrometry (e.g., after crosslinking) a tryptic digest was performed. Samples were either digested in-solution or desired bands from a native or SDS gel were cut out and digested. Importantly, sterilized Eppendorf tubes and disposable glass cover slips or scalpels had to be used to prevent contamination of samples with keratins. In-solution digests were performed overnight at 37 °C using 20-70 μM of protein in a volume of 20-50 μl supplemented with 1 μl of 0.1 mg/ml Trypsin. When specific bands from a gel were analyzed by mass spectrometry, they were cleaved out and cut into 4-5 smaller pieces which were washed with 100 μl of 100% (v/v) methanol for a few seconds. The gel pieces were then completely decolorized in 100 μl discoloration solution in several steps of 20 min incubation at 37 °C and 300 rpm in a thermoshaker. Destained gel pieces were dried in a vacuum centrifuge at 55 °C, resuspended in 50 μl rehydration solution, and incubated for 20 min at 56 °C. Residual liquid was removed and gel pieces were alkylated in 50 μl alkylation solution for 20 min at 20 °C in the dark. Again, residual liquid was removed and gel pieces were washed for 30 s in 1 ml ddH₂O which was disposed. After 15 min incubation at 20 °C with 200 μl dehydration solution, the liquid

was taken out and 100 μ l 100% (v/v) acetonitrile was added for 5 min which was disposed afterwards. The gel pieces were completely dried in a vacuum centrifuge at 55 °C, then cooled to 20 °C, and protein bands were digested with 10 μ l of digestion solution for 10 min at 20 °C. To prevent samples from drying out, an additional 20-30 μ l of 25 mM NH_4HCO_3 , pH 8.0 was added before incubation at 37 °C overnight. Next day, the supernatant was transferred to a new Eppendorf tube and further peptides were eluted from the gel pieces by incubation with 20 μ l elution solution in a sonifying bath for 20 min. Both supernatants were combined and completely dried in a vacuum centrifuge at 55 °C. After addition of 20 μ l 0.1% (v/v) FA, digested protein bands were incubated for 10 min at 20 °C and 300 rpm in a thermoshaker. Samples from tryptic in-solution or in-gel digest were injected onto a pre-column for desalting, followed by automated injection onto a C18 column for peptide separation either on an LTQ or a TOF mass spectrometer.

3.7.4 Limited proteolysis

For mapping a stable core of hAROS, limited proteolysis was performed and 100 μ g His₆-hAROS were digested with GluC protease in a molar ratio of 100:1 in 50 mM Tris/HCl, pH 7.5. Before addition of the protease and at several time-points, 10 μ l of the reaction mix were sampled and the reaction was stopped by addition of 5x SDS sample buffer and incubation at 95 °C for 5 min. After analysis of the limited proteolysis by SDS PAGE, selected SDS PAGE bands were cut out and subjected to tryptic digest for MS analysis.

3.7.5 Analysis of mass spectrometric data

Mass spectrometric data from MS deacetylation activity assays was analyzed with Skyline (MacCross Lab) as described in chapter 3.5.7 using MS/MS spectra raw files. Data from intact protein MS analysis was analyzed directly from the MS spectrum after HPLC separation to determine the protein mass. Protein identification after tryptic digest of samples was performed with MS/MS spectra raw files using Byonic™ (Protein Metrics Inc., CA, USA). If the protein was known, e.g., after crosslinking, the program could be supplemented with the expected protein sequences to reduce unspecific mismatches. Otherwise the MS/MS spectra raw files were aligned against a database containing all sequences deposited to Uniprot¹⁶². Protein identification hits by Byonic™ were then manually analyzed and unspecific hits like trypsin and human keratins or horn proteins were omitted. The remaining hits were ordered according to the number of detected peptides and the significance of their MS/MS spectrum to determine the most likely protein.

3.8 Crystallographic methods

3.8.1 Screening for initial crystallization conditions

Initial crystallization conditions for each protein combination were screened in 96-well format from commercially available screens (Qiagen) with specific stock solutions promoting the protein crystal nucleation. The sitting-drop vapor-diffusion technique was used exclusively. The protein solution was prepared with fresh, pure, and homogenous protein and supplemented by choice with substrates, cofactors, reaction products, activators, inhibitors, or binding partners. This protein stock solution was incubated at 20 °C or 4 °C for 1 h or up to 12 h prior to the experiment. Any precipitated protein was removed by centrifugation at 14,000 rpm for 10 min in a F45-30-11 rotor (Eppendorf). A Phoenix robot (Art Robbins Instruments) was used to pipet 0.2 μ l of the protein stock solution to 0.2 μ l of the reservoir solution into the wells of MRC2 or MRC3 crystallization plates (Molecular Dimensions). These combined crystallization drops were equilibrated against a reservoir of 35 μ l screening stock solution. For the setup of protein-protein screening experiments, an additional Peltier element was used to keep the protein solution cool during the pipetting process. Experiments with compounds solved in DMSO or with Tat peptides were set up at 20 °C. Immediately after pipetting, the MRC2 or MRC3 plate was sealed airtight with a self-adhesive clear tape. Most initial screening crystallization experiments were monitored at 20 °C in an automated ROCK IMAGER 1000 imaging system (Formulatrix[®]) using the ROCK MAKER[®] software (Formulatrix[®]). For initial screening crystallization experiments at 4 °C, the commercial screen stock solutions were pre-cooled, the Peltier element was used for the protein stock solution, and plates were immediately brought to a 4 °C room after airtight closure.

3.8.2 Optimization of initial crystallization conditions

Initial crystallization conditions were manually optimized in 24-well VDXm greased crystallization plates (Hampton Research, 18 mm) using the hanging-drop vapor-diffusion technique to yield larger and better diffracting crystals. The initial crystallization condition was varied in its pH and/or concentration of salt or precipitant and new reservoir stock solutions of 500 μ l each were prepared and transferred into the 24 wells. The protein solution was formulated as in the initial experiment and 1 μ l was pipetted on a cover slip to be mixed with 1 μ l of the varied reservoir stock solution. The cover slip was used to seal the well airtight by carefully pressing it onto the greased edges of the well. Optimization of crystallization conditions was performed at the same temperature that showed crystal nucleation. Crystal growth was manually monitored with a stereo microscope attached to a

digital camera. When initial protein crystals could not be reproduced by hanging-drop vapor-diffusion, the sitting-drop technique was applied using 48-well Swissci MRC Maxi crystallization plates (Molecular Dimensions) with 200 μ l reservoir solution.

In case of crystal size and diffraction quality not being able to be improved by a simple grid optimization around the initial crystallization condition, an additive was searched using a commercially available 96-well additive screen (Hampton Research). The best initial condition regarding pH and precipitant/salt concentration was prepared as 110% stock solution in a total volume of 5 ml. 45 μ l of this reservoir stock solution were put into each of the reservoirs of a MRC2 plate. Using the Phoenix robot, 5 μ l of the 10x stock solutions from the additive screen were then added and mixed with the reservoir solution. 0.2 μ l of the improved reservoir solutions were mixed in the crystallization drop with 0.2 μ l of the protein stock solution prepared as in the original experiment. The crystallization plates were sealed airtight and automatically monitored at 20 °C in the Formulatrix ROCK IMAGER 1000.

3.8.3 Cryoprotection of protein crystals

In order to remove water from protein crystal solvent channels, the crystals were protected with a cryoprotective solution. If not noted otherwise, this solution consisted of the same concentration of the original reservoir solution combined with all small molecule ligands from the protein stock solution used for obtaining the protein crystal as well as 25% (v/v) glycerol. The cryogenicity of a cryoprotective solution was tested in liquid nitrogen prior to use. For diffraction experiments, a single protein crystal was mounted with a cryo loop (Hampton Research) of appropriate size (0.05-0.5 mm) from the hanging or sitting drop and transferred to 2 μ l of cryoprotective solution. After washing it shortly in the cryoprotective solution, the single crystal was taken out again with the cryo loop and flash-cooled by rapid immersion in liquid nitrogen. Crystals were stored in liquid nitrogen until measurement.

3.8.4 X-ray structure analysis and data collection

To evaluate the nucleation of small protein crystals, they were colored with either JBS True Blue (Jena Bioscience) or Izit crystal dye (Hampton Research). Larger crystals were tested *in house* on a maruX generator (marresearch) with CuK α anode to distinguish between protein and salt crystals and to assess the diffraction quality. For this purpose, crystals were mounted in a nitrogen cryostream at 100 K and irradiated by monochromatic radiation with a wavelength of 1.5411 Å. Two images were recorded with a detector distance of 200 mm, whereby the crystal was turned by 1° within 10 min for every image. After the first image the crystal was turned by 89° to gain further insight on the diffraction quality.

Diffraction crystals were sent to a synchrotron for data collection with a high-intensity source. In most cases, the BESSYII electron storage ring (Helmholtz-Zentrum) in Berlin-Adlershof was used. It has two energy-tuneable beamlines, MX 14.1 and MX 14.2, which can be used in the range of 5.5-15.5 keV²²⁴. The radiation source for both beamlines is a superconducting 7T-wavelength shifter allowing protein crystals with a size of just about 15 μm to be measured²²⁴. Crystals were mounted by automated robotic sample-mounting in a nitrogen cryostream of 100 K. If not noted otherwise, datasets were collected at a radiation wavelength of 0.91841 \AA equaling an energy of 13.5 keV. The distance of the Pilatus 6M (MX 14.1) or 2M (MX 14.2) detector was adjusted according to the diffraction quality of the crystal. A diffraction test with two images of 0.5 s exposure time each was performed, where the crystal was turned by 1° within each image and turned by 89° after the first image. The strategy for the dataset collection was evaluated with imosflm²²⁵. Datasets were collected with a rotating angle of 0.1° for $120\text{-}300^\circ$ and an exposure time of 0.2-0.5 s per image. Another synchrotron source for data collection of protein crystals was the beamline PXIII located at the Swiss Light Source (Villigen, CHE) and operated by Paul Scherrer Institute²²⁶. Its radiation source is a 2.9T superbend magnet²²⁶. Datasets were collected at a radiation wavelength of 1.0000 \AA on a Pilatus 2M-F detector. In general, the same strategy was followed as at BESSYII.

3.8.5 Data processing, model building, and structure refinement

Data processing was performed with XDSAPP²²⁷, an automated graphical user interface based on XDS²²⁸. XDSAPP²²⁷ contains all programs of XDS for indexing, integration, scaling, sorting, and data conversion²²⁷. XDSAPP also uses Pointless^{229,230} from the CCP4 suite²³¹ to check for screw axes as well as Phenix.xtriage²³² for basic checks on data quality including twinning, anomalous signal, translational pseudo symmetry, the L-test, and higher metric symmetry²³². Apart from that, datasets with inhibiting Tat peptides were processed with DIALS^{233,234} to separate several sometimes equally strong lattices. In this case, indexing and integration was performed with DIALS^{233,234}, while subsequent processing was executed in command-line using Rebatch, Pointless^{229,230}, Aimless^{229,230}, and cTruncate²³⁵. In contrast to XDSAPP²²⁷, DIALS^{233,234} does not assign reflections for R_{free} . Hence, they were assigned afterwards with CCP4.Uniqueify²³⁶. In general, datasets were processed to a final resolution cutoff of $I/\sigma I$ not lower than 0.5 and $CC_{1/2} = 30\text{-}50\%$ ^{237,238} as long as the completeness in the highest resolution shell did not drop below 90%. The molecular replacement for sirtuin structures was calculated with either MOLREP²³⁹ from the CCP4 suite or Phaser²⁴⁰ from the Phenix suite²⁴¹ using an appropriate model from the protein data base (PDB)⁷⁷. For Hic1-BTB, the program MoRDa²⁴² was applied to find a suitable model and to determine a

solution by comparing the sequence of Hic1-BTB to PDB structures and taking into account the reflection file. The accuracy of the molecular replacement was checked by a refinement cycle with either REFMAC5²⁴³ from the CCP4 suite or Refine²⁴⁴ from the Phenix suite. If the molecular replacement was correct, the program Coot²⁴⁵ (version 0.8.9.1) was used for iterative cycles of model building followed by refinement with REFMAC5²⁴³ or Phenix.Refine²⁴⁴. In case of structures with a resolution below 3.5 Å, geometric restraints were derived from a suitable model deposited to the PDB using ProSMART²⁴⁶ during all further refinement cycles with REFMAC5²⁴³. In all cases, the selected refinement strategy was checked with PDB_REDO²⁴⁷ and adjusted if necessary. Structures were built and refined until the R and R_{free} values did not decrease anymore, while the geometry and difference density were checked with validation tools from Coot²⁴⁵. The structures were finalized by a terminal step of refinement and the model quality was evaluated with MolProbity²⁴⁸. Analysis of structures and comparison to other structures, e.g., superpositions, were conducted with PyMOL²⁴⁹. PyMOL²⁴⁹ was also used for generating figures of the structures. Unless noted otherwise, sirtuins were displayed in cartoon style with the Zn²⁺ ion as yellow sphere and substrate peptides or small-molecule ligands as sticks. Hic1-BTB was also displayed in cartoon style with the Na⁺ ion as light orange sphere. Composite omit maps were calculated with Phenix.Composite_omit_map²⁵⁰ using the refined algorithm to remove phase bias from the 2mF_o-DF_c density. Composite omit maps were contoured at 1 σ. For modelling of N-terminal residues of Tat₃₇₋₅₉ and Tat₃₄₋₅₉, a feature enhanced map²⁵¹ was calculated. Protein interactions with a cocrystallized ligand were shown in 3D with PyMOL²⁴⁹ as orange dotted lines or in 2D with the program Ligplot⁺²⁵².

3.8.6 Crystallization conditions and structure solution of obtained complexes

3.8.6.1 *Mini-Sirt1 apo*

Apo mini-Sirt1 crystals (10 mg/ml) were obtained in 0.1 M Bis-tris propane, pH 8.0, 18% (w/v) PEG 3350, 0.2 M sodium fluoride, 10% (v/v) ethanol, and 0.01 M TCEP at 20 °C in hanging drops under vapor diffusion. They appeared within five days and were shaped as triangular stacked plates the size of 200-350 μm. Crystals were separated with a mounting loop prior to cryo protection in reservoir solution with 18% (v/v) glycerol. The best crystal diffracted up to 3.7 Å at BESSY, MX 14.1 and data was processed in space group C222₁. The structure was solved by molecular replacement with Phaser.MR²⁴⁰ and a mini-Sirt1/STAC complex (PDB: 4ZZH), which was splitted into the NAD⁺- and Zn²⁺-binding domains.

3.8.6.2 *Mini-Sirt1 soaking with tranilast*

Soaking of tranilast was attempted with freshly produced apo mini-Sirt1 crystals. For this purpose, 0.2 μ l of a solution containing 1 mM tranilast in 10% (v/v) DMSO were added to the crystallization drop. Crystals were mounted after 10 min, 60 min, or 24 h and cryoprotected in reservoir solution with 1 mM tranilast and 25% (v/v) glycerol. The best mini-Sirt1/tranilast soaked crystal diffracted up to 3.1 Å at BESSY, MX 14.1. Data was processed in space group C222₁ and solved by molecular replacement with the model from apo mini-Sirt1 using MOLREP²³⁹, revealing a non-bound mini-Sirt1.

3.8.6.3 *Hic1-BTB crystallization*

An initial crystallization condition for 10 mg/ml Hic1-BTB octamer was searched with the commercial screens Classics I and II (Qiagen). After crystallization at 20 °C with the sitting-drop vapor-diffusion method, the protein crystallized overnight in several crystallization conditions in the shape of thin needles, which grew to their final size within 1-3 days. Crystals from the condition 0.1 M sodium cacodylate, pH 6.5, 1.4 M sodium acetate were cryoprotected in 0.1 M sodium cacodylate, pH 6.5, 1.2 M sodium acetate, 20% (v/v) glycerol and a dataset of 2000 images for the best crystal was collected at BESSY, MX 14.1. Data was processed to a resolution of 2.7 Å in space group P2₁2₁2₁ (19). Molecular replacement with MOLREP²³⁹ using diverse BTB domains deposited to the PDB failed. Thus, MoRDa²⁴² was used, which found a solution with six dimers of a BCL-6 BTB structure (PDB: 3LBZ) totaling 12 molecules in the asymmetric unit. After refinement of the solution with REFMAC²⁴³ and subsequent strict deletion of all amino acids that did not fit perfectly into the 2F_o-F_c density, one molecule was rebuilt in Coot²⁴⁵ with the help of Parrot density modification²⁵³. The coordinates of the rebuilt molecule were then copied onto the other 11 molecules and a new merged coordinate file was refined with REFMAC²⁴³. Afterwards, the refined model and density showed that further four molecules had to be added to the asymmetric unit, which was executed in Coot²⁴⁵ by copying the coordinates of one tetramer. Subsequent structure refinement was carried out with Phaser.Refine²⁴⁴ to prevent overfitting.

3.8.6.4 *hSirt3-(118-399) in complex with ac-Tat_46-54*

For crystallization of hSirt3 with ac-Tat_46-54, 10 mg/ml hSirt3-(118-399) were incubated with 2 mM ac-Tat_46-54 for 60 min at 20 °C. Afterwards suitable crystallization conditions were searched with the sitting-drop vapor-diffusion method at 20 °C and the commercial screens JCSG CORE I-II (Qiagen). The hSirt3-(118-399)/ac-Tat_46-54 complex crystallized in the crystallization condition 0.1 M MES, pH 6.0, 30% (w/v) PEG 200, 5% (w/v) PEG 3000

as plates stuck together, which could be easily separated and cryoprotected in reservoir solution with 25% (v/v) glycerol. A dataset of 3000 images for the best crystal diffracting to 1.65 Å was collected at BESSY, MX 14.1. The complex was processed in C222₁ with XDSAPP²²⁷ and solved with Phaser.MR²⁴⁰ using a Sirt3 structure (PDB: 4FVT) as model.

3.8.6.5 *hSirt3-(118-399) cocrystallization with inhibiting Tat peptides*

Initial crystallization conditions for hSirt3-(118-399) in complex with an inhibiting Tat peptide were searched with the commercial JCSG Core suite I-IV (Qiagen) at 20 °C with the sitting-drop vapor-diffusion method. The protein solution contained 10 mg/ml hSirt3-(118-399), 2 mM of the respective Tat peptide in a final concentration of 10% (v/v) DMSO in a buffer of 20 mM Tris/HCl, pH 8.0, 150 mM NaCl, 5% (v/v) glycerol, 1 mM TCEP, and in some cases also 10 mM NAD⁺. To avoid precipitation of the protein prior to crystallization, hSirt3 had to be separately mixed with about two thirds of the volume of buffer, while in another Eppendorf tube, DMSO was added to the Tat peptide and mixed with the latter third of the volume of buffer before combining both solutions. The resulting protein solutions were incubated for 30-60 min at 20 °C. Human Sirt3-(118-399) crystallized with Tat₃₄₋₅₉ in the crystallization condition 20% (w/v) PEG 3350, 0.2 M ammonium formate, while additional supplementation of the protein solution with NAD⁺ led to a crystal in 0.1 M MES, pH 6.5, 12% (w/v) PEG 20000. A complex for hSirt3-(118-399)/Tat₃₇₋₅₉ was obtained in the crystallization condition 0.1 M CHES, pH 9, 20% (w/v) PEG 8000. All crystals were cryoprotected in reservoir solution with 25% (v/v) glycerol prior to collection of a dataset at BESSY, MX 14.1. Due to multiple lattices, all datasets were processed with DIALS^{233,234}. All structures were solved by molecular replacement using Phaser.MR²⁴⁰. For the hSirt3-(118-399)/Tat₃₇₋₅₉ complex, a published hSirt3 structure (PDB: 4BVB) was used as model for molecular replacement, the other complexes were then solved using this first complex.

3.9 Bioinformatical methods

Clustal Omega²⁵⁴ was used to check sequencing results from Eurofins MWG or to generate a multiple protein sequence alignment to determine the sequence identity. Theoretical molecular weights and extinction coefficients of proteins were calculated based on their sequence with the program ProtParam from the ExPASy suite²¹⁰. MarvinSketch²⁵⁵ was used for drawing chemical structures and reactions. Structural models of non-crystallizable proteins were computed based on their sequence using the web server Phyre2²⁵⁶, which compares the protein sequence to proteins already published in the PDB⁷⁷. Secondary structure disorder predictions were assessed with IUPred2A²⁵⁷.

4. Results

4.1 Characterization of human Sirtuin 1 and its intrinsic and extrinsic activity modulation by small molecules

4.1.1 Recombinant expression, purification, and characterization of fl-hSirt1

Preparative heterologous overexpression of human fl-Sirt1 from pET15b was performed according to an established protocol²⁵⁸. In brief, fl-hSirt1 was purified by affinity chromatography (AC), dialysis with His₆-tag cleavage by thrombin, reverse AC, ion exchange chromatography (IEX), and size exclusion chromatography (SEC) (Figure 4.1).

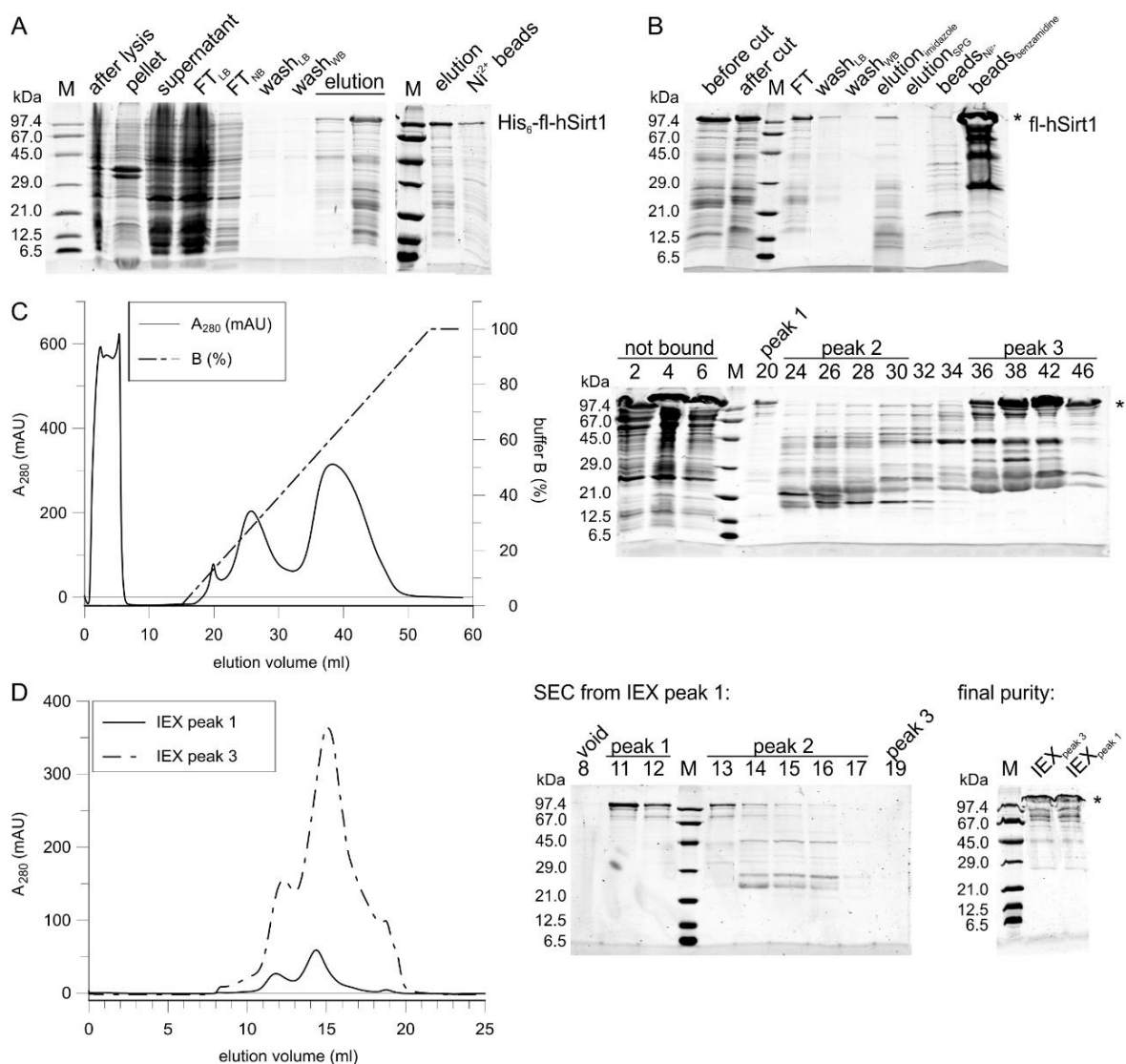


Figure 4.1: Purification of fl-hSirt1 from pET15b. **A** Affinity chromatography (AC) and **B** Reverse AC on Ni²⁺-immobilized beads. **C** IEX on HiTrap Q FF. Fl-hSirt1 eluted at 12.5% buffer B (peak 1) and 60% buffer B (peak 3). **D** SEC on S200 10/300 GL. Fl-hSirt1 eluted at 11.3 ml or 12.4 ml depending on the prior binding to the IEX column. Impure fl-hSirt1 eluted later and was not pooled. Quality assessment of concentrated fl-hSirt1 pools normalized to 5 μ M on SDS PAGE. Abbreviations: FT - flowthrough, LB - lysis buffer, NB - nuclease buffer, WB - wash buffer. Numbers on SDS PAGE gels refer to the respective elution volume from IEX or SEC.

It is worth highlighting that the initial heavy contamination of His₆-fl-hSirt1 with coexpressed and unspecifically bound *E. coli* proteins in affinity chromatography (Figure 4.1A) could be reduced after cleavage of the His₆-tag and reverse AC (Figure 4.1B). IEX was able to further optimize the purity of fl-hSirt1, but afforded a pure peak 1 and a less pure peak 3 containing the majority of fl-hSirt1 (Figure 4.1C). Separate subjection of those two pools to SEC on S200 10/300 GL resulted in fl-hSirt1 of at least 70% purity eluting at 11.3 ml or 12.4 ml (Figure 4.1D) depending on the prior binding to the IEX column. Fl-hSirt1 could be obtained with a yield of 0.5-1.0 mg per 1 l of expression culture.

The two different final fl-hSirt1 pools were evaluated in a coupled enzymatic deacetylation activity assay and revealed a specific activity of 21-25 nmol/(min × mg), which is similar to the specific activity of mini-Sirt1 (Figure 4.2A), demonstrating that all fl-hSirt1 fractions are of comparable activity despite variations in purity and binding behavior to the IEX column. A CD spectrum confirmed the integrity of fl-hSirt1: the recombinant protein has a secondary structure with mostly α -helices, indicated by local minima at 208 nm and 222 nm, and a smaller β -strand content suggested by a local minimum at 215 nm (Figure 4.2B). Subjected to thermal denaturation, fl-hSirt1 exhibits a melting temperature of 41.4 ± 0.3 °C (Figure 4.2C), which makes it applicable for activity assays under native conditions up to 37 °C.

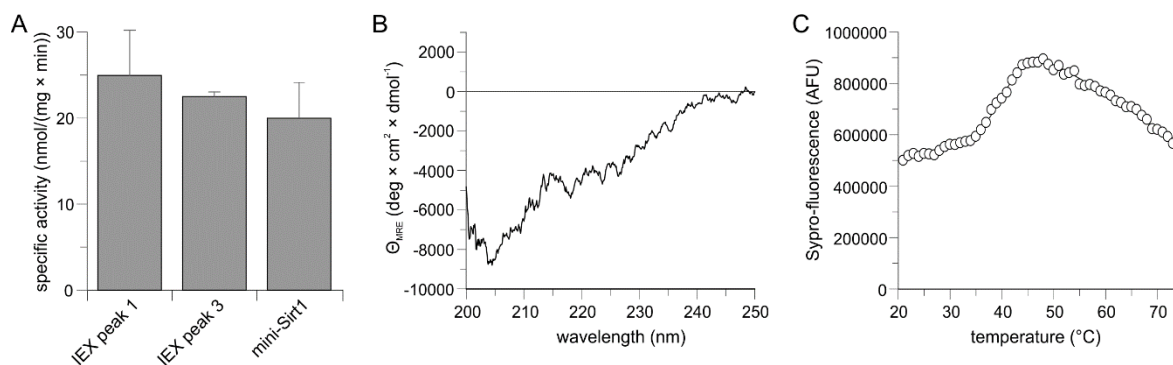


Figure 4.2: Bioanalytical characteristics of fl-hSirt1. **A** Continuous coupled enzymatic activity assay with 1 μ M fl-hSirt1, 500 μ M NAD⁺, and 100 μ M p53short ($n = 2$). **B** CD-spectrum of 0.2 mg/ml fl-hSirt1 indicating a secondary structure with α -helices and β -strands. **C** TSA with 5 μ M fl-hSirt1 in 25 mM HEPES, pH 7.8, 100 mM KCl, 2 mM DTT. **B-C** Fl-hSirt1 from pET32*amod* was used.

Other constructs of fl-hSirt1 with N-terminal solubility enhancing tags like thioredoxin- (TRX), glutathione S-transferase- (GST), SUMO- or Strep-tag were purified in our laboratory with an adapted purification protocol (Norbert Grillenbeck, personal communication). Table 4.1 shows a comparable specific activity for active batches of purified fl-hSirt1 from these constructs. As the solubility enhancing tag was always removed during purification, fl-hSirt1 from such other constructs was used for some experiments presented in this thesis, as depicted in the respective figure captions.

Table 4.1: Specific activity for fl-hSirt1 from different vectors. Coupled enzymatic deacetylation activity assay with 1 μM fl-hSirt1, 500 μM NAD^+ , and 100 μM p53 peptide substrate. Fl-hSirt1 was purified at least three times from each vector, but only batches with measurable deacetylase activity are indicated here.

Fl-hSirt1 from vector	N-terminal tag	Remaining tag	MW (Da)	Specific activity (nmol/(mg \times min))	Number of purified active batches
pET15b	His ₆	none	81825.1	25.2 \pm 7.6	6
pGEX-6P-3	GST	GST	108562.2	21.0	1
pET32a <i>mod</i>	Trx-His ₆	none	82440.8	26.7 \pm 10.8	2
pET15d	His ₆ (N-ter.), Strep (C-ter.)	Strep (C-ter.)	83844.3	39.0	1
pET19b <i>mod-Sumo</i>	His ₆ -Sumo	none	81681	28.2	1
pETM-30.1	His ₆ -GST	none	82134.5	12.5	1

Purification of the N- and C-terminally truncated hSirt1-(183-664) and hSirt1-(214-664) from pET15b was performed in our laboratory according to the described scheme for fl-hSirt1. However, the deacetylase activity of these hSirt1 deletion variants is reduced by at least 50%, with hSirt1-(214-664) being even less active (Figure 4.3).

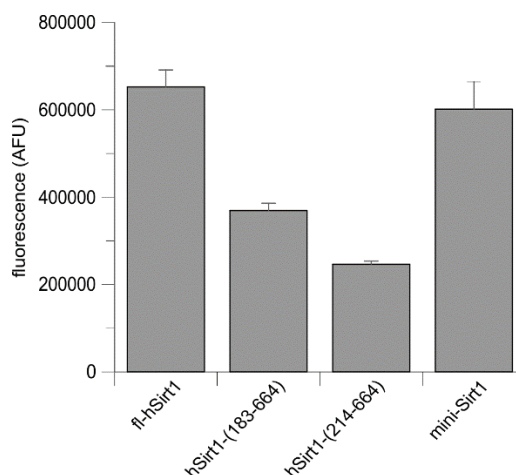


Figure 4.3: Activity of N- and C-terminally truncated hSirt1 variants. Fluor de Lys assay with 1 μM hSirt1, 500 μM NAD^+ , and 100 μM *FdL-1* substrate ($n = 6$).

4.1.2 Recombinant expression, purification, and characterization of human mini-Sirt1

Since expression and purification of fl-hSirt1 is susceptible to low yield, purity, and activity, I cloned and established a model construct of hSirt1 in my previous work²⁵⁹, which is similar to the one described by Dai *et al.* (2015)⁸⁰. This mini-Sirt1 (Figure 1.6A) was purified by affinity chromatography, dialysis with His₆-tag cleavage, reverse AC, dialysis, and SEC (Figure 4.4).

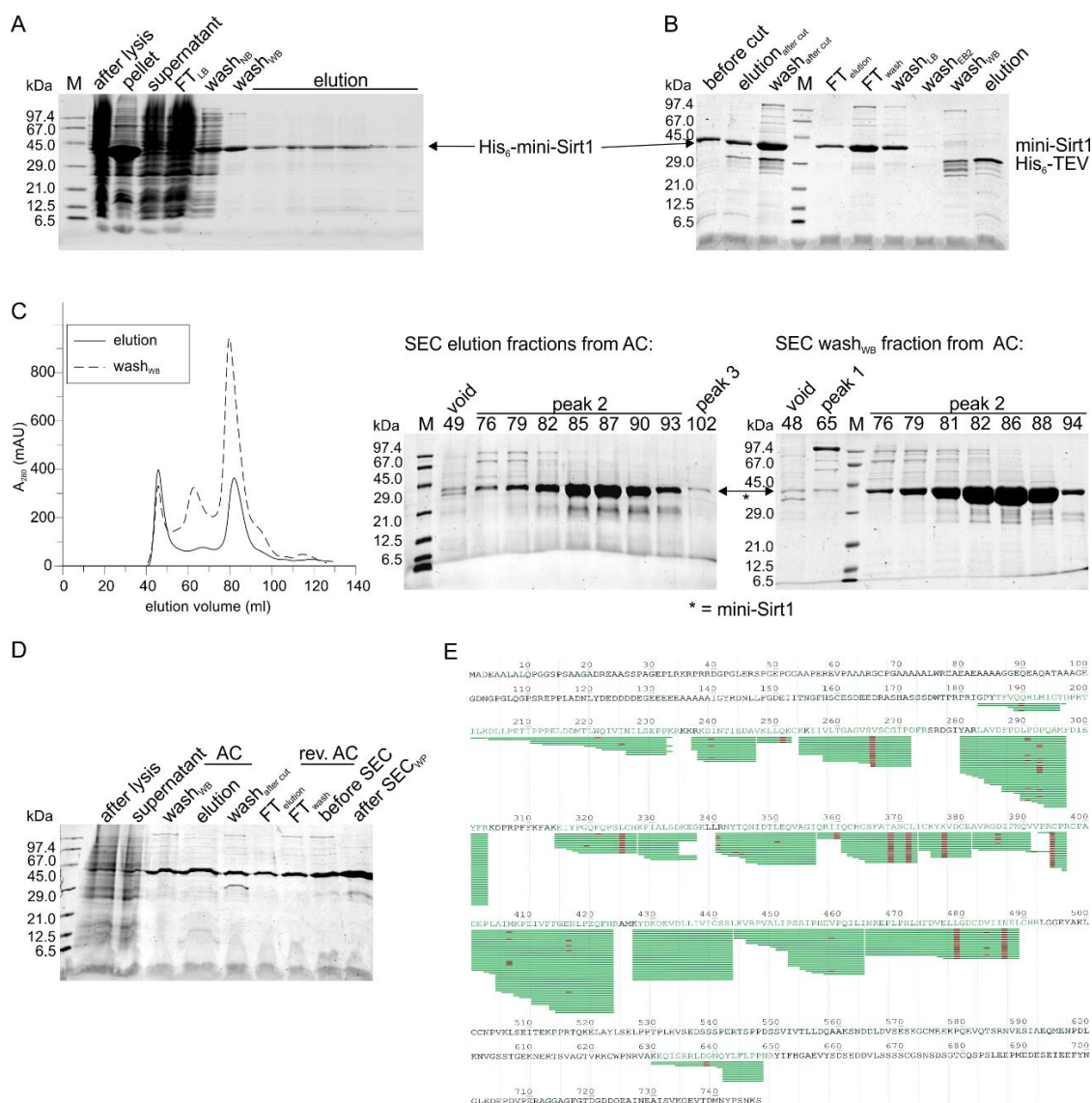


Figure 4.4: Purification of mini-Sirt1. **A** Affinity chromatography and **B** Reverse AC on Ni²⁺-immobilized beads. **C** SEC on S200 16/60 GL. Numbers on SDS PAGE gels refer to the respective elution volume. **D** Quality assessment of mini-Sirt1 samples normalized to 5 μ g. **E** Peptide coverage after tryptic digest of mini-Sirt1 followed by MS analysis. Detected peptides (green) are indicated with identified PTMs (red). Abbreviations: FT - flowthrough, LB - lysis buffer, NB - Ni²⁺-equilibration buffer, WB - wash buffer, EB - elution buffer.

Importantly, His₆-mini-Sirt1 eluted from the AC with two buffers of different imidazole concentrations (Figure 4.4A), resulting in separate purification of both fractions. After His₆-tag cleavage and reverse AC, mini-Sirt1, which previously eluted with a lower imidazole concentration, appeared to be contaminated with a protein of about 29 kDa (Figure 4.4B), that could not be separated during SEC (Figure 4.4C). Mini-Sirt1 eluted at 81.6 ml from SEC on a S200 16/60 column (Figure 4.4C). Except for the contamination with the 29 kDa protein, normalization of the samples for SDS PAGE revealed that the two initial mini-Sirt1 fractions are of comparable purity (Figure 4.4D). Mini-Sirt1 had a final purity of ~90% and yielded 3.5-4.0 mg per 1 l of expression culture. A tryptic digest of an SDS PAGE band of mini-Sirt1 followed by MS analysis undoubtedly identified the target protein (Figure 4.4E).

The purified mini-Sirt1 was subjected to activity and stability assays to assess its bioanalytical properties and compare them to fl-hSirt1. First, a continuous coupled enzymatic deacetylation assay resulted in a specific activity of 29.0 ± 0.6 nmol/(mg \times min) for mini-Sirt1, which is similar to the one for fl-hSirt1 (Figure 4.5A, Table 4.1) and supported by a *Fluor de Lys* assay with different batches of purified proteins (Figure 4.3). While there are small variations in the deacetylase activity of protein batches, these assays demonstrate that mini-Sirt1 is equally active as fl-hSirt1 and can be used as model for fl-hSirt1 in many cases, consistent with the comparison of fl-hSirt1 and a similar mini-Sirt1 construct by Dai *et al.* (2015)⁸⁰. Furthermore, the thermal stability of mini-Sirt1 was examined with a thermal denaturation shift assay in two different buffers: mini-Sirt1 in the SEC buffer yielded a melting temperature (T_m) of 54.4 ± 0.8 °C, while thermal denaturation of mini-Sirt1 in the assay buffer resulted in a T_m of 55.6 ± 0.6 °C (Figure 4.5B). This shows that mini-Sirt1 is stable in both buffers and amenable to *Fluor de Lys* assays at 37 °C.

To target complex crystallization of mini-Sirt1 with small molecules, its thermal stability was also investigated in a variety of other buffers systems. While buffers below pH 6.0 were generally not applicable for mini-Sirt1 due to its theoretical pI of 5.4, buffers from pH 6-10 resulted in a melting curve (Figure 4.5C). The T_m for mini-Sirt1 ranged from 35.9-52.5 °C with the highest melting temperature in 50 mM CHES, pH 9.0 (Figure 4.5C). Addition of NaCl to the buffers was beneficial and increased the mini-Sirt1 melting temperature by up to 4 °C with the greatest effect for 50 mM Tris/HCl, pH 8-8.5 (Figure 4.5C). In addition to NaCl, the effect of other additives on the thermal stability of mini-Sirt1 was tested in a less favorable buffer of 25 mM Bis-tris propane, pH 6.5, where mini-Sirt1 exhibited a melting temperature of 40.6 °C (Figure 4.5D). Salts like sodium acetate, sodium tartrate, or sodium sulfate were able to raise the T_m of mini-Sirt1 by up to 6 °C (Figure 4.5D). Apart from that, increasing glycerol concentration stabilized mini-Sirt1 and enhanced its T_m by up to 6.5 °C (Figure 4.5D). However, as glycerol is not always favorable for complex crystallization, a lower concentration was preferred and a buffer containing 25 mM Bis-tris propane, pH 6.5, 150 mM NaCl, and 5% (v/v) glycerol was considered suitable for cocrystallization of mini-Sirt1 with small molecules (chapters 4.1.4 and 4.1.5).

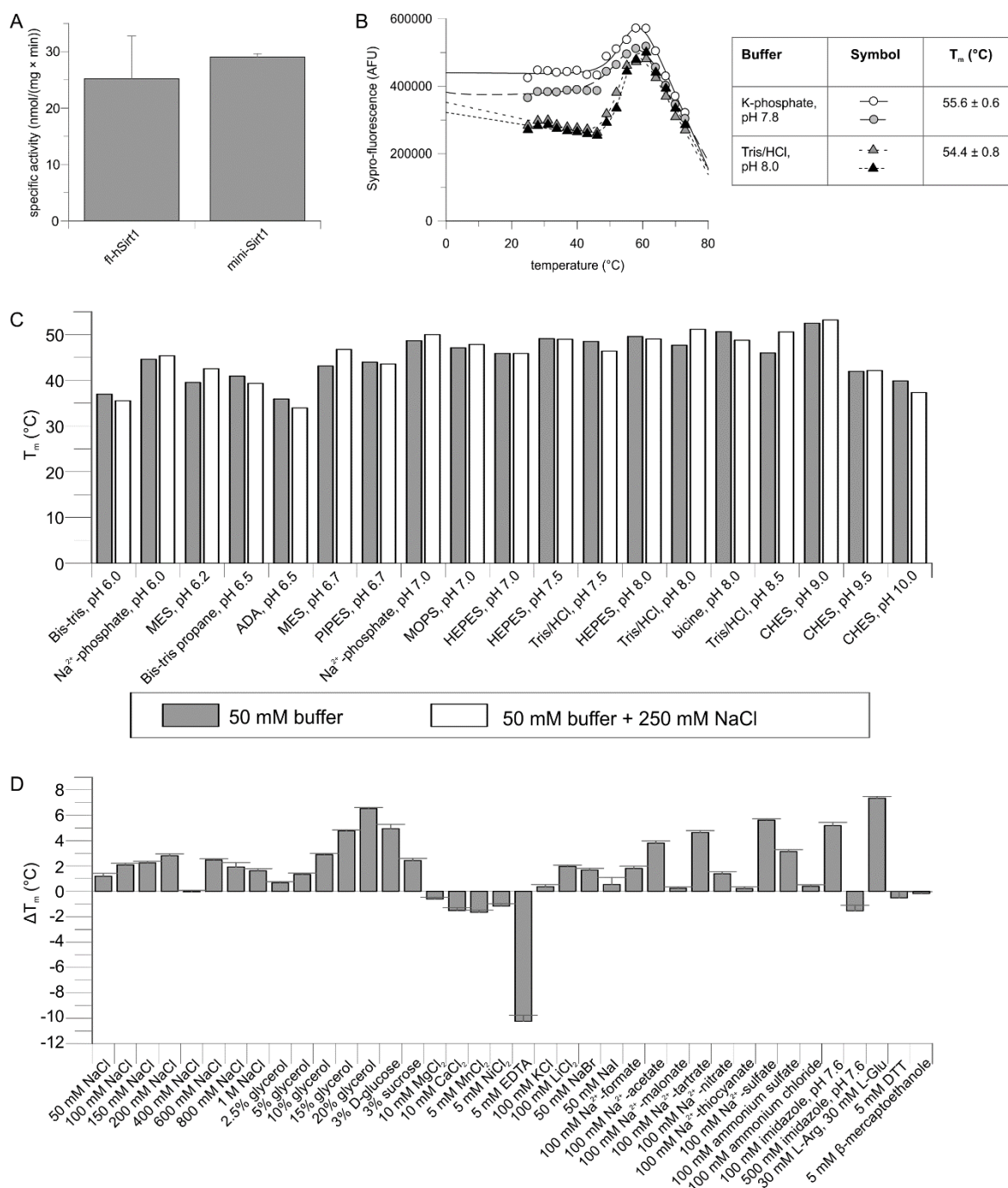


Figure 4.5: Bioanalytical characterization of mini-Sirt1. **A** Continuous coupled enzymatic deacetylation assay with 1 μ M mini-Sirt1 or fl-hSirt1, 500 μ M NAD⁺, and 100 μ M p53short. The specific activity was 29.0 ± 0.6 nmol/(mg × min) for mini-Sirt1 ($n = 2$) and 25.2 ± 7.6 nmol/(mg × min) for fl-hSirt1 ($n = 6$). **B** TSA with 5 μ M mini-Sirt1 in the SEC buffer (25 mM Tris/HCl, pH 8.0, 150 mM NaCl, 5% (v/v) glycerol, 10 mM DTT) and the assay buffer (10 mM potassium phosphate, pH 7.8) ($n = 2$). **C** TSA with 5 μ M mini-Sirt1 in different 50 mM buffers in absence or presence of 250 mM NaCl ($n = 1$). **D** TSA with 5 μ M mini-Sirt1 in 25 mM Bis-tris propane, pH 6.5 and various additives. Error bars refer to the error of the fit ($n = 1$).

Besides mini-Sirt1, other variants based on mini-Sirt1 were cloned and purified according to the described protocol. First, a mini-Sirt1- Δ SBD variant lacking the N-terminal SBD was constructed ranging from hSirt1 residues 214-505 with the ESA/CTR region connected via the approved (GGGS)₂-linker. The recombinant mini-Sirt1- Δ SBD had a lower yield of 0.5 mg per 1 l of expression culture and was ~70% pure (Figure 7.1). Similarly, a mini-Sirt1- Δ ESA

variant was created, ranging from hSirt1 residues 183-505, in which the C-terminal ESA/CTR region and the artificial linker were omitted. Purification of mini-Sirt1- Δ ESA (Figure 7.2) reached a purity of ~80% and a yield of 0.4 mg per 1 l of expression culture (Figure 7.2). Noticeably, SDS PAGE gels revealed several distinct bands around 29 kDa in both cases (Figure 7.1D, Figure 7.2D). Since both the SBD and the ESA/CTR region are relevant for Sirt1 activity^{76,80,93,97}, the deacetylase activity of the mini-Sirt1 deletion variants was investigated with an activity assay, revealing that both mini-Sirt1 deletion variants had a five-fold lower specific activity of 6.3 ± 1.3 nmol/(mg \times min) for mini-Sirt1- Δ SBD and 6.9 ± 0.8 nmol/(mg \times min) for mini-Sirt1- Δ ESA (Figure 4.6A). Nevertheless, both deletion variants were active and amenable to activity assays with modulators.

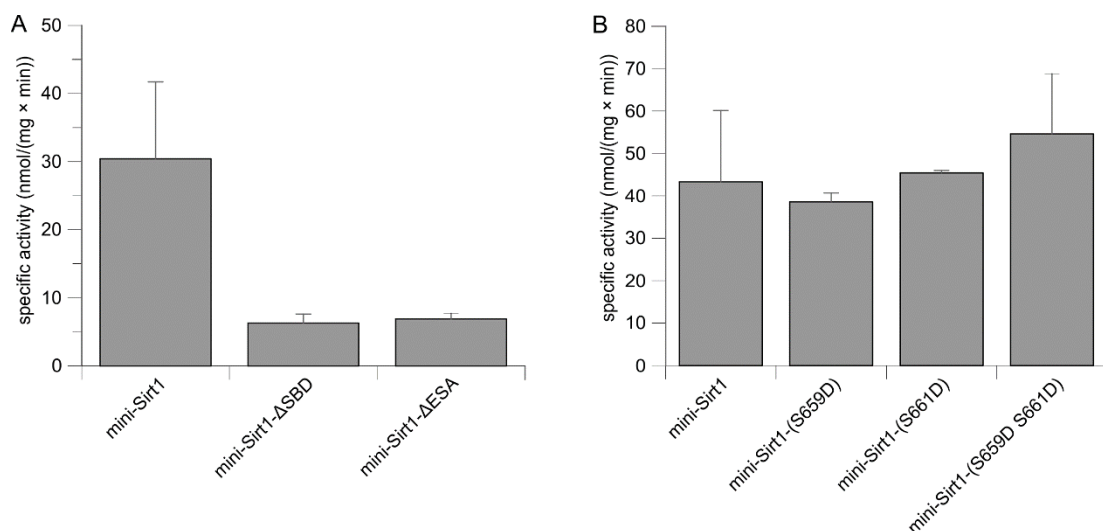


Figure 4.6: Characterization of mini-Sirt1 deletion and mutation variants. **A** Continuous coupled enzymatic assay with 1-5 μ M hSirt1 (normalized to 1 μ M). The specific activity was 30.4 ± 11.3 nmol/(mg \times min) for mini-Sirt1 ($n = 4$), 6.3 ± 1.3 nmol/(mg \times min) for mini-Sirt1- Δ SBD ($n = 5$), and 6.9 ± 0.8 nmol/(mg \times min) for mini-Sirt1- Δ ESA ($n = 5$). **B** Continuous coupled enzymatic assay with 1 μ M hSirt1. The specific activity was 43.3 ± 16.8 nmol/(mg \times min) for mini-Sirt1 ($n = 4$), 38.6 ± 2.1 nmol/(mg \times min) for mini-Sirt1-(S659D) ($n = 2$), 45.4 ± 0.6 nmol/(mg \times min) for mini-Sirt1-(S661D) ($n = 2$), and 54.6 ± 14.2 nmol/(mg \times min) for mini-Sirt1-(S659D S661D) ($n = 4$). **A-B** Assay conditions: 500 μ M NAD⁺ and 100 μ M p53short.

For interaction studies of hSirt1 with Hic1-BTB, mini-Sirt1 mutants were created which mimicked the phosphorylation of hSirt1 Ser659 and Ser661 by casein kinase II. These mutants comprised the original mini-Sirt1 (Figure 1.6A) with either a S659D mutation, or a S661D mutation, or with both mutations. Purification of these mutants was straight-forward and afforded a purity and yield comparable to wild-type mini-Sirt1 (Figure 7.3-Figure 7.5). A continuous coupled enzymatic deacetylation assay confirmed that the specific activity for all three phosphorylation mimicry mutants is similar to the specific activity of mini-Sirt1 (Figure 4.6B). Therefore, the mutations do not hamper Sirt1 activity, but might have an effect on the modulation by Hic1-BTB as investigated later (chapter 4.3.2).

4.1.3 Relevance of the ESA/CTR region for the intrinsic hSirt1 activity

The Sirt1 ESA/CTR region is crucial for the intrinsic Sirt1 activity^{76,80,93} and was predicted to associate with the Sirt1 catalytic core⁹³. In the early stage of this thesis, the effect of the ESA/CTR region on hSirt1 activity was examined with peptides. A first set of 18 peptides comprised 8-mer peptides shifted through the sequence of the ESA/CTR motif, further peptides included different longer and shorter sequence ranges (Table 7.1). In a preliminary continuous coupled enzymatic assay, a peptide spanning the whole ESA/CTR region was found to activate fl-hSirt1 although the enzyme itself contains the ESA/CTR region²⁵⁹ (Figure 4.7A). Furthermore, peptide 21 with the sequence NRYIFH-NH₂ was sufficient to stimulate fl-hSirt1 to the same extent²⁵⁹ (Figure 4.7A). In contrast, none of the 8-mer peptides were able to mediate this activation²⁵⁹. A mass spectrometric assay confirmed that the ESA/CTR region spanning hSirt1 residues 641-665 activates fl-hSirt1 and that peptide 21, comprising hSirt1 residues 647-653, is sufficient for this effect (Figure 4.7B). This stimulating effect of peptide 21 was again tested in continuous coupled enzymatic assays under different conditions, in which peptide solubility was enhanced by presence of 10% (v/v) DMSO, increasing the specific activity of fl-hSirt1 from 21.0 ± 3.1 nmol/(mg × min) to 29.3 ± 3.2 nmol/(mg × min) in presence of peptide 21 (Figure 4.7C). Reducing the substrate and NAD⁺ concentrations by about 50% still resulted in stimulation of fl-hSirt1 by ESA/CTR peptide 21 (Figure 4.7C), showing that the ESA/CTR region can activate fl-hSirt1 under various conditions. Focused on the sequence of the ESA/CTR peptide 21, shorter peptides were synthesized to identify the minimal sequence required for activation of fl-hSirt1 (Table 7.1). In a *Fluor de Lys* assay, fl-hSirt1 was activated by the whole ESA/CTR region (peptide 20) and peptide 21 (NRYIFH-NH₂) as before (Figure 4.7D). In addition, peptide 22 (*ac*-NRYIFH-NH₂), peptide 26 (NRYIF-NH₂), peptide 27 (RYIFH-NH₂), and peptide 30 (RYIF-NH₂) were able to stimulate deacetylation of the artificial *FdL-1* substrate by fl-hSirt1 (Figure 4.7D). This assay highlights that the ESA/CTR motif is able to further enhance the activity of fl-hSirt1, already containing the ESA/CTR region, and that the short ESA/CTR core sequence RYIF is sufficient for this effect (Figure 4.7D). A later published crystal structure of the catalytic domain of hSirt1 in complex with the whole ESA/CTR motif as peptide confirmed that the ESA/CTR folds back towards the catalytic core of Sirt1 elongating the NAD⁺-binding β-sheet by two additional β-strands⁷⁹.

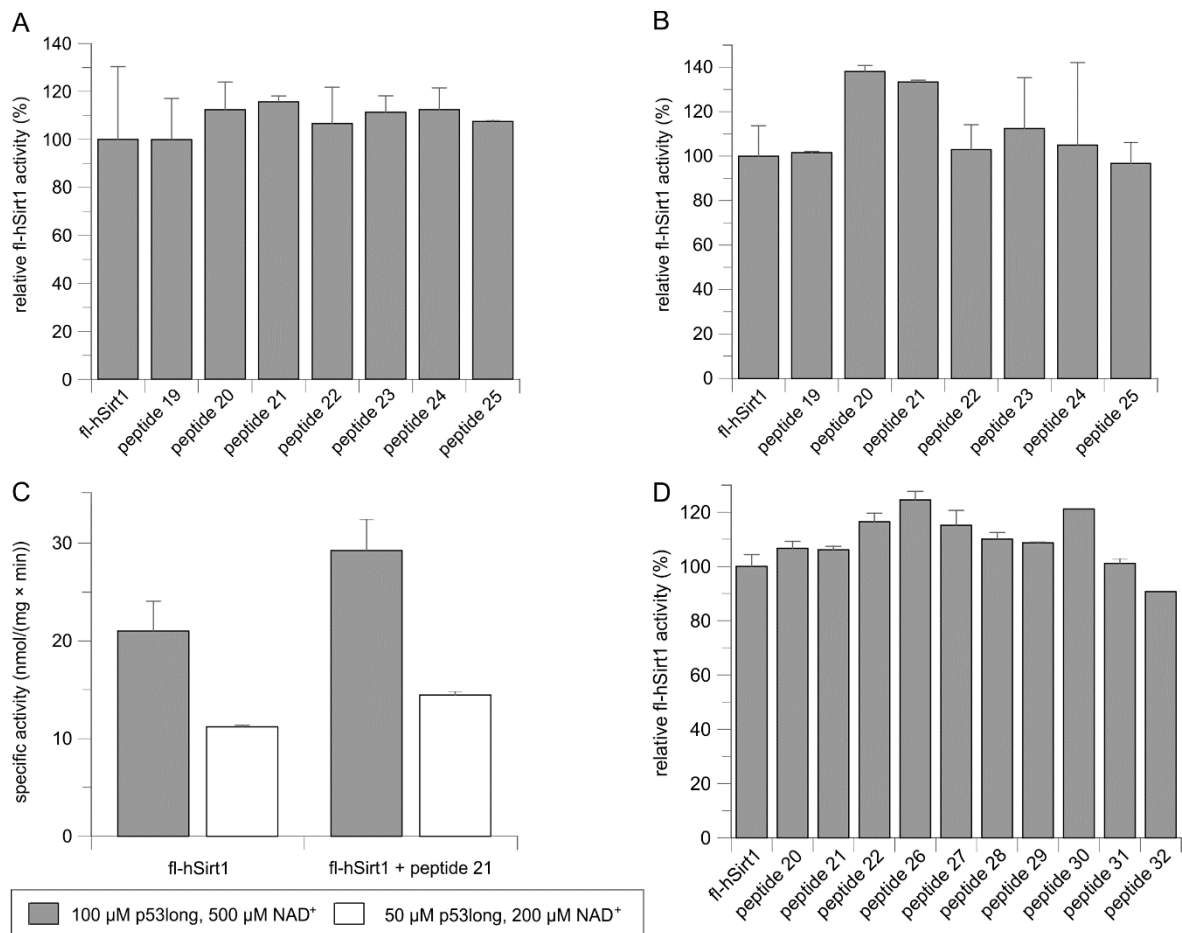


Figure 4.7: Importance of the ESA/CTR region for Sirt1 activity. **A** Continuous coupled enzymatic assay with 2.5 μM His₆-fl-hSirt1, 200 μM p53short, 500 μM NAD⁺, 100 μM ESA/CTR peptide in 5% (v/v) DMSO, and 20 U/ml glutamate dehydrogenase. **B** Mass spectrometric assay with 0.03 μM His₆-fl-hSirt1, 200 μM p53short, 500 μM NAD⁺, and 100 μM ESA/CTR peptide in 5% (v/v) DMSO. **C** Continuous coupled enzymatic assay with 1 μM fl-hSirt1 (pET32*amod*), 100 μM (grey) or 50 μM (white) p53long, 500 μM (grey) or 200 μM (white) NAD⁺, and 100 μM ESA/CTR peptide 21 in 10% (v/v) DMSO. **D** *Fluor de Lys* assay with 1 μM fl-hSirt1 (pET19*bmod-Sumo*), 500 μM NAD⁺, 100 μM *FdL-1* substrate, and 100 μM ESA/CTR peptide in 10% (v/v) DMSO. **A-D** Average and standard deviation calculated from $n = 2$.

4.1.4 Stimulation of hSirt1 activity by small molecules

Dehydroabietic acid (DAA) (Figure 1.9) is a natural phytochemical, which was recently shown to extend *C. elegans* life span through activation of Sirt1¹⁴⁰. In this thesis, the *in vitro* effect of DAA on human Sirt1 was studied: concentrations of 1-10 μM dehydroabietic acid were able to enhance fl-hSirt1 activity in a continuous coupled enzymatic deacetylation assay by about 2-fold (Figure 4.8A). However, precipitation occurred at concentrations above 10 μM DAA leading to pseudo-inhibition (Figure 4.8A). Although DAA did not show any absorbance at the readout wavelength of 340 nm, the variance was high in this assay and an effect of DAA on one of the coupled enzymes was suspected. Hence, the *Fluor de Lys* assay was used subsequently. The next question addressed was, whether the phytochemical could also modulate the activity of hSirt1 deletion variants. Indeed, 0.1-1 μM DAA were sufficient to stimulate mini-Sirt1 deacetylase activity (Figure 4.8B). A negative control excluded an

interaction between DAA and the artificial *FdL-1* substrate. Therefore, only the domains included in mini-Sirt1 are relevant for hSirt1 activation by DAA. Using hSirt1-(214-664) in a *Fluor de Lys* assay also resulted in 1.5-fold stimulation of the sirtuin activity, demonstrating that the SBD might not be necessary for DAA-mediated activation (Figure 4.8B). In this case, even lower concentrations of 0.001-1 μM DAA were sufficient for a 1.2-fold increase of hSirt1-(214-664) activity (Figure 4.8B). Next, the binding affinity of DAA to mini-Sirt1 was examined through microscale thermophoresis resulting in a K_d of 83.0 ± 40.2 nM (Figure 4.8C), consistent with the fact that 100 nM DAA were able to enhance hSirt1 activity.

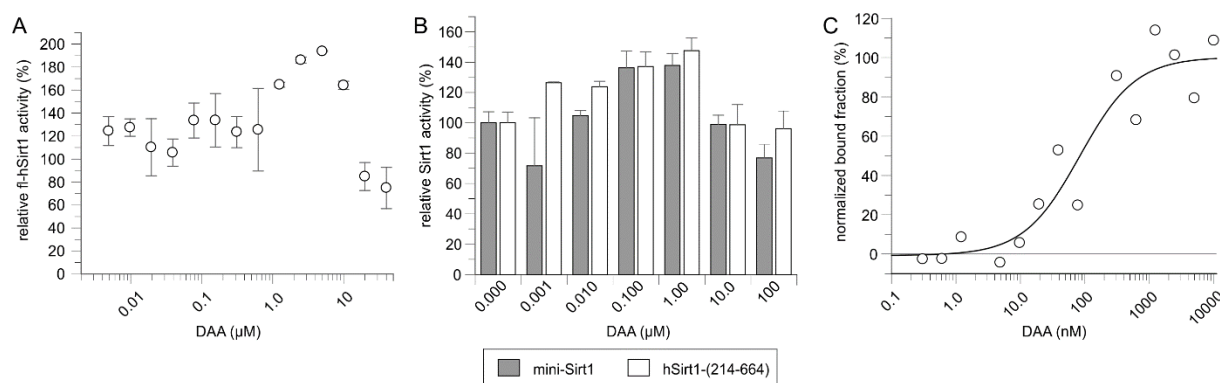


Figure 4.8: Activation of human Sirt1 by dehydroabietic acid (DAA). **A** Continuous coupled enzymatic assay with 1 μM fl-hSirt1 (pET32*amod*), 500 μM NAD^+ , 100 μM p53short, and DAA in 10% (v/v) DMSO ($n = 2$). **B** *Fluor de Lys* assay with 1 μM mini-Sirt1 (grey) or hSirt1-(214-664) (white), 500 μM NAD^+ , 100 μM *FdL-1*, and DAA in 10% (v/v) DMSO ($n = 2$). Assay performed in 20 mM Tris/HCl, pH 8, 150 mM NaCl. **C** MST with 20 nM FITC-labeled mini-Sirt1 and titration of DAA in 5% (v/v) DMSO. The K_d was derived from the initial fluorescence of one measurement with 6% LED power and 10% MST power.

Compared to other known hSirt1 activators like resveratrol or a STAC, DAA-mediated stimulation of hSirt1 activity reveals differences. Under the conditions employed, resveratrol was able to activate fl-hSirt1 in a continuous coupled enzymatic assay, but not mini-Sirt1 (Figure 4.9A). In addition, DAA-mediated stimulation of fl-hSirt1 activity was more potent (Figure 4.8A) than resveratrol-mediated stimulation (Figure 4.9A), which might be due to the substrate-sequence selectivity of resveratrol-mediated activation of hSirt1¹³⁵. In contrast, a synthetic STAC, larger than resveratrol, could weakly activate fl-hSirt1 and mini-Sirt1, but also stimulated hSirt1-(214-664) activity (Figure 4.9B), similar to DAA-mediated activation of hSirt1-(214-664) (Figure 4.8B). Since STAC-binding was mapped to residues 210-230 of the SBD with a crystal structure⁸⁰ and hSirt1-(214-664) could be activated by a STAC and DAA, the question was whether the SBD is actually required for activation of hSirt1 by DAA. Thus, crystallization of mini-Sirt1 in complex with DAA was attempted to solve that question.

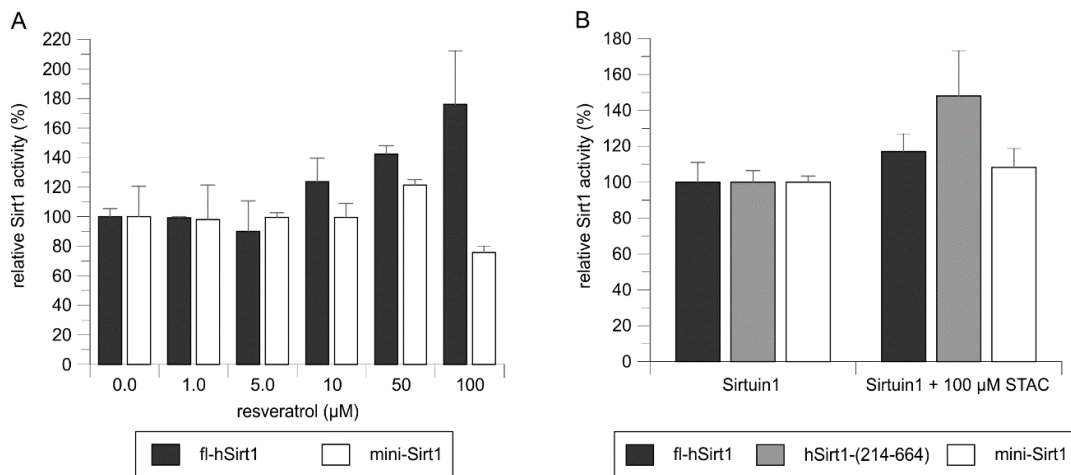


Figure 4.9: Activation of hSirt1 by known activators like resveratrol or a STAC. **A** Continuous coupled enzymatic assay with 1 μM fl-hSirt1 (pET32*amod*; black) or mini-Sirt1 (white), 500 μM NAD⁺, 250 μM SF38Ashort, and different concentrations of resveratrol in 10% (v/v) DMSO ($n = 2$). **B** *Fluor de Lys* assay with 1 μM fl-hSirt1 (pET19B*mod-Sumo*; black), or mini-Sirt1 (white), or hSirt1-(214-664) (grey), 500 μM NAD⁺, 100 μM *FdL-1* substrate, and 100 μM STAC ($n = 2$).

However, screening for initial cocrystallization conditions for a mini-Sirt1/DAA complex at various temperatures and compositions did not yield protein crystals. Since it was not clear, whether the binding sites for STAC and DAA overlapped, mini-Sirt1/STAC crystals were produced for soaking. In this context, the published condition for the mini-Sirt1/STAC complex⁸⁰ (PDB: 4ZZH) using the same STAC activator and setup⁸⁰ was not practicable in our laboratory. Instead, a similar condition (Table 7.4) produced rod-shaped single crystals within 12 h. The best diffraction quality for these mini-Sirt1/STAC complex crystals was at 3.7 Å resolution and structure solution in space group $I2_12_12_1$ validated that the crystals resemble the published complex⁸⁰ (PDB: 4ZZH), although resolution and density coverage for the STAC were worse. In addition, soaking of DAA into such mini-Sirt1/STAC crystals severely damaged the crystals and datasets could not be obtained. On the other hand, soaking of DAA into apo mini-Sirt1 crystals from a previously established crystallization condition (Sandra Weiß, personal communication) did not impair crystal morphology, but led to weaker diffraction. Therefore, cocrystallization of mini-Sirt1 and DAA in that latter crystallization condition was attempted. The best crystal diffracted up to 3.3 Å and the structure was solved in space group $C222_1$. Although resolution was good enough to detect a bound small molecule, DAA was not observed in the crystal structure at neither of the putative activator binding sites for resveratrol or STACs. Further biochemical and structural studies of hSirt1 and dehydroabiatic acid are thus inevitable to derive the mode of activation and the relevant hSirt1 domains necessary for DAA-mediated activation.

4.1.5 Inhibition of hSirt1 by tranilast

Recent studies have suggested an anti-tumor potential for tranilast²⁰⁸ (*N*-[3',4'-dimethoxy-cinnamoyl]-anthranilic acid) (Figure 4.10B). As Sirt1 is involved in many cancers, either through hyperactivation or inhibition, the question arose whether the anti-tumor potential of tranilast is mediated through interaction with Sirt1. In the continuous coupled enzymatic deacetylation assay, low concentrations of tranilast had no effect on fl-hSirt1 activity, but 100 μ M tranilast doubled the relative fl-hSirt1 activity (Figure 4.10A). However, an UV/Vis spectrum of tranilast revealed that its absorbance maximum is at 340 nm (Figure 4.10B), which equals the readout wavelength for the continuous coupled enzymatic assay leading to pseudo-activation. Thus, a mass spectrometric assay was performed indicating that tranilast inhibits fl-hSirt1 with an IC_{50} of about 60 μ M (Figure 4.10C). Despite high variation, an IC_{50} \sim 50 μ M of tranilast against Sirt1 was also supported by other studies (Eric Verdin, personal communication).

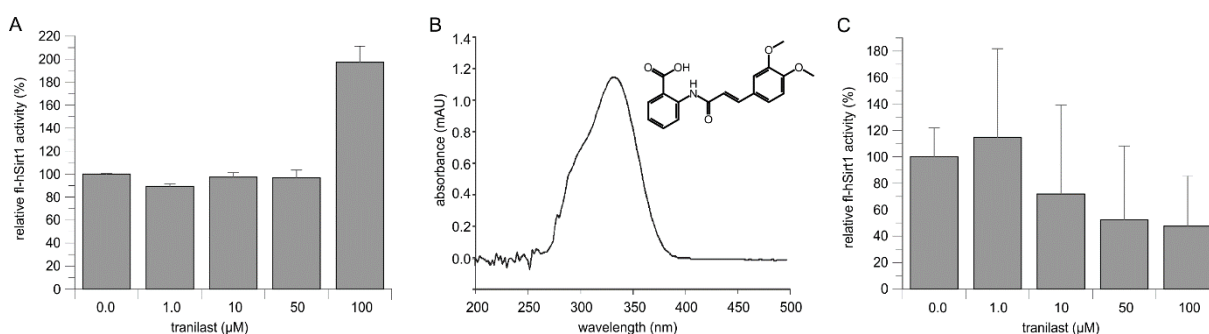


Figure 4.10: Modulation of hSirt1 activity by tranilast. **A** Continuous coupled enzymatic assay with 1 μ M fl-hSirt1 (pET32*amod*), 500 μ M NAD^+ , 100 μ M p53long, and tranilast in 5% (v/v) DMSO ($n = 2$). **B** UV/Vis absorbance spectrum of 1 mM tranilast in water measured with a NanoDrop 2000 UV/Vis spectrophotometer. **C** Mass spectrometric deacetylation assay with 0.03 μ M fl-hSirt1 (pET32*amod*), 500 μ M NAD^+ , 100 μ M p53long, and tranilast in 5% (v/v) DMSO ($n = 2$).

To understand the inhibition mode of tranilast on Sirt1, cocrystallization conditions for a mini-Sirt1/tranilast complex were searched under various conditions and with optional presence of Sirt1-stabilizing ligands, such as NAD^+ , ADPr, or a STAC⁸⁰. Although the SBD is forced in a certain conformation respective to the Sirt1 catalytic core in presence of STAC, tranilast was expected to bind unhindered since inhibitors usually target the active site of an enzyme and previous results showed that binding of a STAC and an inhibitor to mini-Sirt1 are not mutually exclusive⁸⁰. However, needle-shaped crystals (Figure 4.11A) were revealed as tranilast crystals by *in-house* testing. Direct soaking of mini-Sirt1/STAC crystals (Figure 4.11B) with tranilast resulted in heavy precipitation (Figure 4.11C), indicating poor solubility of tranilast despite formation of the previously seen tranilast crystals. In addition, some of the mini-Sirt1/STAC crystals dissolved and the remaining ones lost their diffraction quality. In contrast, soaking of apo mini-Sirt1 crystals with tranilast did neither impact the

crystal shape (Figure 4.11D), nor the diffraction quality. The best mini-Sirt1/tranilast soaked crystal diffracted up to 3.1 Å. Data was solved in space group $C222_1$ and refined to final R and R_{free} values of 23.7% and 32.3% (Table 7.5).

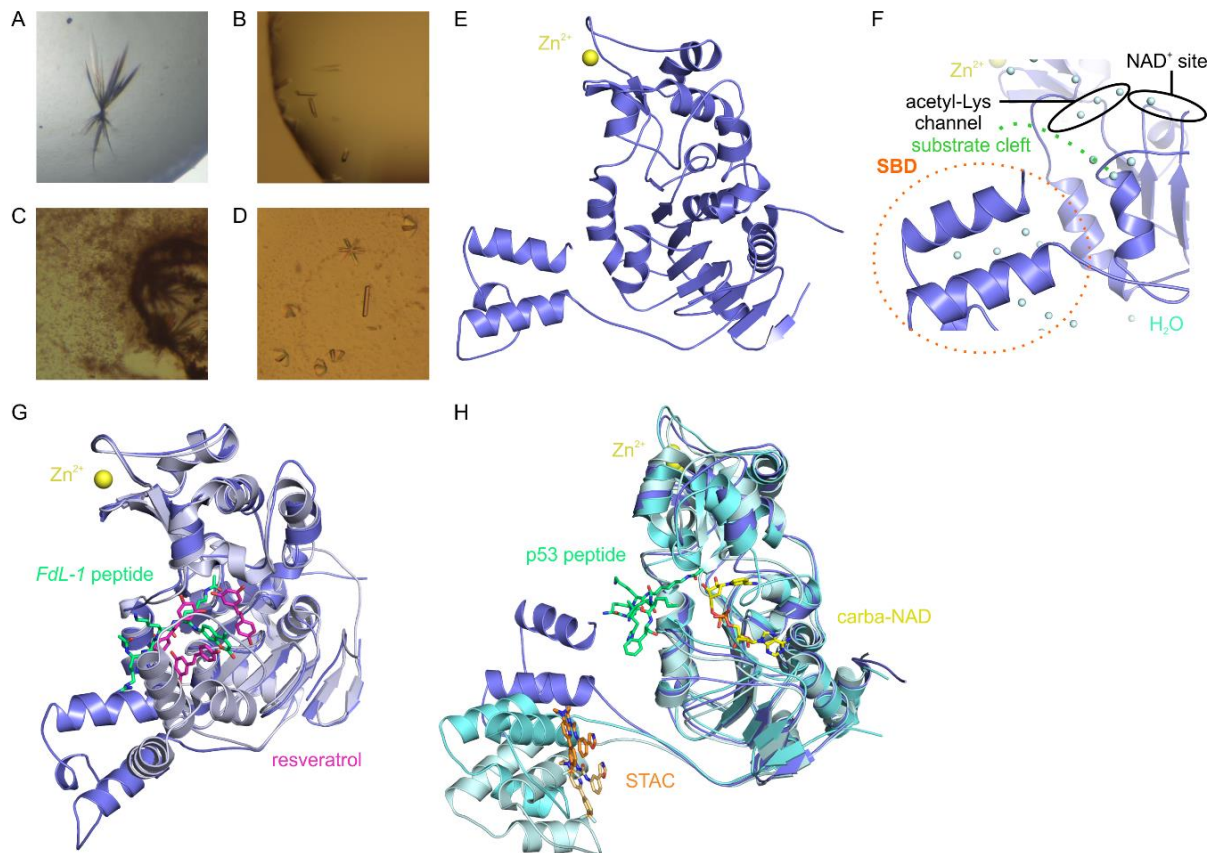


Figure 4.11: Crystallization of a mini-Sirt1 and tranilast complex. **A** Cocrystallization of 10 mg/ml mini-Sirt1 with 10 mM ADPr, 2 mM tranilast, and 1 mM STAC in 9% (v/v) DMSO in the crystallization condition 0.1 M sodium phosphate citrate, pH 4.2, 2 M ammonium sulfate at 20 °C. **B** Cocrystallization of 10 mg/ml mini-Sirt1 with 1.22 mM STAC in the crystallization condition 0.1 M Tris/HCl, pH 8.5, 10% (w/v) PEG 8000, 0.2 M MgCl₂ at 20 °C before soaking and **C** after soaking with tranilast. **D** Apo mini-Sirt1 crystals after soaking with tranilast in a final concentration of 1 mM tranilast in 10% (v/v) DMSO. **E** Structure of apo mini-Sirt1 after soaking with tranilast. **F** Catalytic center of the mini-Sirt1/tranilast soaked crystal. The substrate binding cleft and NAD⁺-binding pockets A-C are occupied with water molecules (cyan). **G** Superposition of apo mini-Sirt1 (blue) with a mini-Sirt1/p53-AMC/resveratrol complex (PDB: 5BTR; light blue). The artificial p53-AMC substrate (lime) and resveratrol (pink) are shown as sticks. **H** Superposition of apo mini-Sirt1 (blue) with a mini-Sirt1/STAC complex (PDB: 4ZZH; pale teal) and a mini-Sirt1/STAC/p53/carba-NAD complex (PDB: 4ZZJ; aquamarine). The STAC (pale orange/orange), p53 peptide (lime), and carba-NAD (yellow) are shown as sticks.

The resulting structure of mini-Sirt1 after soaking with tranilast resembles a typical hSirt1 structure^{79–81} with the SBD at some distance from the catalytic core and the ESA/CTR region folded back to the lower part of the Rossmann fold domain (Figure 4.11E). The soaked inhibitor tranilast was not bound to the SBD as expected, which is supported by the absence of signal in electron density maps in this region. However, putative small-molecule inhibitor binding sites at the hSirt1 substrate binding cleft, the acetyl-Lys binding channel, or the NAD⁺ binding site were also only occupied with water molecules (Figure 4.11F), rendering the obtained structure to apo mini-Sirt1. Interestingly, comparison of apo mini-Sirt1 to ligand-

bound mini-Sirt1 structures reveals differences in the location of the SBD. Superposition to a mini-Sirt1/*FdL-1*/resveratrol complex (PDB: 5BTR), resulting in an RMSD = 0.884 Å for 263 C_α atoms, shows that the SBD in apo mini-Sirt1 is turned further away from the catalytic core (Figure 4.11G). In contrast, binding of the *FdL-1* substrate in the mini-Sirt1/*FdL-1*/resveratrol complex allows the SBD to associate with the catalytic core locking the substrate in the binding cleft (Figure 4.11G). Superposition of apo mini-Sirt1 with a mini-Sirt1/STAC complex (PDB: 4ZZH) results in an RMSD = 1.307 Å for 266 C_α atoms and shows that the SBD locations in both structures also do not overlap (Figure 4.11H). Binding of the STAC together with substrate and carba-NAD (PDB: 4ZZJ; RMSD = 1.417 Å for 269 C_α atoms) moves the SBD towards the catalytic core, but not as close as binding of resveratrol with substrate does (Figure 4.11G, H). Therefore, apo mini-Sirt1 exhibits an even further outward-turned position of the SBD, which causes a small rigid-body movement of the SBD upon binding of any hSirt1 ligand consistent with the suggested model from previous studies of mini-Sirt1/activator complexes⁸⁰. Concerning the binding site of tranilast and a possible competitiveness to substrate or NAD⁺, further crystallographic studies are necessary.

4.2 Modulation of hSirt1 activity by hAROS

4.2.1 Recombinant expression and purification of His₆-hAROS

His₆-hAROS was previously purified in our laboratory by refolding after recombinant overexpression in *E. coli*²⁵⁸. The resulting yield and purity were low and due to the lack of native hAROS for comparison, the correct refolding could not be confirmed²⁵⁸. Before optimizing the refolding procedure, conditions for the overexpression and purification of folded hAROS directly from *E. coli* were investigated (Figure 4.12A, B). However, His₆-hAROS was insoluble in all tested cell lines (Figure 4.12C, D) and thus the original purification protocol²⁵⁸ was employed. Solubilization and unfolding was thereby performed with guanidinium hydrochloride. Subsequently, His₆-hAROS was purified by affinity chromatography and subjected to *on-column* refolding through a series of buffers with decreasing urea concentration (Figure 4.13A). This process did not separate co-expressed *E. coli* proteins of lower molecular weight (Figure 4.13A), but removal of 10 mM imidazole from the original refolding buffers²⁵⁸ increased the yield of soluble recombinant protein. After dialysis, His₆-hAROS eluted from a Superose 12 10/300 GL SEC column at 14.7 ml (Figure 4.13B). Lower molecular weight impurities could not be separated by SEC resulting in His₆-hAROS with a purity of ~75% (Figure 4.13C). A further purification step such as IEX was omitted due to a low yield of 0.1-0.2 mg per 1 l of expression culture. Likewise, the His₆-

Results

tag was not cleaved because hAROS was only used in interaction studies and crystallization, requiring higher purity, was not attempted.

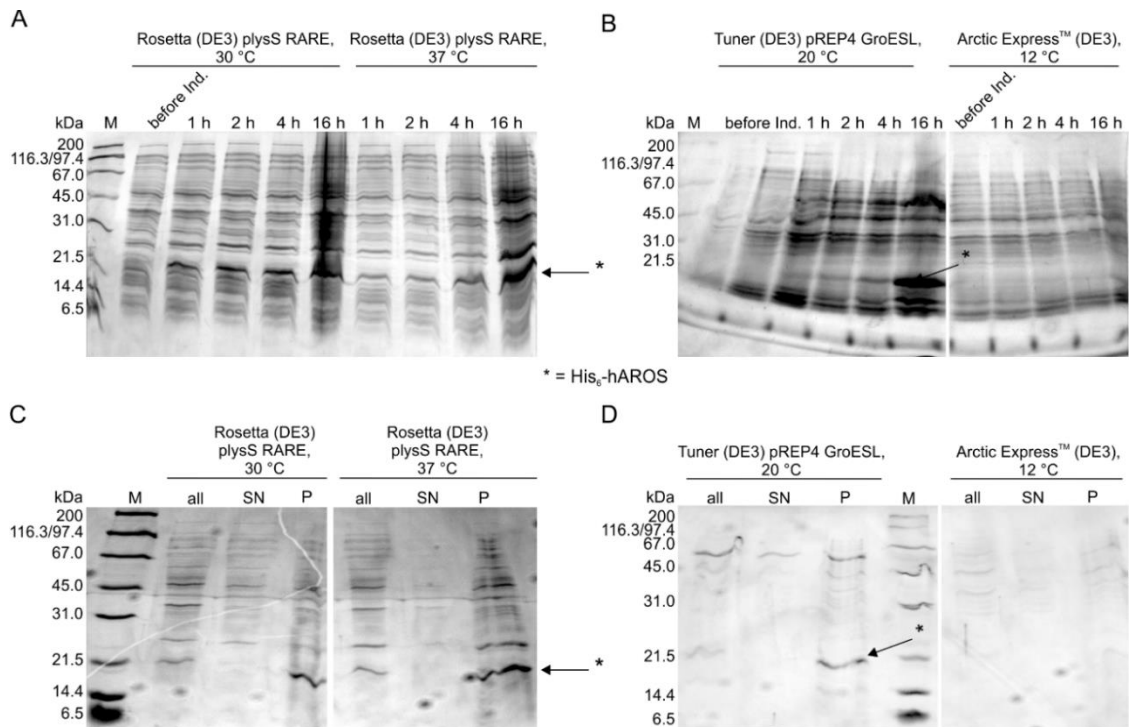


Figure 4.12: Test expressions of His₆-hAROS in LB medium. **A, B** Expression of His₆-hAROS before and after induction in *E. coli* Rosetta (DE3) plysS RARE at 30 °C or 37 °C, *E. coli* Tuner (DE3) pREP4 GroESL at 20 °C, and *E. coli* Arctic Express™ (DE3) at 12 °C. **C, D** Cell lysis of the test expressions from **A** and **B** 16 h after induction. Abbreviations: Ind. - induction, all - whole protein after lysis, P - pellet, SN - supernatant.

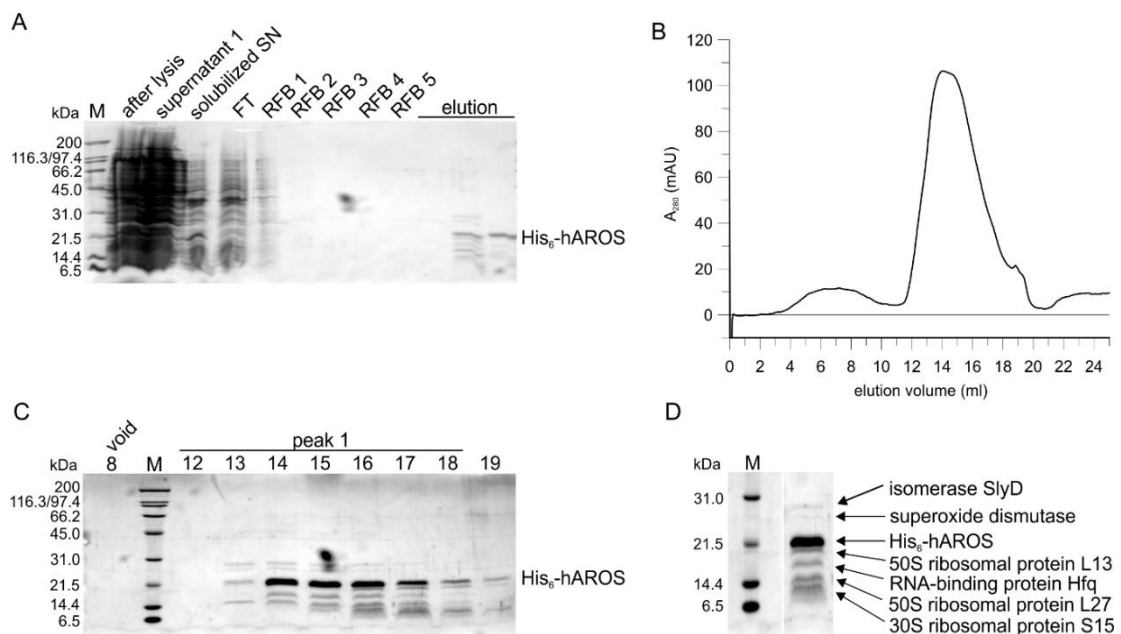


Figure 4.13: Purification of His₆-hAROS by refolding. **A** Affinity chromatography on Ni²⁺-immobilized beads with refolding of His₆-hAROS. Abbreviations: SN -supernatant, RFB - refolding buffer. **B** SEC of His₆-hAROS on Superose S12 10/300 GL with **C** SDS-PAGE. Numbers refer to the respective elution volume from SEC. **D** MS analysis of protein bands from concentrated His₆-hAROS (17.5 kDa). Contamination with FKBP-type peptidyl-prolyl cis-trans isomerase SlyD (Uniprot: P0A9K9; 20.9 kDa), superoxide dismutase [Mn] (Uniprot: P00448; 23.1 kDa), 50S ribosomal protein L13 (Uniprot: P0AA10; 16.0 kDa), RNA-binding protein Hfq (Uniprot: P0A6X3; 11.2 kDa), 50S ribosomal protein L27 (Uniprot: P0A7L8; 9.1 kDa), and 30S ribosomal protein S15 (Uniprot: P0ADZ4; 10.3 kDa).

Mass spectrometric analysis of co-purified *E. coli* proteins from SDS PAGE bands revealed that particularly RNA-associated proteins such as *E. coli* 50S ribosomal protein L13, RNA-binding protein Hfq, 50S ribosomal protein L27, and 30S ribosomal protein S15 could not be separated from the target protein (Figure 4.13D). In other purifications of His₆-hAROS not depicted here, *E. coli* proteins like 30S ribosomal protein S2, GTP cyclohydrolase 1, 50S ribosomal protein L28, or major outer membrane prolipoprotein Lpp were also observed. The thermal stability of the purified His₆-hAROS was examined with a TSA. Although SEC was performed in HEPES, pH 7.5, the refolded protein did not show any melting curve for HEPES, pH < 8 ($T_m = 50.7 \pm 0.7$ °C in HEPES, pH 8.0) (Figure 4.14). Several other buffers in the range of pH 7.7-8.5 showed robust thermal stability for His₆-hAROS with $T_m \sim 50$ °C and the highest $T_m = 56.2 \pm 2.8$ °C was obtained in 50 mM Tris/HCl, pH 7.5 (Figure 4.14).

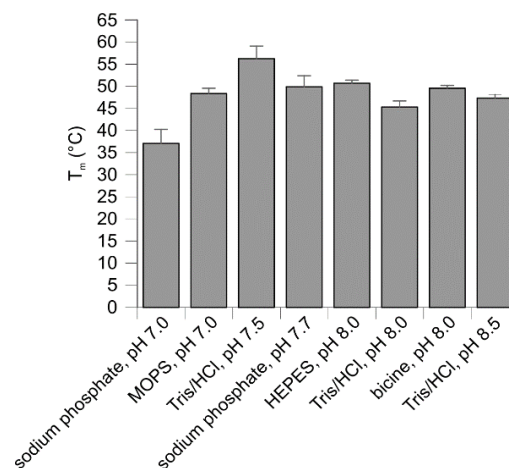


Figure 4.14: Thermal denaturation of refolded His₆-hAROS. TSA of 5 μ M His₆-hAROS in different 50 mM buffers as well as in 20 mM sodium phosphate, pH 7.7. Error bars represent the error of the fit ($n = 1$).

4.2.2 Regulation of hSirt1 activity by recombinant refolded hAROS

The interaction of hSirt1 with refolded hAROS was examined with a pulldown, where His₆-hAROS was immobilized to Ni²⁺-beads and fl-hSirt1 or buffer was added. However, SDS PAGE revealed that both proteins are still bound to the beads after elution - either in a protein-protein complex or isolated (Figure 4.15A). Therefore, *Blue Native* PAGE with a fixed concentration of fl-hSirt1 and increasing concentrations of His₆-hAROS was performed (Figure 4.15B) to detect whether both proteins interact *in vitro*. Similarly, an interaction between hAROS and fl-hSirt1 was not detected, although the faint band for fl-hSirt1 (multimeric with a molecular weight > 240 kDa) vanished with increasing concentration of His₆-hAROS (Figure 4.15B). But fl-hSirt1 was also contaminated with several *E. coli* proteins related to insufficient purification (Figure 4.15B, bands 1-6). His₆-hAROS was detected in SDS-PAGE band 7 together with *E. coli* 50S ribosomal protein L13, but also in bands 4-6 together with fl-hSirt1 and *E. coli* proteins (Figure 4.15B). Therefore, His₆-hAROS might

Results

have interacted either directly with fl-hSirt1 or with one of the *E. coli* proteins. As fl-hSirt1 could only be obtained with 70% purity, *Blue Native* PAGE was conducted with mini-Sirt1 and different concentrations of His₆-hAROS (Figure 4.15C). MS analysis of SDS-PAGE bands indicated that mini-Sirt1 (Figure 4.15C, bands 1-4) and His₆-hAROS run accordingly to their monomeric size (Figure 4.15C, bands 6-8). The previously discovered band for His₆-hAROS at higher molecular weight (Figure 4.15B, bands 4-6) was identified here as *E. coli* 50S ribosomal protein L13 and *E. coli* 30S ribosomal protein S15 (Figure 4.15C, band 5). Increasing concentrations of His₆-hAROS led to the appearance of a faint band above mini-Sirt1, which was identified as mini-Sirt1 together with those two ribosomal proteins (Figure 4.15C, bands 9-10). *Blue Native* PAGE thus failed to detect a complex between hSirt1 and hAROS.

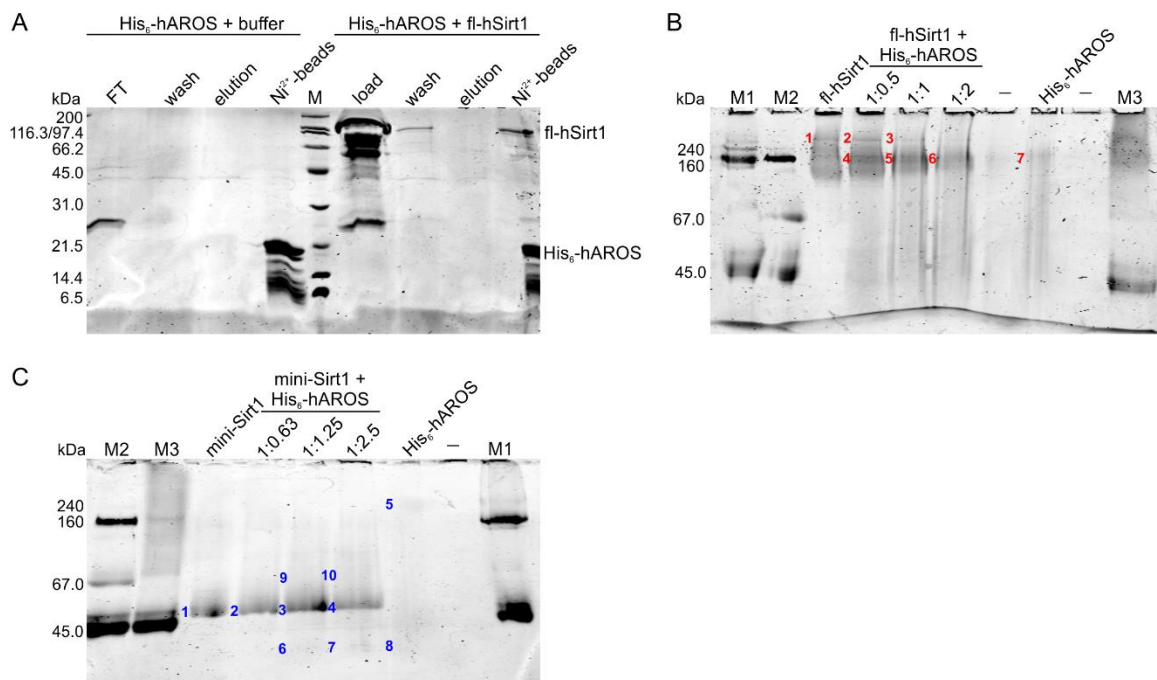


Figure 4.15: Interaction between hSirt1 and refolded His₆-hAROS. **A** Pull-down with immobilized His₆-hAROS and fl-hSirt1 (pET32amod). **B** *Blue Native* PAGE with 25 µg fl-hSirt1 (pET32amod) and different concentrations of His₆-hAROS (12.5/25/50 µg). Fl-hSirt1 appears in two “complexes”: the first complex includes *E. coli* 60 kDa chaperonin groL (bands 1-3), the second one consists of fl-hSirt1 and *E. coli* catalase HPII, *E. coli* NADP-specific glutamate dehydrogenase, and *E. coli* glutamine-fructose-6-phosphate aminotransferase (bands 4-6). His₆-hAROS was detected in band 7 together with *E. coli* 50S ribosomal protein L13 and in fl-hSirt1 “complex 2” (bands 4-6). **C** *Blue Native* PAGE with 10 µg mini-Sirt1 and different concentrations of His₆-hAROS (6.25/12.5/25 µg). Mini-Sirt1 runs as monomeric band (bands 1-4) as well as His₆-hAROS (bands 6-8). Band 5 was identified as *E. coli* 50S ribosomal protein L13 and *E. coli* 30S ribosomal protein S15, whereas bands 9-10 showed mini-Sirt1 together with the latter two proteins. Marker for *Blue Native* PAGE: M1 - 160/45 kDa, M2 - 240/67/45 kDa, M3 - 45 kDa.

In addition to the attempt of visualizing an interaction between isolated hSirt1 and hAROS, the direct effect of hAROS on hSirt1 activity was investigated. In a continuous coupled enzymatic assay, His₆-hAROS inhibited GST-fl-hSirt1 with an IC₅₀ between 10-20 µM (Figure 4.16A). A control with His₆-hAROS, which had been denatured at 95 °C for 5 min

prior to the assay, did not repress GST-fl-hSirt1 activity (Figure 4.16A), confirming that the activity-modulating effect is mediated by hAROS. To elucidate the hSirt1 domains necessary for inhibition by hAROS, a *Fluor de Lys* assay was performed revealing that mini-Sirt1 is not affected by His₆-hAROS (Figure 4.16B). Although inhibition of fl-hSirt1 by His₆-hAROS was not additionally examined with the *Fluor de Lys* assay, these results suggest that other parts of hSirt1's N- or C-terminal extensions may be required for interaction and inhibition by hAROS.

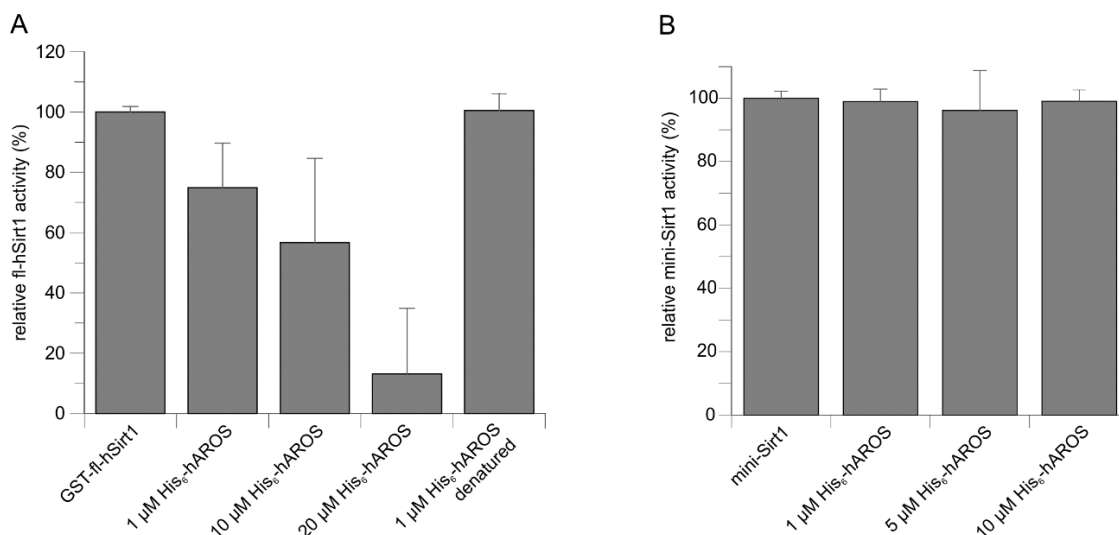


Figure 4.16: Modulation of hSirt1 activity by hAROS. **A** Continuous coupled enzymatic assay with 1 μ M GST-fl-hSirt1, 500 μ M NAD⁺, 100 μ M p53long, and His₆-hAROS including a control with 1 μ M denatured His₆-hAROS ($n = 4$). **B** *Fluor de Lys* assay with 1 μ M mini-Sirt1, 500 μ M NAD⁺, 100 μ M *FdL-1* substrate, and His₆-hAROS ($n = 2$). The reaction was stopped after 30 min.

For mapping of a stable core of hAROS, limited proteolysis with GluC protease was performed showing that digested His₆-hAROS forms an apparent stable fragment of 8-12 kDa (Figure 4.17A). The co-purified *E. coli* RNA-binding proteins (Figure 4.17A, bands 2-6) were degraded by GluC protease. The overnight digested sample was then subjected to thermal denaturation. Remarkably, the digested hAROS core fragment exhibited a $T_m = 35.1 \pm 3.8$ °C, which is 10 °C lower compared to the intact protein (Figure 4.17B). Mass spectrometric analysis confirmed that the prominent digested SDS-PAGE band (Figure 4.17A, band 7) is His₆-hAROS. MS analysis with the more specific ByonicTM software allowed determination of the peptide coverage: peptides from non-digested His₆-hAROS (Figure 4.17A, band 1) covered hAROS residues 8-29, 70-99, and 114-136 (Figure 4.17C). The His₆-hAROS core fragment (Figure 4.17A, band 7) showed well-represented peptides for hAROS residues 8-29, 41-52, 58-65, 82-96, and 114-128 (Figure 4.17D). His₆-hAROS thus seems to be digested by GluC from either its N- or its C-terminus forming various stable core fragments, which accumulate on the SDS PAGE at the same molecular weight. The strong representation of

Results

peptides from hAROS residues 8-29, 82-96, and 114-128 in the core fragment (Figure 4.17D) raises also the possibility of a cleavage of hAROS between residues 65-73 generating two hAROS fragments of about the same molecular weight of 7 kDa. In summary, His₆-hAROS seems to contain one or more stable core fragments with defined secondary structure that might be used for interaction studies with hSirt1.

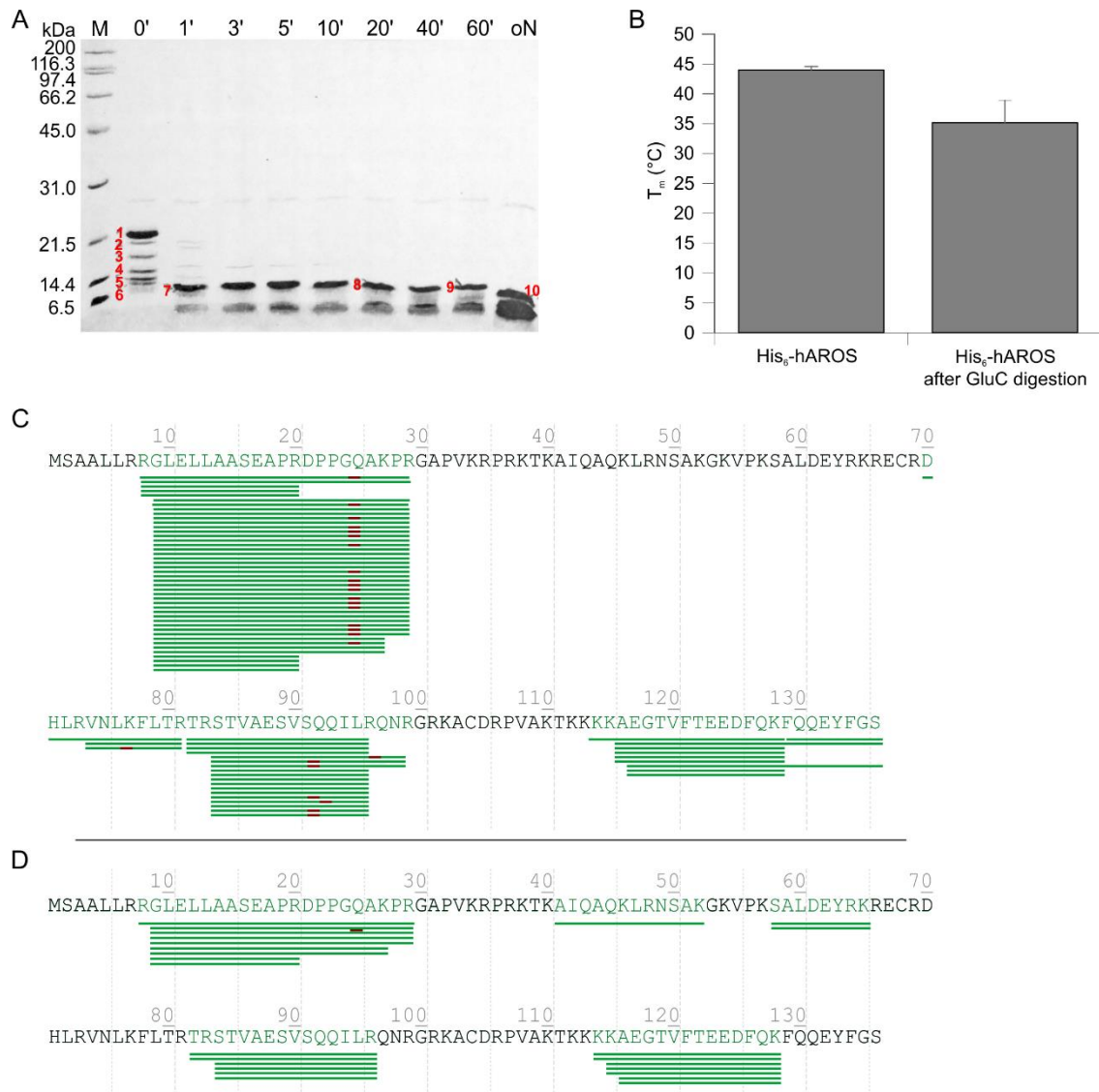


Figure 4.17: Limited proteolysis of His₆-hAROS. **A** Limited proteolysis with His₆-hAROS and GluC protease. His₆-hAROS (band **1**) is digested to a stable core fragment (band **7-10**). Copurified *E. coli* RNA-associated proteins *E. coli* 50S ribosomal protein L13 (band **2**), major outer membrane prolipoprotein Lpp (band **3**), RNA-binding protein Hfq (band **4**), 30S ribosomal protein S15 (band **5**), and 50S ribosomal protein L28 (band **6**) are degraded by GluC. **B** Thermal denaturation shift assay in 50 mM Tris/HCl, pH 7.5 with the overnight GluC-digested His₆-hAROS and intact His₆-hAROS. The core fragment exhibits a $T_m = 35.1 \pm 3.8$ °C, while intact His₆-hAROS has a $T_m = 44.0 \pm 0.6$ °C. Error bars represent the error of the fit. **C** Analysis of the MS peptide coverage of intact His₆-hAROS (band **1**) and **D** of the hAROS core fragment (band **7**) by Byonic™ (Protein Metrics Inc.). Significant peptides are shown as green lines with PTM-modified residues in red.

4.3 Elucidation of the mechanism of Sirt1 activity modulation by Hic1-BTB

4.3.1 Recombinant expression, purification, and characterization of human Hic1-BTB

As the focus of this work was on the interaction between hSirt1 and the BTB/POZ domain of human Hic1, a Hic1-BTB construct was cloned into a pET15b vector. Since the exact sequence boundaries of the Hic1 BTB domain were not known, a Phyre² search^{256,260} with fl-Hic1 was performed, followed by sequence alignment of the five best hits for the N-terminal domain to select the construct boundaries (Figure 7.7). Although the original vector contained isoform 2 of human Hic1 (Uniprot: Q14526), which lacks 19 residues on its N-terminus, all residue numbers refer to its canonical isoform 1 and the final Hic1-BTB construct comprised amino acids 20-154 of human Hic1. Hic1-BTB was purified by affinity chromatography, dialysis with His₆-tag cleavage, reverse AC, dialysis, and SEC (Figure 4.18).

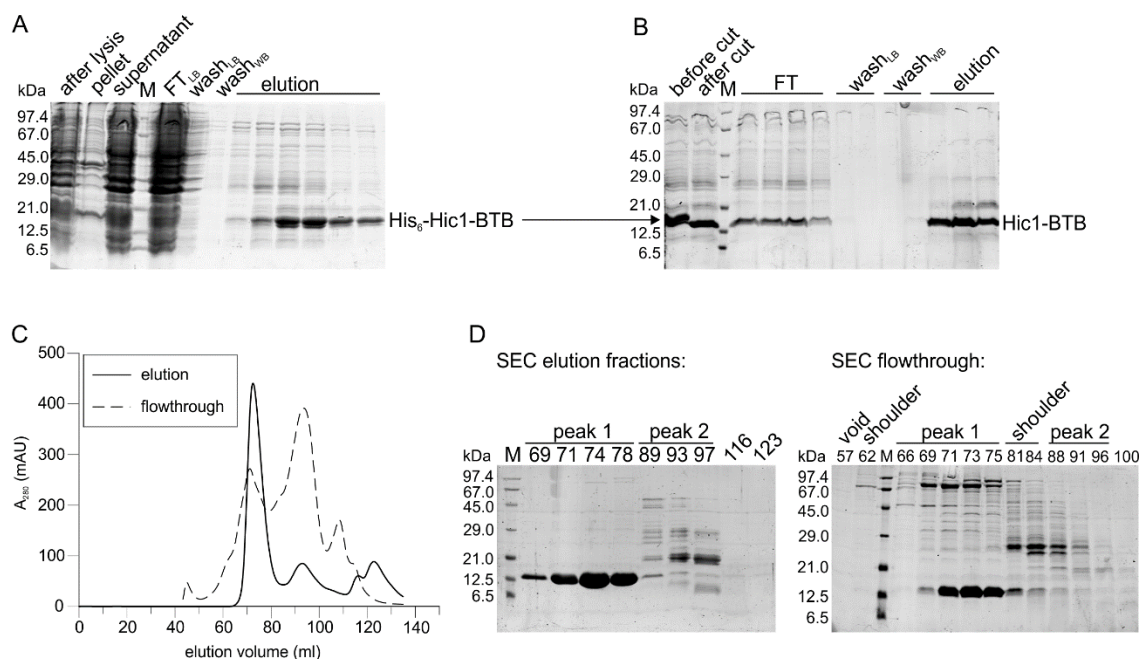


Figure 4.18: Purification of Hic1-BTB from pET15b. **A** Affinity chromatography and **B** Reverse AC on Ni²⁺-immobilized beads. **C** SEC on S200 16/60 GL. Hic1-BTB elutes at 72 ml as apparent octamer. **D** SDS PAGE of the SECs from **C**. Numbers refer to the respective elution volume from SEC. Abbreviations: FT - flowthrough, LB - lysis buffer, WB - wash buffer.

Remarkably, Hic1-BTB eluted as double band from AC (Figure 4.18A), which is reduced to a single band after cleavage of the His₆-tag by thrombin (Figure 4.18B). Both bands were verified as the target Hic1-BTB construct by MS analysis (Figure 4.19A). However, one band seems to include the N-terminal His₆-tag, whereas the other one lacks it (Figure 4.19A). Furthermore, a part of Hic1-BTB eluted with the flowthrough from reverse AC, but a larger amount bound unspecifically to the beads and eluted with a higher imidazole concentration as purer protein (Figure 4.18B). Therefore, the two fractions of Hic1-BTB were separately treated. During gel filtration, Hic1-BTB eluted at 72 ml from S200 16/60 GL as an apparent

Results

octamer (Figure 4.18C). SDS PAGE confirms that the fraction of Hic1-BTB, which bound unspecifically to the Ni²⁺-immobilized beads during reverse AC, is purer (Figure 4.18D). As the A₂₆₀ absorbance correlated with elution of the less pure Hic1-BTB fraction during SEC, this fraction was contaminated with DNA and discarded. Pure Hic1-BTB could be obtained from pET15b with 95% purity and a yield of 4 mg per 1 l of expression culture.

The purified Hic1-BTB has a molecular weight of 14780.2 Da in solution (Figure 4.19B), confirming the theoretical molecular weight obtained from ExPASy ProtParam²¹⁰ (Table 7.3). In a CD spectrum, Hic1-BTB exhibits a defined secondary structure with mostly α -helical content indicated by local minima at 208 nm and 222 nm (Figure 4.19C). The stability of Hic1-BTB was investigated with thermal denaturation resulting in a melting temperature of 49-52 °C in different buffer systems between pH 4-8 (Figure 4.19D), suggesting that Hic1-BTB can tolerate various conditions as needed for subsequent interaction studies with hSirt1.

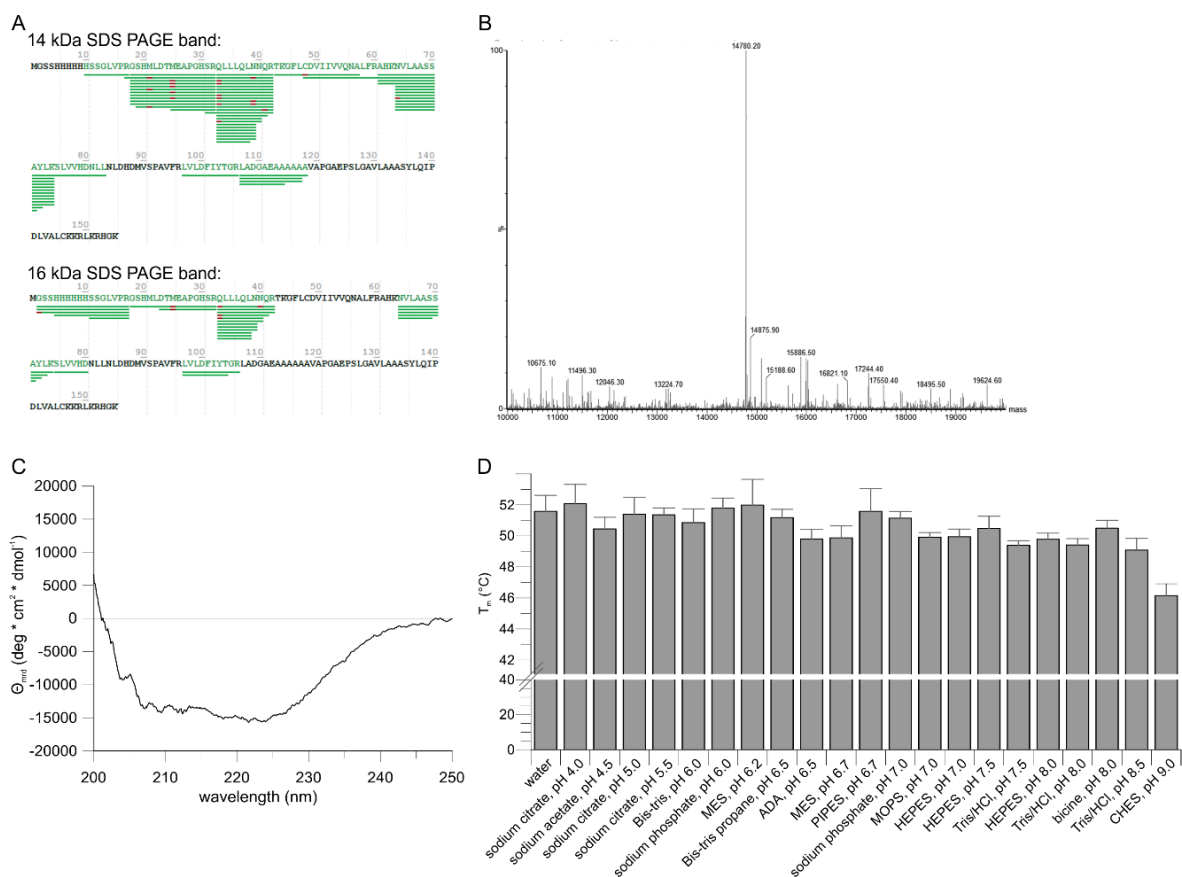


Figure 4.19: Bioanalytical characterization of Hic1-BTB from pET15b. **A** Mass spectrometric analysis after tryptic digest of the 14 kDa and 16 kDa bands from SDS PAGE after affinity chromatography. **B** Mass spectrometric analysis of the intact mass of 5 μg Hic1-BTB in 0.1% (v/v) FA after purification. Hic1-BTB has a molecular weight of 14780.2 Da. **C** CD spectrum of 0.2 mg/ml Hic1-BTB. **D** Thermal denaturation shift assay of 5 μM Hic1-BTB in different 50 mM buffers with 250 mM NaCl. Error bars refer to the error of the fit ($n = 1$).

Hic1-BTB was also subcloned into a pET15b*mod* vector with N-terminal His₆-tag followed by a TEV cleavage site, which allowed the use of recombinantly purified TEV protease from our laboratory. Despite the same vector backbone except for the proteolytic cleavage site, purification of Hic1-BTB from pET15b*mod* was carried out with a different protocol. In brief, after affinity chromatography on Ni²⁺-immobilized beads, in which Hic1-BTB eluted as double band (Figure 4.20A), reverse AC was performed on an ÄKTApriime plus system with HisTrap HP column to separate the protease from cleaved Hic1-BTB (Figure 4.20B), which otherwise binds unspecifically to the beads. The elution of Hic1-BTB could thus be finetuned to a single peak at 40% buffer B, with the second half of the peak being purer than the first half (Figure 4.20B), demanding separate treatment of both fractions. Depending on varying purity of the eluted Hic1-BTB, a cation exchange chromatography was then performed. Afterwards, Hic1-BTB eluted from SEC on a S200 10/300 GL column not only as apparent octamer at 13.2 ml, but also as dimer at 15.2 ml (Figure 4.20C). SDS PAGE shows that both Hic1-BTB peaks differ in their purity (Figure 4.20D) which was also inconsistent across different purifications (purity of the dimer between 60-90%). Pure Hic1-BTB dimer from pET15b*mod* yielded about 0.2-0.4 mg per 1 l of expression culture.

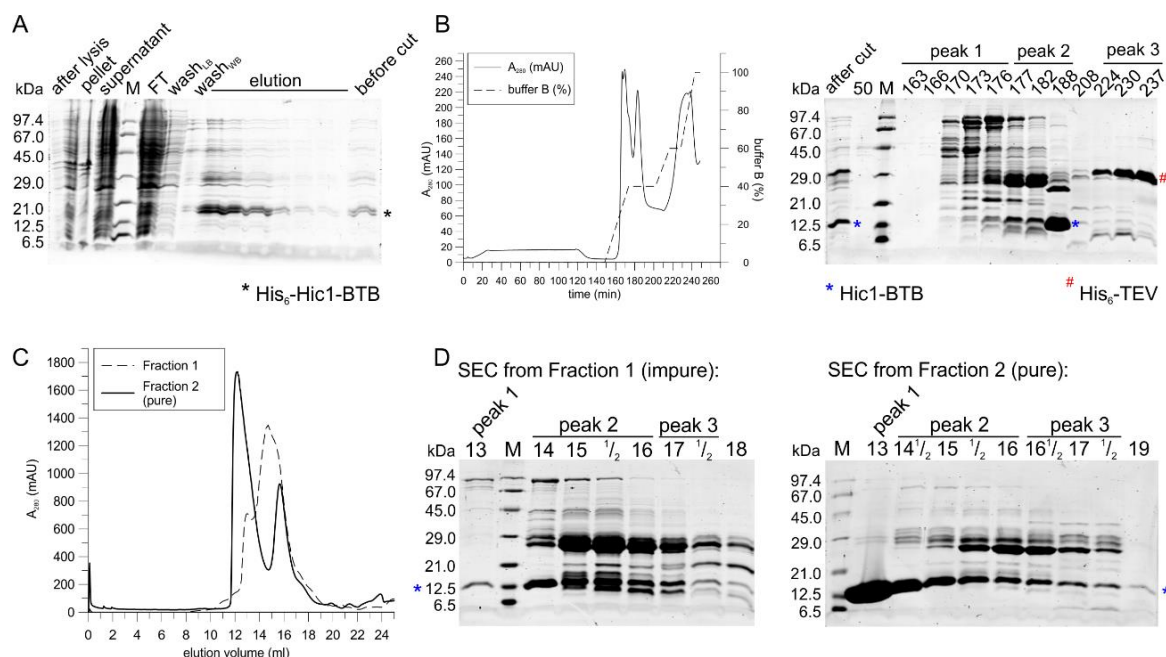


Figure 4.20: Purification of Hic1-BTB from pET15b*mod*. **A** Affinity chromatography on Ni²⁺-immobilized beads. **B** Reverse AC on ÄKTApriime plus with a 5 ml HisTrap HP column. Numbers on SDS PAGE refer to the elution time from reverse AC. **C** SEC on S200 10/300 GL. An apparent Hic1-BTB octamer elutes at 13.2 ml, while a dimer elutes at 15.2 ml. **D** SDS PAGE analysis of the SECs from **C**. Numbers refer to the elution volume from SEC. Abbreviations: FT - flowthrough, LB - lysis buffer, WB - wash buffer.

As BTB domain containing proteins are prone to oligomerization^{182,261}, a dimer of Hic1-BTB was interesting for interaction studies with Sirt1. The yield of Hic1-BTB dimer from pET15b*mod* was optimized by adaption of the purification buffers as a result of analytical gel

filtrations (Figure 7.8). In particular, the use of 0.05% (v/v) Tween[®] 20 and 5% (v/v) glycerol were beneficial for dimer formation (Figure 7.8). However, octameric Hic1-BTB from pET15b*mod* was more abundant than the dimer. Both Hic1-BTB dimer and octamer were used for interaction studies with Sirt1. In the following, the Hic1-BTB octamer used was always purified from pET15b, while Hic1-BTB dimer was obtained from pET15b*mod*.

4.3.2 Biochemical characterization of the interaction between Sirt1 and Hic1-BTB

To study the interaction between isolated fl-hSirt1 and human Hic1-BTB, *Blue Native* PAGE was performed using different concentrations of Hic1-BTB octamer: the band for fl-hSirt1 (Figure 4.21A, band 1) seemed to disappear with increasing concentration of Hic1-BTB, while another band became stronger. MS analysis also showed that Hic1-BTB seems to occur at two molecular weights (Figure 4.21A, bands 3-7), while only one band contained fl-hSirt1 (Figure 4.21A, band 2). Since the bands for fl-hSirt1 and Hic1-BTB seemed to accumulate at the same molecular weight without complex formation, *Blue Native* PAGE was repeated with mini-Sirt1 (Figure 4.21B). Mini-Sirt1 was clearly identified in bands 1 and 6 by mass spectrometric analysis, but the supposed bands 7 and 8 for Hic1-BTB could not be confirmed (Figure 4.21B). The putative interaction bands 2, 4, and 5 were identified as Hic1-BTB as well and only band 3 might contain both proteins (Figure 4.21B). However, aggregation was observed in the loading pockets of the gel, with the amount of precipitated protein being directly proportional to the concentration of Hic1-BTB. As optimization of the *Native* PAGE conditions did not solve this issue, the method was unable to detect complex formation.

Instead, crosslinking of equimolar amounts of mini-Sirt1 and Hic1-BTB dimer in presence of DSS was attempted (Figure 4.21C). In this case, the two proteins formed self-crosslinks, but no inter-protein crosslinks (Figure 4.21C). In particular, mini-Sirt1 shows two higher-molecular weight multimers and Hic1-BTB displays a dimer and tetramer (Figure 4.21C). Crosslinking with mini-Sirt1 was repeated with the purer Hic1-BTB octamer in presence of DSS, revealing only self-crosslinks for a Hic1-BTB dimer, trimer, and tetramer (Figure 4.21D). Since this procedure did not create inter-protein crosslinks, the crosslinker and the protein concentrations were varied and Hic1-BTB dimer was used in 3-fold excess to mini-Sirt1 in presence of glutaraldehyde (Figure 4.21E) or DMS (Figure 4.21F). However, under the conditions employed, inter-protein crosslinks were also not formed (Figure 4.21E, F).

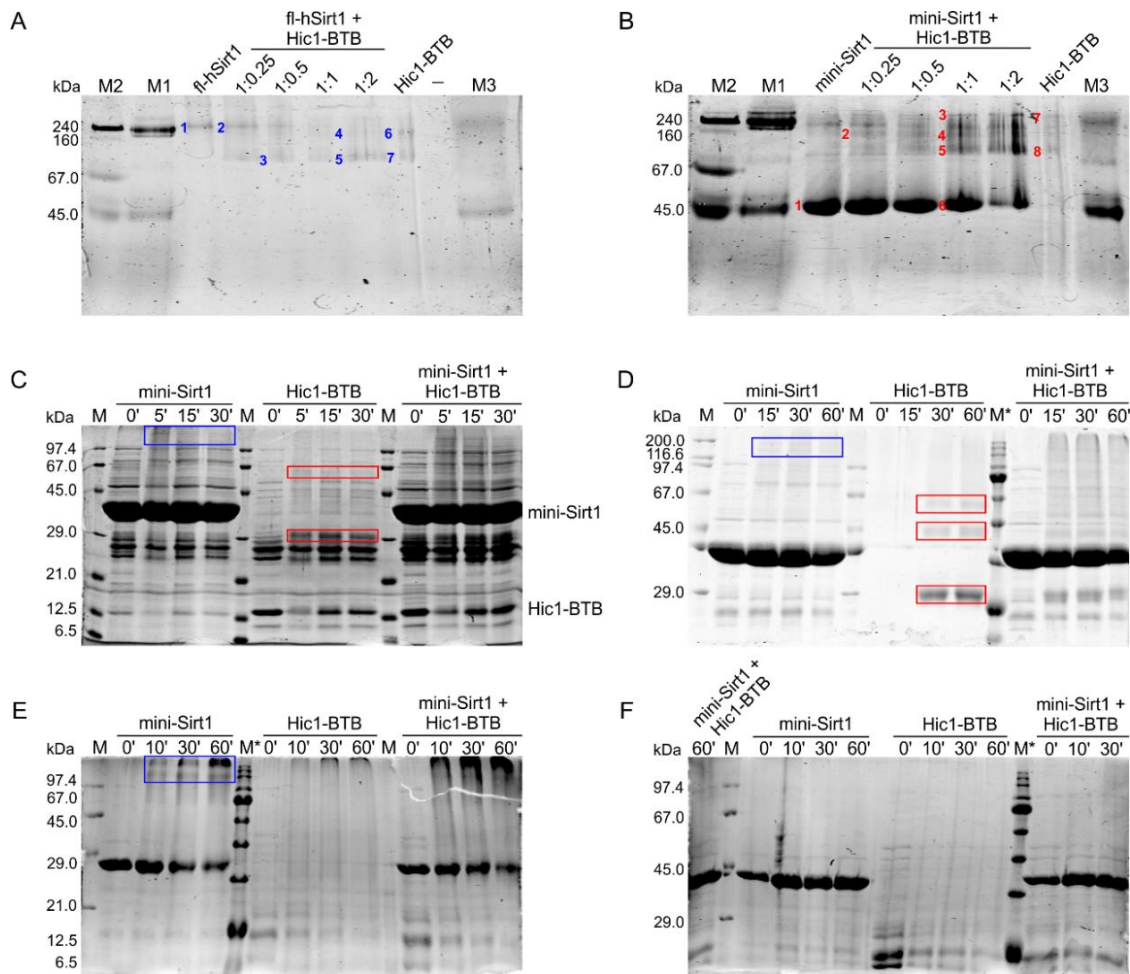


Figure 4.21: Interaction studies between *hSirt1* and *Hic1-BTB*. **A** Blue Native PAGE with 25 μ g fl-*hSirt1* (pET32*amod*) and *Hic1-BTB* octamer (6.25/12.5/25/50 μ g). MS analysis identified band **1** as fl-*hSirt1*, bands **3-7** as *Hic1-BTB*, and band **2** as both proteins. **B** Blue Native PAGE with 25 μ g mini-*Sirt1* and *Hic1-BTB* octamer (6.25/12.5/25/50 μ g). MS analysis identified bands **1** and **6** as mini-*Sirt1*. Bands **7** and **8** are *Hic1-BTB* (not confirmed by MS). Bands **2**, **4**, and **5** were revealed as *Hic1-BTB*, while band **3** might be a complex of mini-*Sirt1* and *Hic1-BTB*. Marker for Blue Native PAGE in **A** and **B**: M1 - 160/45 kDa, M2 - 240/67/45 kDa, M3 - 45 kDa. **C** Crosslinking of 70 μ M mini-*Sirt1* and 70 μ M *Hic1-BTB* dimer with 2.82 mM DSS in 5% (v/v) DMSO. Self-crosslinks for mini-*Sirt1* are observed at high molecular weight (blue box), dimers and tetramers of *Hic1-BTB* are indicated at 30 kDa and 60 kDa (red boxes). **D** Crosslinking of 50 μ M mini-*Sirt1* and 50 μ M *Hic1-BTB* octamer with 2.82 mM DSS in 5% (v/v) DMSO. Self-crosslinks of *Hic1-BTB* (red boxes) and mini-*Sirt1* (blue box) are indicated. **E** Crosslinking of 16 μ M mini-*Sirt1* and 50 μ M *Hic1-BTB* dimer with 1 mM glutaraldehyde or **F** 1.69 mM DMS. Marker M* in **D-F**: 245, 190, 135, 100, 80, 58, 46, 32, 25, 22, 17, 11 kDa.

As visualization of a protein-protein complex failed, the interaction was investigated with a thermal denaturation shift assay using equimolar amounts of fl-*hSirt1* or mini-*Sirt1* with *Hic1-BTB* octamer (Figure 4.22A). In both cases, the *hSirt1* melting temperature was slightly increased in presence of *Hic1-BTB* (Figure 4.22A), indicating that *hSirt1* and *Hic1-BTB* interact and that the stability of *hSirt1* is enhanced in presence of *Hic1-BTB*. To elucidate whether *Hic1-BTB* also affects *hSirt1* activity, a continuous coupled enzymatic assay with fl-*hSirt1* and *Hic1-BTB* octamer was performed, showing a weak stimulatory effect for 5-10 μ M *Hic1-BTB* octamer (Figure 4.22B). However, precipitation occurred at higher concentrations of *Hic1-BTB* causing pseudo-inhibition (Figure 4.22B). Consequently, the buffer was

Results

optimized and subsequent assays were performed in 20 mM Tris/HCl, pH 7.8, 150 mM NaCl, 10 mM MgCl₂, and 0.05% (v/v) Tween[®] 20. Repeating the assay with mini-Sirt1 and Hic1-BTB octamer in the new buffer also indicated a weak hSirt1 activation by low concentrations of Hic1-BTB octamer and showed that Hic1-BTB did not precipitate anymore (Figure 4.22C).

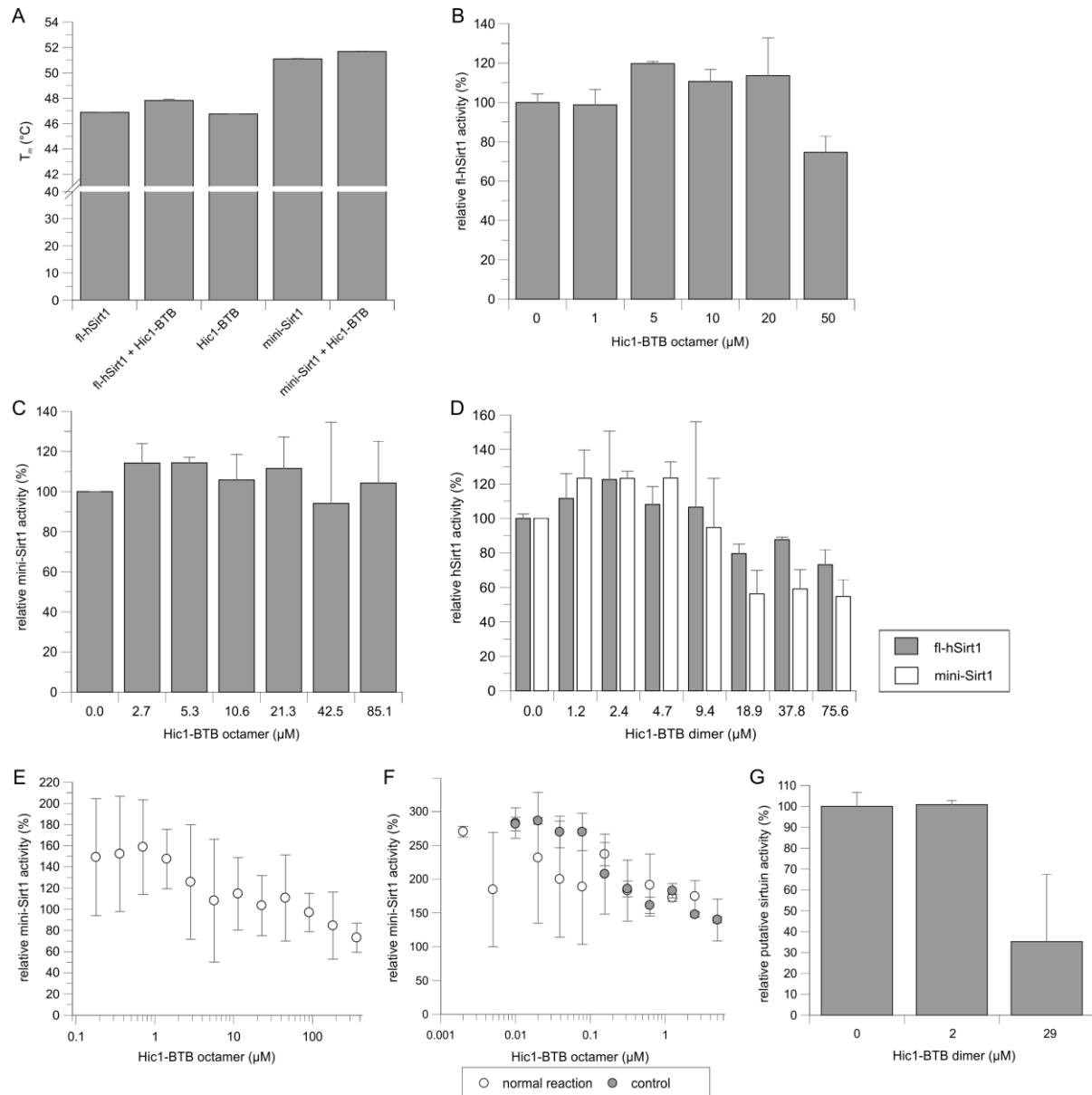


Figure 4.22: Modulation of hSirt1 stability and activity by Hic1-BTB. **A** TSA of 5 μ M fl-hSirt1 or mini-Sirt1 with 5 μ M Hic1-BTB octamer in 25 mM HEPES, pH 7.8, 150 mM NaCl, 2 mM DTT. Hic1-BTB increases the fl-hSirt1 T_m from 46.9 °C to 47.8 °C and the mini-Sirt1 T_m from 51.1 °C to 51.7 °C. Hic1-BTB has a T_m = 46.8 °C (n = 2). **B** Continuous coupled enzymatic assay with 1 μ M fl-hSirt1 (pET32amod), 500 μ M NAD⁺, 100 μ M p53short, and Hic1-BTB octamer in 10 mM potassium phosphate, pH 7.8 (n = 4). **C** Continuous coupled enzymatic assay with 1 μ M mini-Sirt1, 500 μ M NAD⁺, 100 μ M p53short, and Hic1-BTB octamer (n = 2). **D** Continuous coupled enzymatic assay with 1 μ M fl-hSirt1 or mini-Sirt1, 500 μ M NAD⁺, 100 μ M p53short, and Hic1-BTB dimer (n = 3). **E** Fluor de Lys assay with 1 μ M mini-Sirt1, 500 μ M NAD⁺, 100 μ M FdL-1, and Hic1-BTB octamer (n = 8). **F** Fluor de Lys assay with 1 μ M mini-Sirt1, 250 μ M NAD⁺, 50 μ M FdL-1, and Hic1-BTB octamer. Hic1-BTB was either added for the sirtuin deacetylation reaction (white) or after stopping the reaction (grey) (n = 3). **G** Continuous coupled enzymatic assay with 150 μ M NAM, 500 μ M NAD⁺, 100 μ M p53short, and Hic1-BTB dimer (n = 2). **C-G** The optimized Hic1-BTB assay buffer was used.

In addition to the Hic1-BTB octamer, the dimeric species also seems to activate fl-hSirt1 and mini-Sirt1 at concentrations from 1-10 μM in the coupled continuous enzymatic assay, but higher concentrations resulted again in inhibition of hSirt1 activity (Figure 4.22D). This demonstrates that the Hic1-BTB dimer and octamer do not differ in their activity modulating effect on hSirt1 and that only domains included in mini-Sirt1 are sufficient for this effect (Figure 4.22C, D). Due to the conflicting activity-modulating effect exerted by different concentrations of Hic1-BTB, a *Fluor de Lys* assay was performed with mini-Sirt1 and Hic1-BTB octamer, displaying the same pattern for the activity of mini-Sirt1 (Figure 4.22E). As the variation was high, a control was carried out where Hic1-BTB octamer was added after stopping the reaction (Figure 4.22F). This control revealed that the activating effect of Hic1-BTB on hSirt1 activity in the *Fluor de Lys* assay might be artificial (Figure 4.22F) and is likely mediated by an interaction of Hic1-BTB with the fluorophore of the *FdL-1* substrate. In contrast, a control for the continuous coupled enzymatic assay (Figure 4.22B-D) using NAM for starting the coupled reactions showed that Hic1-BTB dimer does likely not affect the coupled enzymes (Figure 4.22G). Therefore, the BTB domain of human Hic1 might have a dual effect on the deacetylase activity of human Sirt1 *in vitro*.

Next, the binding affinity of Hic1-BTB and hSirt1 was investigated with microscale thermophoresis. Labeling hSirt1 with FITC and titrating Hic1-BTB dimer resulted in a $K_d = 0.56 \pm 0.13 \mu\text{M}$ for fl-hSirt1 and a comparable $K_d = 0.60 \pm 0.12 \mu\text{M}$ for mini-Sirt1 (Figure 4.23A). To exclude any artificial effect, e.g., from the labeling reaction, the experiment was repeated with FITC-labeled Hic1-BTB dimer and titration of hSirt1 (Figure 4.23B). In this setup, the K_d was $0.50 \pm 0.10 \mu\text{M}$ for fl-hSirt1 and $0.28 \pm 0.09 \mu\text{M}$ for mini-Sirt1 (Figure 4.23B), validating a sub-micromolar affinity between Hic1-BTB dimer and hSirt1. These experiments also show that only domains included in mini-Sirt1 are necessary for the interaction between hSirt1 and the BTB domain of Hic1 as already indicated by activity assays (Figure 4.22). To narrow down the Sirt1 regions involved in the interaction, MST was conducted with FITC-labeled Hic1-BTB dimer and titration of the mini-Sirt1- ΔSBD and mini-Sirt1- ΔESA deletion mutants (Figure 4.23C). The mini-Sirt1- ΔESA deletion mutant exhibits a comparable K_d of $0.48 \pm 0.08 \mu\text{M}$, while the one for mini-Sirt1- ΔSBD was higher at $0.91 \pm 0.19 \mu\text{M}$ (Figure 4.23C). In conclusion, the hSirt1 catalytic domain is sufficient for the interaction with Hic1-BTB, but the SBD might slightly enhance affinity.

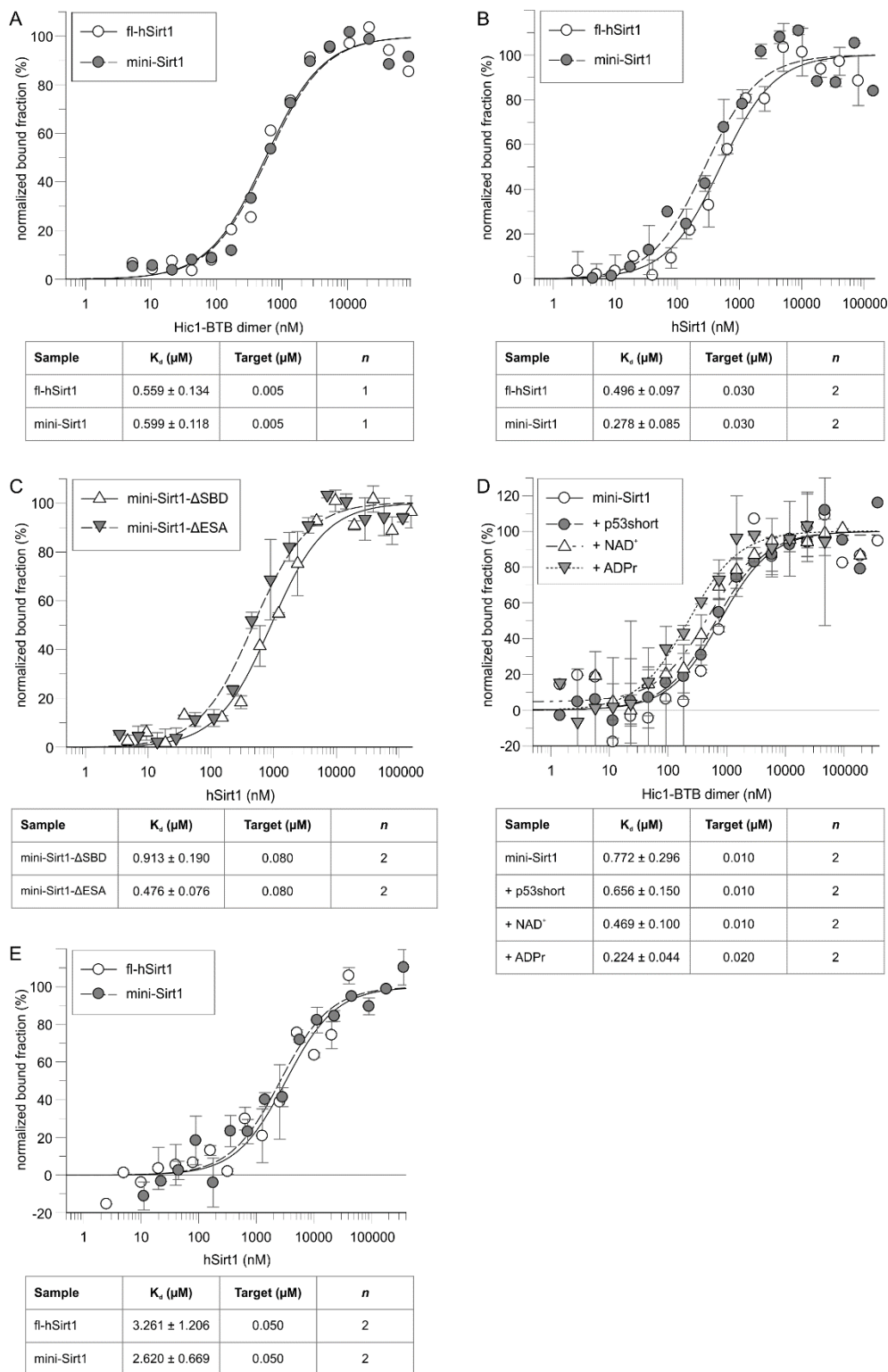


Figure 4.23: Binding affinity for human Sirt1 and the BTB domain of Hic1. **A** MST of fl-hSirt1 or mini-Sirt1 with titration of Hic1-BTB dimer. **B** MST of Hic1-BTB dimer with titration of fl-hSirt1 or mini-Sirt1. **C** MST of Hic1-BTB dimer with titration of mini-Sirt1- ΔSBD or mini-Sirt1- ΔESA . **D** MST of mini-Sirt1 with titration of Hic1-BTB dimer in presence of 1 mM p53short, or 3 mM NAD^+ , or 10 mM ADPr. **E** MST of Hic1-BTB octamer with titration of fl-hSirt1 or mini-Sirt1. **A-E** All experiments were performed at 6% LED power, 40% MST power, and 25 °C and analyzed from the initial fluorescence. The target concentration refers to the fixed concentration of FITC-labeled protein.

Furthermore, an influence on the K_d of mini-Sirt1 to Hic1-BTB was investigated in presence of Sirt1 ligands such as NAD^+ , p53short substrate, or ADPr. While the measured K_d for Hic1-

BTB dimer was $0.77 \pm 0.30 \mu\text{M}$ in this case, the binding affinity increased with bound mini-Sirt1 ligands and resulted in the highest affinity of $0.22 \pm 0.04 \mu\text{M}$ in presence of ADPr (Figure 4.23D). The K_d for Hic1-BTB dimer to mini-Sirt1 yielded $0.66 \pm 0.15 \mu\text{M}$ in presence of substrate and $0.47 \pm 0.10 \mu\text{M}$ in presence of NAD^+ (Figure 4.23D). Including the error and small measurement variations, this shows that Sirt1 ligands are not necessary for the interaction with the Hic1 BTB domain, but any bound natural or nature-derived Sirt1 ligand enhances the affinity for Hic1-BTB, presumably through increased Sirt1 stability. Finally, the binding affinity for Hic1-BTB octamer was examined resulting in K_d 's of $3.26 \pm 1.21 \mu\text{M}$ for fl-hSirt1 and $2.62 \pm 0.67 \mu\text{M}$ for mini-Sirt1 (Figure 4.23E). Although the dissociation constant is higher than for the Hic1-BTB dimer, the experiment demonstrates that both oligomeric species have a low- or sub-micromolar binding affinity for hSirt1.

The presented studies show that isolated hSirt1 interacts with the isolated BTB domain of human Hic1 and needs only its catalytic domain for this interaction. However, previous studies suggested that a CK2-mediated phosphorylation of hSirt1 Ser659 and Ser661 in the ESA region upon genotoxic stress is crucial for the interaction of hSirt1 and Hic1¹⁸⁵. Since the role of these phosphorylations for the interaction of hSirt1 with Hic1-BTB was not clear, their influence was investigated within this work. Therefore, mini-Sirt1 was phosphorylated *in vitro* by CK2, followed by *Blue Native* PAGE in presence of Hic1-BTB octamer (Figure 4.24A). However, reaction and control experiment did not differ and putative interaction bands were not formed (Figure 4.24A). As the phosphorylation state of mini-Sirt1 could not be verified with the current MS setup in our laboratory, mini-Sirt1 phosphorylation mimicry mutants were used for further experiments. Mini-Sirt1 single mutants of S659D and S661D, as well as the double mutant were purified as described earlier (Figure 7.3-Figure 7.5). The purified mini-Sirt1 mutants were pre-incubated with Hic1-BTB dimer and electrophoretically separated in *Clear Native* PAGE, which is performed like *Blue Native* PAGE without Coomassie dye in the buffers to prevent precipitation (Figure 4.24B). But formation of a clear interaction band between any of the mini-Sirt1 phosphorylation mimicry mutants and Hic1-BTB dimer could not be observed and MS-analysis similarly could not identify weak bands (Figure 4.24B).

Thus, a continuous coupled enzymatic assay with the mini-Sirt1 phosphorylation mimicry mutants and Hic1-BTB octamer was conducted (Figure 4.24C). While wild-type mini-Sirt1 is activated at low concentrations and inhibited at high concentrations of Hic1-BTB octamer (Figure 4.24C) as previously seen (Figure 4.22C), the effect is only clearly observed for the

mini-Sirt1 S659D S661D double mutant (Figure 4.24C). Furthermore, MST with labeled mini-Sirt1 phosphorylation mimicry mutants and titration of Hic1-BTB dimer was performed (Figure 4.24D) under the same conditions as previous experiments. Apparently, none of the phosphorylation mimicry mutations affect the binding affinity of mini-Sirt1 and Hic1-BTB dimer as the K_d for all measurements ranged from 1.05-1.26 μM (Figure 4.24D). Therefore, phosphorylation of hSirt1 Ser659 and Ser661 by CK2 is probably not necessary for the interaction of hSirt1 with the BTB domain of Hic1.

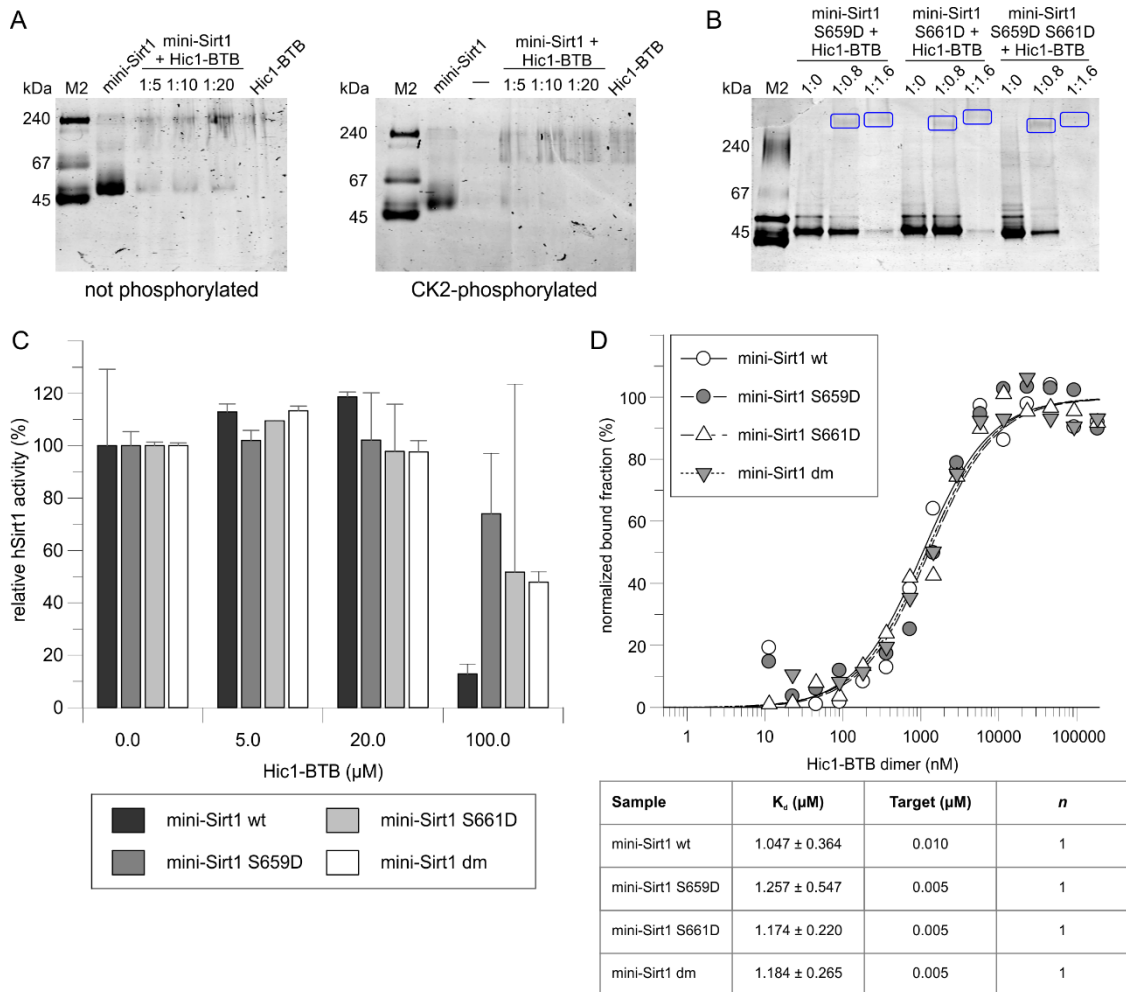


Figure 4.24: Impact of the phosphorylation of hSirt1 Ser659 and Ser661 on the interaction between hSirt1 and Hic1-BTB. **A** Blue Native PAGE of 5 μg mini-Sirt1 and 25/50/100 μg Hic1-BTB octamer after overnight phosphorylation of mini-Sirt1 by CK2. **B** Clear Native PAGE of 15 μg mini-Sirt1 phosphorylation mimicry mutants with 12.5/25 μg Hic1-BTB dimer. Bands in blue boxes were analyzed by MS without results. Marker for Native PAGE in **A** and **B**: M2 - 240/67/45 kDa. **C** Continuous coupled enzymatic assay with 1 μM mini-Sirt1 wild-type or phosphorylation mimicry mutant, 500 μM NAD^+ , 100 μM p53short, and Hic1-BTB octamer ($n = 2$). **D** MST with mini-Sirt1 wild-type or phosphorylation mimicry mutant and titration of Hic1-BTB dimer. Settings: 6% LED power, 40% MST power, 25 $^\circ\text{C}$. The experiment was analyzed from the initial fluorescence. The error represents the error of the fit. The target concentration is the fixed concentration of labeled protein.

4.3.3 Structural characterization of Hic1-BTB

For analysis of the interaction mode and the interaction surface between Hic1-BTB and hSirt1, attempts were made to crystallize Hic1-BTB alone and in complex with mini-Sirt1.

Isolated Hic1-BTB crystallized in the shape of needles, which reached a final size of 500 μm within three days and diffracted up to 2.7 \AA (Figure 4.25A). Data was solved in space group $P2_12_12_1$ and refined to final R and R_{free} values of 22.5% and 28.4% (Table 7.6). The structure shows 16 Hic1-BTB molecules in the asymmetric unit (Figure 4.25B). The BTB domain of Hic1 is mostly α -helical with seven α -helices embracing a solution-exposed hydrophobic patch of three β -strands (Figure 4.25C). Dimer formation occurs via strand exchange of the N-terminal α 1-helix from amino acids 29-43 (Figure 4.25D). Notably, this dimeric interface is stabilized by four salt bridges between Glu25 and Arg31 as well as between His29 and Asp140 of the respective monomers (Figure 4.25D). The two monomers within a homodimer superimpose with a mean RMSD = 0.404 ± 0.105 \AA for 92-109 C_α atoms (Figure 4.25C).

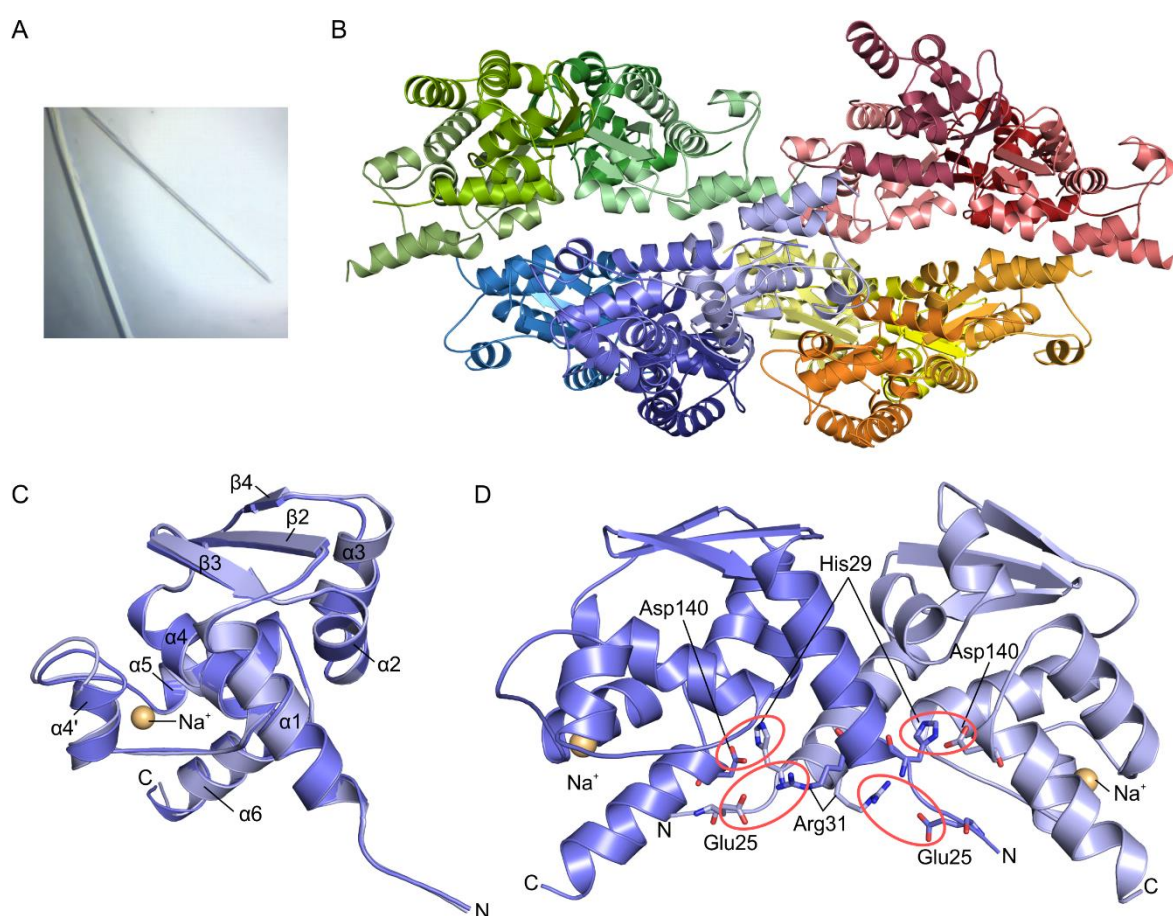


Figure 4.25: Crystallization and structure of Hic1-BTB. **A** Crystallization of 10 mg/ml Hic1-BTB octamer in 0.1 M sodium cacodylate, pH 6.5, 1.4 M sodium acetate at 20 $^{\circ}\text{C}$. **B** Asymmetric unit of the structure of Hic1-BTB octamer with 16 molecules shown by different colors. The two octamers are composed of two tetramers each shaded either in blue and green or in red and orange colors. **C** Superposition of two Hic1-BTB monomers comprising the homodimer. Hic1-BTB forms seven α -helices and three solvent-exposed β -strands, which are numbered from the N-terminus according to common BTB domain numbering. **D** Hic1-BTB dimer formed via strand exchange of the α 1-helix with four salt bridges (red circles).

Analysis of the crystal contacts in the asymmetric unit using the PDBe PISA server²⁶² indicates a favor for a Hic1-BTB dimer and octamer (Table 4.2). The Hic1-BTB dimer buries an interface of about 1500 \AA^2 and has a complexation significance score (CSS) > 0.55

(Table 4.2). As the free energy of assembly dissociation ΔG^{diss} is high, the dimeric species can be considered as a physiological unit of the BTB domain of Hic1. Tetramer formation occurs via head-to-head assembly of two dimers in one plane. The tetrameric interface covers the solvent-exposed β -strands, thereby creating two additional salt bridges between Arg59 and Asp79 of the two opposite dimers. The tetramers are slightly shifted in their plane to form two octamers stabilized by four further salt bridges between Asp87 of the outer tetramer and Lys150 of the inner tetramer as well as Lys73 of the outer tetramer and Asp85 of the inner tetramer (Figure 4.25B). Formation of a tetramer and an octamer seems to play an auxiliary role in complexation, with the octamer being more favorable than the tetramer based on the values for the solvation free energy gain upon interfacing ΔG^{int} (Table 4.2). Assembly of the octamer covers an interface of 19780 \AA^2 requiring an external driving force for dissociation (Table 4.2). Based on this analysis, the tetrameric interface of Hic1-BTB seems to be an artifact of the composition of the asymmetric unit of the crystal, whereas the Hic1-BTB dimer and octamer are probably relevant in solution as already observed in SEC.

Table 4.2: Analysis of interfaces in the crystal structure of Hic1-BTB by PDBe PISA ²⁶². Average values are given for all comparable interfaces. The “single” interfaces refer to assembly of two non-dimer or non-tetramer-associated chains, whereas “all” refers to assembly of two dimers or tetramers. The values in brackets for CSS are derived from the last refinement cycle with REFMAC, while all other values are derived from the finalized structure refined with Phenix.Refine. Abbreviations: HB - hydrogen bonds, SB - salt bridges, ΔG^{int} - solvation free energy gain upon interfacing, ΔG^{ass} - solvation free energy gain upon assembly of all chains, ΔG^{diss} - free energy of assembly dissociation, CSS - complexation significance score, *n. a.* - not available.

Oligomeric interface	Symmetry operation	Interaction surface (\AA^2)	HB	SB	ΔG^{int} (kcal/mol)	ΔG^{ass} (kcal/mol)	ΔG^{diss} (kcal/mol)	CSS
dimer	x, y, z	1438.7	16	6	-17.5	-40.5	13.8	0.547 (1.000)
tetramer (single)	x, y, z	477.8	5	3	-3.3	<i>n. a.</i>	<i>n. a.</i>	0.106 (0.126)
octamer (single)	x, y, z	567.4	4	4	-7.0	<i>n. a.</i>	<i>n. a.</i>	0.031 (0.047)
octamer (all)	x, y, z	19780	26	14	<i>n. a.</i>	-189.2	5.0	<i>n. a.</i>

A structure-based sequence alignment with BTB domains from other BTB-ZF proteins shows that the fold of Hic1-BTB is highly similar (Figure 4.26A). But in some cases the $\alpha 1$ -helix is preceded by a $\beta 1$ -strand (Figure 4.26B) extending the dimer interface through interactions with $\beta 5$ ²⁶¹, which is lacking in Hic1-BTB. Instead, Hic1-BTB has an extension of 13 amino acids at this latter site including a poly-alanine region that folds into an additional $\alpha 4'$ -helix (Figure 4.26A, B). Only the distantly related BTB/POZ domains from the Skp1 family have a similar $\alpha 4'$ -helix ²⁶³ (Figure 4.26B). Interestingly, Hic1-BTB amino acids 108-125 involving the $\alpha 4'$ -helix seem to complex a metal ion, whose nature could not be undoubtedly clarified,

but the crystallization condition suggested placement of a sodium ion (Figure 4.25C). Dimer formation of Hic1-BTB via the N-terminal α 1-helix results in a so-called swapped dimer like in BCL-6²⁶¹, where the respective α 1-helices of both monomers intersect (Figure 4.26C). Irrespective of the presence of an N-terminal β 1-strand, BTB/POZ domains from BTB-ZF proteins can also constitute a non-swapped dimer, e. g., in FAZF²⁶¹, where the α 1-helix is shorter and the N-terminus folds back towards the same monomeric chain, resulting in intra-chain interactions of β 1 and β 5²⁶¹ (Figure 4.26D). The structure of Hic1-BTB is thus comparable to structures of other swapped BTB domains from BTB-ZF proteins, but shows the special feature of an additional α 4'-helix at the known site for a β 5-strand.

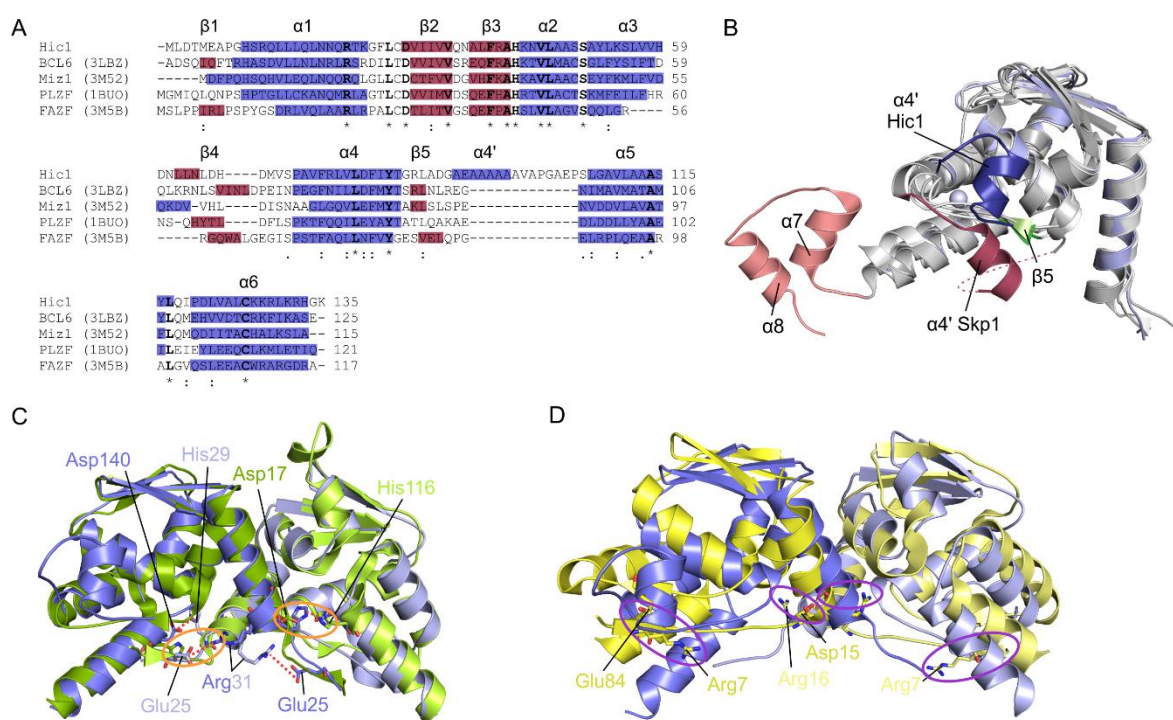


Figure 4.26: Comparison of the Hic1-BTB fold with structures of BTB domains from other BTB-ZF proteins.

A Sequence alignment of BTB domains from BTB-ZF proteins calculated with Clustal Omega²⁵⁴. The secondary structure (blue for α -helices, red for β -strands) along with the common numbering for structural BTB elements is indicated. PDB codes used for comparison are in brackets. **B** Superposition of Hic1-BTB (light blue) with the BTB domains from BCL-6 (PDB: 3LBZ; white), PLZF (PDB: 1BUO; light grey), Miz1 (PDB: 3M52; middle grey), and Skp1 (PDB: 1FQV; dark grey). The unique Hic1-BTB α 4'-helix is colored blue, while the β 5-strands from BCL-6 and Miz1 are green. The α 4'-helix of Skp1 is colored red and the α 7- and α 8-helices, unique to the Skp1-family, are shown in salmon. **C** Superposition of a Hic1-BTB homodimer (blue) with a swapped homodimer of BCL-6 (PDB: 3LBZ; green) resulting in an RMSD = 0.902 Å for 193 C α atoms. Salt bridges are displayed as orange circles (BCL-6) or red dotted lines (Hic1-BTB). **D** Superposition of a Hic1-BTB homodimer (blue) with a non-swapped homodimer of FAZF (PDB: 3M5B; yellow) resulting in an RMSD = 3.733 Å for 121 C α atoms. Salt bridges in FAZF are displayed as purple circles.

In addition to Hic1-BTB octamer, the dimeric species of the BTB domain was subjected to crystallization. While the typical needle-shaped crystals appeared in several crystallization conditions, they were often too thin for mounting or had low resolution (5-6 Å). Similarly, attempts were made to cocrystallize the octameric and dimeric species of Hic1-BTB with mini-Sirt1. Despite various screening conditions and optional presence of stabilizing hSirt1

ligands, such as p53short substrate, NAD^+ , or ADPr, no crystals grew for a complex of Hic1-BTB octamer and mini-Sirt1. Interestingly, a crystal from cocrystallization of Hic1-BTB dimer and mini-Sirt1 diffracted up to 3.5 Å and was solved in space group $\text{P2}_1\text{2}_1\text{2}_1$. Although the crystal morphology differed from low resolution crystals of isolated Hic1-BTB dimer in the same crystallization condition, the resulting structure contained only Hic1-BTB in the same asymmetric unit composition as previously seen (Figure 4.25B) and placement of mini-Sirt1 was not supported by the electron density maps. This structure shows that Hic1-BTB crystallizes independently of the oligomeric species initially used for the setup. In addition, a sodium ion at the $\alpha 4'$ -helix could not be observed in this structure, indicating that it is a crystallographic artifact and not necessary for the structural integrity of the BTB domain of Hic1. Despite failure to cocrystallize a complex of hSirt1 and Hic1-BTB, the obtained Hic1-BTB structure can be used for analysis of putative interfaces for the interaction with hSirt1.

4.4 Biochemical and structural characterization of hSirt1-inhibition by HIV1-Tat

4.4.1 Bioanalytical characterization of HIV1-Tat Cys⁻

For recombinant overexpression in *E. coli*, a HIV1-Tat variant, in which the seven cysteine exchanges C22S, C25A, C27A, C30A, C31A, C34S, and C37A were conducted²⁰⁹, was purified by collaborators from the Department of Biopolymers, University of Bayreuth, Germany. The resulting Tat Cys⁻ could be obtained with 95% purity and has a molecular weight of 9.7 kDa despite its running behavior on SDS-PAGE (Figure 4.27A). A CD spectrum of Tat Cys⁻ indicates no stable defined secondary structure (Figure 4.27B) consistent with previous NMR studies that revealed an elongated Tat Cys⁻¹⁹⁹. However, upon treatment of Tat Cys⁻ with 2,2,2-trifluoroethanol (TFE), the protein exhibits a propensity for formation of α -helices as indicated by local minima at 208 nm and 222 nm (Figure 4.27C).

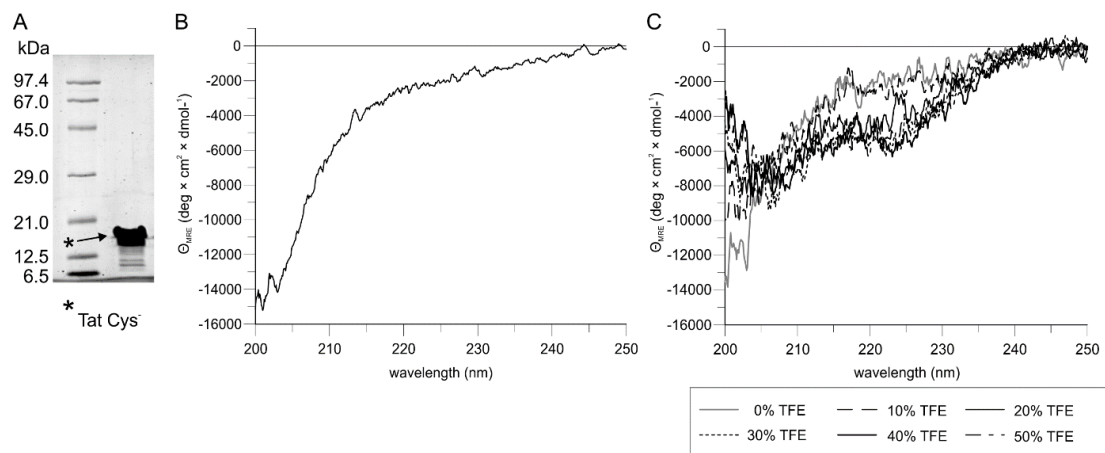


Figure 4.27: Bioanalytical properties of HIV1-Tat Cys⁻. **A** Purity and running behavior of 5 μM Tat Cys⁻ on SDS-PAGE. **B** CD spectrum of 0.2 mg/ml Tat Cys⁻ at 20 °C. **C** CD spectrum of 10 μM Tat Cys⁻ treated with TFE at 20 °C. Helix formation can be observed at 20% (v/v) TFE and above.

4.4.2 Modulation of hSirt1 activity by Tat Cys⁻

Since previous interaction studies between hSirt1 and HIV1-Tat were either performed *in vivo*^{125,204} or with a synthetic 72-amino acid Tat peptide²⁰⁴, this study first investigated whether the recombinant Tat Cys⁻ is able to repress hSirt1 activity *in vitro*. In a continuous coupled enzymatic assay with a natural p53-derived substrate, fl-hSirt1 was inhibited by Tat Cys⁻ with an IC₅₀ of about 20 μM (Figure 4.28A), showing that pure recombinant Tat Cys⁻ can interact with isolated fl-hSirt1 and repress its activity *in vitro*. In addition, a *Fluor de Lys* assay with an artificial *FdL-1* substrate revealed that Tat Cys⁻ inhibits fl-hSirt1 with an IC₅₀ = 3.6 ± 0.8 μM (Figure 4.28B), comparable to synthetic Tat from previous studies²⁰⁴.

To elucidate which regions of fl-hSirt1 are necessary for Tat-mediated inhibition, several hSirt1 deletion constructs were tested in activity assays. First, a *Fluor de Lys* assay with hSirt1-(183-664) and hSirt1-(214-664) showed that Tat Cys⁻ can repress the deacetylase activity of both constructs with an IC₅₀ of about 25 μM (Figure 4.28C). This demonstrates that the far N- and C-terminal regions of hSirt1, spanning around 200 amino acids each, are not essential for interaction with Tat. Furthermore, the deacetylation activity of the functional mini-Sirt1 construct was investigated in presence of Tat Cys⁻. While deacetylation of p53 by mini-Sirt1 was inhibited by Tat Cys⁻ with an IC₅₀ of 17.2 ± 3.2 μM, deacetylation of the artificial *FdL-1* by mini-Sirt1 was repressed with an IC₅₀ = 2.3 ± 0.9 μM (Figure 4.28D), consistent with results obtained for fl-hSirt1 (Figure 4.28A, B). Therefore, the region between hSirt1 amino acids 505-641 is also not necessary for inhibition by Tat. Finally, mini-Sirt1 deletion constructs lacking either the SBD or the ESA/CTR region, both of which are Sirt1-specific sirtuin regions^{76,79,80}, were tested in deacetylation activity assays with Tat Cys⁻. Although the effect at low-micromolar doses of Tat Cys⁻ was weak, 30 μM Tat Cys⁻ were sufficient to inhibit both mini-Sirt1-ΔSBD and mini-Sirt1-ΔESA to a similar residual activity as seen for fl-hSirt1 or mini-Sirt1 (Figure 4.28E). This demonstrates that only the catalytic domain of hSirt1 is necessary for HIV1 Tat-mediated inhibition.

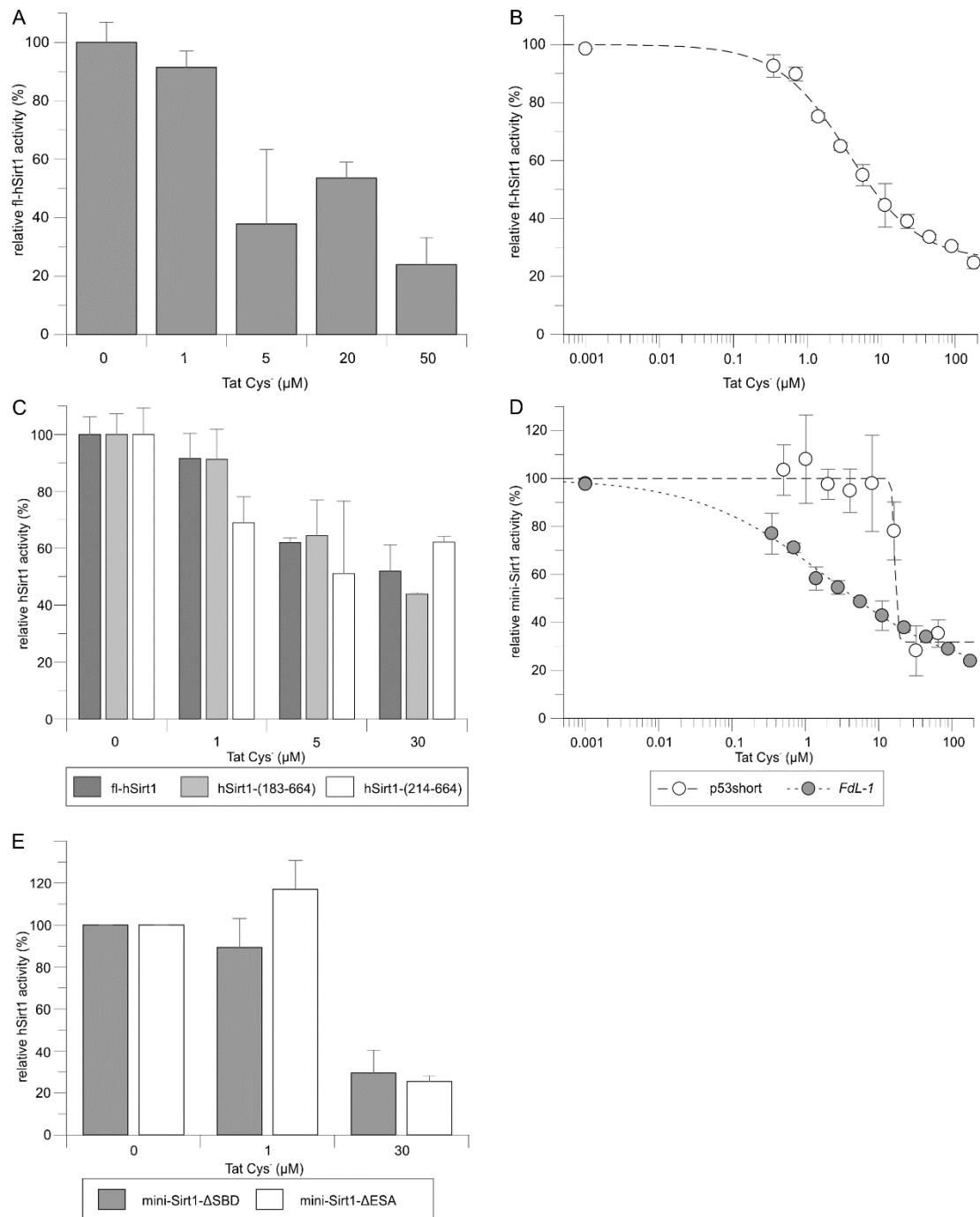


Figure 4.28: Inhibition of hSirt1 by Tat Cys. **A** Continuous coupled enzymatic assay with 1 μM fl-hSirt1 (pET32*amod*), 500 μM NAD⁺, and 100 μM p53short substrate ($n = 2$). **B** *Fluor de Lys* assay with 1 μM fl-hSirt1, 500 μM NAD⁺, and 230 μM *FdL-1* substrate. $IC_{50} = 3.6 \pm 0.8 \mu\text{M}$ ($n = 3$). **C** *Fluor de Lys* assay with 1 μM fl-hSirt1 (pET32*amod*), or 1 μM hSirt1-(183-664), or 1 μM hSirt1-(214-664), 500 μM NAD⁺, and 100 μM *FdL-1* ($n = 2$). **D** Tat Cys⁺-mediated inhibition of 1 μM mini-Sirt1 in a *Fluor de Lys* assay with 144 μM *FdL-1* ($IC_{50} = 2.3 \pm 0.9 \mu\text{M}$, $n = 3$) or in a continuous coupled enzymatic assay with 200 μM p53short ($IC_{50} = 17.2 \pm 3.2 \mu\text{M}$, $n = 5$). **E** Continuous coupled enzymatic assay with 1 μM mini-Sirt1-ΔSBD or 1 μM mini-Sirt1-ΔESA, 500 μM NAD⁺, and 100 μM p53short ($n = 3$). Substrate K_m determinations for **B** and **D** in Figure 7.9 and Figure 7.10.

4.4.3 Specificity of Tat-mediated inhibition of human sirtuin isoforms

As the structure and sequence of the catalytic core of sirtuins are conserved³³, the isoform specificity of Tat-mediated inhibition was investigated. In the continuous coupled enzymatic assay, the K_m values for different sirtuin substrates were determined first (Figure 7.10),

followed by analysis of the effect of 65 μM Tat Cys⁻ on the deacylase activity of 1 μM sirtuin in presence of the respective substrate at its K_m (Figure 4.29A): hSirt1, hSirt2, and hSirt3 show a robust and comparable deacetylase activity for their preferred peptide substrate, which is repressed by Tat Cys⁻ to a similar residual specific activity (Figure 4.29A). For hSirt2, the effect of Tat Cys⁻ on the deacetylation of p53short, a hSirt1 substrate, was also investigated, as Tat Cys⁻ was later found to bind to the hSirt2 substrate α -tubulin with a $K_d \sim 700 \mu\text{M}$ (Figure 7.11). In this case, Tat Cys⁻ did not clearly suppress hSirt2-mediated deacetylation of p53short (Figure 4.29A). The desuccinylase activity of hSirt5 and the demyristoylase activity of hSirt6 were too low for observing an impact of Tat Cys⁻ (Figure 4.29A). In summary, Tat Cys⁻ seems to act as inhibitor for the deacetylase activity of at least hSirt1 and hSirt3.

Next, the binding affinities of FITC-labeled Tat Cys⁻ were determined for fl-hSirt1, mini-Sirt1, hSirt2-(43-356), and hSirt3-(93-399) using microscale thermophoresis. In all cases, the K_d was derived from the initial fluorescence because the concentration-dependent change in fluorescence was related to binding as validated with an SD test. Fl-hSirt1 shows the highest affinity for Tat Cys⁻ with a K_d of $0.34 \pm 0.24 \mu\text{M}$ (Figure 4.29B). The K_d values for mini-Sirt1 and hSirt3 are slightly higher and amount to $1.79 \pm 0.47 \mu\text{M}$ and $1.37 \pm 0.36 \mu\text{M}$, respectively (Figure 4.29B). In contrast, hSirt2 has a much lower binding affinity for Tat Cys⁻ with $6.67 \pm 0.05 \mu\text{M}$ (Figure 4.29B). Despite small differences in the affinities, isolated Tat Cys⁻ thus binds directly to hSirt1-3 *in vitro* with a low micromolar K_d . Thus, the specific IC_{50} values for inhibition of hSirt1-3 by Tat Cys⁻ were investigated with the *Fluor de Lys* assay. As before, the K_m values for the *FdL-1* substrate were determined for each sirtuin isoform (Figure 7.9). Afterwards, the IC_{50} for Tat-mediated inhibition was assessed for 1 μM sirtuin at the respective K_m for *FdL-1*, showing that fl-hSirt1 and mini-Sirt1 are equally inhibited by Tat Cys⁻ with IC_{50} values of $3.6 \pm 0.8 \mu\text{M}$ and $2.3 \pm 0.9 \mu\text{M}$ (Figure 4.29C). In contrast, inhibition of hSirt2 and hSirt3 by Tat Cys⁻ is weaker with IC_{50} values of $11.0 \pm 4.4 \mu\text{M}$ and $12.1 \pm 4.2 \mu\text{M}$ (Figure 4.29C). Due to the conflictive results for hSirt2 inhibition by Tat Cys⁻ for different substrates, an influence of Tat Cys⁻ on the artificial *FdL-1* substrate was investigated but could not be observed. Therefore, these results show that Tat Cys⁻ is able to bind and inhibit human Sirt1, Sirt2, and Sirt3 *in vitro*, although the potency of Tat-mediated inhibition of the three isoforms varies.

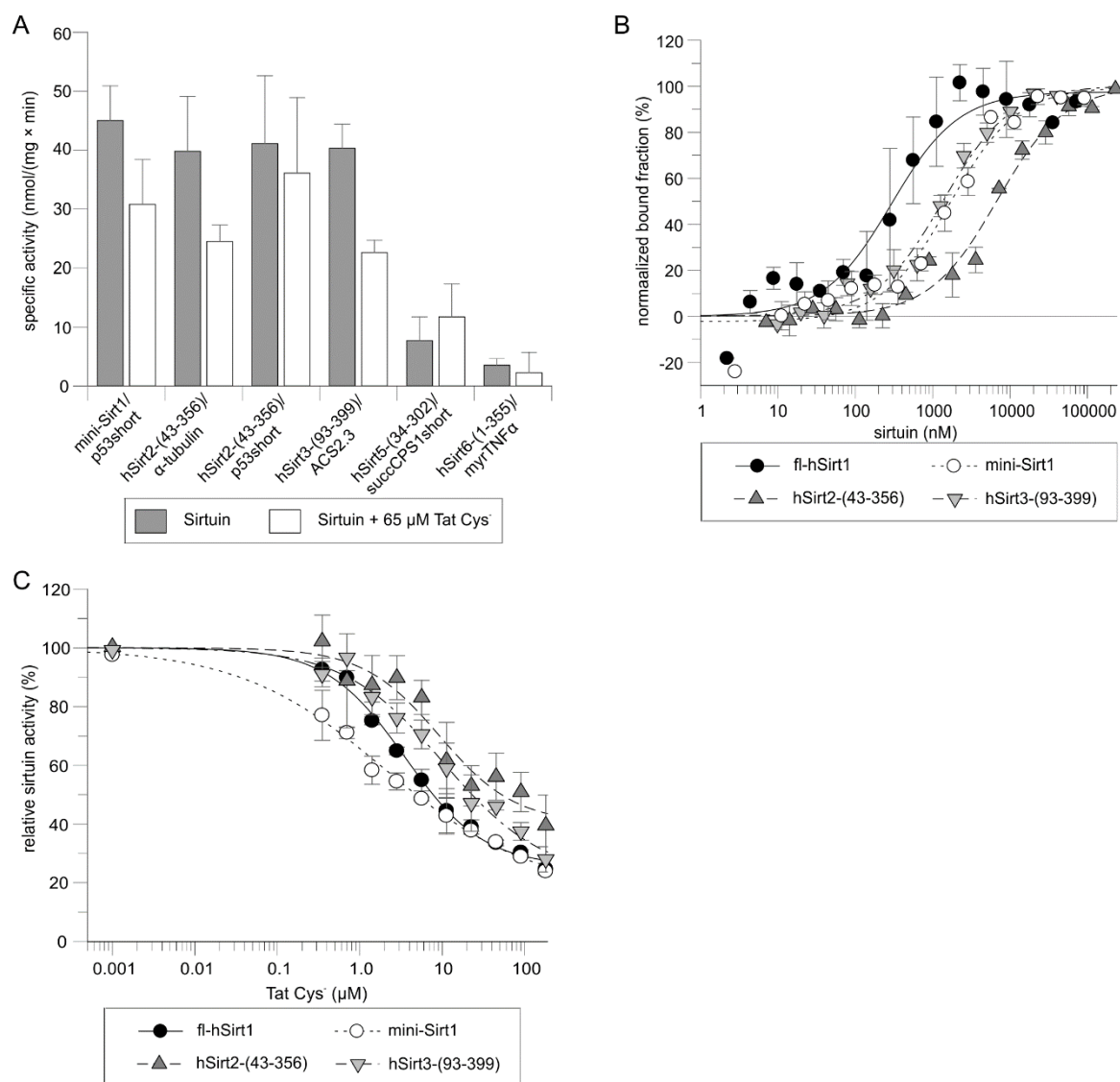


Figure 4.29: Tat-mediated inhibition of human sirtuin isoforms. **A** Specificity of Tat-mediated inhibition of human sirtuins. Continuous coupled enzymatic deacylation assay with 1 μ M sirtuin, 500 μ M NAD⁺, and the corresponding substrate at the determined K_m (Figure 7.10) ($n = 3$). **B** MST of 20 nM Tat Cys⁻ (hSirt2), 40 nM Tat Cys⁻ (mini-Sirt1), or 80 nM Tat Cys⁻ (fl-hSirt1, hSirt3) with titration of hSirt1-3 at 12% LED power, 30% MST power, and 25 $^{\circ}$ C ($n = 2$). The K_d was 0.34 ± 0.24 μ M for fl-hSirt1, 1.79 ± 0.47 μ M for mini-Sirt1, 6.67 ± 0.05 μ M for hSirt2-(43-356), and 1.37 ± 0.36 μ M for hSirt3-(93-399). **C** Fluor de Lys assay with 1 μ M sirtuin, 500 μ M NAD⁺, and *FdL-1* substrate at the determined K_m (Figure 7.9) ($n = 3$). The IC_{50} for Tat-mediated inhibition was 3.6 ± 0.8 μ M for fl-hSirt1, 2.3 ± 0.9 μ M for mini-Sirt1, 11.0 ± 4.4 μ M for hSirt2-(43-356), and 12.1 ± 4.2 μ M for hSirt3-(93-399).

4.4.4 Mapping of general sirtuin-interacting regions on Tat Cys⁻

Next, the region of Tat Cys⁻, which is necessary for interaction with human Sirt1, Sirt2, and Sirt3, was investigated. Focused on hSirt1, a 2D-(¹H, ¹⁵N)-HSQC NMR spectrum was recorded with (¹H, ¹⁵N)-labeled Tat Cys⁻ and titration of mini-Sirt1 (Figure 4.30A). While many signals disappeared from the 2D-(¹H, ¹⁵N)-HSQC NMR spectrum after addition of mini-Sirt1, analysis of the chemical shifts indicates that the region from HIV1-Tat-(64-87) is not involved in the interaction with hSirt1 (Figure 4.30A). The relevance of the N-terminal region from HIV1-Tat residues 1-20 was ambiguous because of the general lack of signals for

this region (Figure 4.30A). Thus, two new constructs of Tat Cys⁻ were cloned, lacking one or both terminal regions, and the resulting Tat Cys⁻-(1-63) and Tat Cys⁻-(21-63) proteins were purified as described. However, cleavage of the N-terminal solubility enhancing His₆-GB1-tag resulted in unspecific binding of the target proteins to Ni²⁺-immobilized beads and promoted aggregation. Therefore, the tag was kept and activity assays were performed with an additional control with His₆-GB1-tag to exclude any influence of the tag. In a continuous coupled enzymatic assay, Tat Cys⁻-(1-63) and Tat Cys⁻-(21-63) were able to repress fl-hSirt1 and mini-Sirt1 activity with IC₅₀ values of 10-30 μM (Figure 4.30B). This effect was validated with a *Fluor de Lys* assay, where both shortened Tat Cys⁻ proteins appeared to inhibit fl-hSirt1 with a slightly higher potency than mini-Sirt1 (Figure 4.30C). The NMR studies and the results from activity assays with the shortened Tat Cys⁻ proteins demonstrate that only the region from HIV1-Tat residues 21-63 is essential for inhibition of hSirt1.

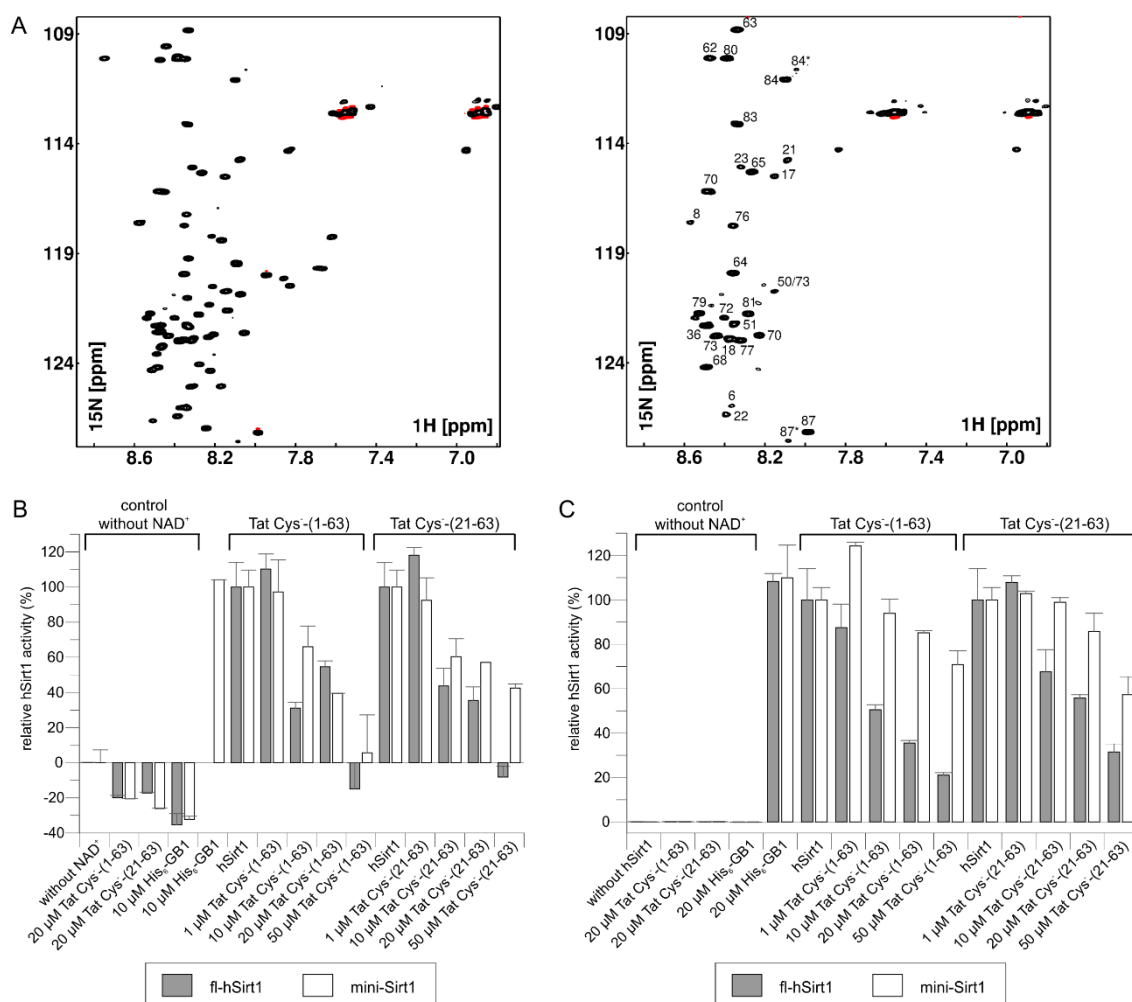


Figure 4.30: Determination of interacting regions on Tat Cys⁻ for inhibition of hSirt1 on protein level. **A** 2D-(¹H, ¹⁵N)-HSQC NMR spectrum of (¹H, ¹⁵N)-labeled Tat Cys⁻ before (left) and after titration of mini-Sirt1 (right). The NMR spectra were recorded by collaborators from the Department of Biopolymers, University of Bayreuth, Germany. **B** Continuous coupled enzymatic assay with 100 μM p53short and **C** *Fluor de Lys* assay with 100 μM FdL-1. Assays were performed with 1 μM fl-hSirt1 (pET19bmod-Sumo; grey) or mini-Sirt1 (white), 500 μM NAD⁺, and different concentrations of Tat Cys⁻-(1-63) or Tat Cys⁻-(21-63) as indicated (*n* = 2).

Since HIV1-Tat is a disordered protein (Figure 4.27B) and purification of recombinant shortened Tat Cys⁻ proteins was afflicted with difficulties, the exact Tat region necessary for inhibition of hSirt1 was determined using short synthetic Tat peptides (Table 3.1). The first focus was on the region around HIV1-Tat Lys50, which can be deacetylated by Sirt1¹²⁵. The effect of acetylated and non-acetylated Tat₄₆₋₅₄ peptide on fl-hSirt1 activity was thus investigated in a continuous coupled enzymatic assay (Figure 4.31A). While Tat₄₆₋₅₄ did not have a distinct impact, fl-hSirt1 activity was enhanced by up to 3-fold in presence of ac-Tat₄₆₋₅₄ (Figure 4.31A). This latter effect can be considered as artificial pseudo-activation because of the availability of more substrate for fl-hSirt1. Due to the weak effect of Tat₄₆₋₅₄ on fl-hSirt1, the *Fluor de Lys* assay was used for clarification. At the previously determined substrate K_m (Figure 7.9), Tat₄₆₋₅₄ was titrated to mini-Sirt1 or hSirt3-(93-399), showing that Tat₄₆₋₅₄ can indeed inhibit both sirtuin isoforms (Figure 4.31B). However, the derived IC₅₀ values are manifold increased compared to the ones for Tat Cys⁻ with $46.3 \pm 31.4 \mu\text{M}$ for mini-Sirt1 and $40.0 \pm 5.2 \mu\text{M}$ for hSirt3 (Figure 4.31B). This indicates that the area around HIV1-Tat Lys50 might be relevant for inhibition of hSirt1-3, but residues further N- or C-terminal from Lys50 probably contribute to increased potency.

For elucidating whether acetylated Tat acts as “supersubstrate”, which stays bound after deacetylation by hSirt1 and blocks access for other substrates²⁰⁴, ac-Tat₄₆₋₅₄ was used as substrate for mini-Sirt1 resulting in a K_m = $297.0 \pm 87.7 \mu\text{M}$ (Figure 4.31C). Although measured under NAD⁺-rate limiting conditions, this substrate K_m is comparable to the one for the standard mini-Sirt1 substrate peptide p53short (Figure 7.10). In addition, an inhibitory effect of accumulating deacetylated Tat₄₆₋₅₄ was not observed at later timepoints of the assay, indicating that the deacetylated substrate is quickly released from mini-Sirt1. Furthermore, the binding affinity of acetylated and non-acetylated Tat₄₆₋₅₄ to mini-Sirt1 was investigated with MST: mini-Sirt1 bound stronger to ac-Tat₄₆₋₅₄ with a K_d of $13.9 \pm 2.2 \mu\text{M}$, while the K_d for deacetylated Tat₄₆₋₅₄ was $60.7 \pm 5.4 \mu\text{M}$ (Figure 4.31D), matching the high IC₅₀ of this Tat peptide for inhibition of mini-Sirt1 (Figure 4.31B). These results demonstrate that acetylated and non-acetylated Tat can bind to hSirt1 *in vitro*. However, due to the lower affinity of Tat₄₆₋₅₄ compared to its acetylated counterpart, Tat likely does not act as a “supersubstrate”.

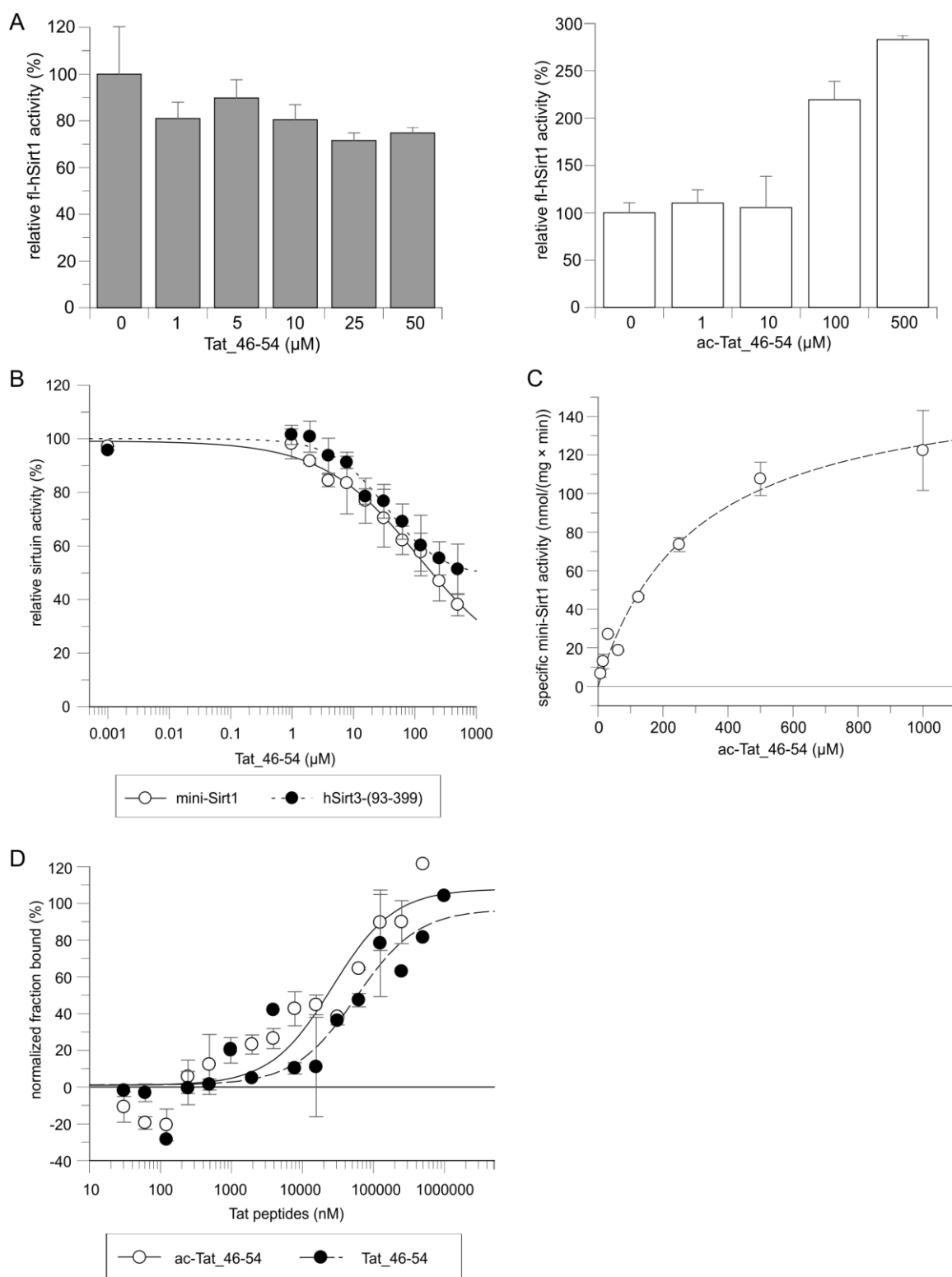


Figure 4.31: Relevance of the acetylation site at Tat Lys50 for inhibition of hSirt1. **A** Continuous coupled enzymatic assay with 1 μM fl-hSirt1 (pET32amod), 500 μM NAD⁺, 100 μM p53short, and Tat₄₆₋₅₄ or ac-Tat₄₆₋₅₄ ($n = 2$). **B** Fluor de Lys assay with 1 μM mini-Sirt1 or hSirt3-(93-399), 500 μM NAD⁺, *FdL-1* at the previously determined K_m (Figure 7.9), and titration of Tat₄₆₋₅₄ in presence of 15% (v/v) DMSO. $IC_{50} = 46.3 \pm 31.4$ μM for mini-Sirt1 and 40.0 ± 5.2 μM for hSirt3-(93-399) ($n = 3$). **C** Continuous coupled enzymatic assay with 1 μM mini-Sirt1, 500 μM NAD⁺, and titration ac-Tat₄₆₋₅₄. $K_m = 297.0 \pm 87.7$ μM ($n = 2$). **D** MST of 20 nM FITC-labeled mini-Sirt1 and titration of ac-Tat₄₆₋₅₄ or Tat₄₆₋₅₄ in presence of 10% (v/v) DMSO. The K_d was 13.9 ± 2.2 μM for ac-Tat₄₆₋₅₄ and 60.7 ± 5.5 μM for Tat₄₆₋₅₄ ($n = 2$). Settings: 25 °C, 12% LED power, and 20% MST power. K_d values were derived from thermophoresis.

Next, the exact binding site of ac-Tat₄₆₋₅₄ to hSirt1-3 was examined by crystallization. Cocrystallization of mini-Sirt1 with ac-Tat₄₆₋₅₄ and STAC afforded crystals the size of 350 μm and a structure was solved in space group $I4_122$ to 4.0 \AA resolution. However, the geometry of the structure could not be improved resulting in final R and R_{free} values of 34.6% and 38.5%. Although the acetylated Tat peptide appeared to bind in the substrate binding cleft, presence of ac-Tat₄₆₋₅₄ was doubted because the $2mF_o-DF_c$ density covered only parts of the peptide backbone and not a single sidechain. Since the diffraction quality of those crystals could not be improved, hSirt3 was cocrystallized with ac-Tat₄₆₋₅₄ to confirm the binding site. Several initial crystallization conditions for a hSirt3-(118-399)/ac-Tat₄₆₋₅₄ complex were identified (Table 7.7) with the best crystal diffracting to 1.65 \AA . The complex structure was solved in space group $C222_1$ and refined to final R and R_{free} values of 18.3% and 21.0% (Table 7.8). The overall structure of hSirt3-(118-399)/ac-Tat₄₆₋₅₄ represents a typical sirtuin/substrate complex and can be superimposed to a hSirt3/ac-ACS/carba-NAD complex with an RMSD = 0.327 \AA for 234 C_α atoms (Figure 4.32A), showing that the backbone and most sidechain positions of the ac-Tat₄₆₋₅₄ and the ac-ACS peptide overlay. A $2mF_o-DF_c$ composite omit map covers the complete Tat peptide including all sidechains except for Gln54 (Figure 4.32B). Due to the large number of arginines and lysines, the positively charged ac-Tat₄₆₋₅₄ has a strong affinity for the negatively charged residues in the hSirt3 substrate binding cleft (Figure 4.32C). Analysis of the binding mode of ac-Tat₄₆₋₅₄ with Ligplot⁺ ²⁵² reveals that hSirt3 forms twelve hydrogen bonds with the acetylated Tat peptide (Figure 4.32D). More specifically, seven sidechain hydrogen bonds are created between HIV1-Tat Ser46 and hSirt3 Leu298, between Arg49 and Gly295, between ac-Lys50 and Val292, between Arg52 and Glu181, and between Arg53 and Leu322 (Figure 4.32D). In addition, five backbone hydrogen bonds between Tat ac-Lys50 and hSirt3 Gly295/Glu296, between Lys51 and Glu325, and between Arg53 and Glu323, as well as 13 hydrophobic interactions complete a strong binding mode (Figure 4.32D).

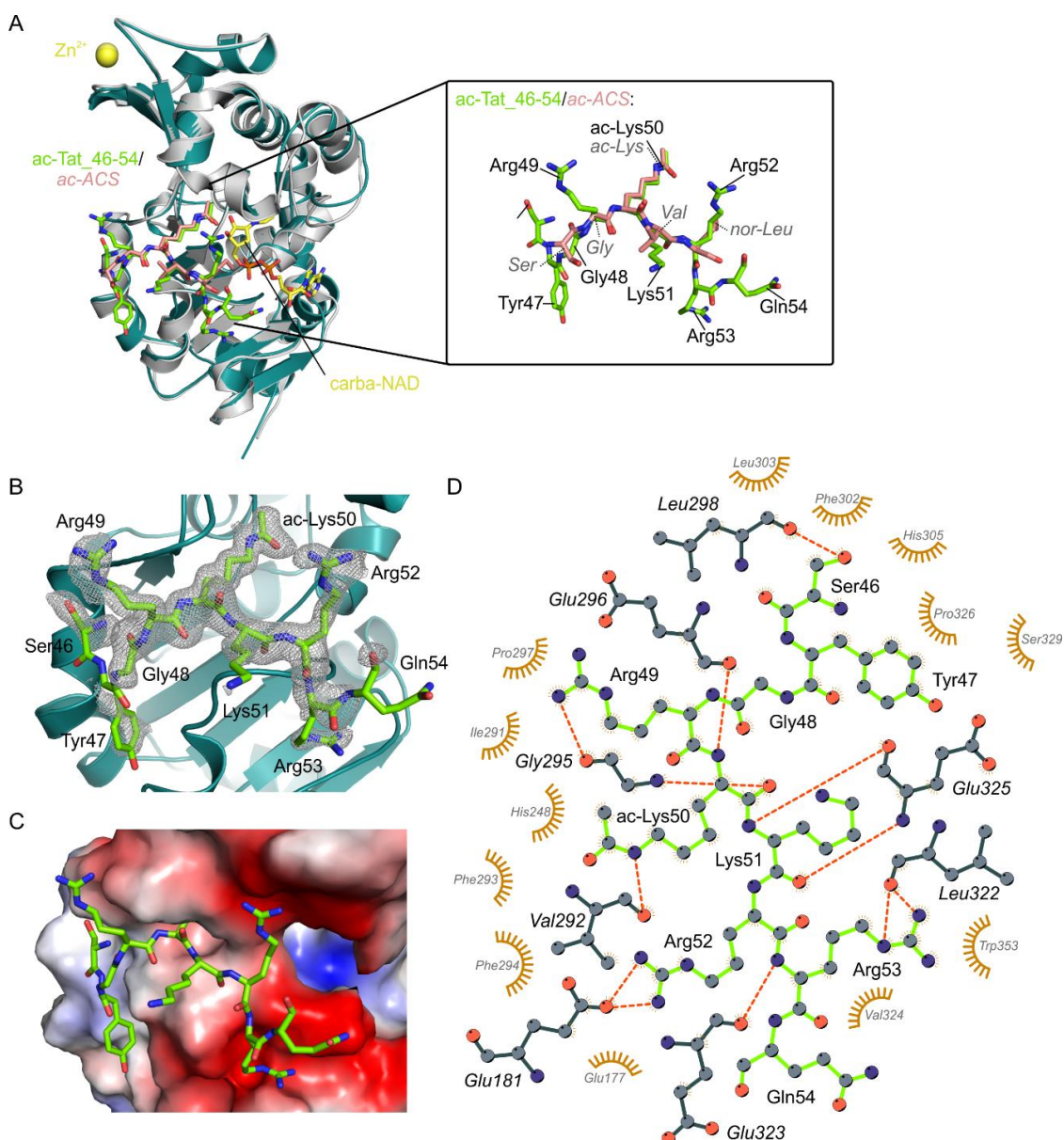


Figure 4.32: Complex structure of hSirt3-(118-399) with ac-Tat_46-54. **A** Superposition of the hSirt3-(118-399)/ac-Tat_46-54 complex (teal) with a hSirt3/ac-ACS/carba-NAD complex (PDB: 4FVT; white). The box highlights the bound substrate peptides ac-Tat_46-54 (lime) and ac-ACS (salmon). **B** Binding site of ac-Tat_46-54 (lime) in the hSirt3 complex (teal). The $2mF_o-DF_c$ composite omit map (contoured at 1σ) covers the complete ac-Tat_46-54 peptide. **C** Electrostatic surface representation of the binding site of ac-Tat_46-54 to hSirt3-(118-399) shown from -57.988 (red) to $+57.988$ (blue) kT/e . **D** Interacting amino acids of ac-Tat_46-54 with hSirt3-(118-399), shown by Ligplot⁺ ²⁵². Ac-Tat_46-54 forms twelve hydrogen bonds (red dotted lines) and diverse hydrophobic interactions (orange half circles) with hSirt3. The ac-Tat_46-54 peptide is shown with green bonds and normal lettered labels, whereas residues from hSirt3 (teal) are shown in *italics*.

For identifying putative interacting amino acids in hSirt1, the hSirt3-(118-399)/ac-Tat_46-54 complex was superimposed to a mini-Sirt1/STAC/p53/carba-NAD complex resulting in an RMSD = 1.177 Å for 208 C_α atoms (Figure 4.33A). Similar to the hSirt3/ac-ACS/carba-NAD complex (Figure 4.32A), the acetylated Tat peptide overlays with the backbone and most sidechain positions of the p53 substrate in the mini-Sirt1 complex (Figure 4.33A). Due to a similar composition and charge of both substrate peptides, this suggests that mini-Sirt1 binds ac-Tat_46-54 in the same mode as it binds p53. Indeed, removing the p53 peptide from the

mini-Sirt1 complex in Coot²⁴⁵ and replacing it with ac-Tat_46-54 reveals that the acetylated Tat peptide would be able to form diverse interactions with mini-Sirt1 strengthening its binding position (Figure 4.33B). Mini-Sirt1 and ac-Tat_46-54 thereby seem to interact via six sidechain hydrogen bonds, three backbone hydrogen bonds, and ten hydrophobic interactions (Figure 4.33B). Although the binding site in mini-Sirt1 needs to be confirmed, these comparisons together with the hSirt3-(118-399)/ac-Tat_46-54 complex demonstrate that acetylated HIV1-Tat as substrate for hSirt1-3 binds like other sirtuin substrates.

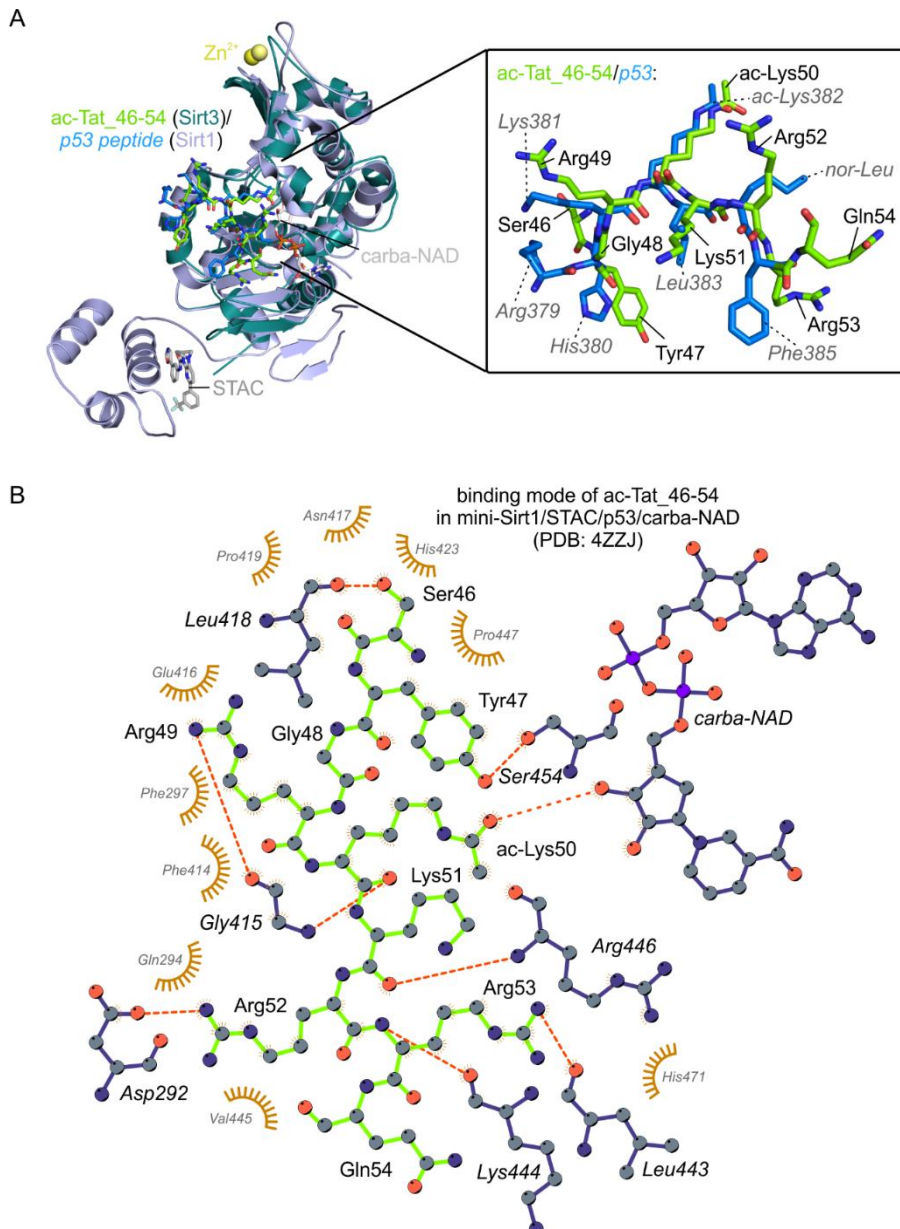


Figure 4.33: Mapping of the binding site of ac-Tat_46-54 in mini-Sirt1. **A** Superposition of the hSirt3-(118-399)/ac-Tat_46-54 complex (teal) with a mini-Sirt1/STAC/p53/carba-NAD complex (light blue; PDB: 4ZZJ). The box highlights the overlay of ac-Tat_46-54 (lime) and p53 peptide (marine blue). **B** Ligplot²⁵² presentation of the hypothetical interacting amino acids of ac-Tat_46-54 with mini-Sirt1. Hydrogen bonds are displayed as red dotted lines and hydrophobic interactions are depicted as orange half-circles. The ac-Tat_46-54 peptide is shown with green bonds and normal lettered labels, whereas residues from mini-Sirt1 and carba-NAD (both blue) are shown in *italics*.

4.4.5 Biochemical and structural characterization of the HIV1-Tat region necessary for inhibition of human Sirt1-3

As HIV1-Tat residues 21-63 appear to be relevant for inhibition of hSirt1-3 (Figure 4.30B, C) and in particular the region around Tat Lys50 might be critical (Figure 4.31B), further studies were performed with different synthetic peptides derived from HIV1-Tat (Table 3.1). In a continuous coupled enzymatic assay with the respective natural substrate peptides, Tat₃₁₋₆₀ was able to strongly inhibit hSirt1-3 (Figure 4.34A). Further peptides, which might be potent inhibitors of all three or single isoforms include Tat₂₀₋₃₀, Tat₃₄₋₅₄, Tat₃₄₋₅₉, Tat₃₅₋₄₄, and Tat₄₉₋₆₀ (Figure 4.34A). Since inhibition of mini-Sirt1 by synthetic Tat peptides was less potent in this particular assay than inhibition of hSirt2 and hSirt3 by the same peptides (Figure 4.34A), mini-Sirt1-inhibition was also investigated with the *Fluor de Lys* assay using an additional control reaction, where the respective Tat peptide was added after stopping the reaction (Figure 4.34B). The control reaction confirmed that none of the synthetic Tat peptides has any effect on the substrate fluorophore (Figure 4.34B). In addition, this assay showed that mini-Sirt1 can be inhibited by Tat₃₁₋₄₉, Tat₃₁₋₆₀, Tat₃₄₋₅₄, Tat₃₄₋₅₉, Tat₃₇₋₅₄, and Tat₄₉₋₆₀, while Tat₂₀₋₃₀ and Tat₃₅₋₄₄ do not seem to have an impact (Figure 4.34B). Both assays demonstrate that the region of HIV1-Tat residues 31-63 appears to be sufficient for inhibition of hSirt1-3.

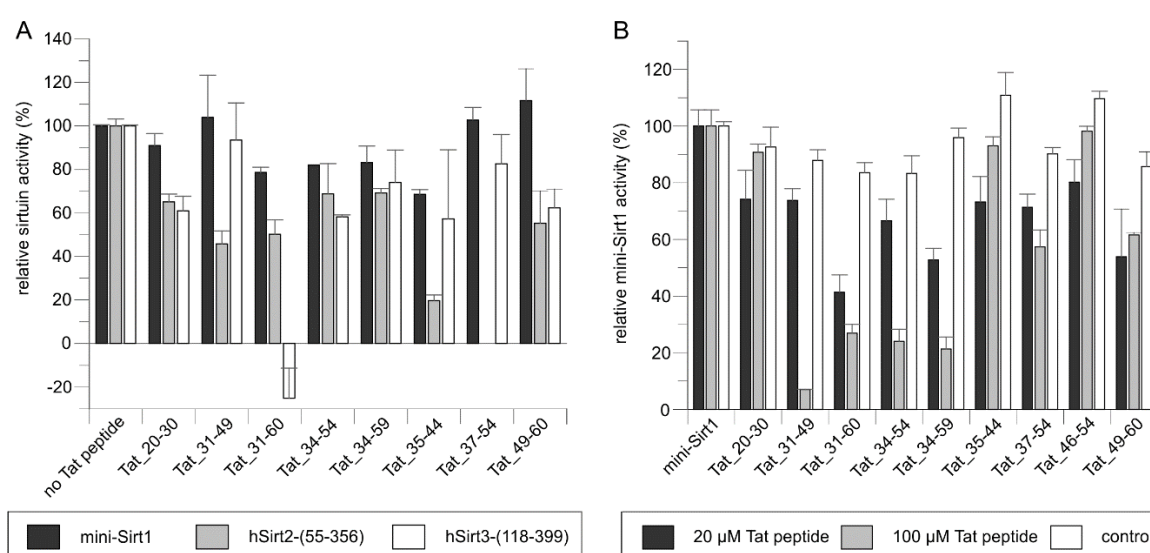


Figure 4.34: Inhibition of the deacetylase activity of hSirt1-3 by synthetic Tat peptides. **A** Continuous coupled enzymatic assay with 1 μ M sirtuin in presence of 500 μ M NAD⁺, substrate at half of the determined K_m (100 μ M p53short/ACS2.3, 50 μ M α -tubulin), and 100 μ M Tat peptides in 5% (v/v) DMSO ($n = 2$). **B** *Fluor de Lys* assay with 1 μ M mini-Sirt1, 500 μ M NAD⁺, 144 μ M *FdL-1* (Figure 7.9), and Tat peptides in 15% (v/v) DMSO or 20% (v/v) DMSO (only for Tat₃₄₋₅₄, Tat₃₄₋₅₉, and Tat₃₇₋₅₄) ($n = 3$).

Since the most potent inhibition of hSirt1-3 was achieved by Tat₃₁₋₆₀ and Tat₃₁₋₄₉ (Figure 4.34), their IC₅₀ for repression of mini-Sirt1 or hSirt3-(93-399) activity was evaluated with a *Fluor de Lys* assay (Figure 4.35A, B). Strikingly, the IC₅₀ for mini-Sirt1 inhibition by

Results

Tat₃₁₋₆₀ was $6.4 \pm 5.1 \mu\text{M}$ - almost equal to inhibition by Tat Cys⁻ - (Table 4.3), while the IC₅₀ for Tat₃₁₋₄₉ increased to $277.5 \pm 91.5 \mu\text{M}$ (Figure 4.35A). For hSirt3, this effect was not as pronounced as for mini-Sirt1 and Tat₃₁₋₆₀ suppressed hSirt3-(93-399) with an IC₅₀ of $44.3 \pm 7.7 \mu\text{M}$ compared to an IC₅₀ of $61.7 \pm 52.5 \mu\text{M}$ for Tat₃₁₋₄₉ (Figure 4.35B). In MST experiments, the K_d for Tat₃₁₋₆₀ to mini-Sirt1 amounted to $11.5 \pm 2.7 \mu\text{M}$ and the K_d for Tat₃₁₋₄₉ was $662.6 \pm 80.5 \mu\text{M}$ (Figure 4.35C, Table 4.4). Although binding was not saturated, these results indicate that HIV1-Tat residues 31-49 alone are not sufficient for potent inhibition of hSirt1. However, part of this region may be required for sirtuin inhibition.

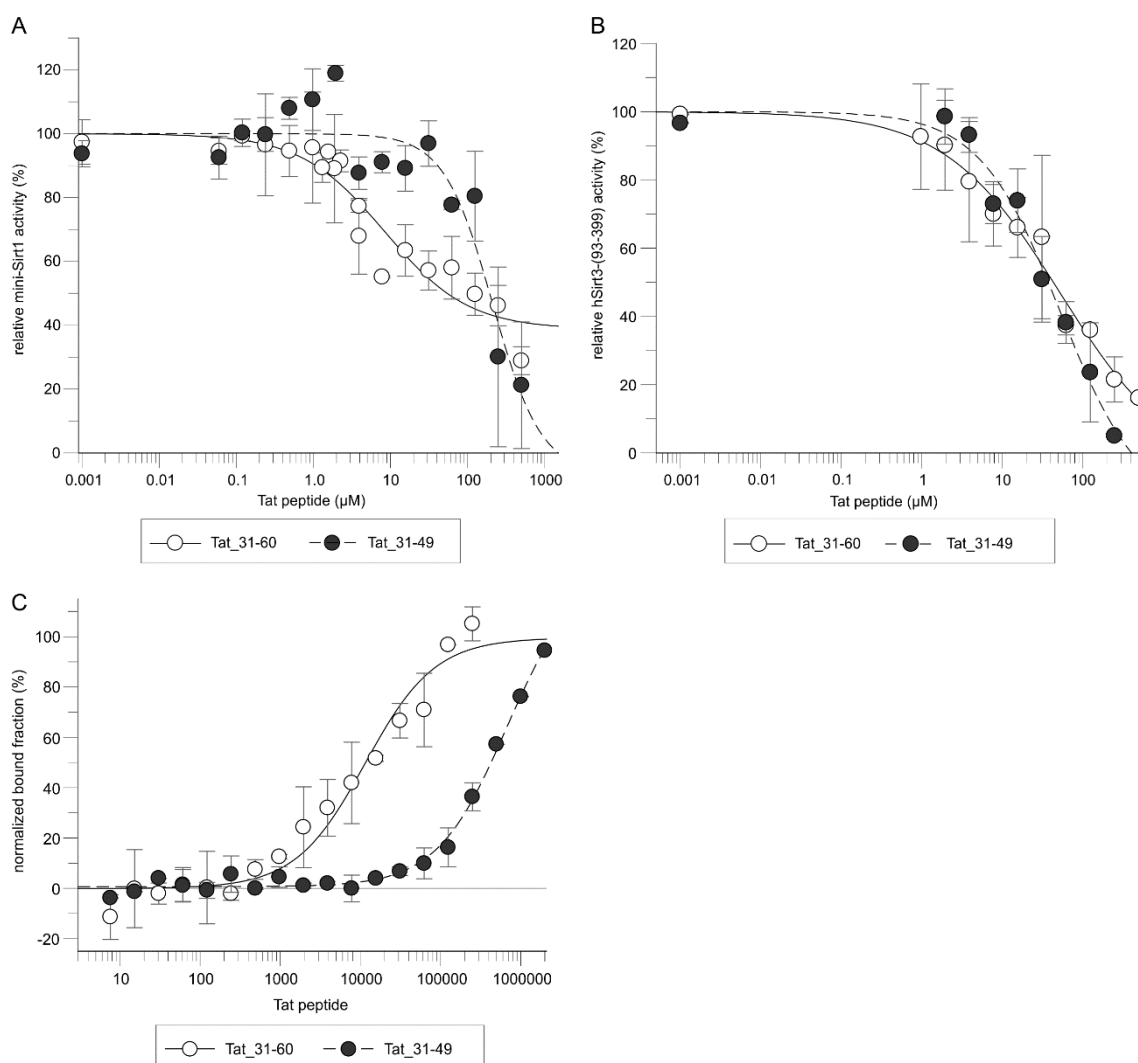


Figure 4.35: Inhibition of mini-Sirt1 and hSirt3 by Tat₃₁₋₄₉ and Tat₃₁₋₆₀. **A** Fluor de Lys assay with 1 μM mini-Sirt1, 500 μM NAD⁺, 144 μM *FdL-1* (Figure 7.9), and Tat₃₁₋₄₉ or Tat₃₁₋₆₀ in 15% (v/v) DMSO. The IC₅₀ was $277.5 \pm 91.5 \mu\text{M}$ for Tat₃₁₋₄₉ and $6.4 \pm 5.1 \mu\text{M}$ for Tat₃₁₋₆₀ ($n = 3$). **B** Fluor de Lys assay with 1 μM hSirt3-(93-399), 500 μM NAD⁺, 135 μM *FdL-1* (Figure 7.9), and Tat₃₁₋₄₉ or Tat₃₁₋₆₀ in 15% (v/v) DMSO. The IC₅₀ was $61.7 \pm 52.5 \mu\text{M}$ for Tat₃₁₋₄₉ and $44.3 \pm 7.7 \mu\text{M}$ for Tat₃₁₋₆₀ ($n = 3$). **C** MST of 20 nM FITC-labeled mini-Sirt1 with titration of Tat peptides in presence of 15% (v/v) DMSO. The K_d was $11.5 \pm 2.7 \mu\text{M}$ for Tat₃₁₋₆₀ and $662.6 \pm 80.5 \mu\text{M}$ for Tat₃₁₋₄₉ ($n = 2$). K_d values were derived from the initial fluorescence. Settings: 25 °C, 12% LED power, 20% MST power.

Therefore, the region of HIV1-Tat residues 31-60 was shortened from both ends and the IC₅₀ values for the resulting synthetic Tat peptides were evaluated with *Fluor de Lys* assays under 108

the same conditions. The N-terminally shortened Tat₃₄₋₅₉ was able to repress the deacetylase activity of mini-Sirt1 with an IC₅₀ of $2.6 \pm 1.0 \mu\text{M}$ (Figure 4.36A, Table 4.3). Further removal of N-terminal residues in Tat₃₇₋₅₉ did hardly change the potency for inhibition of mini-Sirt1 and resulted in an IC₅₀ of $4.5 \pm 0.6 \mu\text{M}$ (Figure 4.36A). However, removal of C-terminal amino acids in Tat₃₄₋₅₄ had a clear impact on the potency of mini-Sirt1 inhibition and yielded an IC₅₀ of $105.2 \pm 53.5 \mu\text{M}$ (Figure 4.36A). Therefore, the region of HIV1-Tat residues 55-59 seems to be critical for the inhibition potency and the inhibitory region was narrowed down again from the N-terminus. Finally, Tat₄₉₋₆₀ including Lys50 (Figure 4.31) was sufficient for inhibition of mini-Sirt1 with an IC₅₀ of $1.5 \pm 0.9 \mu\text{M}$, which is similar to the IC₅₀ for Tat Cys⁻ (Figure 4.36A, Table 4.3). However, Tat₃₇₋₅₉ and Tat₄₉₋₆₀ were lacking some efficacy since the residual mini-Sirt1 activity was higher than in presence of Tat Cys⁻ (Figure 4.28D) or Tat₃₁₋₆₀ (Figure 4.35A). The binding affinity of the two most potent peptides Tat₄₉₋₆₀ and Tat₃₄₋₅₉ for mini-Sirt1 was then investigated by MST. The longer peptide Tat₃₄₋₅₉ had a K_d of $46.2 \pm 15.3 \mu\text{M}$, whereas Tat₄₉₋₆₀ bound with a K_d of $1.76 \pm 0.59 \mu\text{M}$ (Figure 4.36B, Table 4.4). These results suggest that the region of HIV1-Tat amino acids 49-60 is the relevant region for binding and inhibiting mini-Sirt1 *in vitro*.

Next, selected Tat peptides were examined for their inhibition potency on fl-hSirt1, hSirt2, and hSirt3. In contrast to mini-Sirt1, fl-hSirt1 was preferably repressed by Tat₃₄₋₅₉ over Tat₄₉₋₆₀ (Figure 4.36C). In particular, the IC₅₀ values for both peptides were 3-4-fold increased compared to Tat Cys⁻ (Table 4.3) and resulted in $9.8 \pm 5.4 \mu\text{M}$ for Tat₃₄₋₅₉ and $14.3 \pm 8.7 \mu\text{M}$ for Tat₄₉₋₆₀ (Figure 4.36C). The same behavior occurred for hSirt2-(43-356), whereby Tat₃₄₋₅₉ had an IC₅₀ of $46.4 \pm 33.2 \mu\text{M}$ and Tat₄₉₋₆₀ inhibited hSirt2 with an IC₅₀ of $69.6 \pm 31.0 \mu\text{M}$ (Figure 4.36D) compared to the initially higher IC₅₀ of $12 \mu\text{M}$ for Tat Cys⁻ (Table 4.3). On the contrary, the results for hSirt3 rather reflect the inhibitory effect of Tat on mini-Sirt1. In this case, Tat₄₉₋₆₀ was sufficient to repress hSirt3-(93-399) with an IC₅₀ of $19.3 \pm 11.2 \mu\text{M}$ (Figure 4.36E) - almost equal to the IC₅₀ of Tat Cys⁻ for hSirt3 (Table 4.3). The longer peptides Tat₃₄₋₅₉ and Tat₃₄₋₅₄ inhibited hSirt3-(93-399) with IC₅₀ values of $37.7 \pm 19.4 \mu\text{M}$ and $29.7 \pm 7.9 \mu\text{M}$, respectively (Figure 4.36E). Concerning the region of HIV1-Tat necessary for inhibition of the deacetylase activity of human Sirt1-3, Tat residues 34-59 appear to be able to strongly and efficiently suppress all human sirtuin isoforms with IC₅₀ values almost equal to the respective ones for Tat Cys⁻.

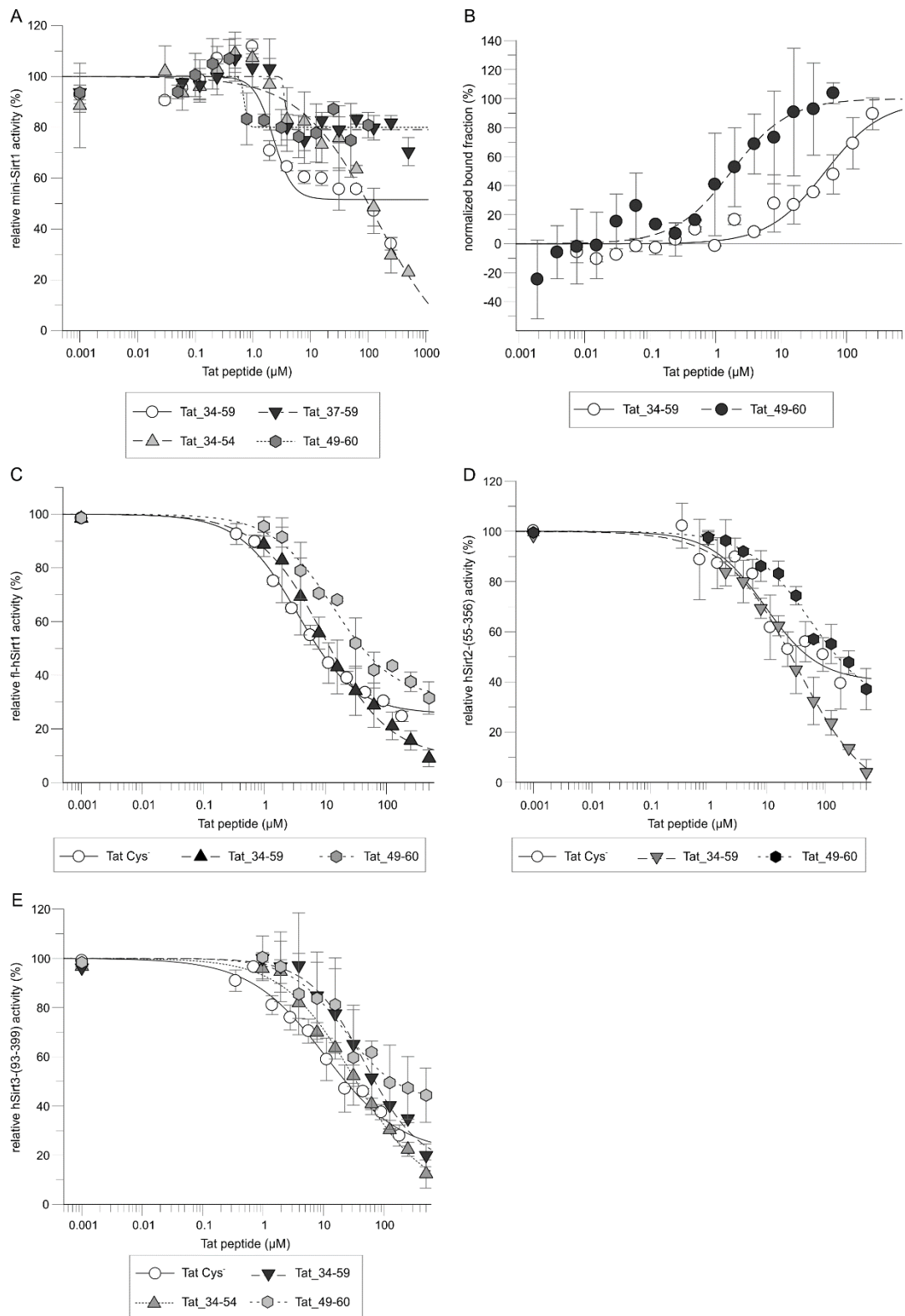


Figure 4.36: Inhibition of hSirt1-3 by Tat peptides derived from the HIV1-Tat region 31-60. **A** Inhibition of mini-Sirt1 with an IC_{50} of $2.6 \pm 1.0 \mu\text{M}$ for Tat₃₄₋₅₉, $4.5 \pm 0.6 \mu\text{M}$ for Tat₃₇₋₅₉, $105.2 \pm 53.5 \mu\text{M}$ for Tat₃₄₋₅₄, and $1.5 \pm 0.9 \mu\text{M}$ for Tat₄₉₋₆₀. **B** MST of 20 nM FITC-labeled mini-Sirt1. Settings: 25 °C, 12% LED, and 20% MST. The K_d was derived from the initial fluorescence and resulted in $46.2 \pm 15.3 \mu\text{M}$ for Tat₃₄₋₅₉ and $1.76 \pm 0.59 \mu\text{M}$ for Tat₄₉₋₆₀. **C** Inhibition of fl-hSirt1 with an IC_{50} of $9.8 \pm 5.4 \mu\text{M}$ for Tat₃₄₋₅₉ and $14.3 \pm 8.7 \mu\text{M}$ for Tat₄₉₋₆₀. **D** Inhibition of hSirt2-(43-356) with an IC_{50} of $46.4 \pm 33.2 \mu\text{M}$ for Tat₃₄₋₅₉ and $69.6 \pm 31.0 \mu\text{M}$ for Tat₄₉₋₆₀. **E** Inhibition of hSirt3-(93-399) with an IC_{50} of $29.7 \pm 7.9 \mu\text{M}$ for Tat₃₄₋₅₄, $37.7 \pm 19.4 \mu\text{M}$ for Tat₃₄₋₅₉, and $19.3 \pm 11.2 \mu\text{M}$ for Tat₄₉₋₆₀. **A-E** Tat peptides were added in 15% (v/v) DMSO (Tat₃₇₋₅₉, Tat₄₉₋₆₀) or 20% (v/v) DMSO (Tat₃₄₋₅₄, Tat₃₄₋₅₉). *Fluor de Lys* assays ($n = 3$) were performed with 1 μM sirtuin, 500 μM NAD^+ , and *FdL-1* at the previously determined K_m values (Figure 7.9).

Table 4.3: Inhibition of hSirt1-3 by synthetic peptides derived from HIV1-Tat. IC₅₀ values ($n > 3$) were determined in the *Fluor de Lys* assay with 1 μ M sirtuin, 500 μ M NAD⁺, and *FdL-1* at the respective K_m (Figure 7.9). The Tat peptides were titrated in presence of 15% (v/v) DMSO or 20% (v/v) DMSO (only for Tat₃₄₋₅₄, Tat₃₄₋₅₉). The values for inhibition of hSirt1-3 by Tat Cys⁻ (without DMSO) are given as comparison (Figure 4.29C). Abbreviations: *n. d.* - not determined.

Tat peptide	IC ₅₀ for mini-Sirt1 (μ M)	IC ₅₀ for fl-hSirt1 (μ M)	IC ₅₀ for hSirt2-(43-356) (μ M)	IC ₅₀ for hSirt3-(93-399) (μ M)
Tat Cys ⁻	2.3 \pm 0.9	3.6 \pm 0.8	11.0 \pm 4.4	12.1 \pm 4.2
Tat ₃₁₋₄₉	277.5 \pm 91.5	<i>n. d.</i>	<i>n. d.</i>	61.7 \pm 52.5
Tat ₃₁₋₆₀	6.4 \pm 5.1	<i>n. d.</i>	<i>n. d.</i>	44.3 \pm 7.7
Tat ₃₄₋₅₄	105.2 \pm 53.5	<i>n. d.</i>	<i>n. d.</i>	29.7 \pm 7.9
Tat ₃₄₋₅₉	2.6 \pm 1.0	9.8 \pm 5.4	46.4 \pm 33.2	37.7 \pm 19.4
Tat ₃₇₋₅₉	4.5 \pm 0.6	<i>n. d.</i>	<i>n. d.</i>	<i>n. d.</i>
Tat ₄₆₋₅₄	46.3 \pm 31.4	<i>n. d.</i>	<i>n. d.</i>	40.0 \pm 5.2
Tat ₄₉₋₆₀	1.5 \pm 0.9	14.3 \pm 8.7	69.6 \pm 31.0	19.3 \pm 11.2

Table 4.4: Binding affinity of synthetic Tat peptides for mini-Sirt1. K_d values ($n = 2$) were derived from MST at 25 °C and 12% LED power. Tat peptides were added in 15% (v/v) DMSO or 20% (v/v) DMSO (only for Tat₃₄₋₅₉). For determination of the K_d of Tat Cys⁻ for mini-Sirt1 (Fig. 4.33B), DMSO was omitted.

Tat peptide	K _d for mini-Sirt1 (μ M)	Labeled protein (μ M)	MST power (%)	K _d analysis method
Tat Cys ⁻	1.8 \pm 0.5	0.040 μ M Tat Cys ⁻	30	initial fluorescence
Tat ₃₁₋₄₉	662.6 \pm 80.5	0.020 μ M mini-Sirt1	20	initial fluorescence
Tat ₃₁₋₆₀	11.5 \pm 2.7	0.020 μ M mini-Sirt1	20	initial fluorescence
Tat ₃₄₋₅₉	46.2 \pm 15.3	0.020 μ M mini-Sirt1	20	initial fluorescence
Tat ₄₆₋₅₄	60.7 \pm 5.4	0.020 μ M mini-Sirt1	20	thermophoresis
Tat ₄₉₋₆₀	1.8 \pm 0.6	0.020 μ M mini-Sirt1	20	initial fluorescence

For confirming the sirtuin-inhibiting region of HIV1-Tat, crystallographic studies were performed with the crystallization constructs mini-Sirt1, hSirt2-(55-356), and hSirt3-(118-399) using the most efficient peptides Tat₃₄₋₅₉, Tat₃₇₋₅₉, and Tat₄₉₋₆₀. Mini-Sirt1 and hSirt2-(55-356) crystallized only in presence of Tat₄₉₋₆₀, but the solved structures did not contain Tat. In case of mini-Sirt1, the best crystal diffracted to 2.3 Å and was solved in space group C222₁ to final R and R_{free} values of 23.8% and 30.5% revealing a new crystallization condition for apo mini-Sirt1 (Table 7.4), where a PEG molecule was bound at the acetyl-Lys site. In case of hSirt2-(55-356), a crystal obtained in presence of Tat₄₉₋₆₀ and ADPr diffracted to 2.48 Å resolution and was solved in space group P2₁2₁2₁ to final R and R_{free} values of 18.6% and 21.6%. However, the substrate binding cleft, in which Tat₄₉₋₆₀ was expected, was occupied by a loop from the adjacent hSirt2-(55-356) molecule, which had already been observed in that specific crystallization condition previously²⁶⁴.

In contrast, hSirt3-(118-399) crystallized with various inhibiting Tat peptides and under different conditions (Table 7.7). The best crystal for a hSirt3-(118-399)/Tat₃₄₋₅₉ complex diffracted to 2.15 Å and was refined in space group P2₁ to final R and R_{free} values of 19.5% and 24.0% (Table 7.9). The complex structure reveals that Tat₃₄₋₅₉ binds in the substrate binding cleft and further wraps around hSirt3 (Figure 4.37A). Superposition of the hSirt3-(118-399)/Tat₃₄₋₅₉ complex with the previously described hSirt3-(118-399)/ac-Tat₄₆₋₅₄ complex results in an RMSD = 0.270 Å for 246 C_α atoms (Figure 4.37A). The superposition of the Tat₃₄₋₅₉ and ac-Tat₄₆₋₅₄ peptides shows that the backbone and sidechain positions of HIV1-Tat residues 49-53 overlap exactly (Figure 4.37B). Due to the inherent flexibility of Tat (Figure 4.27B), only residues 45-57 of Tat₃₄₋₅₉ are visible in a 2mF_o-DF_c composite omit map (Figure 4.37C).

The residues of hSirt3 and Tat₃₄₋₅₉, which are involved in the interaction, were analyzed with Ligplot⁺²⁵²: Tat₃₄₋₅₉ is able to form five sidechain hydrogen bonds between Tat Lys50 and hSirt3 Val292, between Arg52 and Glu177/Glu181, and between Arg53 and Leu322 (Figure 4.37D). In addition, five backbone hydrogen bonds are created between Tat Lys50 and hSirt3 Gly295/Glu296, between Lys51 and Glu325, and between Arg53 and Glu323 (Figure 4.37D). Further fourteen hydrophobic interactions complete a strong binding mode of Tat₃₄₋₅₉ (Figure 4.37D). Interestingly, among those interactions are also two hydrogen bonds of Tat Arg52 with Val258 and Gln260 of the second hSirt3 molecule in the asymmetric unit as well as two hydrophobic interactions mediated by Thr255 and Gln300 of this hSirt3 molecule (Figure 4.37D). The hSirt3 residues involved are located at the center of the zinc-binding domain of hSirt3. To elucidate whether these interactions play a role in nature or are merely a result of crystal packing, the structure was analyzed with the PDBe PISA server²⁶², revealing that only assembly of the interface between hSirt3 chain A and Tat₃₄₋₅₉ chain C is assessed as significant according to a CSS = 1.0 and $\Delta G^{\text{int}} = -3.5$ kcal/mol (Table 4.5). Therefore, the PISA analysis suggests that the two additional hydrogen bonds from Tat Arg52 to the second hSirt3 molecule are caused by crystal packing (Table 4.5).

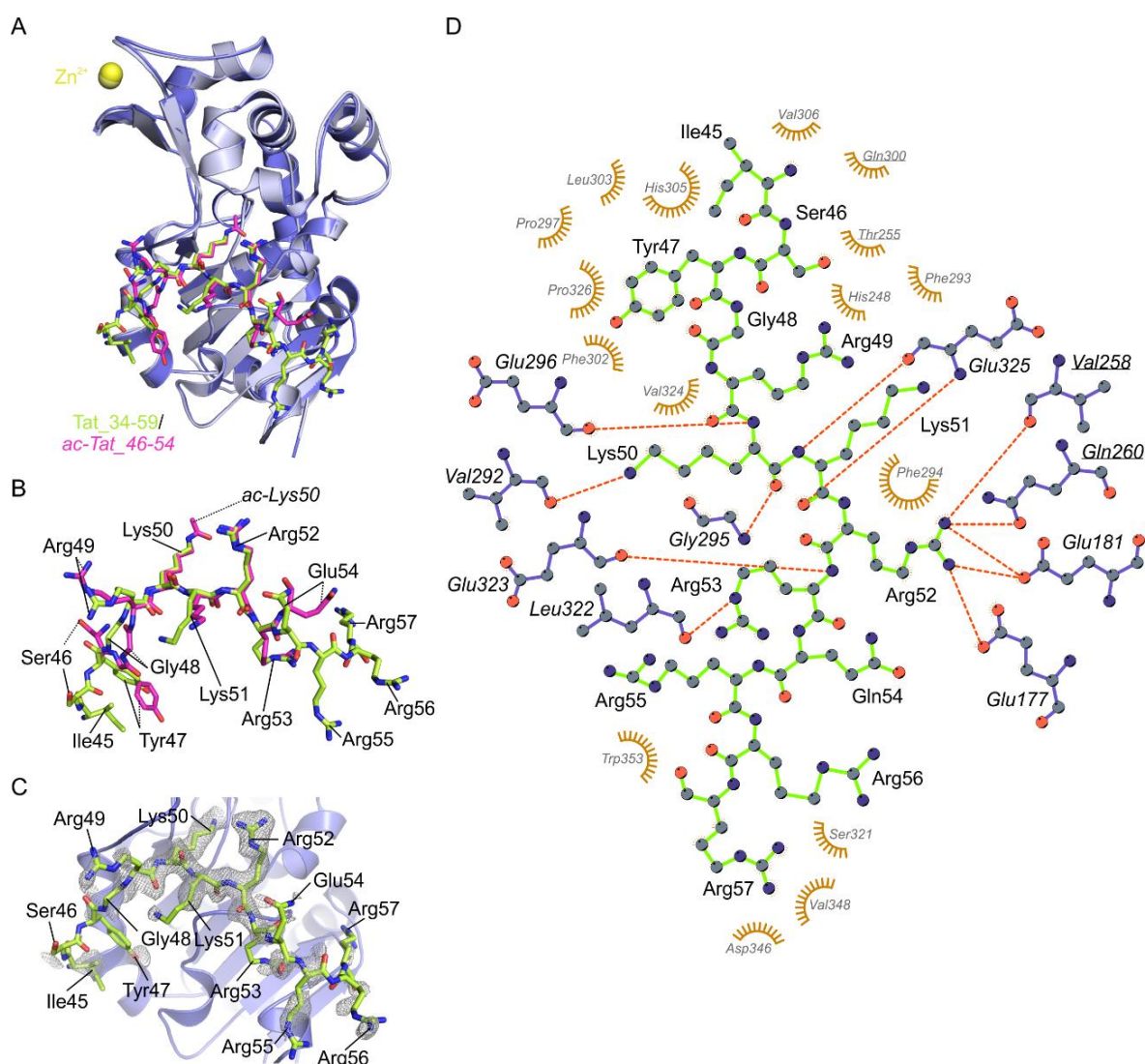


Figure 4.37: Structure of hSirt3-(118-399) in complex with Tat₃₄₋₅₉. **A** Superposition of the hSirt3-(118-399)/Tat₃₄₋₅₉ complex (blue) with the hSirt3-(118-399)/ac-Tat₄₆₋₅₄ complex (light blue). **B** Highlight of the superposition of the Tat₃₄₋₅₉ peptide (lime) and the ac-Tat₄₆₋₅₄ peptide (pink). **C** 2mF_o-DF_c composite omit map of the Tat₃₄₋₅₉ peptide (lime) contoured at 1 σ . **D** Interacting amino acids of Tat₃₄₋₅₉ with hSirt3-(118-399) as analyzed by Ligplot⁺ ²⁵². Tat₃₄₋₅₉ forms ten hydrogen bonds (red dotted lines) and several hydrophobic interactions (orange half circles) with hSirt3. Tat₃₄₋₅₉ is shown with green bonds and normal lettered labels, whereas residues from hSirt3 (blue) are shown in *italics* and residues from the other hSirt3 molecule in the asymmetric unit are *underlined in italics*.

Table 4.5: Analysis of interfaces in the hSirt3-(118-399)/Tat₃₄₋₅₉ complex by PDBE PISA ²⁶². HSirt3-(118-399) is depicted by A and B and Tat₃₄₋₅₉ by C and D. Abbreviations: HB - hydrogen bonds, SB - salt bridges, ΔG^{int} - solvation free energy gain upon interfacing, ΔG^{diss} - free energy of assembly dissociation, *n. a.* - not available, CSS - complexation significance score.

Interaction interface	Symmetry operation for assembly	Interaction surface (\AA^2)	HB	SB	ΔG^{int} (kcal/mol)	ΔG^{diss} (kcal/mol)	CSS
AC	x, y, z	858.8	12	5	-3.5	0.8	1.000
BD	x, y, z	748.8	9	3	-1.6	<i>n. a.</i>	0.000
AD	x, y, z	192.9	2	0	1.6	<i>n. a.</i>	0.000
BC	x, y, z	185.9	2	0	-0.1	<i>n. a.</i>	0.000

Since the hSirt3-(118-399)/Tat_34-59 complex did not show electron density for all residues of the Tat peptide, hSirt3 was also cocrystallized with Tat_37-59 to reduce part of the terminal flexibility of Tat. The best crystal for a hSirt3-(118-399)/Tat_37-59 complex diffracted to 1.95 Å (Table 7.7) and the structure was solved in space group $P2_1$ to final R and R_{free} values of 22.1% and 27.0% (Table 7.9). The overall structure is similar to the hSirt3-(118-399)/Tat_34-59 complex and can be superimposed with an RMSD = 0.943 Å for 534 C_{α} atoms (Figure 4.38A). A focus on the Tat_34-59 and Tat_37-59 peptides shows that they differ in their arrangement of N-terminal amino acids 45-46 and C-terminal amino acids 56-57 (Figure 4.38A). However, a $2mF_o-DF_c$ composite omit map validates the binding mode of Tat_37-59 in the hSirt3-(118-399)/Tat_37-59 complex and covers HIV1-Tat residues 44-57 including most sidechains (Figure 4.38B). The small differences in the location of the terminal residues of both inhibiting Tat peptides are thus thought to derive from the local molecular surroundings of the respective crystal packing. Analysis of the interactions between Tat_37-59 and hSirt3 reveals that six sidechain hydrogen bonds, five backbone hydrogen bonds, and twelve hydrophobic interactions are formed (Figure 4.38C). In particular, sidechain hydrogen bonds are created between Tat Arg49 and hSirt3 Gly295, between Lys50 and Val292, between Arg52 and Glu177/Glu181, and between Arg56 and Leu347, whereas backbone hydrogen bonds are formed between Tat Lys50 and hSirt3 Gly295/Glu296, between Lys51 and Glu325, and between Arg53 and Glu323 (Figure 4.38C). In other words, the hSirt3-(118-399)/Tat_37-59 structure differs from the Tat_34-59 complex by formation of two additional sidechain hydrogen bonds between Tat Arg49 and hSirt3 Gly295 as well as between Tat Arg56 and hSirt3 Leu347 (Figure 4.38C), while the hSirt3-(118-399)/Tat_34-59 structure shows another sidechain hydrogen bond between Tat Arg53 and hSirt3 Leu322 (Figure 4.37D). Mapping of the hydrogen bonds between Tat_37-59 and hSirt3 in the structure shows that Tat amino acids 49-53, which are located in the center of the hSirt3 substrate binding cleft, mediate most interactions (Figure 4.38D). But the C-terminal amino acids 54-57 of HIV1-Tat, which bind closer to the bottom of the hSirt3 NAD^+ -binding domain, are also able to form interactions (Figure 4.38D).

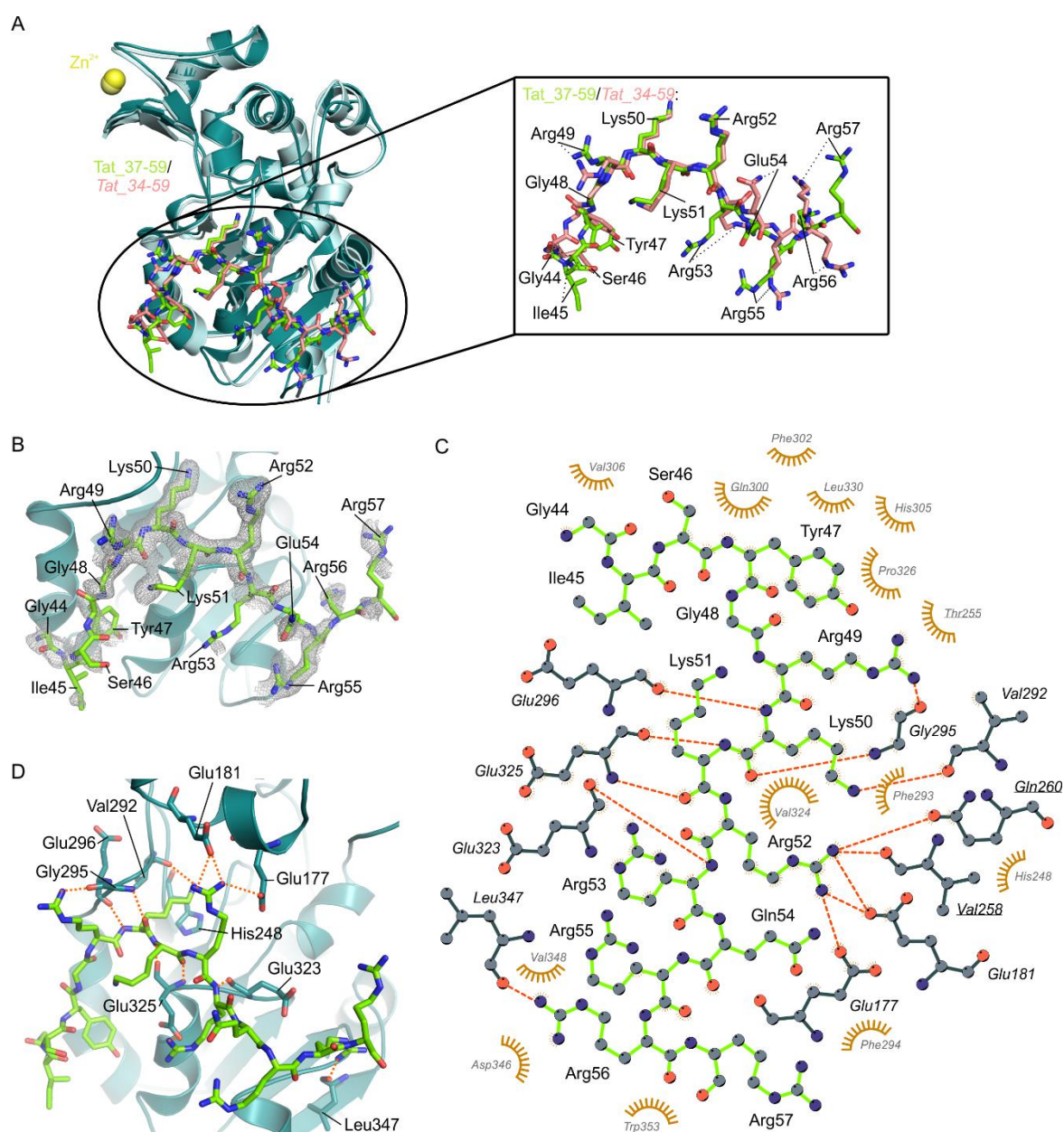


Figure 4.38: Structure of hSirt3-(118-399) in complex with Tat₃₇₋₅₉. **A** Superposition of the hSirt3-(118-399)/Tat₃₇₋₅₉ complex (teal) with the hSirt3-(118-399)/Tat₃₄₋₅₉ complex (light cyan). The box highlights the superposition of the Tat₃₇₋₅₉ peptide (lime) and the Tat₃₄₋₅₉ peptide (salmon). **B** 2mF_o-DF_c composite omit map of the Tat₃₇₋₅₉ peptide (lime) contoured at 1 σ . **C** Ligplot⁺²⁵² presentation of the interacting amino acids of Tat₃₇₋₅₉ with hSirt3-(118-399). Tat₃₇₋₅₉ forms eleven hydrogen bonds (red dotted lines) and several hydrophobic interactions (orange half-circles) with hSirt3. Tat₃₇₋₅₉ is shown with green bonds and normal lettered labels, whereas residues from hSirt3 (teal) are shown in *italics* and residues from the other hSirt3 molecule in the asymmetric unit are underlined in italics. **D** Visualization of the hydrogen bonds between Tat₃₇₋₅₉ (lime) and hSirt3 (teal).

In the hSirt3-(118-399)/Tat₃₇₋₅₉ structure, the two hydrogen bonds from Tat Arg52 to the Val258/Gln260 of the adjacent hSirt3 molecule and the hydrophobic interactions of hSirt3 Thr255 and Gln300 are also pronounced (Figure 4.38C). But analysis with the PDBE PISA server²⁶² suggests that these interactions are the result of the crystal packing according to a low CSS and a positive ΔG^{int} (Table 4.6). In this structure, both hSirt3/Tat₃₇₋₅₉ assemblies in the asymmetric unit receive the highest CSS = 1.0 and differ only slightly in the number of

hydrogen bonds and salt bridges as well as the solvation free energy gain upon complexation (Table 4.6). Notably, the asymmetric unit of this crystal would support stable complexation of a hSirt3 dimer with or without the two bound Tat₃₇₋₅₉ peptides (Table 4.6). There is no experimental evidence, however, that hSirt3 and Tat might actually form a hetero-tetramer in solution. In summary, both hSirt3 structures with inhibiting Tat peptides appear to be equal and demonstrate that deacetylated HIV1-Tat binds like its acetylated counterpart into the sirtuin substrate binding cleft to inhibit the deacetylase activity of hSirt1-3.

Table 4.6: Analysis of interfaces in the hSirt3-(118-399)/Tat₃₇₋₅₉ complex by PDBe PISA²⁶². HSirt3-(118-399) is depicted by A and B and Tat₃₇₋₅₉ by C and D. Abbreviations: HB - hydrogen bonds, SB - salt bridges, ΔG^{int} - solvation free energy gain upon interfacing, ΔG^{diss} - free energy of assembly dissociation, *n. a.* - not available, CSS - complexation significance score.

Interaction interface	Symmetry operation for assembly	Interaction surface (Å ²)	HB	SB	ΔG^{int} (kcal/mol)	ΔG^{diss} (kcal/mol)	CSS
AC	x, y, z	820.5	13	6	-3.2	1.1	1.000
BD	x, y, z	742.3	11	5	-5.2	2.2	1.000
AB	x, y, z	506.7	0	0	-9.9	<i>n. a.</i>	0.296
AD	x, y, z	217.6	6	1	1.8	<i>n. a.</i>	0.030
BC	x, y, z	225.2	7	1	1.6	<i>n. a.</i>	0.050
ABCD	x, y, z	5024.5	37	13	-14.9	0.6	<i>n. a.</i>

Since the hSirt3-(118-399)/Tat₃₇₋₅₉ structure displays more residues of HIV1-Tat with better density coverage (Figure 4.38B) and more pronounced interactions (Figure 4.38C) than the hSirt3 complex with Tat₃₄₋₅₉ (Figure 4.37C, D), this structure will be used for the following comparisons to hSirt1. Superposition of hSirt3-(118-399)/Tat₃₇₋₅₉ with a mini-Sirt1/STAC/p53/carba-NAD complex (PDB: 4ZZJ) results in an RMSD = 1.199 Å for 210 C_α atoms (Figure 4.39A). As expected, the inhibiting Tat peptide binds similar to the acetylated p53 peptide (Figure 4.39A), which is also supported by their charge composition matching the negatively charged substrate binding cleft (Figure 4.32C). Putative interacting amino acids between mini-Sirt1 and Tat₃₇₋₅₉ were analyzed with PyMOL²⁴⁹ (Figure 4.39B): hydrogen bond pairs are apparently formed between Tat Arg49/Lys50 and mini-Sirt1 Gly415/Glu416 (Figure 4.39B) similar to their interaction with hSirt3 Gly295/Glu296 (Figure 4.38D). In addition, Tat Arg52 seems to be connected via a hydrogen bond to mini-Sirt1 Asp292 (Figure 4.39B), which might replace the hydrogen bonds to Glu177/Glu181 in hSirt3 (Figure 4.38D). The C-terminal part of the Tat₃₇₋₅₉ backbone might form three further hydrogen bonds between Tat Lys51 and mini-Sirt1 Arg446, between Arg53 and Lys444, and between Arg56 and Pro468 (Figure 4.39B). Notably, mini-Sirt1 Arg446 is involved in a salt bridge to Glu230 in the SBD⁹⁷. As mini-Sirt1 mediates these interactions via the peptide

bond (Figure 4.39B), the hydrogen bonds seem to be the equivalent to the ones mediated by hSirt3 Glu325, Glu323, and Leu347 to the respective HIV1-Tat amino acids (Figure 4.38D). This comparison of the binding mode of Tat₃₇₋₅₉ to hSirt3 and mini-Sirt1 shows that HIV1-Tat most likely binds equally to mini-Sirt1 and thus, the hSirt3-(118-399)/Tat₃₇₋₅₉ structure is a good model.

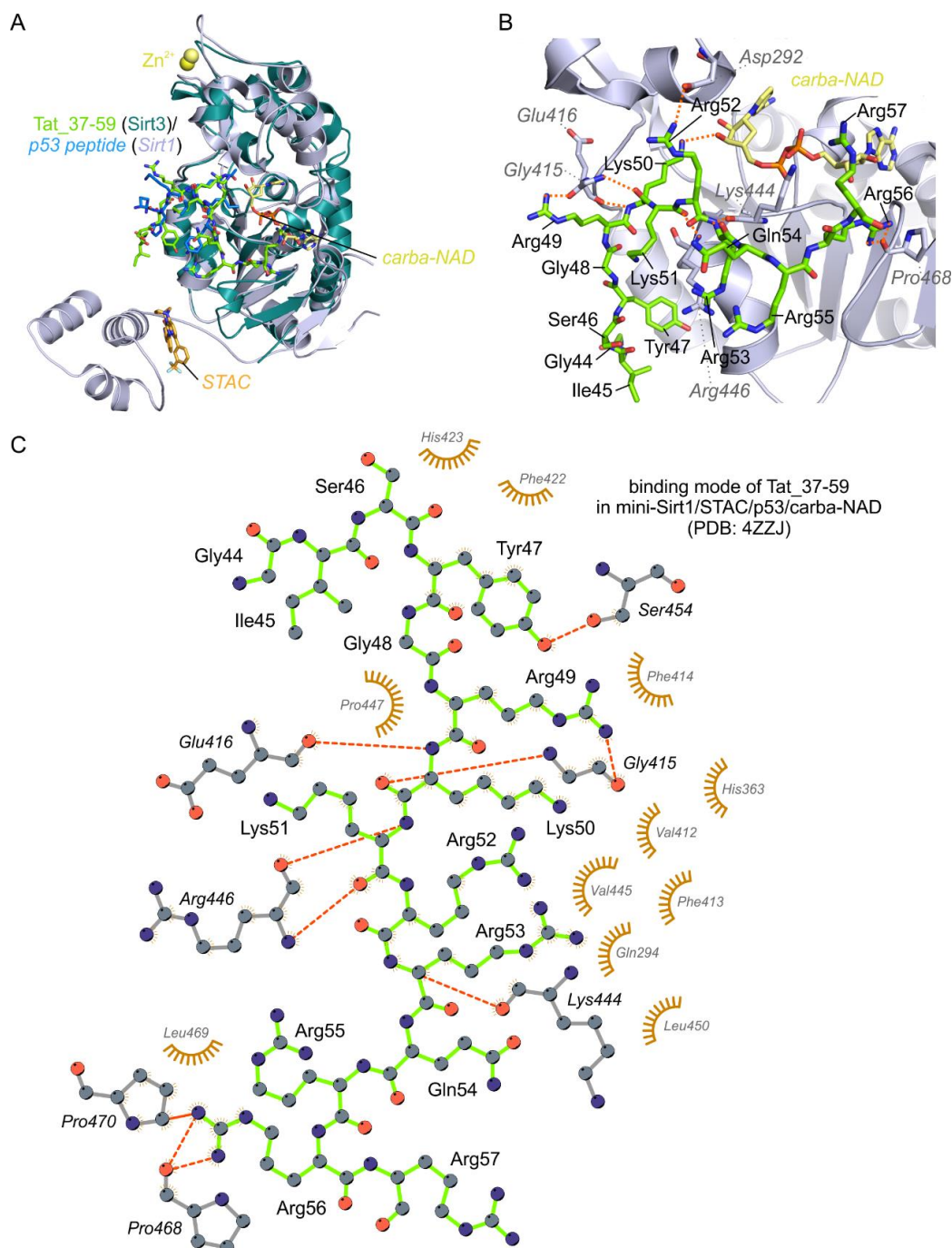


Figure 4.39: Mapping of the binding site of Tat₃₇₋₅₉ in mini-Sirt1/STAC/p53/carba-NAD. **A** Superposition of the hSirt3-(118-399)/Tat₃₇₋₅₉ complex (teal) with a mini-Sirt1/STAC/p53/carba-NAD complex (grey; PDB: 4ZZJ). **B** Hydrogen bonds between Tat₃₇₋₅₉ (lime) and mini-Sirt1 (grey) as suggested by PyMOL²⁴⁹. **C** Ligplot⁺²⁵² presentation of the hypothetical interacting amino acids of Tat₃₇₋₅₉ with mini-Sirt1. Tat₃₇₋₅₉ might be able to form ten hydrogen bonds (red dotted lines) and eleven hydrophobic interactions (orange half-circles) with mini-Sirt1. Tat₃₇₋₅₉ is shown with green bonds and normal lettered labels, whereas residues from mini-Sirt1 (grey) are shown in *italics*.

For a more detailed analysis with Ligplot⁺ ²⁵², the p53 peptide was removed from the mini-Sirt1 complex in Coot ²⁴⁵ and replaced by Tat₃₇₋₅₉ (Figure 4.39C). Besides an additional eleven hydrophobic interactions between Tat₃₇₋₅₉ and mini-Sirt1, Ligplot⁺ ²⁵² shows two further putative sidechain hydrogen bonds between Tat Tyr47 and mini-Sirt1 Ser454 and between Arg56 and Pro470 (Figure 4.39C). However, in both comparisons of the binding mode of Tat₃₇₋₅₉ in the mini-Sirt1/STAC/p53/carba-NAD complex (Figure 4.39B, C), HIV1-Tat is lacking additional specific interactions between its C-terminal amino acids 53-59 and mini-Sirt1. Such interactions would have been expected due to the more potent inhibition of mini-Sirt1 by Tat peptides including these residues (Table 4.3). Since the Sirt1 SBD is a flexible domain, which is turned away from the Sirt1 catalytic core in the mini-Sirt1/STAC/p53/carba-NAD structure, the binding mode of Tat₃₇₋₅₉ was also compared to a another mini-Sirt1/substrate complex containing *FdL-1* and resveratrol (PDB: 5BTR). Superposition of hSirt3-(118-399)/Tat₃₇₋₅₉ to this latter structure results in an RMSD = 1.053 Å for 207 C_α atoms and shows the SBD in much closer vicinity to the substrate binding cleft with the binding site of Tat (Figure 4.40A).

Analysis of putative interactions with mini-Sirt1 in PyMOL ²⁴⁹ validates that Tat₃₇₋₅₉ seems to form the same hydrogen bonds to mini-Sirt1 Gly415, Glu416, Lys444, and Pro468 (Figure 4.40B) as already indicated from comparison to the mini-Sirt1/STAC/p53/carba-NAD complex (Figure 4.39B). But surprisingly, the closer location of the SBD in the mini-Sirt1/resveratrol/*FdL-1* complex (Figure 4.40A) leads to a clash of HIV1-Tat Arg53 with mini-Sirt1 Arg446 and Glu230 (Figure 4.40C), disrupting the important salt bridge ⁹⁷ between those mini-Sirt1 residues (Figure 1.6C). Furthermore, HIV1-Tat Gln54 clashes with the sidechain of mini-Sirt1 Leu206 while forming additional hydrogen bonds to Leu202, Leu206, and Thr209, which are located in the Sirt1-specific SBD (Figure 4.40D). Another additional sidechain hydrogen bond is created between Tat Arg55 and mini-Sirt1 Leu205 (Figure 4.40D). These structural comparisons suggest that HIV1-Tat inhibits hSirt1-3 predominantly by binding in the substrate binding cleft. But in case of hSirt1, an additional contribution to the inhibition could be mediated by impairment of the binding of the Sirt1 SBD to the catalytic core and by disruption of the salt bridge between Arg446 and Glu230 ⁹⁷. Since all additional interactions are mediated from the C-terminal amino acids 53-57 of Tat₃₇₋₅₉, these comparisons also provide a possible explanation for the higher potency of mini-Sirt1 inhibition by Tat peptides containing these C-terminal residues versus the lack of such higher potency for hSirt3 (Table 4.3), which does not have an SBD.

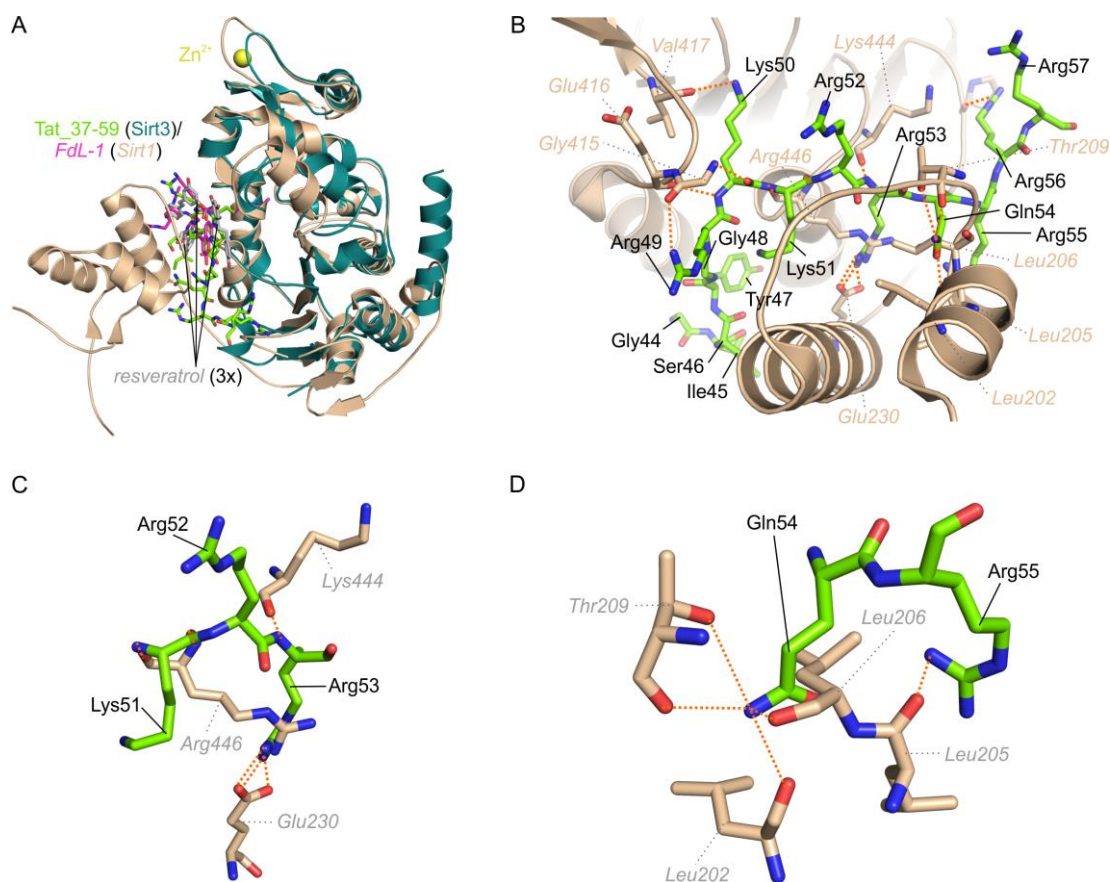


Figure 4.40: Mapping of the binding site of Tat₃₇₋₅₉ in mini-Sirt1/resveratrol/FdL-1. **A** Superposition of the hSirt3-(118-399)/Tat₃₇₋₅₉ complex (teal) with a mini-Sirt1/resveratrol/FdL-1 complex (cream; PDB: 5BTR). **B** Hydrogen bonds between Tat₃₇₋₅₉ and mini-Sirt1 as suggested by PyMOL²⁴⁹. **C** Disruption of the salt bridge between mini-Sirt1 Arg446 and Glu230 by binding of Tat. **D** Additional hydrogen bonds between Tat₃₇₋₅₉ might emanate from mini-Sirt1 Leu202, Leu205, Leu206, and Thr209, which are located in the SBD. **B-D** Putative hydrogen bonds between Tat₃₇₋₅₉ (lime) and mini-Sirt1 are shown as orange dotted lines.

Since an actual structure for the complex of hSirt1 and HIV1-Tat is not available, crosslinking was employed to get further hints on the sirtuin isoform-specific interaction. Therefore, the lysine-reactive crosslinker DSS or the CID-cleavable DSSO (Figure 4.41) were used in excess to an equimolar ratio of mini-Sirt1 and Tat Cys⁻. In both cases, SDS-PAGE revealed inter-protein crosslinks, which appeared within 5 min and were not present in the negative controls with the isolated proteins (Figure 4.41A, B). In case of DSS as a crosslinker, mass spectrometric analysis revealed crosslinks between Tat Lys19 and hSirt1 Lys203 and between Tat Lys28 and hSirt1 Lys430 (Table 4.7). Crosslinking of mini-Sirt1 and Tat Cys⁻ with DSSO resulted in one clearly distinct crosslink between Tat Lys71 and hSirt1 Lys238 (Table 4.8).

Table 4.7: Crosslinking of mini-Sirt1 and Tat Cys⁻ in presence of DSS. Experiments were performed four times, followed by tryptic in gel or in solution digest and MS analysis with either an LTQ or a TOF instrument.

HIV1-Tat residue	Fl-hSirt1 residue	Best Pep 2D	Hits out of $n = 4$
19	203	7.2×10^{-11}	3
28	430	4.5×10^{-10}	3

Table 4.8: Crosslinking of mini-Sirt1 and Tat Cys⁻ in presence of DSSO. Experiments were performed four times, followed by tryptic in gel or tryptic in solution digest and MS analysis with either an LTQ or a TOF instrument ($n = 16$). The respective DSSO-modified lysines are highlighted in bold red letters.

Tat Cys ⁻ peptide	Mini-Sirt1 peptide	HIV1-Tat residue	Fl-hSirt1 residue	Hits out of $n = 16$
RPSQGGQTHQDPI K QPSSQPR	R K DINTIEDAVK	71	238	12
RPSQGGQTHQDPI K QPSSQPR	K DINTIEDAVK	71	238	10

Since none of the crosslinked Tat residues are visible in the hSirt3-(118-399)/Tat₃₇₋₅₉ structure, they were mapped on a superposition with the two previously compared mini-Sirt1/substrate complexes to evaluate whether the crosslinks are compatible with the structural model based on the hSirt3/Tat₃₇₋₅₉ complex (Figure 4.41C-E). In addition, the structure of Tat₁₋₄₉ from a complex with PTEFb²⁰⁰ (PDB: 3MI9) was consulted although Tat might change its structure depending on the binding partner (Figure 5.4). The visible amino acids of both Tat peptides overlap by five residues, but a direct superposition of Tat₁₋₄₉ with Tat₃₇₋₅₉ would produce a severe clash with mini-Sirt1. Nevertheless, the crosslinked HIV1-Tat Lys28 and hSirt1 Lys430 appear to be in such close proximity that the crosslink is highly possible (Figure 4.41C). Concerning the crosslink between Tat Lys19 and hSirt1 Lys203, the likeliness depends on the location of the SBD respective to the hSirt1 catalytic core as well as on the actual structure of HIV1-Tat amino acids 1-49 in complex with hSirt1 (Figure 4.41D). In contrast, the C-terminal crosslink between Tat Lys71 and hSirt1 Lys238 has a strong possibility according to the structures: the straight distance from the C_α atom of Tat Arg57 to the C_α atom of mini-Sirt1 Lys238 is 25.7 Å (Figure 4.41E) and should be able to accommodate 14 amino acids and the crosslinker since Tat₅₈₋₇₁ will most likely form small turns. In summary, the crosslinks between Tat Lys28 and hSirt1 Lys430 and between Tat Lys71 and hSirt1 Lys238 are compatible with the suggested Tat binding site in hSirt1 based on the hSirt3-(118-399)/Tat₃₇₋₅₉ structural model (Figure 4.41C, E). Thus, Tat appears to bind into the sirtuin substrate binding cleft with its basic region, while its N-terminal cysteine-rich and core regions might form small helices at the entrance of the substrate binding cleft and the C-terminal glutamine-rich region of HIV1-Tat wraps further between the hSirt1 SBD and catalytic core towards the bottom of the Rossmann fold domain.

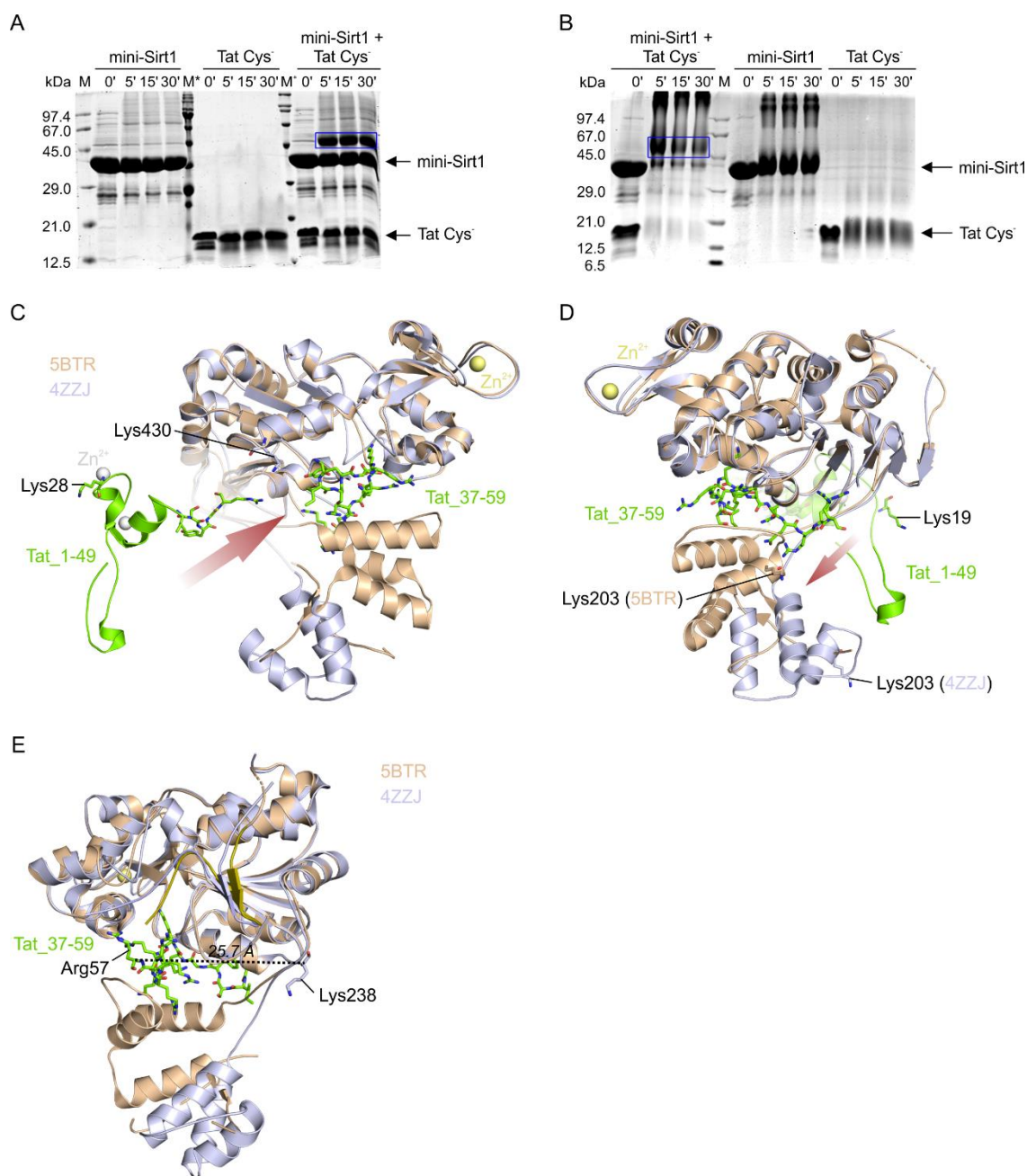


Figure 4.41: Crosslinking of mini-Sirt1 with Tat Cys. **A** Crosslinking of mini-Sirt1 and Tat Cys in a molar ratio of 1:1 in presence of a 56-fold molar excess of DSS or **B** DSSO. Inter-protein crosslinks are marked with blue boxes. M* = 245, 190, 135, 100, 80, 58, 46, 32, 25, 22, 17, 11 kDa. **C-E** Mapping of the identified crosslinks. The hSirt3-(118-399)/Tat_37-59 (lime) complex was superimposed to a mini-Sirt1/STAC/p53/carbam-NAD complex (PDB: 4ZZJ; grey) and a mini-Sirt1/resveratrol/*FdL-1* complex (PDB: 5BTR; cream). For better clarity, hSirt3, the p53 and *FdL-1* substrates as well as small-molecule activators are not shown. **C** Crosslink between Tat Lys28 and hSirt1 Lys430. **D** Crosslink between Tat Lys19 and hSirt1 Lys203. **E** Crosslink between Tat Lys71 and hSirt1 Lys238. The ESA/CTR is shaded in darker colors.

4.4.6 Elucidation of the inhibitory mechanism of HIV1-Tat on hSirt1-3

Besides a structural view on the regulation of sirtuin activity by HIV1-Tat, assays and binding studies were performed to elucidate whether Tat competes with the sirtuin substrate or the sirtuin cofactor NAD⁺. For investigation of substrate competition, the K_m value of *FdL-1* substrate was determined for mini-Sirt1 (Figure 4.42A) and hSirt3-(93-399) (Figure 4.42B) in

presence of an excess of 3 mM NAD^+ and different concentrations of Tat Cys^- . In both cases, the substrate K_m increases with increasing concentrations of Tat Cys^- (Figure 4.42A, B, Table 4.9), confirming that HIV1-Tat and the sirtuin substrate are competitive. While mini-Sirt1 and hSirt3-(93-399) have a similar K_m for *FdL-1* in absence of Tat, the steeper increase of the *FdL-1* K_m value for mini-Sirt1 in presence of Tat is probably related to the 4-fold lower IC_{50} of Tat Cys^- for mini-Sirt1 compared to hSirt3-(93-399) (Table 4.3). Concerning competition of HIV1-Tat to the sirtuin cofactor NAD^+ , K_m values for NAD^+ were determined for mini-Sirt1 (Figure 4.42C) and hSirt3-(93-399) (Figure 4.42D) in presence of 400 μM *FdL-1* and different concentrations of Tat Cys^- . The resulting K_m values for NAD^+ for mini-Sirt1 and hSirt3-(93-399) show no Tat-dependent change (Figure 4.42C, D, Table 4.9), suggesting that HIV1-Tat is not competitive to NAD^+ .

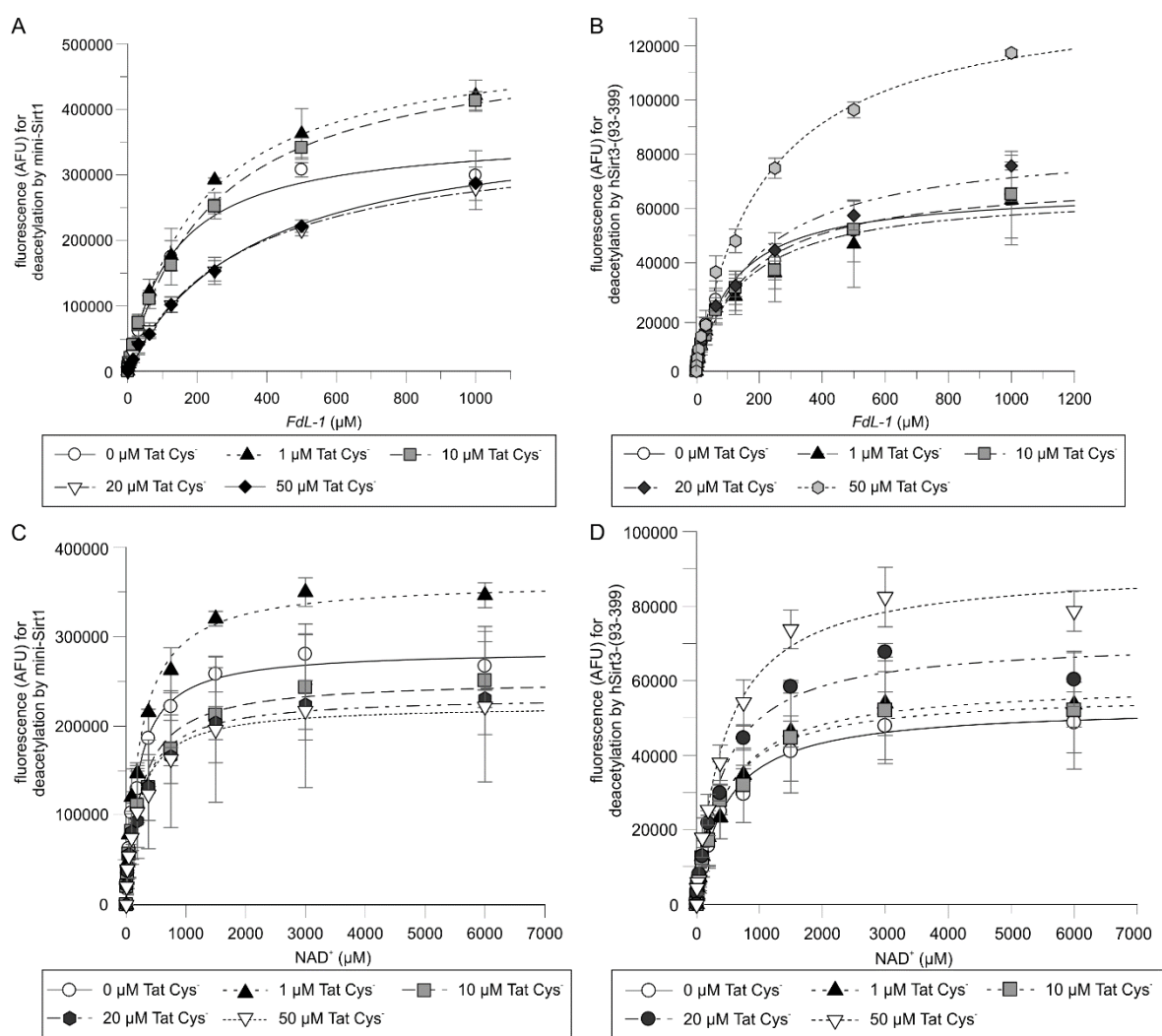


Figure 4.42: Competition of Tat Cys^- against sirtuin substrate and sirtuin cofactor. **A** K_m determination of *FdL-1* for 1 μM mini-Sirt1 in presence of different concentrations of Tat Cys^- . **B** K_m determination of *FdL-1* for 1 μM hSirt3-(93-399) in presence of different concentrations of Tat Cys^- . **C** K_m determination of NAD^+ for 1 μM mini-Sirt1 in presence of different concentrations of Tat Cys^- . **D** K_m determination of NAD^+ for 1 μM hSirt3-(93-399) in presence of different concentrations of Tat Cys^- . **A-D** All *Fluor de Lys* assays were performed under the same conditions. K_m values are summarized in Table 4.9 ($n = 3-6$).

Table 4.9: Michaelis-Menten constants (K_m) for sirtuin substrate and cofactor in presence of Tat Cys⁻. Fluor de Lys assays with 1 μ M mini-Sirt1 or hSirt3-(93-399). *FdL-1* K_m determinations ($n = 3-6$) were performed in presence of an excess of 3 mM NAD⁺, while NAD⁺ K_m determinations were conducted at 400 μ M *FdL-1*.

Tat Cys ⁻ (μ M)	<i>FdL-1</i> substrate		NAD ⁺	
	K_m for mini-Sirt1 (μ M)	K_m for hSirt3-(93-399) (μ M)	K_m for mini-Sirt1 (μ M)	K_m for hSirt3-(93-399) (μ M)
0	136.4 \pm 13.9	133.9 \pm 52.2	190.7 \pm 45.5	470.4 \pm 172.0
1	207.8 \pm 8.1	157.5 \pm 70.1	230.7 \pm 59.7	432.8 \pm 132.1
10	245.0 \pm 28.2	165.5 \pm 6.9	248.3 \pm 103.0	446.5 \pm 187.4
20	326.0 \pm 82.8	196.3 \pm 16.0	225.6 \pm 95.5	430.6 \pm 67.3
50	377.4 \pm 74.2	206.9 \pm 32.6	238.1 \pm 112.1	443.1 \pm 85.3

Competition of HIV1-Tat to sirtuin ligands was also investigated with MST, whereby the respective sirtuin was titrated to FITC-labeled Tat Cys⁻ in presence of different sirtuin ligands. All K_d values were evaluated from the initial fluorescence due to a concentration-dependent change of the initial fluorescence, which was related to binding. For mini-Sirt1, the K_d of $1.79 \pm 0.47 \mu$ M increased to about 4μ M in presence of p53short (Figure 4.43A) with a substrate concentration-dependent change (Table 4.10). Controversial to activity assays, the K_d in presence of NAD⁺ also increased with a cofactor concentration-dependent change (Figure 4.43A, Table 4.10). However, MST in presence of NAD⁺ suffered from high standard deviations, the lack of a defined upper baseline, and bleaching although NAD⁺ does not exhibit fluorescence at the excitation wavelength used. Concerning competition to the structurally related ADPr, the K_d for Tat Cys⁻ to mini-Sirt1 was also higher (Figure 4.43, Table 4.10). The affinity of fl-hSirt1 to Tat Cys⁻ was impaired by presence of p53short in a substrate concentration-dependent manner and the K_d values in presence of NAD⁺ and ADPr were slightly increased as well (Figure 4.43B, Table 4.10). In contrast, hSirt2-(43-356) showed a stronger affinity in presence of p53short and NAD⁺, but bound weaker in presence of ADPr (Figure 4.43C, Table 4.10). The lacking competitiveness of Tat Cys⁻ and substrate in case of hSirt2 (Figure 4.43C) is likely due to the use of a hSirt1 substrate. But the hSirt2 substrate α -tubulin could not be used because Tat Cys⁻ bound to α -tubulin with a $K_d \sim 700 \mu$ M (Figure 7.11). Binding of hSirt3-(93-399) to Tat Cys⁻ displayed a substrate concentration-dependent decrease in binding affinity, while the binding affinity in presence of NAD⁺ and ADPr was also decreased, but without a cofactor concentration-dependency (Figure 4.43D, Table 4.10). Therefore, the results from hSirt3 complex structures with Tat peptides (Figure 4.32, Figure 4.37, Figure 4.38), K_m determinations (Table 4.9), and K_d determinations (Table 4.10) leave no doubt that HIV1-Tat binding to hSirt1-3 is competitive to sirtuin substrate binding.

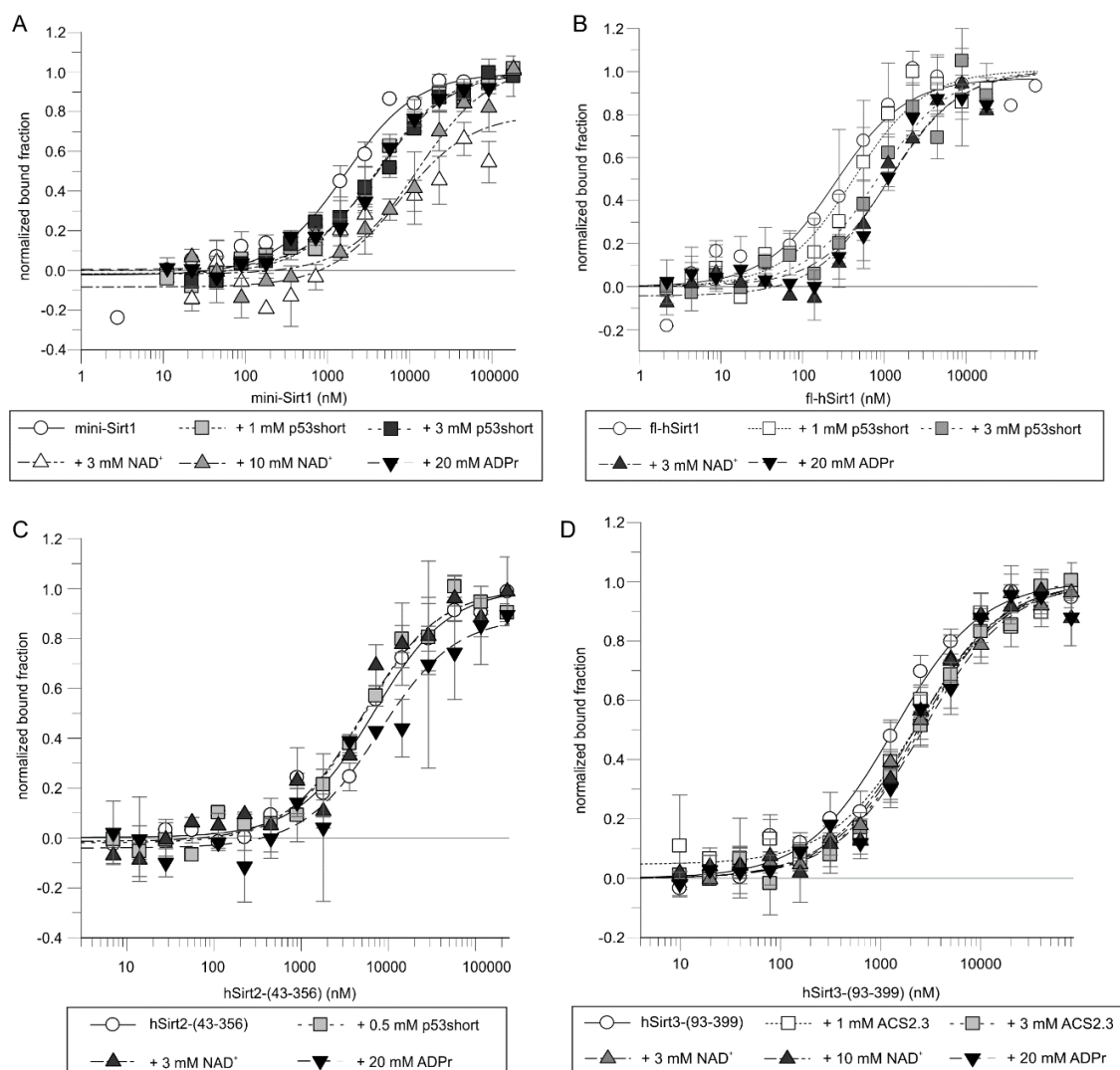


Figure 4.43: Binding affinity of Tat to hSirt1-3 in presence of sirtuin ligands. A MST of 40 nM Tat Cys⁻ with titration of mini-Sirt1. B MST of 80 nM Tat Cys⁻ with titration of fl-hSirt1. C MST of 20 nM Tat Cys⁻ with titration of hSirt2-(43-356). D MST of 80 nM Tat Cys⁻ with titration of hSirt3-(93-399). A-D All measurements were performed at 25 °C, 12% LED power, and 30% MST power. K_d values (Table 4.10) were derived from the initial fluorescence ($n = 2$).

Table 4.10: Binding affinity of Tat to hSirt1-3 in presence of sirtuin ligands. MST of FITC-labeled Tat Cys⁻ with titration of human sirtuins in presence of substrate, NAD⁺, or ADPr. Abbreviation: *n. d.* - not determined.

Sirtuin ligand	K_d for mini-Sirt1 (μM)	K_d for fl-hSirt1 (μM)	K_d for hSirt2-(43-356) (μM)	K_d for hSirt3-(93-399) (μM)
hSirt and Tat Cys ⁻	1.79 ± 0.47	0.34 ± 0.24	6.67 ± 0.05	1.37 ± 0.36
+ 0.5 mM substrate	<i>n. d.</i>	<i>n. d.</i>	5.35 ± 0.67	<i>n. d.</i>
+ 1 mM substrate	3.74 ± 0.24	0.43 ± 0.12	<i>n. d.</i>	2.34 ± 0.28
+ 3 mM substrate	4.10 ± 0.26	0.86 ± 0.31	<i>n. d.</i>	2.73 ± 0.46
+ 2 mM NAD ⁺	<i>n. d.</i>	<i>n. d.</i>	4.97 ± 0.19	<i>n. d.</i>
+ 3 mM NAD ⁺	6.96 ± 5.20	1.04 ± 0.43	<i>n. d.</i>	2.15 ± 0.29
+ 10 mM NAD ⁺	13.09 ± 6.43	<i>n. d.</i>	<i>n. d.</i>	2.21 ± 0.07
+ 20 mM ADPr	4.26 ± 1.41	1.19 ± 0.20	7.67 ± 1.98	2.67 ± 0.36

To resolve whether Tat and NAD⁺ influence each others binding to hSirt1-3, hSirt3-(118-399) was cocrystallized with Tat₃₄₋₅₉ and NAD⁺. The best crystal for a hSirt3-(118-399)/Tat₃₄₋₅₉/NAD⁺ complex diffracted to 2.3 Å resolution and was solved in space group P2₁2₁2₁ to final R and R_{free} values of 22.0% and 27.5% (Table 7.10). The resulting structure superimposes to hSirt3-(118-399)/Tat₃₄₋₅₉ with an RMSD = 1.380 Å for 539 C_α atoms and to hSirt3-(118-399)/Tat₃₇₋₅₉ with an RMSD = 0.706 Å for 504 C_α atoms (Figure 4.44A).

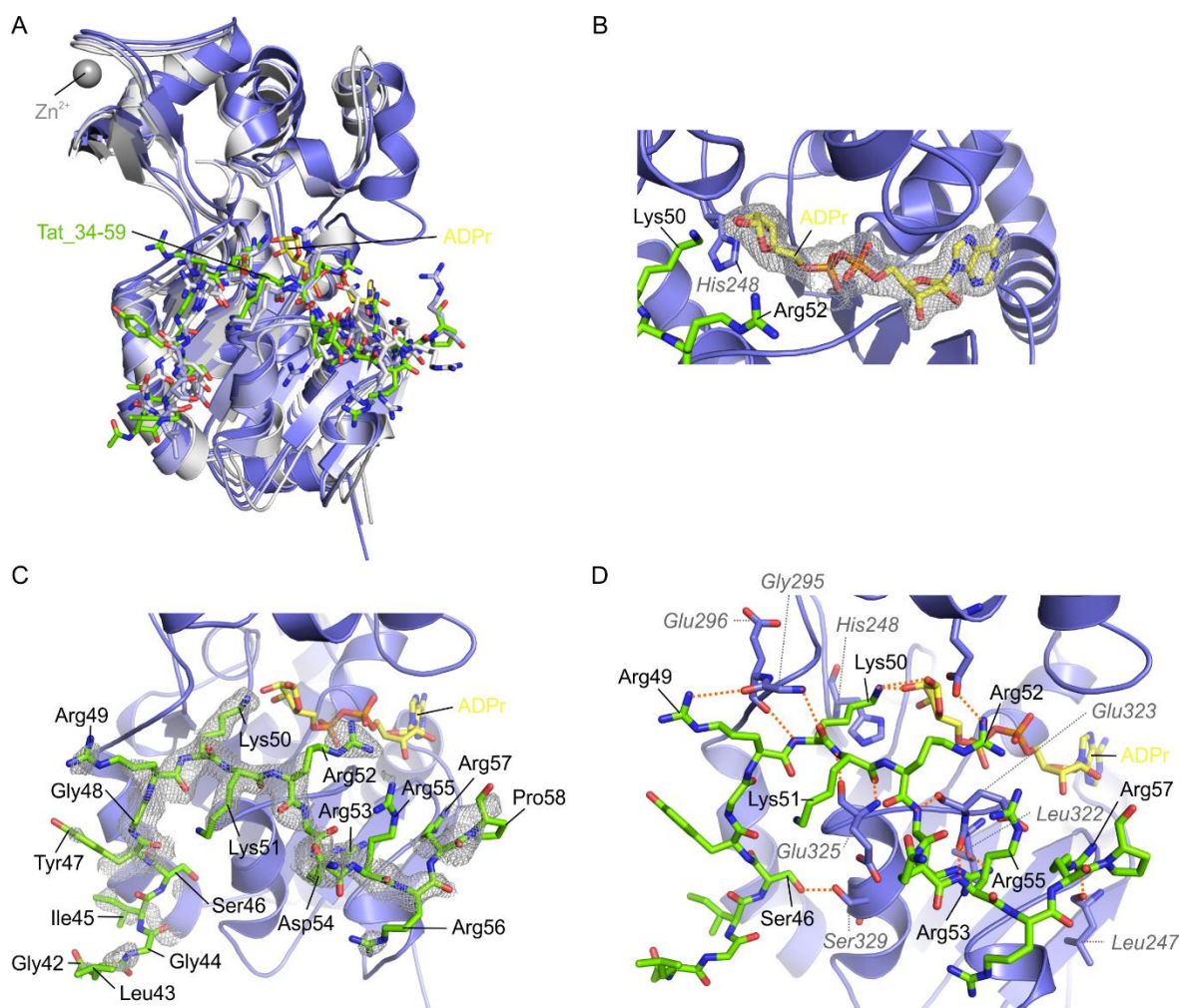


Figure 4.44: Structure of hSirt3-(118-399) in complex with Tat₃₄₋₅₉ and NAD⁺ (ADPr). **A** Superposition of hSirt3-(118-399)/Tat₃₄₋₅₉/NAD⁺ (blue) with hSirt3-(118-399)/Tat₃₄₋₅₉ (white) and hSirt3-(118-399)/Tat₃₇₋₅₉ (light blue). **B** 2mF_o-DF_c composite omit map of ADPr (yellow) contoured at 1 σ . **C** 2mF_o-DF_c composite omit map of Tat₃₄₋₅₉ (lime) contoured at 1 σ . Residues 42-58 of Tat₃₄₋₅₉ are visible. **D** Hydrogen bonds (orange dotted lines) emanating from Tat₃₄₋₅₉ (lime) to hSirt3 (blue) and ADPr (yellow).

Despite cocrystallization with NAD⁺, the cofactor was hydrolyzed during crystallization since a 2mF_o-DF_c composite omit map shows clear coverage for ADPr (Figure 4.44B). Concerning the Tat₃₄₋₅₉ peptide, residues 42-58 are visible in the 2mF_o-DF_c composite omit map (Figure 4.44C). Thus, the new complex reveals density for two further N-terminal and one further C-terminal amino acid compared to the hSirt3-(118-399)/Tat₃₇₋₅₉ complex, while one additional hydrogen bond is formed between Tat Ser46 and hSirt3 Ser329 (Figure 4.44D).

More importantly, no clashes can be observed between Tat₃₄₋₅₉ and ADPr and Tat Lys50 forms hydrogen bonds to the ribose moiety of ADPr (Figure 4.44D). Therefore, binding of HIV1-Tat and NAD⁺ to hSirt1-3 appears to be not mutually exclusive. HIV1-Tat thus inhibits the deacetylase activity of hSirt1-3 by competing with the sirtuin substrate for the same binding site, while providing additional potency for hSirt1 inhibition through impairment of the SBD binding to the hSirt1 catalytic core via HIV1-Tat residues 53-59.

5. Discussion

5.1 Characterization of recombinant human Sirtuin 1

5.1.1 Human fl-Sirt1 and truncated variants

Recombinant fl-hSirt1 was purified according to an established protocol²⁵⁸ with small corrections. However, the resulting target protein was only 70% pure (Figure 4.1D), thus its purity and yield should be improved. For example, an often observed incomplete cleavage of the N-terminal His₆-tag by thrombin (Figure 4.1B) can be avoided by using thrombin in larger excess²⁶⁵. In this regard, the incubation time with the protease must be shortened to prevent unspecific thrombin-mediated cleavage of fl-hSirt1 after any arginine or lysine²⁶⁵, which could lead to fl-hSirt1 degradation products. To improve purity and yield of fl-hSirt1, expression and purification with various solubility enhancing tags and alternative proteolytic cleavage sites were also tested in our laboratory (Table 4.1). But these constructs hardly resulted in purer target protein and often caused more severe problems like inactive enzyme, impossibility to separate the solubility enhancing tag after cleavage, or an even lower yield. In addition, the reproducibility for obtaining active and at least 70% pure fl-hSirt1 could only be achieved with the described construct from pET15b and partly with fl-hSirt1 from pET32*amod*. The tested constructs suggest that recombinant expression of fl-hSirt1 in *E. coli* might be most feasible with an expression vector using only an N-terminal His₆-tag with a more specific proteolytic cleavage site such as for TEV.

N- and C-terminal deletion variants of fl-hSirt1 were also purified in our laboratory, but *Fluor de Lys* assays revealed that the activity of hSirt1-(183-664) and hSirt1-(214-664) is reduced by at least 50% (Figure 4.3). This is rather surprising, because both constructs contain the hSirt1 catalytic core and the ESA/CTR region, which are crucial for the intrinsic activity of hSirt1^{76,80,93}. However, despite the predicted structural flexibility of N- and C-terminal regions of fl-hSirt1, their truncation might have caused a decreased thermal stability of the resulting proteins. Since fl-hSirt1 exhibited a melting temperature of 41 °C (Figure 4.2C) and the *Fluor de Lys* assay is performed at 37 °C, the melting temperature of a stable hSirt1 deletion variant is even more critical for this assay. Furthermore, the activity of hSirt1-(214-664) was lower than the activity of hSirt1-(183-664) (Figure 4.3). The Sirt1 STAC-binding domain (SBD) comprising residues 183-230 is relevant for Sirt1 activity-modulation by allosteric activators (STACs)^{47,80,97,98}. Upon STAC-binding, the SBD exerts a lever-like rigid-body movement towards the catalytic core of Sirt1⁸⁰ with formation of a salt bridge between

Glu230 and Arg446⁹⁷, thereby lowering the K_m for the substrate and increasing the deacetylase activity^{47,80,98}. Lacking most of the SBD, hSirt1-(214-664) might not be able to form this productive deacetylation conformation, thereby suffering from a higher K_m for the substrate. Despite the lower activity of hSirt1-(183-664) and hSirt1-(214-664), both hSirt1 deletion variants are suitable for deacetylation assays with modulators as long as their activity is compared to the respective samples without modulator and not to fl-hSirt1.

5.1.2 Mini-Sirt1 as a model for mimicking fl-hSirt1

As discussed in the first chapter, expression and purification of fl-hSirt1 is often sensitive to issues like low yield, activity, and/or purity. Thus, a mini-Sirt1 variant according to Dai *et al.* (2015)⁸⁰ was established²⁵⁹ comprising all domains relevant for Sirt1 activity (Figure 1.6A). Mini-Sirt1 shows many benefits over fl-hSirt1 in expression and purification. But during reverse affinity chromatography of mini-Sirt1 (Figure 4.4B) and mini-Sirt1 deletion variants (Figure 7.1, Figure 7.2), a contaminant the size of 29 kDa was sometimes observed, which could not be separated. Most likely, this contaminant was introduced with His₆-TEV protease recombinantly produced in our laboratory, demanding a fine-tuned use of this highly active protease to prevent contamination of the target protein. Altogether, mini-Sirt1 reached a purity above 90% and could be concentrated to at least 40 mg/ml without precipitation, thereby enabling the use of high concentrations in binding or crystallization experiments.

The bioanalytical characteristics of mini-Sirt1 were examined by activity assays showing that different batches of mini-Sirt1 exhibit comparable activity to fl-hSirt1 in activity assays with native (Figure 4.2A, Figure 4.5A) or fluorogenic substrate (Figure 4.3). This confirms that our mini-Sirt1 is a functional hSirt1 construct comprising all domains necessary for hSirt1 activity consistent with previous studies⁸⁰. Compared to fl-hSirt1, the melting temperature of mini-Sirt1 is at least 10 °C higher (Figure 4.2C, Figure 4.5B) and stable across various buffer systems from pH 6.5-10 (Figure 4.5B-D). This increased thermal stability is probably linked to mini-Sirt1 consisting only of distinctly structured regions with small flexible loops in between, whereas fl-hSirt1 has large N- and C-terminal flanking regions and the region from amino acids 505-640 with predicted intrinsic disorder (Figure 7.6). While such intrinsically disordered regions fail to form a stable structure, they still exhibit biological activity, for example in accommodation of PTMs or in recognition of binding partners²⁶⁶. Screening for stabilizing additives in a TSA indicated that the current purification buffers are well adapted to the properties of mini-Sirt1 and that the stability of mini-Sirt1 is not impaired by small changes in buffer composition (Figure 4.5D) as needed for certain interaction studies.

Several deletion and mutation variants based on mini-Sirt1 were purified. While purification of mini-Sirt1 deletion variants lacking the SBD or the ESA/CTR region resulted in lower yield and purity of the recombinant proteins (Figure 7.1, Figure 7.2), phosphorylation mimicry mutants remained unaffected (Figure 7.3-Figure 7.5) and also showed similar activity as mini-Sirt1 (Figure 4.6B). In contrast, mini-Sirt1- Δ SBD and mini-Sirt1- Δ ESA displayed a five-fold lower specific activity for natural p53 substrate at 20 °C (Figure 4.6A), in line with the previously determined lower activity of truncated fl-hSirt1 variants on artificial *FdL-1* substrate at 37 °C (Figure 4.3). The decreased activity of the mini-Sirt1- Δ ESA variant is thereby consistent with previous studies showing that the hSirt1 catalytic domain has only an intrinsic activity of 15%^{76,80} at most compared to fl-hSirt1, while addition of the ESA/CTR region restores the activity of the catalytic core⁸⁰ or an N-terminally elongated SBD-catalytic core variant^{76,93}. However, while addition of the SBD was shown to increase the activity of the catalytic core of hSirt1 to about 50% of the activity of a hSirt1-(160-665) construct⁷⁶, lack of the SBD should only impair STAC-mediated activation of hSirt1^{47,80,170}, but not the intrinsic activity of hSirt1 as previously demonstrated with slightly different mini-Sirt1- Δ SBD variants⁸⁰. It is thus difficult to speculate why our mini-Sirt1- Δ SBD variant displayed such low activity, but the use of different vectors, construct boundaries, or linkers might contribute to the final activity of the resulting protein. After all, mini-Sirt1- Δ SBD and - Δ ESA are amenable for deacetylation assays with Sirt1 activity modulators as long as their activity is compared to their respective samples without modulator.

In scope of this work, apo mini-Sirt1 was crystallized since recent crystal structures of hSirt1 were always complexed with ligands⁷⁸⁻⁸¹ or did not include the SBD⁷⁹. An apo mini-Sirt1 structure of moderate resolution was obtained after a failed soaking attempt, resembling previous structures of hSirt1 with the catalytic core comprising a Rossmann fold for NAD⁺-binding and a smaller domain for Zn²⁺-binding (Figure 4.11E). Superposition with mini-Sirt1 complex structures containing activators such as resveratrol⁸¹ or a STAC⁸⁰ in conjunction with substrate and/or carba-NAD shows that the SBD in apo mini-Sirt1 is turned further away from the catalytic core than in any known mini-Sirt1/ligand structure (Figure 4.11G, H). This provides enough space for binding an activator of any size, allowing the subsequent rigid body movement of the SBD towards the catalytic core upon binding of a substrate, which locks the substrate in place. However, for successful soaking of apo mini-Sirt1 crystals with small molecules, the diffraction quality of the crystals, and the soaking procedure still have to be improved, for example by optimization with an additive screen or by seeding.

5.2 Modulation of hSirt1 activity by small molecules

5.2.1 Importance of the Sirt1-specific ESA/CTR region for hSirt1 activity

In contrast to other mammalian sirtuin isoforms, the Sirt1 catalytic core has relatively low activity^{76,80}, but N- and C-terminal extensions potentiate Sirt1's deacetylation activity⁷⁶. In particular, the C-terminal ESA/CTR region^{79,93} serves as an “on switch” for Sirt1 activity⁹³ and addition of this motif to the catalytic core of Sirt1 can restore the deacetylase activity comparable to fl-Sirt1^{76,80,93}. Within this thesis, activity modulation of fl-hSirt1 by the ESA/CTR motif was investigated, showing that a peptide comprising the whole ESA/CTR region could activate fl-hSirt1 and a peptide with the sequence NRYIFH-NH₂ seemed to be sufficient for this activating effect²⁵⁹ (Figure 4.7A). Initial doubts about the activating effect due to high errors (Figure 4.7A) were excluded with different types of activity assays under various conditions (Figure 4.7B-D), which confirmed the stimulating effect for fl-hSirt1 by both ESA/CTR peptides. Most importantly, the ESA/CTR core sequence RYIF was identified as the minimal sequence necessary for activation of fl-hSirt1 (Figure 4.7D).

The fact that the ESA/CTR motif can serve as activator for fl-hSirt1, which already contains the ESA/CTR region, is completely new. While Kang *et. al* (2011) showed that mutation of G654P and D660R within the ESA/CTR region does not restore the activity of a murine mini-Sirt1 variant and addition of a mutated G654P/D660R-ESA/CTR peptide to fl-Sirt1 leads to inhibition of fl-Sirt1, the addition of wild-type ESA/CTR peptide failed to further enhance the fl-Sirt1 deacetylase activity⁹³. In addition, Pan *et. al* (2012) later indicated that addition of hSirt1-(584-665) to hSirt1-(160-665), both containing the ESA/CTR motif, is unlikely to enhance hSirt1-(160-665) deacetylase activity, but high error deviations raised doubts⁷⁶. The here described enhancement of hSirt1 activity might be due to a small conformational change after binding of the ESA/CTR peptide⁹³, similar to the binding of activators at the SBD^{80,97}. However, structural investigation rather suggests a model of increased Sirt1 stability upon binding of the ESA/CTR region⁷⁹⁻⁸¹. The first Sirt1 structure including the ESA/CTR region⁷⁹, published after the ESA/CTR activity studies presented here, showed that this C-terminal part folds back towards the catalytic core and extends the β -sheet of the NAD⁺-binding domain by two additional β -strands⁷⁹ (Figure 5.1A). Since the ESA/CTR region was added as peptide, the crystallization condition produced a model where two Sirt1 molecules in the asymmetric unit formed a putative dimer via association of two ESA/CTR peptides, raising the question whether it was a crystallographic artifact (Figure 5.1A). Later Sirt1 structures included the ESA/CTR connected to the catalytic core through a linker and showed

that it binds indeed to the bottom part of the Rossmann fold^{80,81} (Figure 5.1B) supporting the model of increased Sirt1 stability. Interestingly, the core sequence RYIF, which was sufficient for activation of fl-hSirt1 (Figure 4.7D), comprises the exact length of the second β -strand of the ESA/CTR region, which binds directly to the NAD⁺-binding domain, elongates the Rossmann fold β -sheet, and forms β -staple interactions (Figure 5.1C). This might explain how peptide 21 or peptide 30 are able to stimulate hSirt1 deacetylation through formation of a stabilized hSirt1 enzyme. However, it is still not clear why fl-hSirt1, already including the ESA/CTR region, can be activated as well. Possibly, the RYIF-peptide elongates the Rossmann fold β -sheet even more similar to the crystal structures by Davenport *et al.*⁷⁹ (Figure 5.1A), leading to a decreased K_m for NAD⁺⁷⁶ or for the cofactor and the substrate⁸⁰. Further activity assays and kinetic studies with mini-Sirt1 and the mini-Sirt1- Δ ESA deletion mutant should reveal a detailed activation mechanism in the future.

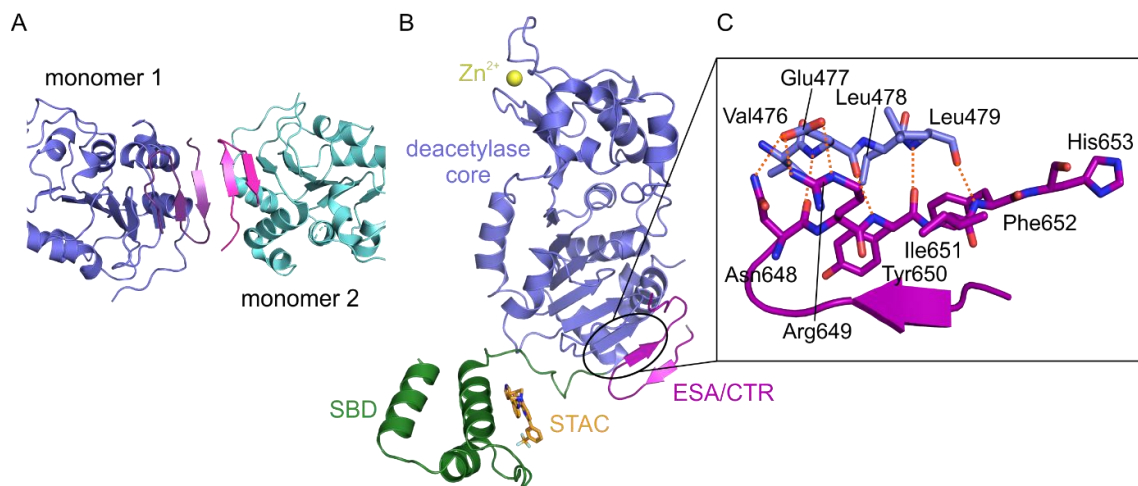


Figure 5.1: Mediation of conformational stability for fl-hSirt1 by the ESA/CTR region. **A** Structure of Sirt1-cat (blue/aquamarine) with ESA/CTR (purple/pink) showing two molecules each in the asymmetric unit (PDB: 4IG9)⁷⁹. **B** Structure of mini-Sirt1/STAC (PDB: 4ZZH)⁸⁰ with the SBD (green) binding a STAC (orange), the catalytic core (blue), and the ESA/CTR region (purple). **C** Highlight of the β -staple interactions between residues 649-652 (identical to peptide 30) of the hSirt1 ESA/CTR region (purple) and hSirt1 residues 476-479 of the NAD⁺-binding domain (blue). Hydrogen bonds are shown as orange dotted lines.

5.2.2 Stimulation of hSirt1 activity by dehydroabietic acid

In scope of this work, modulation of hSirt1 activity by dehydroabietic acid (DAA) was investigated showing that the relative activity of fl-hSirt1 is increased to 160-195% in presence of 1-10 μ M DAA (Figure 4.8A). An additional beneficial effect of 0.1-1 μ M DAA on mini-Sirt1 activity was validated with a *Fluor de Lys* assay (Figure 4.8B), demonstrating that DAA-mediated stimulation of hSirt1 is at a sub-micromolar level and does only require domains included in mini-Sirt1. These results confirm results from a FRET-based assay published during our studies on DAA-mediated activation of hSirt1¹⁴⁰. Although DAA appeared to activate hSirt1-(214-664) as well, it could not be undoubtedly resolved whether

the SBD is required for DAA-mediated activation of hSirt1, because only part of the SBD was lacking in the hSirt1 deletion variant used. Compared to already characterized classes of hSirt1 activators, a STAC could also stimulate hSirt1-(214-664) (Figure 4.9B) and STAC-binding was mapped to hSirt1 residues 210-230 of the SBD with a crystal structure⁸⁰. In contrast, resveratrol, which could not mediate activation of mini-Sirt1 (Figure 4.9A), was shown to require either the catalytic domain¹⁵⁵ or the catalytic domain in conjunction with the SBD⁸¹. Similarly contradictory, resveratrol-binding was mapped to either residues in the catalytic core or to residues 214-230 from the SBD due to several bound molecules in a crystal structure⁸¹. Thus, a hSirt1 construct starting from residue 230 and lacking the complete SBD should clarify the relevance of the SBD for DAA-mediated hSirt1 activation.

DAA bound to mini-Sirt1 with a high binding affinity of ~83 nM (Figure 4.8C). Surface plasmon resonance (SPR) studies have evaluated the K_d for DAA to hSirt1 to 492 μ M, slightly higher than the K_d for resveratrol to hSirt1 (144 μ M)¹⁴⁰, and indicated a binding independent from NAD^+ ($K_d = 592 \mu$ M in presence of NAD^+)¹⁴⁰. Despite a high binding affinity, initial screening for cocrystallization conditions of mini-Sirt1 and the activator failed as well as soaking of DAA into existing mini-Sirt1/(STAC) crystals. This might be a hint that the binding sites for STAC and DAA do overlap - at least to some extent - and that the SBD is necessary for DAA-mediated activation of Sirt1. Cocrystallization of mini-Sirt1 and DAA in a known crystallization condition resulted in a structure, whose difference density did not support binding of DAA. For obtaining a mini-Sirt1/DAA complex structure, the soaking or cocrystallization procedure thus needs to be finetuned. Apo mini-Sirt1 crystals might also be used for seeding in combination with a mini-Sirt1/DAA protein solution to promote nucleation of mini-Sirt1/DAA complex crystals.

5.2.3 Biochemical and structural studies of tranilast and hSirt1

Tranilast appeared to inhibit fl-hSirt1 *in vitro* with an $IC_{50} \sim 60 \mu$ M (Figure 4.10C), but activity analyses showed a high variation. Possible causes for such high variation in the mass spectrometric assay include material loss upon filtration of samples prior to MS analysis, an MS running time of more than 50 h for all samples, and semi-automated selection of peaks for acetylated and deacetylated substrate. Based on an otherwise confirmed inhibition of hSirt1 by tranilast (Eric Verdin, personal communication), cocrystallization of mini-Sirt1 and tranilast was attempted, but did not yield protein crystals (Figure 4.11A). In addition, soaking of tranilast into mini-Sirt1/STAC crystals was performed as previously demonstrated⁸⁰ (PDB: 4ZZI) since we managed to reproduce such crystals yielding a highly similar mini-

Sirt1/STAC structure. However, mini-Sirt1/STAC crystals were found to be very sensitive to the soaking process (Figure 4.11C), which was also observed for soaking of DAA into mini-Sirt1/STAC crystals, indicating that either the soaking procedure has to be finetuned or that the use of such crystals for seeding with a mini-Sirt1/compound/(STAC) protein solution may be more appropriate to promote the nucleation process. In contrast, soaking of tranilast into apo mini-Sirt1 crystals did not affect the crystal morphology (Figure 4.11D) or the diffraction quality (Table 7.5), but did also not result in a complex structure (Figure 4.11F). The same was observed for soaking of DAA into apo mini-Sirt1 crystals suggesting that crystallization of mini-Sirt1 in this condition does not stabilize binding of small molecules. It is therefore inevitable to find further crystallization conditions for mini-Sirt1 that would allow soaking or cocrystallization with small molecule modulators.

5.3 Modulation of hSirt1 activity by hAROS

5.3.1 Characterization of refolded His₆-hAROS

For interaction studies with hSirt1, soluble overexpression of hAROS was investigated under several conditions, but the target protein was always expressed insolubly (Figure 4.12). Following an established refolding protocol²⁵⁸, His₆-hAROS was purified with low yield and appeared to be contaminated with RNA-associated proteins (Figure 4.13D). Although the A₂₆₀ absorbance during SEC of His₆-hAROS often correlated with the A₂₈₀ absorbance, an excess of RNase A and DNase I during cell lysis is unlikely to be sufficient to separate the RNA-associated proteins from His₆-hAROS. After all, hAROS is also referred to as 40S ribosomal protein S19-binding protein 1 (RPS19BP1)¹⁵² and was previously found to form a complex with *E. coli* RPS19¹⁵¹. Other complexes with RNA-associated proteins thus seem likely and affinity chromatography of His₆-hAROS indeed suggests that earlier elution fractions are complexes, whereas later fractions contain isolated His₆-hAROS (Figure 4.13A). An additional wash with 10-50 mM imidazole might remove the complexes, followed by elution of isolated His₆-hAROS with high imidazole concentrations. However, this procedure is associated with loss of recombinant protein and requires a larger initial yield.

The purified His₆-hAROS showed a stable melting curve in various buffers between pH 7.7-8.5 (Figure 4.14) indicating that it is folded. Consistent with this observation, a previously recorded CD spectrum of refolded His₆-hAROS showed an unusual secondary structure, but clearly deviated from random conformation by featuring regions with 33% α -helices, 12% β -strands, and some poly-(Pro) conformations¹⁵⁵. In contrast, secondary structure prediction with the Phyre² server²⁶⁰ suggests 72% α -helices and no β -strands (Figure 5.2A). However,

some α -helices have a low confidence level correlating with a high confidence level for disorder (Figure 5.2A). An IUPred2A²⁵⁷ prediction supports disorder for hAROS residues 13-64 and 94-110 (Figure 5.2B). Consistent with Phyre², the region from hAROS residues 68-88 seems to contain secondary structure elements which are also a binding site for an interaction partner (Figure 5.2B). The region from hAROS residues 23-68 might host a binding site as well (Figure 5.2B). Since this latter region is predicted to be disordered, it might undergo induced folding upon binding of the interaction partner^{257,267}. This feature would characterize hAROS as partly intrinsically disordered protein (IDP), which recognizes its binding partners with a disordered segment and induces subsequent folding of this disordered segment to carry out the interaction function²⁶⁷. Both regions from hAROS residues 23-68 and 68-88 might further act as coupled binding motif due to their low ANCHOR2 score²⁵⁷, whereas the N-terminal region from hAROS residues 1-22 seems to act as single or predominant binding region for an interaction partner (Figure 5.2B). The prediction from IUPred2A highlights that expression of hAROS together with its binding partner hSirt1 in a coexpression system might be beneficial to generate soluble recombinant protein with high yields.

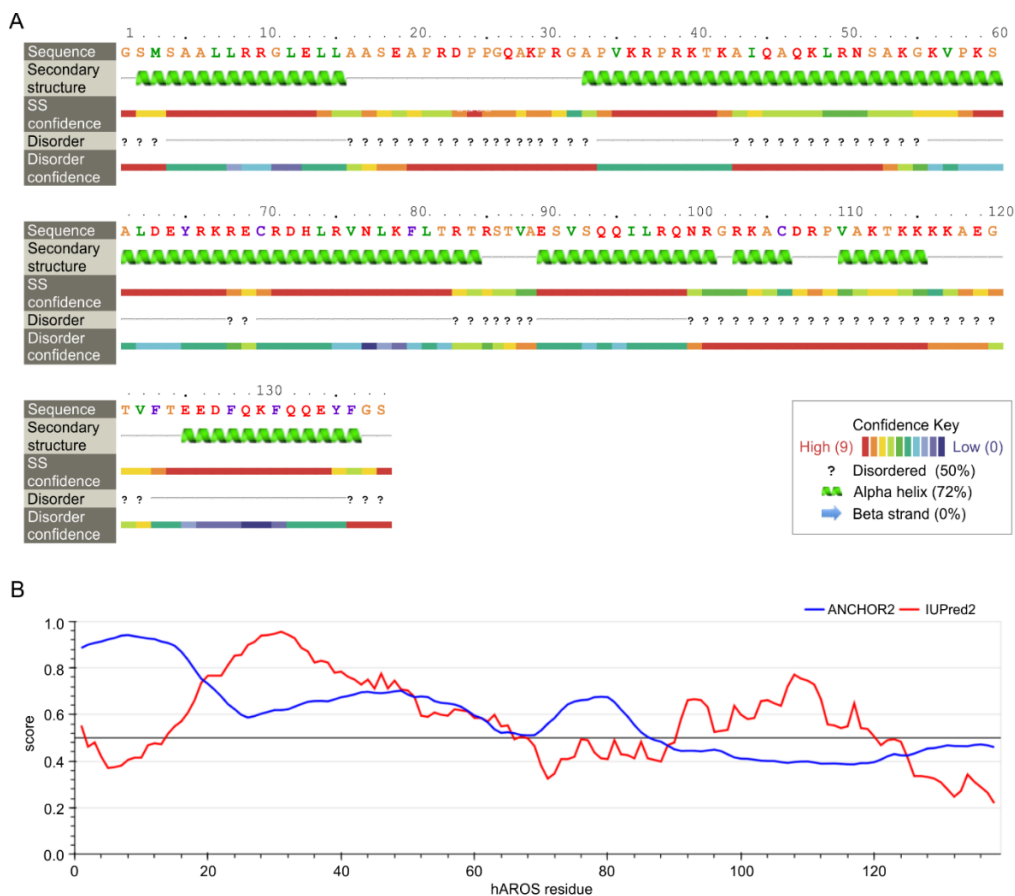


Figure 5.2: Secondary structure and disorder prediction of human AROS. **A** Secondary structure prediction for hAROS using Phyre²²⁶⁰ in intensive mode. The confidence is color-depicted from red = high to blue = low. **B** Disorder and binding site prediction for hAROS using IUPred2A²⁵⁷ in long disorder mode. Predicted disordered regions (red) and predicted binding regions (blue) both have a score > 0.5. For both predictions, the sequence of hAROS from pET15b without its His₆-tag was used, generating an offset of two amino acids.

5.3.2 Interaction between hSirt1 and hAROS

The refolded His₆-hAROS was investigated in interaction studies with hSirt1 to confirm that it is capable of interaction *in vitro*. However, neither a pulldown, nor *Blue Native* PAGE could undoubtedly identify a complex of the isolated proteins (Figure 4.15). Since a complex of Sirt1 and AROS was already detected by co-immunoprecipitation and Western Blots^{150,156}, other methods of direct interaction, which require only a small amount of protein, but have high sensitivity, were considered more appropriate. Indeed, a continuous enzyme-coupled deacetylation assay confirmed that isolated hSirt1 and hAROS interact and that His₆-hAROS is able to inhibit GST-fl-hSirt1 (Figure 4.16A). This is consistent with previous studies by Lakshminarasimhan *et al.*¹⁵⁵ and Kokkola *et al.*¹⁵⁶, who found an inhibitory effect of hAROS on hSirt1 with the degree of inhibition depending on the conditions of the assay. An initially detected weak *in vitro* activation of hSirt1 by hAROS¹⁵⁰ could not be confirmed. While His₆-hAROS is thus able to repress fl-hSirt1 activity, mini-Sirt1 activity was not affected (Figure 4.16B), indicating that other regions of hSirt1 are required for hAROS-mediated repression. In this regard, the *Fluor de Lys* assay with mini-Sirt1 and His₆-hAROS followed a 30 min reaction and subsequent studies indicated that mini-Sirt1 may have already deacetylated the substrate by that time. Thus, a weak inhibitory effect of His₆-hAROS might have been masked by the rapid deacetylation reaction of mini-Sirt1. While assay optimization for mini-Sirt1 and hAROS is clearly inevitable, Kokkola *et al.* also showed that fl-hSirt1 is necessary for the interaction with hAROS¹⁵⁶ and could not confirm the initially identified sufficient interaction region of hSirt1 residues 114-217¹⁵⁰. In addition, later studies found that hSirt1 Ser682 might be critical for the interaction of Sirt1 and AROS since DNA damage-induced phosphorylation at this site disrupts the complex¹⁵⁷. On the N-terminal region, residues 1-52 of hSirt1 comprising the A-motif might also be necessary for interaction with AROS⁹¹. Therefore, further assays or binding studies with hSirt1 deletion variants are required to clarify the minimal necessary hSirt1 region for interaction with hAROS.

Limited proteolysis of His₆-hAROS indicated that His₆-hAROS forms one or more stable core fragments (Figure 4.17A), which exhibit a melting curve and thus contain structured elements (Figure 4.17B). Future studies will have to investigate whether such hAROS fragment is also sufficient for inhibition of hSirt1. In fact, peptides derived from hAROS were previously able to repress hSirt1¹⁵⁶. In particular, hAROS peptides comprising residues 1-19, 26-42, or 78-99, which overlap with the three predicted hAROS binding regions for unknown partners (Figure 5.2B), and the putative structurally ordered hAROS region 109-126 were able to

inhibit fl-hSirt1¹⁵⁶. These peptide studies and the detailed MS analysis of the hAROS core fragment (Figure 4.17D) support a theory of a structurally elongated hAROS wrapping around hSirt1 with several binding regions, thereby directly or indirectly inhibiting hSirt1 deacetylase activity, e. g., by blocking access to the substrate binding pocket. Subsequent studies should thus focus on the construction of hAROS deletion mutants to examine their inhibitory function and binding ability to fl-hSirt1. Such deletion mutants might still be able to form a stable fold as proven by limited proteolysis with thermal denaturation. In addition, a shorter construct combined with a larger solubility enhancing purification tag might allow for the purification of hAROS as soluble protein resulting in higher yields and the possibility for more experiments to be done with one purification batch.

5.4 Interaction of the BTB domain of Hic1 with Sirt1

5.4.1 Expression and purification of Hic1-BTB

In scope of this work, the question was addressed, whether the isolated Hic1 BTB/POZ domain can interact with hSirt1. Thus, a construct of Hic1-(20-154) was designed according to known BTB folds (Figure 7.7). Interestingly, Hic1-BTB was expressed with and without N-terminal His₆-tag from different vectors (Figure 4.18A, Figure 4.19A, Figure 4.20A), which might have been caused by a hybrid expression vector. New selection and amplification of a single colony might thus prevent the double band formation. Both bands were reduced to a single band after proteolytic cleavage and pure Hic1-BTB eluted from the reverse AC with high imidazole concentrations (Figure 4.18B, Figure 4.20B). Subsequently, Hic1-BTB from pET15b eluted from SEC as highly pure apparent octamer (Figure 4.18C), which showed a defined mostly α -helical secondary structure (Figure 4.19C) and high stability (Figure 4.19D). In contrast, Hic1-BTB from pET15b*mod* eluted from SEC as apparent octamer and dimer (Figure 4.20C), with the yield and purity of the desired dimer being inconsistent. Both Hic1-BTB constructs have advantages in their purification process, in particular the different oligomerization species, which allow to study the interaction mode with hSirt1 in depth.

5.4.2 Oligomerization state of the BTB domain of Hic1 in solution

For assessing the oligomeric state of Hic1-BTB, an equation was applied reflecting the elution behavior of a protein of known molecular weight on the corresponding SEC column. But several purifications could not clarify whether the appearing Hic1-BTB dimer is actually a dimer or whether the peak is caused by the elution of abundant Hic1-BTB octamer together with a protein of ~27 kDa (Figure 4.20D). In addition, this method is less accurate than measurements involving, e. g., the refractive index²⁶⁸ or hydrodynamic radius^{269,270} of a

protein. Consequently, either SEC coupled to multiangle laser light scattering²⁶⁸ (SEC-MALLS), or sedimentation velocity analytical ultracentrifugation²⁶⁹, or determination of NMR heteronuclear spin relaxation rates²⁷⁰ should be performed.

Different oligomeric species of Hic1-BTB associated with different functions may seem likely, since BTB-ZF proteins are known to oligomerize¹⁸². The ability to homodimerize, heterodimerize, or recruit corepressors is particularly important for the role of many BTB-ZF proteins as transcription factors¹⁸². For example, the BTB-ZF protein B-cell lymphoma 6 (BCL-6) can homodimerize for direct regulation of p53 transcription, heterodimerize with Myc-interacting zinc finger protein 1 (Miz-1) for regulation of p21 transcription, or recruit the corepressor silencing mediator of retinoic acid and thyroid hormone receptor (SMRT) as homodimeric complex¹⁸². Besides dimers, higher oligomerization states of BTB-ZF proteins are rare²⁶¹. So far, only the *Drosophila melanogaster* BTB-ZF protein GAGA is known to form higher oligomers to increase its binding specificity and select for promoters with multiple GAGA-binding elements²⁷¹. Crosslinking suggested that GAGA can form dimers, trimers, tetramers, and hexamers²⁷¹. Similarly, crosslinking of Hic1-BTB was performed in this work to study the interaction with hSirt1. While no hSirt1/Hic1-BTB crosslinks occurred under the conditions employed, Hic1-BTB oligomers could be detected. Crosslinking of Hic1-BTB dimer with DSS revealed weak SDS PAGE bands for a monomer and dimer (Figure 4.21C), whereas crosslinking of Hic1-BTB octamer with DSS resulted in dimers, trimers, and tetramers, but not octamers (Figure 4.21D). Thus, Hic1-BTB is suggested to be able to form at least strongly associated and biologically relevant dimers in solution.

The obtained crystal structure of Hic1-BTB supports dimers, tetramers, and octamers (Figure 4.25B). Although a crystal structure captures a protein in a specific conformation, which can also depend on the crystallization condition and crystallographic contacts, two Hic1-BTB structures were gained from different crystallization conditions and different oligomeric species in solution, resulting in the same unit cell composition. However, analysis with the PDBe PISA server²⁶² suggests that only the Hic1-BTB dimer and octamer are stable in solution since they require a strong external driving force for dissociation (Table 4.2). Although the tetrameric species was observed in crosslinking and crystallographic studies, Hic1-BTB tetramers are probably not stable in solution (Table 4.2) and tetramerization likely occurs immediately prior to octamerization. As discussed for other BTB-ZF proteins, these data suggest that the dimeric species of Hic1-BTB may be used for interaction with other proteins, while the octameric species is likely preferred in absence of interaction partners.

5.4.3 Analysis of the interaction of Hic1-BTB with hSirt1

In vivo, the BTB domain of Hic1 co-immunoprecipitated with Sirt1^{184,185}, thus an interaction of the two isolated proteins was investigated. However, *Blue Native* PAGE of Hic1-BTB and hSirt1 resulted in false positive complexes because different oligomeric species of both proteins accumulated in the same area (Figure 4.21A, B). In particular, Hic1-BTB did not form a clear band and was observed to precipitate in the loading pockets, which might be due to the high pI of Hic1-BTB and possibly a complexation with Coomassie. Aggregation of Hic1-BTB in turn would cause fl-hSirt1 to precipitate, explaining why the fl-hSirt1 band seemed to disappear with increasing concentration of Hic1-BTB (Figure 4.21A). *Blue Native* PAGE was thus not suitable, but crosslinking of mini-Sirt1 and Hic1-BTB under various conditions also did not show an inter-protein complex (Figure 4.21C-F). All crosslinkers used are homobifunctional crosslinkers that target primary amines like the lysine side chain or the N-terminus of the protein through their N-hydroxysuccinimide (NHS) ester (e.g., DSS) or their imidoester (e.g., DMS)²⁷². However, the interaction surface between hSirt1 and Hic1-BTB might not involve lysines on either proteins. Thus, a heterobifunctional crosslinker with a maleimide on one side targeting the sulfhydryl group of cysteines or a carbodiimide targeting the carboxyl group of aspartate or glutamate might be a better choice²⁷².

For further investigation of the interaction, a TSA was performed revealing that the melting temperature for fl-hSirt1 and mini-Sirt1 increased in presence of Hic1-BTB octamer (Figure 4.22A). Although this is a first hint for an interaction between isolated hSirt1 and Hic1-BTB, the apparent stability enhancing effect might also have occurred through the overlap of both melting curves since the T_m for Hic1-BTB is comparable to the one for fl-hSirt1 (Figure 4.22A). In activity assays, Hic1-BTB seems to have a dual effect on fl-hSirt1 activity, which is more pronounced for the dimeric than for the octameric species: Hic1-BTB concentrations below 10 μ M seem to activate hSirt1, whereas higher concentrations lead to inhibition (Figure 4.22B-D). In this regard, the *Fluor de Lys* assay was not applicable for Hic1-BTB, probably due to an interaction of Hic1-BTB with the fluorophore of the artificial substrate (Figure 4.22F). The continuous coupled enzymatic assay showed no artificial impact of Hic1-BTB, but high concentrations of Hic1-BTB might still slightly precipitate despite buffer optimization, explaining the high variance of a control reaction (Figure 4.22G). For clarification of the activity-modulating effect of Hic1-BTB on hSirt1 activity *in vitro*, the mass spectrometric assay should be conducted because it requires only the minimal necessary cofactors for the reaction, while allowing for a direct readout of the amount of acetylated and

deacetylated substrate²¹⁶. Interestingly, Hic1-BTB can modulate mini-Sirt1 activity in the same manner as fl-hSirt1 activity suggesting that only regions included in mini-Sirt1 are relevant for the interaction of both proteins. Although fl-Hic1 represses hSirt1 expression *in vivo* by formation of a transcriptional repression complex with hSirt1 via the Hic1 BTB/POZ domain¹⁸⁴, these results suggest that the isolated BTB/POZ domain of human Hic1 can activate isolated hSirt1. Such activation might be relevant in unstressed healthy cells to prevent the p53-induced apoptosis pathway^{109,184}, but could also be necessary after DNA damage for subsequent deacetylation of Hic1 Lys314¹⁸⁸, which facilitates sumoylation of Hic1 and recruitment of the NuRD complex¹⁸⁸ for induction of apoptosis^{181,189}.

Consistent with activity assays, binding studies disclosed a comparable K_d for the affinity of Hic1-BTB dimer to fl-hSirt1 and mini-Sirt1 (Figure 4.23A, B). In addition, the interaction with Hic1-BTB was mapped to the catalytic core of hSirt1 with potential relevance of the SBD (Figure 4.23C). The hSirt1 ESA/CTR region, however, does not seem to be required for interaction with the isolated BTB domain of Hic1 (Figure 4.23C). Although fl-Hic1 failed to coimmunoprecipitate with a hSirt1- Δ ESA deletion variant in a previous study¹⁸⁵, this does not contradict the results obtained within this work because different Hic1 regions are known to interact with hSirt1^{184,185,188} and thus different hSirt1 regions might be sufficient for the interaction with either separate Hic1 regions or all Hic1 regions together. Furthermore, Sirtuin ligands are not necessary for interaction with the BTB domain of Hic1 (Figure 4.23D), suggesting that Hic1-BTB binds to hSirt1 regardless of an enzyme-substrate complex. Although slightly tighter binding was observed when the hSirt1 NAD⁺-binding pocket was occupied (Figure 4.23D), this is likely mediated by increased hSirt1 stability since the K_d for Hic1-BTB and mini-Sirt1 in presence of ADPr (Figure 4.23D) did not deviate from a previously obtained K_d for apo mini-Sirt1 (Figure 4.23B). Finally, the K_d for Hic1-BTB octamer and hSirt1 was 6-fold higher than the one for Hic1-BTB dimer (Figure 4.23E). This might indicate that dissociation of Hic1-BTB octamer to dimers is required prior to interaction of a dimer with hSirt1.

A further aspect of the presented studies was the fact that previous studies suggested a genotoxic stress-induced CK2-mediated phosphorylation of hSirt1 Ser659 and Ser661 was necessary for interaction with fl-Hic1 and subsequent deacetylation of Hic1 Lys314¹⁸⁵. An attempt of *in vitro* phosphorylation of mini-Sirt1 by CK2 followed by *Blue Native* PAGE failed (Figure 4.24A), either because CK2-mediated phosphorylation did not work under the conditions employed, or because *Blue Native* PAGE was not optimal for detecting a complex

involving Hic1-BTB. The activity of mini-Sirt1 phosphorylation mimicry mutants, however, was modulated by Hic1-BTB comparably to the activity of wild-type mini-Sirt1 (Figure 4.24C) and they also had a similar binding affinity (Figure 4.24D). Although the denoted mutations are not exact reflections of a phosphorylated serine, these results indicate that phosphorylations of hSirt1 S659 and S661 are not necessary for interaction with Hic1-BTB. In conclusion, the presented studies suggest that the BTB domain of Hic1 interacts with the catalytic domain of hSirt1, presumably by enhancing hSirt1 activity, independently of genotoxic stress-induced phosphorylations in the hSirt1 ESA region. Thus, the activation of hSirt1 by Hic1-BTB might be relevant for unstressed healthy cells, consistent with the previously discovered Hic1-Sirt1-p53 regulative loop¹⁸⁴.

5.4.4 Structural characterization of Hic1-BTB and putative interaction sites with hSirt1

For molecular and structural insights into the interaction mode of Hic1-BTB and hSirt1, crystallization of the BTB domain of Hic1 was attempted alone or in complex with mini-Sirt1. A structure for the complex could not be achieved, but two structures of Hic1-BTB octamer (Figure 4.25B) and dimer were obtained. Both structures from different crystallization conditions showed an identical unit cell with 16 monomers. Although this asymmetric unit composition is quite unusual, the space group was confirmed with Pointless^{229,230}, Phenix.Xtriage²³², and LABELIT²⁷³ and twinning was also excluded. Despite the presence of mini-Sirt1 in the protein solution for the second obtained structure with the dimeric Hic1-BTB, the sirtuin was absent in the structure. CocrySTALLIZATION of mini-Sirt1 with Hic1-BTB dimer was attempted since cocrySTALLIZATION with the Hic1-BTB octamer was unsuccessful and the Hic1-BTB octamer also showed a higher K_d for mini-Sirt1 than the dimer (Figure 4.23E). Thus, the dimeric species of Hic1-BTB was suggested to most likely interact with hSirt1. But despite formation of a Hic1-BTB and mini-Sirt1 complex during pre-incubation, Hic1-BTB might prefer its shielded octameric oligomerization state in the harsh crystallization conditions and thus disrupt the complex. The determination of the exact interaction site of Hic1-BTB with hSirt1 could thus be helpful and would allow the use of a shorter Hic1-BTB construct or a Hic1 peptide for cocrySTALLIZATION with mini-Sirt1. To identify putative interaction sites of Hic1-BTB with mini-Sirt1, the structure of Hic1-BTB will be analyzed in the following.

The fold of Hic1-BTB is highly similar to BTB domains from other BTB-ZF proteins, but does not contain a β 1-strand preceding the dimer-mediating α 1-helix, nor a β 5-strand (Figure 4.26A). As the crystallized Hic1-BTB construct was lacking 19 N-terminal amino

acids, such β 1-strand might form for Hic1-BTB as well. But since Hic1-BTB has an extension of 13 amino acids, folding into an additional α 4'-helix at the site of a usual β 5-strand, the existence of a β 1-strand is highly doubted (Figure 4.26A, B). While BTB/POZ domains from BTB-ZF proteins have sometimes gaps or extensions in their sequence²⁶¹, the existence of an additional structurally folded element has only been observed for the distantly related BTB/POZ domains from the Skp1 family²⁶³ (Figure 4.26B). Interestingly, the Hic1-BTB α 4'-helix seems to complex a metal ion (Figure 4.25C), whose nature could not be clarified. However, this metal ion complexation is likely a result of the crystallization condition since the other Hic1-BTB structure did not exhibit this density. Thus, research will have to show whether the additional α 4'-helix in Hic1-BTB actually needs to complex a metal ion for the function of Hic1-BTB as transcriptional repressor, and whether the helix plays a role in oligomerization or interaction with other proteins.

Hic1-BTB forms a biologically significant homodimer (Figure 4.25D), which is swapped via the α 1-helix and stabilized by four salt bridges. Salt bridges are sometimes observed at the dimer interface of other BTB domains, mostly at the hinge region where the N-terminal loop turns into the α 1-helix²⁶¹. But usually, not more than two salt bridges fix the dimeric conformation in swapped BTB homodimers²⁶¹, while non-swapped dimers may exhibit an additional pair of salt bridges between the β 1- and β 5-strands²⁶¹ (Figure 4.26E). The current state of research suggests that hydrophobic residues in α 1, α 2, and α 3 mainly contribute to the type of BTB dimerization, whereas β 1 and β 5 interactions play an auxiliary role²⁶¹. Since Hic1-BTB features also several hydrogen bonds in its dimeric interface (Figure 5.3A), the Hic1-BTB homodimer can be considered as a highly stable oligomeric species, consistent with analysis of the Hic1-BTB interfaces (Table 4.2). The Hic1-BTB homodimer has several surface-exposed regions that might participate in interaction with other proteins. The largest of these regions shows a strong positive charge close to the termini and the swapped α 1-helices (Figure 5.3A). This BTB region often binds other proteins, for example BCL-6 recruits the co-repressor SMRT through interactions with the β 1-strand and the helices α 1, α 2, and α 3²⁷⁴. The positively charged pocket between α 1, α 2, and α 3 was also shown to bind small molecule inhibitors of BCL-6^{275,276}. Another strongly positively charged region of Hic1-BTB comprises the C-terminal helices α 5 and α 6 (Figure 5.3A). This region, together with the additional helices α 7 and α 8 (Figure 4.26B), is involved in binding of Skp1 to F-box proteins^{182,263}. During MST-measurements of FITC-labeled Hic1-BTB with hSirt1, a binding curve was also observed for the so-called T-Jump region directly after switching on the MST

laser ²¹⁹. Such binding curve can be associated with binding in close proximity of the label ²¹⁹. As FITC labels the amino moiety of lysines and the $\alpha 5$ - and $\alpha 6$ -helices of Hic1-BTB contain many lysines (Figure 4.26A), these helices were suggested to be involved in binding of hSirt1. Therefore, Hic1-BTB deletion mutants were cloned, which lacked either the $\alpha 6$ -helix (comprising Hic1 amino acids 20-137 or 20-140) or both $\alpha 5$ - and $\alpha 6$ -helices (comprising Hic1 amino acids 20-125). However, none of these constructs could be expressed and purified, probably due to limited folding of the residual BTB domain. Thus, it remains to be shown whether this Hic1-BTB region really participates in interaction with hSirt1.

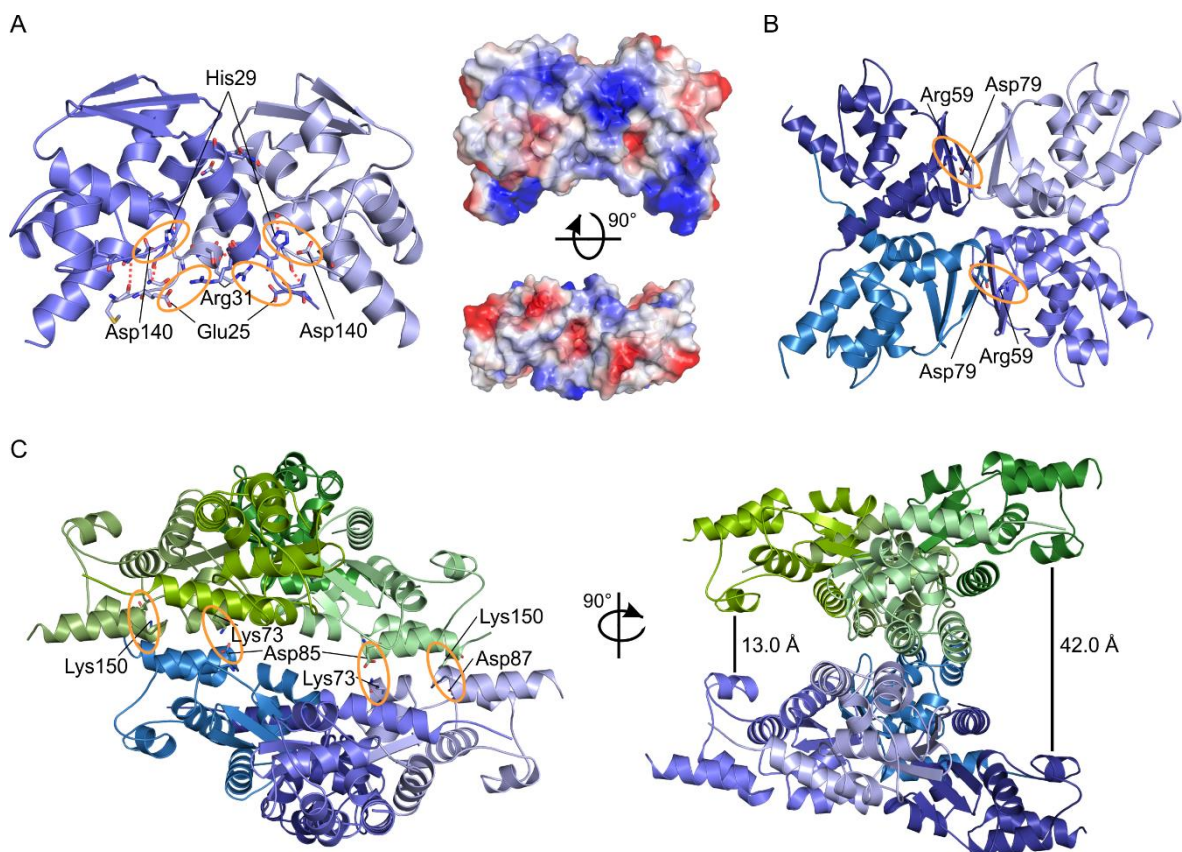


Figure 5.3: Analysis of homooligomerization interfaces of Hic1-BTB and potential binding sites for hSirt1. **A** Dimerization interface of Hic1-BTB. Four salt bridges (orange circles) are formed between the two monomers (blue/light blue). In addition, several hydrogen bonds (red dotted lines) stabilize the dimeric Hic1-BTB species. Electrostatic surface representation of Hic1-BTB dimer shown from -69.861 (red) to +69.861 (blue) $k_B T/e_c$. **B** Interface of the Hic1-BTB tetramer with two additional salt bridges (orange circles) between Arg59 and Asp79 of the opposite dimers. **C** Hic1-BTB octamer with four salt bridges (orange circles) between Asp87/Lys150 and Lys73/Asp85. The second view is rotated by 90° around the y-axis and shows the “clamp”, which might sandwich a binding partner like hSirt1 in its wider gap. The distances are measured between C α of Ala114 of the respective $\alpha 4'$ -helices.

The region around $\alpha 4'$ as well as the three β -strands is negatively charged and might likewise serve as interacting region for other proteins (Figure 5.3A). In the structure of Hic1-BTB, those β -strands are part of the interface of a homotetramer - a dimer of dimers (Figure 5.3B). According to the results from PDBe PISA ²⁶² (Table 4.2) and the behavior of Hic1-BTB in SEC (Figure 4.18C, Figure 4.20C), the tetrameric state of Hic1-BTB is probably not stable in

solution and might be formed shortly prior to octamerization. This tetrameric species is thus not considered as putative hSirt1-interacting Hic1-BTB species.

Octamerization of Hic1-BTB occurs mostly via the $\alpha 5$ - and $\alpha 6$ -helices of two diagonally opposite monomers of the below lying tetramer with two diagonally opposite monomers of the above lying tetramer (Figure 5.3C) - another reason why those helices might be involved in protein-protein interactions. Through distortion of the two tetrameric planes, this two-point interface results in the non-involved monomers being further apart. While the distance between Ala114 within the $\alpha 4'$ -helix of one monomer and Ala114 of the below lying monomer is 13.0 Å on one side of the Hic1-BTB octamer, this distance is significantly larger on the other side and amounts to 42.0 Å (Figure 5.3C). The arrangement of monomers within a Hic1-BTB octamer creates the illusion that Hic1-BTB might act as a clamp which sandwiches hSirt1 with the wider one of the two gaps (Figure 5.3C). In this work, both the Hic1-BTB dimer and octamer have been shown to interact with hSirt1 and subsequent binding and activity studies with Hic1-BTB peptides should determine the actual binding site of Hic1-BTB to hSirt1. This would allow crystallization studies with the most promising Hic1-BTB peptide and mini-Sirt1 for verification or, in case of failure of the first, a docking study with existing structures of Hic1-BTB and mini-Sirt1 using appropriate restraints.

5.5 Biochemical and structural characterization of hSirt1 inhibition by HIV1-Tat

5.5.1 Characterization of HIV1-Tat Cys⁻

For recombinant overexpression of HIV1-Tat in *E. coli* and for preparation of monomeric reduced Tat for NMR studies¹⁹⁹, seven cysteine exchanges were conducted²⁰⁹. The resulting Tat Cys⁻ showed no defined secondary structure in a CD spectrum (Figure 4.27B). This is in line with a prediction from IUPred2A²⁵⁷ indicating that Tat Cys⁻ is disordered (Figure 5.4A) and thus belongs to the class of intrinsically disordered proteins (IDPs)^{266,277,278}. The NMR structure of Tat Cys⁻ does not deviate from the NMR structure of wild-type HIV1-Tat²⁰⁹ measured under the same conditions (Figure 5.4B). But HIV1-Tat from another isolate adopts a different NMR structure¹⁹⁹ (Figure 5.4C). As several NMR studies of HIV1-Tat from different isolates and with different local conformations have been published in the past 20 years^{199,209,279,280}, this shows that the structure of Tat depends on the conditions employed²⁷⁷.

Such structural variability also explains Tat's capability to interact with multiple partners - even at the same time - and to affect multiple biological functions²⁷⁷, possibly by adopting different local conformations²⁷⁸. IUPred2A²⁵⁷ predicts that Tat Cys⁻ residues 28-56 undergo

a conformational change and adopt a distinct secondary structure upon binding of a partner (Figure 5.4A). In fact, CD spectroscopy in presence of TFE²²² indicated that Tat Cys⁻ has the propensity to form α -helices (Figure 4.27C). A recent crystal structure of HIV1-Tat in complex with P-TEFb also showed a helical structure for Tat residues 29-41, which may be stabilized by two zinc ions²⁰⁰ (Figure 5.4D). It is not clear, however, whether Tat adopts the same structure with different binding partners and whether the structural integrity depends on the complexation of metal ions. The current state of research suggests that different regions of Tat follow different mechanisms of conformational change upon association with their binding partner²⁷⁸. For example, Tat residues 29-32 and 61-89 are proposed to follow an induced fit mechanism²⁷⁸, where binding occurs before conformational change^{267,278}. In contrast, Tat residues 49-62 are suggested for conformational selection, where a local conformation similar to the bound form is selected by the target protein²⁷⁸. Thus, high resolution crystal structures in conjunction with dynamic NMR measurements are needed to study the interaction between hSirt1 and HIV1-Tat Cys⁻.

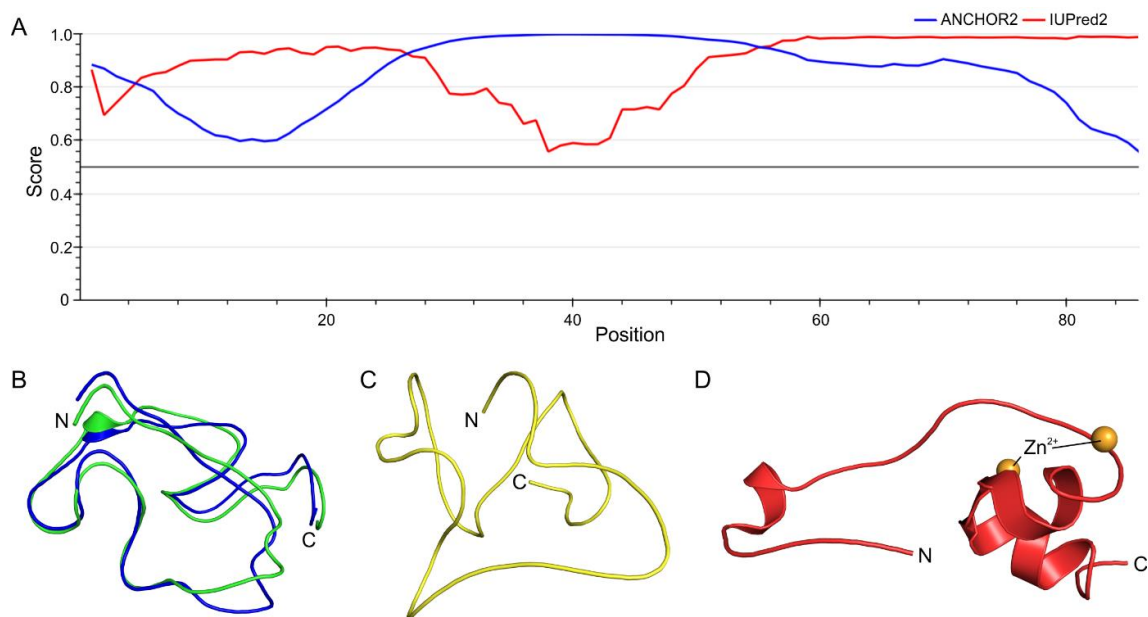


Figure 5.4: Structure prediction and conformations of HIV1-Tat. **A** Disorder and binding site prediction for Tat Cys⁻ using IUPred2A²⁵⁷ in long disorder mode. Predicted disordered regions (red) and binding regions (blue) have a score > 0.5. **B** Superposition of an NMR structure of Tat Cys⁻ (PDB: 1TAC; blue) with an NMR structure of wild-type HIV1-Tat (PDB: 1TBC; green)²⁰⁹ (RMSD = 0.153 Å for 74 C α atoms). **C** NMR structure of HIV1-Tat T40K (PDB: 1TIV; yellow). **D** Crystal structure of HIV1-Tat (red) from a complex with human P-TEFb (not depicted) (PDB: 3MI9)²⁰⁰.

5.5.2 Inhibition of human sirtuin isoforms by HIV1-Tat Cys⁻

While HIV1-Tat was found to inhibit hSirt1 *in vivo*^{125,204}, this study focused on the *in vitro* effect of recombinant Tat Cys⁻ on human sirtuin isoforms. Indeed, fl-hSirt1-mediated deacetylation of a natural p53-derived substrate was repressed by Tat Cys⁻ (Figure 4.28A), demonstrating that isolated and pure Tat Cys⁻ is able to bind directly to isolated fl-hSirt1 *in*

vitro and inhibit its deacetylase activity. In a *Fluor de Lys* assay, Tat Cys⁻ inhibited fl-hSirt1 with a lower IC₅₀ (Figure 4.28B), which coincides with the IC₅₀ reported by Kwon *et al.*²⁰⁴ using recombinant fl-hSirt1 and a synthetic Tat-(1-72) peptide in the same type of assay. These results show that the cysteine deletions in Tat Cys⁻ do not interfere with its ability to interact with hSirt1. Thus, a putative cysteine-mediated interaction of Tat with the Zn²⁺ ion of hSirt1, which is essential to hSirt1's structural integrity³³, can also be excluded. Similarly, Tat does not seem to require zinc binding for inhibition of hSirt1, as such metal cofactor would be complexed by cysteines.

For determination of the regions of hSirt1 which are necessary for Tat-mediated inhibition, activity assays with hSirt1 deletion constructs were performed showing that N- and C-terminal regions of hSirt1 are not essential for the interaction with Tat Cys⁻ (Figure 4.28C). In addition, the region from hSirt1 residues 505-641 (Figure 4.28D) as well as the Sirt1-specific SBD and ESA/CTR region (Figure 4.28E) do not impact Tat-mediated inhibition of hSirt1. Similar to the inhibition of fl-hSirt1 by Tat Cys⁻ (Figure 4.28A, B), the viral protein repressed mini-Sirt1 deacetylation of natural p53short substrate and artificial *FdL-1* substrate with an IC₅₀ differing almost by 10-fold (Figure 4.28D). Since the inhibition potency of Tat Cys⁻ on hSirt1 seems to depend on the substrate, this might indicate a substrate-competitive inhibition of hSirt1. While previous co-immunoprecipitation assays already showed that only the hSirt1 catalytic domain is necessary for binding of Tat²⁰⁴, these new results indicate that the catalytic domain of hSirt1 is also sufficient for Tat-mediated inhibition *in vitro*.

In addition to hSirt1, Tat Cys⁻ was able to repress the deacetylase activity of human Sirt2 and Sirt3 to a similar extent (Figure 4.29C). Although Tat-mediated inhibition of hSirt2 showed different potencies depending on the substrate, which were partly influenced by incompatibility with Tat (Figure 4.29A), hSirt2 can be repressed by Tat Cys⁻ as shown with a different substrate (Figure 4.29C) that did not interact with Tat (Figure 4.30C). Human Sirt1-3 also bound to Tat Cys⁻ *in vitro* (Figure 4.29B), whereby hSirt1 had the highest binding affinity and was inhibited with the lowest IC₅₀ (Figure 4.29C). In contrast to hSirt1-3, the effect of Tat Cys⁻ on the primary deacetylase activities of hSirt5 and hSirt6 was not clear (Figure 4.29A) and requires a higher initial deacetylase activity. While Tat previously failed to coimmunoprecipitate with any other human sirtuin isoform¹²⁵, the new results suggest that isolated HIV1-Tat is able to bind to and inhibit isolated hSirt1-3 *in vitro*. In the physiological context, inhibition of hSirt1 during HIV1 infection is necessary to promote HIV1 transcription by activation of infected CD4⁺ T-cells as well as activation of p65 in NF-κB²⁰⁴. Furthermore,

inhibition of hSirt1 by Tat initiates apoptosis of non-infected CD4⁺ T-cells by hyperacetylation of the hSirt1 target p53^{205,206}. Besides that, only repression of hSirt2 by HIV1-Tat might be physiologically relevant as hSirt2 can shuttle from the cytosol to the nucleus³⁷, whereas hSirt3 is strictly located in the mitochondria³⁷ and HIV1-Tat is only found in the nucleus¹⁹³ or the cytoplasm²⁰⁵. Nevertheless, those sirtuin isoforms can serve as models to elucidate the inhibition mechanism of HIV1-Tat on hSirt1, since the binding affinity and inhibition potency of hSirt2 and hSirt3 by Tat Cys⁻ are comparable *in vitro*.

5.5.3 Sirtuin activity-modulating potential of HIV1-Tat Lys50

In comparison to inhibition by Tat Cys⁻ (Figure 4.29C), the IC₅₀ for inhibition of hSirt1 and hSirt3 by a Tat₄₆₋₅₄ peptide was 15-fold increased, indicating that other parts N- or C-terminal to Tat Lys50 might be relevant for potent inhibition. This assumption is supported by the fact that the binding affinity for Tat₄₆₋₅₄ to mini-Sirt1 was 40-fold lower (Figure 4.31D) compared to the one for Tat Cys⁻ (Figure 4.29C). An ac-Tat₄₆₋₅₄ peptide had a higher affinity for mini-Sirt1 than Tat₄₆₋₅₄ (Figure 4.31D) and was also deacetylated by mini-Sirt1 *in vitro* (Figure 4.31C). Deacetylation of ac-Tat₄₆₋₅₄ by hSirt2 and hSirt3 was not investigated within this study since hSirt1-3 were already shown to deacetylate a synthetic ac-Tat₁₋₇₂ peptide¹²⁵. Together, these results confirm that acetylated and non-acetylated Tat can bind to hSirt1 *in vitro* as proposed by Pagans *et al.*¹²⁵. However, previously, both forms of HIV1-Tat were bound equally well to hSirt1 in coimmunoprecipitation assays¹²⁵. The more sensitive assays employed here, resulting in a different affinity of acetylated and non-acetylated Tat peptide (Figure 4.31D), suggest that Tat does not act as a “supersubstrate”²⁰⁴, which stays bound after its own deacetylation and blocks access for other substrates. In addition, an accumulation of deacetylated Tat substrate, and thus hSirt1 inhibition, was not observed at later times of the assay (Figure 4.31C), indicating that deacetylated Tat is quickly released from the sirtuin substrate binding pocket.

For investigation of the binding mode of ac-Tat₄₆₋₅₄, hSirt3 was cocrystallized with the peptide yielding a high resolution complex, which resembles a hSirt3/substrate structure (Figure 4.32A). The hSirt3-(118-399)/ac-Tat₄₆₋₅₄ structure superimposes well with mini-Sirt1 including overlapping backbone and sidechain positions of ac-Tat₄₆₋₅₄ and the hSirt1 substrate p53 (Figure 4.33A). Binding of ac-Tat₄₆₋₅₄ is supported by charge complementarity of the sirtuin substrate cleft and the Tat peptide (Figure 4.32C) in both complexes and by similar interactions between hSirt1/hSirt3 and ac-Tat₄₆₋₅₄ (Figure 4.32D, Figure 4.33B). Therefore, the hSirt3-(118-399)/ac-Tat₄₆₋₅₄ complex shows that acetylated

HIV1-Tat binds to hSirt1 and hSirt3 like known sirtuin substrates, consistent with the previously identified deacetylation of HIV1-Tat by hSirt1-3¹²⁵.

5.5.4 Mapping of the sirtuin-inhibiting region on HIV1-Tat

Since the close vicinity of HIV1-Tat Lys50 did not prove to be sufficient for inhibition of hSirt1-3 and Tat may have various binding regions as indicated by IUPred2A analysis (Figure 5.4A), other regions of Tat were investigated for their sirtuin-inhibiting potential. First, NMR studies showed that the C-terminal region of HIV1-Tat does not contribute to binding, while the effect of the N-terminal region was not clear (Figure 4.30A). But Tat Cys⁻(1-63) and Tat Cys⁻(21-63) were still able to inhibit hSirt1 (Figure 4.30B, C) and thus, the region of HIV1-Tat residues 21-63 was considered essential for inhibition of hSirt1 *in vitro*.

Further mapping of the sirtuin-inhibiting region of HIV1-Tat was then performed with synthetic peptides. While the longest peptide Tat₃₁₋₆₀ inhibited hSirt1-3 most efficiently (Figure 4.34A) and with an IC₅₀ comparable to Tat Cys⁻ (Figure 4.35A), other Tat peptides had a less pronounced effect (Figure 4.34A). Notably, the first assay (Figure 4.34A) was performed in presence of 100 μM Tat peptide at half of the respective sirtuin substrate K_m. This entailed that for mini-Sirt1 and hSirt3, Tat peptide and sirtuin substrate were used at a molar ratio of 1:1, while the Tat peptide was used in a molar excess of 2:1 for hSirt2, explaining the lacking specificity of hSirt2 repression by Tat peptides (Figure 4.34A). As HIV1-Tat and sirtuin substrate were suspected to be competitive²⁰⁴ (Figure 4.28A-C), the results for hSirt2 should be treated with caution. In summary, these assays indicate that major contribution to the inhibition of human Sirt1-3 is provided by HIV1-Tat residues 31-60, whereby residues 31-49 alone are not sufficient for potent repression (Figure 4.35A, B). But residues from this latter region may contribute to inhibition together with HIV1-Tat residues C-terminal of the critical residues around Arg49, which are included in the Tat₃₁₋₆₀ peptide.

The next question addressed was whether there are two interacting inhibitory regions or one larger region. Most importantly, IC₅₀ determinations showed that the C-terminal HIV1-Tat residues 55-59 seem to play a key role in the inhibition potency for mini-Sirt1 (Figure 4.36A), but could not be confirmed in case of hSirt3 (Figure 4.36E). On the N-terminal side of Tat Lys50, Tat₄₉₋₆₀ was sufficient to inhibit mini-Sirt1 and hSirt3 comparably to Tat Cys⁻, but further N-terminal residues were necessary to provide a high potency for inhibition of fl-hSirt1 and hSirt2 (Table 4.3). Since measurements with the Tat₄₉₋₆₀ peptide were lacking some efficacy despite the low IC₅₀ (Figure 4.36A) combined with a high variance for the derived IC₅₀ values (Figure 4.36C-E), HIV1-Tat residues 34-59 were considered to be

sufficient for robust and highly potent inhibition of the deacetylase activity of hSirt1-3 *in vitro*. Regarding the physiological role of this region, HIV1-Tat residues 49-60 comprise the basic region including a nuclear localization signal from Tat residues 48-53¹⁹⁷ and a cell penetrating signal from Tat residues 48-61¹⁹⁷. The basic Tat region is responsible for binding to the TAR RNA¹⁹⁶ and to the nuclear import receptor importin- α ¹⁹⁷. Interestingly, Tat residues 49-52 were also identified as the central interacting region with hSirt3 in crystal structures, as discussed below.

5.5.5 Mechanism of inhibition of hSirt1-3 by HIV1-Tat

Two complex structures of hSirt3-(118-399) with Tat₃₄₋₅₉ (Figure 4.37) or Tat₃₇₋₅₉ (Figure 4.38) were obtained within this work showing that the inhibitory Tat peptides bind in the sirtuin substrate binding cleft (Figure 4.37A, Figure 4.38A) like an acetylated Tat substrate peptide (Figure 4.32A). In fact, the sidechain and backbone of HIV1-Tat residues from the -1 to the +2 positions respective to the critical Lys50 overlap exactly and independently of the acetylation status of Lys50 (Figure 4.37B). This entails that the same hydrogen bonds are formed between Tat amino acids 49-52 and hSirt3 (Figure 4.32D, Figure 4.37D, Figure 4.38C) to bind the strongly positively charged Tat peptide in the negatively charged hSirt3 substrate binding cleft (Figure 4.32C). Binding of the acetylated and non-acetylated Tat peptides to hSirt3 differed only at two points: first, the ac-Tat₄₆₋₅₄ peptide was able to form an additional hydrogen bond between Ser46 and hSirt3 Leu298 (Figure 4.32D), which is probably caused by increased flexibility of the amino acids at the termini of the peptides. Second, the inhibiting Tat₃₄₋₅₉ and Tat₃₇₋₅₉ peptides formed sidechain hydrogen bonds from Tat Arg52 to Val258 and Gln260 of the second hSirt3 molecule in the asymmetric unit (Figure 4.37D, Figure 4.38C). As these latter interactions could be ascribed to be solely a result of crystal packing (Table 4.5, Table 4.6), an interaction of HIV1-Tat with the sirtuin Zn²⁺-binding domain was excluded as inhibitory mechanism.

The difference between binding of Tat₃₄₋₅₉ and Tat₃₇₋₅₉ to hSirt3 lies in the location of the terminal amino acids 44-46 and 56-57 of HIV1-Tat (Figure 4.38A) associated with an additional hydrogen bond from Arg56 to hSirt3 Leu347 in the hSirt3-(118-399)/Tat₃₇₋₅₉ complex (Figure 4.38C). As the positions of these amino acids in the respective complexes were confirmed with 2mF_o-DF_c composite omit maps (Figure 4.37C, Figure 4.38B), the small variations likely derive from the local molecular surroundings of the respective crystal packing and show that both hSirt3 structures with inhibiting Tat peptides appear to be equal. Therefore, HIV1-Tat can bind in its acetylated form as a substrate to the hSirt3 substrate

binding cleft or in its deacetylated form as an inhibitor in the same mode. In this scenario, most interactions are mediated from Tat amino acids 49-52. Since these hydrogen bonds are either emanating from the Tat peptide bonds or hSirt3 Glu/Gln residues (Figure 4.38D), matching the charge composition of HIV1-Tat and the substrate binding cleft (Figure 4.32C), they have equivalents within the hSirt1 substrate binding cleft (Figure 4.39B, Figure 4.40B). Indeed, previous studies showed that mutation of amino acids in the acetyl-lysine binding region of hSirt1 prevents binding of Tat²⁰⁴. Thus, the basic region of HIV1-Tat residues 49-52 seems to be essential for binding to and inhibiting hSirt1-3. In addition, the comparable binding mode of HIV1-Tat in hSirt3 and mini-Sirt1 shows that the hSirt3-(118-399) complexes with Tat peptides are valid models for elucidating features contributing to the binding and inhibition potency of specific sirtuin isoforms.

One of such contributions is derived from the structural explanation for the stronger inhibition of mini-Sirt1 by Tat peptides including amino acids 55-59, which was not evident in hSirt3 (Table 4.3). In this context, comparison to different mini-Sirt1/substrate complexes showed that the location of the Sirt1-specific SBD seems to be crucial (Figure 4.39A, B, Figure 4.40A, B). While comparison of the binding mode of Tat₃₇₋₅₉ to a mini-Sirt1/STAC/p53/carba-NAD complex did only show interactions similar to the ones to hSirt3 (Figure 4.39B), superposition to a mini-Sirt1/resveratrol/*FdL-1* complex highlighted two features (Figure 4.40B): due to the closer vicinity of the SBD, additional hydrogen bonds may be formed between HIV1-Tat Gln54 and hSirt1 Leu203, Leu206, and Thr209 as well as between Tat Arg55 and hSirt1 Leu205 (Figure 4.40D). Strikingly, the sidechain of Tat Arg53 seems to clash with the sidechain of hSirt1 Arg446 and disrupt the important salt bridge⁹⁷ between hSirt1 Arg446 and Glu230 (Figure 4.40C). However, the sidechain position of Arg53 in the 2mF_o-DF_c maps of the hSirt3 complexes with inhibiting Tat peptides (Figure 4.37C, Figure 4.38B) was not as clear as in the hSirt3 complex with ac-Tat₄₆₋₅₄ at 1.65 Å resolution (Figure 4.32B). In addition, the SBD was not essential for Tat-mediated inhibition of hSirt1 (Figure 4.28E), suggesting that the observed interactions of Tat amino acids 55-59 with the hSirt1 SBD only contribute to a higher inhibition potency by impairing the binding of the SBD to the catalytic core of hSirt1.

This model is supported by crosslinking experiments which disclosed a crosslink between Tat Lys71 and hSirt1 Lys238 (Table 4.8). Mapping of the crosslink position on mini-Sirt1 (Figure 4.41E) shows that the C-terminal glutamine-rich region of HIV1-Tat might wind from the exit of the sirtuin substrate binding cleft towards the bottom of the Rossmann fold domain,

while Tat always remains between the SBD and the catalytic core. The C-terminal amino acids 60-86 of HIV1-Tat would be close to the ESA/CTR region⁹³ and could additionally disturb its binding to the catalytic core (Figure 4.41E). However, NMR experiments showed no relevance for the C-terminal amino acids 60-86 of Tat for binding to mini-Sirt1 (Figure 4.30A) and neither was the ESA/CTR region essential for Tat-mediated inhibition of hSirt1 (Figure 4.28E).

N-terminal of the last defined amino acid Gly44 of Tat₃₇₋₅₉ (Figure 4.38A), another crosslink between Tat Lys28 and hSirt1 Lys430 was revealed (Table 4.7). Mapping with a structure of Tat₁₋₄₉²⁰⁰ indicated that the involved lysines might be located in immediate vicinity at the entrance of the substrate binding cleft of hSirt1 (Figure 4.41C). However, the intrinsically disordered protein Tat might change its structure in presence of different binding partners^{277,278} (Figure 5.4). Depending on the structure of the N-terminal Tat residues 1-49 in the presence of hSirt1-3, further isoform-specific interactions might increase the respective potency of Tat-mediated inhibition. In the following, the obtained structure of Tat₃₇₋₅₉ will be compared to published structures of HIV1-Tat apo or in complex with diverse binding partners to elucidate its most likely fold in presence of sirtuins.

Previous NMR studies as well as CD spectroscopy (Figure 4.27B) have shown that HIV1-Tat and the Tat Cys⁻ variant adopt a disordered structure in absence of binding partners^{199,209} (Figure 5.4B, C). The structures of Tat₃₇₋₅₉, Tat₃₄₋₅₉, and ac-Tat₄₆₋₅₄ in presence of hSirt3 are elongated and superimpose with RMSD values between 1.1-1.2 Å for 8-12 C_α atoms (Figure 5.5A). This fold for the basic region of HIV1-Tat is consistent with other structures of Tat in presence of different binding partners (Figure 5.5B). For example, a Tat₄₈₋₅₅ peptide from a complex with importin- α ¹⁹⁷ (PDB: 5SVZ) overlays to Tat₃₇₋₅₉ with an RMSD = 1.074 Å for eight C_α atoms and an acetylated Tat₄₆₋₅₆ peptide from a complex with PCAF²⁸¹ (PDB: 1JM4) superimposes with an RMSD = 2.066 Å for ten C_α atoms (Figure 5.5B). Therefore, the high structural similarity of the sirtuin substrate binding cleft, together with the hitherto low variability of the fold of the basic region of HIV1-Tat, leave no doubt that HIV1-Tat residues 49-57 will bind to hSirt1 and hSirt2 in the same conformation and mode as they bind to hSirt3. This also supports the previous assumption that the basic region of Tat undergoes conformational selection, where a local conformation similar to the bound form is selected by the target protein prior to binding²⁷⁸.

Concerning the N-terminal proline/acidic, cysteine-rich, and core regions of HIV1-Tat, Tat₃₇₋₅₉ superimposes with a Tat₁₋₄₉ peptide from a complex with Cdk9 and cyclin T1²⁰⁰

(PDB: 3MI9) with an RMSD = 2.359 Å for six C_α atoms, while superposition to apo Tat Cys⁻ (PDB: 1TAC) results in an RMSD = 4.052 Å for 14 C_α atoms (Figure 5.5C). While apo Tat Cys⁻ is disordered and exhibits an elongated conformation for the basic region, Tat₁₋₄₉ forms two helices from amino acids 29-34 and 35-41, which may additionally be stabilized by coordination of two Zn²⁺ ions (Figure 5.5C). As discussed earlier, HIV1-Tat residues 28-56 are suggested for adoption of a distinct structure upon binding a partner (Figure 5.4A), independently of the cysteine deletion mutations (Figure 4.27C, Figure 5.4A), and thus the cysteine-rich and core regions of HIV1-Tat might also form those helices in presence of hSirt1-3 (Figure 5.5C). In addition, an induced fit mechanism was proposed for the region of HIV1-Tat 29-32²⁷⁸, where binding occurs before conformational change, thus being able to prevent the observed clash with the sirtuin structure (Figure 4.41C). Tat therefore appears to bind into the sirtuin substrate binding cleft with its basic region, while its N-terminal cysteine-rich and core regions might form small helices at the entrance of the substrate binding cleft as supported by the expected close vicinity of Tat Lys28 and hSirt1 Lys430 from crosslinking.

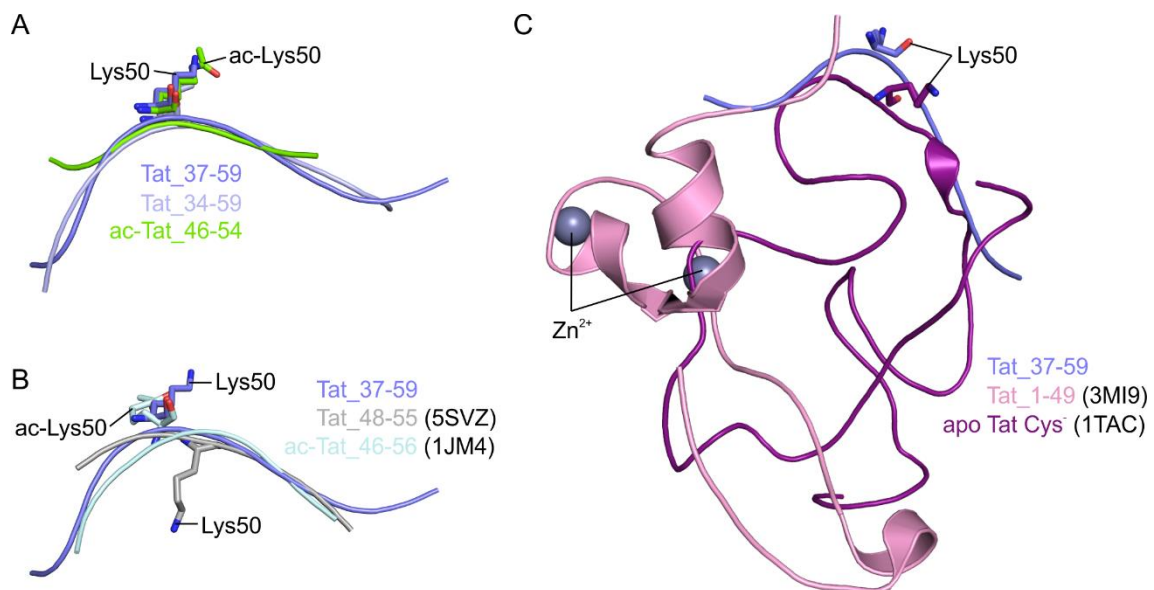


Figure 5.5: Comparison of Tat₃₇₋₅₉ to other structures of HIV1-Tat. **A** Superposition of Tat₃₇₋₅₉ (blue) with Tat₃₄₋₅₉ (RMSD = 1.231 Å for 12 C_α atoms; light blue) and ac-Tat₄₆₋₅₄ (RMSD = 1.095 Å for 8 C_α atoms; green) from the obtained hSirt3-(118-399) complexes (Table 7.8, Table 7.9). **B** Superposition of Tat₃₇₋₅₉ (blue) with Tat₄₈₋₅₅ from a complex with importin- α (PDB: 5SVZ; grey) and with ac-Tat₄₆₋₅₆ from a complex with PCAF (PDB: 1JM4; cyan). **C** Superposition of Tat₃₇₋₅₉ (blue) with Tat₁₋₄₉ (pink) from a complex with Cdk9 and cyclin T1 (PDB: 3MI9) or with apo Tat Cys⁻ (PDB: 1TAC; purple).

Not surprisingly, HIV1-Tat was found to be competitive to the sirtuin substrate. While this was initially assumed due to different IC₅₀ values for different hSirt1 substrates (Figure 4.28A, B, D), a detailed analysis using assays (Table 4.9) and MST (Table 4.10) showed that binding of Tat Cys⁻ and sirtuin substrate is indeed mutually exclusive. The presented results are in accordance with previous studies by Kwon *et al.*²⁰⁴, who found that

mutation of the acetyl-lysine binding site prevents binding of HIV1-Tat. Previously, Tat was also suggested to act as a “supersubstrate”, which is deacetylated by hSirt1 and then stays bound to block access for other substrates²⁰⁴. The K_m for ac-Tat₄₆₋₅₄ (Figure 4.31C) was comparable to the K_m for other hSirt1 substrates, suggesting that Tat is deacetylated directly after binding to hSirt1. Despite a defined upper baseline, the different binding affinities for an ac-Tat₄₆₋₅₄ peptide and a non-acetylated Tat₄₆₋₅₄ peptide (Figure 4.31D) indicate that deacetylated HIV1-Tat is then quickly released from the hSirt1 substrate binding pocket. This would be consistent with reports that hSirt1-mediated deacetylation of Tat is required for rapid initiation of the next cycle of HIV1 transcription, since only deacetylated Tat can bind to the TAR RNA²⁰¹ (Figure 1.13C). Concerning Tat-dependent inhibition of the hSirt1 pathways associated with deacetylation of p65²⁰¹ and p53²⁰⁵, a HIV1-Tat K50A mutant was able to induce p65 hyperacetylation at a comparable rate as wild-type HIV1-Tat²⁰⁴, indicating that prior deacetylation of Tat is not required for Tat-mediated inhibition of hSirt1. Thus, deacetylation of HIV1-Tat by hSirt1 and inhibition of hSirt1 by Tat seem to be two independent mechanisms *in vivo* instead of a “supersubstrate”-induced mechanism.

Regarding a putative competition of Tat and NAD⁺ binding to hSirt1-3, contradictory results were obtained from activity assays (Table 4.9) and MST experiments (Table 4.10). While K_m determinations of NAD⁺ for mini-Sirt1 and hSirt3-(93-399) suggested that NAD⁺ binding does not impair Tat binding (Table 4.9), MST experiments showed a weaker binding affinity of Tat Cys⁻ in presence of NAD⁺ for mini-Sirt1, fl-hSirt1 and hSirt3-(93-399) (Table 4.10). However, MST in presence of NAD⁺ resulted in unavoidable bleaching which might have influenced the K_d derived from initial fluorescence. Another method like isothermal titration calorimetry might be more appropriate. An obtained structure of hSirt3-(118-399)/Tat₃₄₋₅₉ showed ADPr instead of the cocrystallized NAD⁺ (Figure 4.44). Although one might assume that Tat and NAD⁺ are thus competitive, causing NAD⁺ hydrolysis, such non-enzymatic NAD⁺ hydrolysis is often observed in sirtuin crystal structures^{79,126,282}. Since Tat Lys50 provides also sidechain hydrogen bonds for the 2' and 3' OH moieties of ADPr ribose (Figure 4.44D), which are important for the deacetylation mechanism (Figure 1.7), this rather suggests that HIV1-Tat and NAD⁺ are not competitive and can bind to hSirt1-3 at the same time. These structural observations coincide with studies by Kwon *et al.*, in which mutation of amino acids within the NAD⁺ binding pocket of hSirt1 did not hinder binding of Tat²⁰⁴.

In conclusion, the presented studies show that HIV1-Tat inhibits the deacetylase activity of hSirt1, hSirt2, and hSirt3 *in vitro* by competing for the same binding site with the sirtuin

substrate, but not with the sirtuin cofactor NAD⁺. Binding of HIV1-Tat to hSirt1-3 is also not dependent on the previously shown complexation of Zn²⁺ ions and neither does Tat interact with the sirtuin zinc-binding domain. Instead, the basic region of HIV1-Tat binds into the sirtuin substrate binding cleft, whereby the major contribution for binding and inhibition is provided by Tat amino acids 49-52. A higher potency for the physiologically relevant inhibition of hSirt1 is mediated by Tat amino acids 53-59, which seem to interfere with the rigid-body movement of the SBD towards the catalytic core of hSirt1 by disruption of the salt bridge between hSirt1 Glu230 and Arg446.

6. References

1. Seet, B. T., Dikic, I., Zhou, M. M. & Pawson, T. Reading protein modifications with interaction domains. *Nat. Rev. Mol. Cell Biol.* **7**, 473–483 (2006).
2. Jensen, O. N. Interpreting the protein language using proteomics. *Nat. Rev. Mol. Cell Biol.* **7**, 391–403 (2006).
3. Yang, X. J. Multisite protein modification and intramolecular signaling. *Oncogene* **24**, 1653–1662 (2005).
4. Appella, E. & Anderson, C. W. Post-translational modifications and activation of p53 by genotoxic stress. *Eur. J. Biochem.* **2772**, 2764–2772 (2001).
5. Brooks, C. L. & Gu, W. Ubiquitination, phosphorylation and acetylation: the molecular basis for p53 regulation. *Curr. Opin. Cell Biol.* **15**, 164–171 (2003).
6. Cohen, P. The regulation of protein function by multisite phosphorylation - a 25 year update. *Trends Biochem. Sci.* **25**, 596–601 (2000).
7. Sims, R. J., Nishioka, K. & Reinberg, D. Histone lysine methylation: A signature for chromatin function. *Trends Genet.* **19**, 629–639 (2003).
8. Lis, H. & Sharon, N. Protein glycosylation. Structural and functional aspects. *Eur. J. Biochem.* **218**, 1–27 (1993).
9. Schedin-Weiss, S., Winblad, B. & Tjernberg, L. O. The role of protein glycosylation in Alzheimer disease. *FEBS J.* **281**, 46–62 (2014).
10. Welchman, R. L., Gordon, C. & Mayer, R. J. Ubiquitin and ubiquitin-like proteins as multifunctional signals. *Nat. Rev. Mol. Cell Biol.* **6**, 599–609 (2005).
11. Choudhary, C., Weinert, B. T., Nishida, Y., Verdin, E. & Mann, M. The growing landscape of lysine acetylation links metabolism and cell signalling. *Nat. Rev. Mol. Cell Biol.* **15**, 536–550 (2014).
12. Allfrey, V. G., Faulkner, R. & Mirsky, A. E. Acetylation and methylation of histones and their possible role in the regulation of RNA synthesis. *Proc. Natl. Acad. Sci. U. S. A.* **51**, 786–94 (1964).
13. L'Hernault, S. W. & Rosenbaum, J. L. *Chlamydomonas* α -tubulin is posttranslationally modified by acetylation on the ϵ -amino group of a lysine. *Biochemistry* **24**, 473–478 (1985).
14. Gu, W. & Roeder, R. G. Activation of p53 sequence-specific DNA binding by acetylation of the p53 C-terminal domain. *Cell* **90**, 595–606 (1997).
15. Ott, M. *et al.* Acetylation of the HIV-1 Tat protein by p300 is important for its transcriptional activity. *Curr. Biol.* **9**, 1489–1492 (1999).
16. Choudhary, C. *et al.* Lysine acetylation targets protein complexes and co-regulated major cellular functions. *Science (80-.)*. **325**, 834–840 (2009).
17. Guan, K. L. & Xiong, Y. Regulation of intermediary metabolism by protein acetylation. *Trends Biochem. Sci.* **36**, 108–116 (2011).
18. Jiang, T., Zhou, X., Taghizadeh, K., Dong, M. & Dedon, P. C. N-formylation of lysine in histone proteins as a secondary modification arising from oxidative DNA damage. *Proc. Natl. Acad. Sci.* **104**, 60–65 (2007).
19. Garrity, J., Gardner, J. G., Hawse, W., Wolberger, C. & Escalante-Semerena, J. C. N-lysine propionylation controls the activity of propionyl-CoA synthetase. *J. Biol. Chem.* **282**, 30239–30245 (2007).
20. Chen, Y. *et al.* Lysine propionylation and butyrylation are novel post-translational modifications in histones. *Mol. Cell. Proteomics* **6**, 812–819 (2007).
21. Tan, M. *et al.* Identification of 67 histone marks and histone lysine crotonylation as a new type of histone modification. *Cell* **146**, 1016–1028 (2011).
22. Peng, C. *et al.* The first identification of lysine malonylation substrates and its regulatory enzyme. *Mol. Cell. Proteomics* (2011).

23. Du, J. *et al.* Sirt5 is a NAD-dependent protein lysine demalonylase and desuccinylase. *Science (80-.)*. **334**, 806–809 (2011).
24. Zhang, Z. *et al.* Identification of lysine succinylation as a new post-translational modification. *Nat. Chem. Biol.* **7**, 58–63 (2011).
25. Tan, M. *et al.* Lysine glutarylation is a protein posttranslational modification regulated by SIRT5. *Cell Metab.* **19**, 605–617 (2014).
26. Jiang, H. *et al.* SIRT6 regulates TNF- α secretion through hydrolysis of long-chain fatty acyl lysine. *Nature* **496**, 110–113 (2013).
27. Berndsen, C. E. & Denu, J. M. Catalysis and substrate selection by histone/protein lysine acetyltransferases. *Curr. Opin. Struct. Biol.* **18**, 682–689 (2008).
28. Weinert, B. T. *et al.* Lysine succinylation is a frequently occurring modification in prokaryotes and eukaryotes and extensively overlaps with acetylation. *Cell Rep.* **4**, 842–851 (2013).
29. Pannek, M. *et al.* Crystal structures of the mitochondrial deacylase Sirtuin 4 reveal isoform-specific acyl recognition and regulation features. *Nat. Commun.* **8**, 1–13 (2017).
30. Gallinari, P., Di Marco, S., Jones, P., Pallaoro, M. & Steinkühler, C. HDACs, histone deacetylation and gene transcription: From molecular biology to cancer therapeutics. *Cell Res.* **17**, 195–211 (2007).
31. Imai, S., Armstrong, C. M., Kaerberlein, M. & Guarente, L. Transcriptional silencing and longevity protein Sir2 is an NAD-dependent histone deacetylase. *Nature* **403**, 795–800 (2000).
32. Smith, J. S. *et al.* A phylogenetically conserved NAD⁺-dependent protein deacetylase activity in the Sir2 protein family. *Proc. Natl. Acad. Sci.* **97**, 6658–6663 (2000).
33. Yuan, H. & Marmorstein, R. Structural basis for sirtuin activity and inhibition. *J. Biol. Chem.* **287**, 42428–42435 (2012).
34. Sharma, S. & Taliyan, R. Targeting histone deacetylases: A novel approach in Parkinson's disease. *Hindawi Publ. Corp. Park. Dis.* 1–11 (2015).
35. Haigis, M. C. & Sinclair, D. A. Mammalian Sirtuins: Biological insights and disease relevance. *Annu. Rev. Pathol. Mech. Dis.* **5**, 253–295 (2010).
36. Kaerberlein, M., McVey, M. & Guarente, L. The Sir2/3/4 complex and Sir2 alone promote longevity in *Saccharomyces cerevisiae* by two different mechanisms. *Genes Dev.* **13**, 2570–2580 (1999).
37. Michan, S. & Sinclair, D. Sirtuins in mammals: insights into their biological function. *Biochem. J.* **404**, 1–13 (2007).
38. López-Otín, C., Blasco, M. A., Partridge, L., Serrano, M. & Kroemer, G. The hallmarks of aging. *Cell* **153**, (2013).
39. McCay, C. M., Crowell, M. F. & Maynard, L. A. The effect of retarded growth upon the length of life span and upon the ultimate body size. *J. Nutr.* (1935).
40. Baur, J. A. Resveratrol, Sirtuins, and the promise of a DR mimetic. *Mech. Aging Dev.* **131**, 261–269 (2010).
41. Fontana, L. & Partridge, L. Promoting health and longevity through diet: From model organisms to humans. *Cell* **161**, 106–118 (2015).
42. Lin, S. J., Ford, E., Haigis, M., Liszt, G. & Guarente, L. Calorie restriction extends yeast life span by lowering the level of NADH. *Genes Dev.* **18**, 12–16 (2004).
43. Anderson, R. M., Bitterman, K. J., Wood, J. G., Medvedik, O. & Sinclair, D. A. Nicotinamide and PNC1 govern lifespan extension by calorie restriction in *Saccharomyces cerevisiae*. *Nature* **423**, 181–185 (2003).
44. Lin, S. J., Defossez, P. A. & Guarente, L. Requirement of NAD and SIR2 for life-span extension by calorie restriction in *Saccharomyces cerevisiae*. *Science (80-.)*. **289**, 2126–2128 (2000).

References

45. Bordone, L. *et al.* SIRT1 transgenic mice show phenotypes resembling calorie restriction. *Aging Cell* **6**, 759–767 (2007).
46. Feige, J. N. *et al.* Specific SIRT1 activation mimics low energy levels and protects against diet-induced metabolic disorders by enhancing fat oxidation. *Cell Metab.* **8**, 347–358 (2008).
47. Milne, J. C. *et al.* Small molecule activators of SIRT1 as therapeutics for the treatment of type 2 diabetes. *Nature* **450**, 712–716 (2007).
48. Howitz, K. T. *et al.* Small molecule activators of sirtuins extend *Saccharomyces cerevisiae* lifespan. *Nature* **425**, 191–196 (2003).
49. North, B. J., Marshall, B. L., Borra, M. T., Denu, J. M. & Verdin, E. The human Sir2 ortholog, SIRT2, is an NAD⁺-dependent tubulin deacetylase. *Mol. Cell* **11**, 437–444 (2003).
50. Vaquero, A. *et al.* SirT2 is a histone deacetylase with preference for histone H4 Lys 16 during mitosis. *Genes Dev.* **20**, 1256–1261 (2006).
51. Verdin, E., Hirschey, M. D., Finley, L. W. S. & Haigis, M. C. Sirtuin regulation of mitochondria: Energy production, apoptosis, and signaling. *Trends Biochem. Sci.* **35**, 669–675 (2010).
52. Cimen, H. *et al.* Regulation of succinate dehydrogenase activity by SIRT3 in mammalian mitochondria. *Biochemistry* **49**, 304–311 (2010).
53. Schlicker, C. *et al.* Substrates and regulation mechanisms for the human mitochondrial sirtuins Sirt3 and Sirt5. *J. Mol. Biol.* **382**, 790–801 (2008).
54. Schwer, B., Bunkenborg, J., Verdin, R. O., Andersen, J. S. & Verdin, E. Reversible lysine acetylation controls the activity of the mitochondrial enzyme acetyl-CoA synthetase 2. *Proc. Natl. Acad. Sci.* **103**, 10224–10229 (2006).
55. Haigis, M. C. *et al.* SIRT4 inhibits glutamate dehydrogenase and opposes the effects of calorie restriction in pancreatic β cells. *Cell* **126**, 941–954 (2006).
56. Mathias, R. A. *et al.* Sirtuin 4 is a lipoamidase regulating pyruvate dehydrogenase complex activity. *Cell* **159**, 1615–1625 (2014).
57. Nishida, Y. *et al.* SIRT5 regulates both cytosolic and mitochondrial protein malonylation with glycolysis as a major target. *Mol. Cell* **59**, 321–332 (2015).
58. Nakagawa, T., Lomb, D. J., Haigis, M. C. & Guarente, L. SIRT5 deacetylates carbamoyl phosphate synthetase 1 and regulates the urea cycle. *Cell* **137**, 560–570 (2009).
59. Michishita, E. *et al.* SIRT6 is a histone H3 lysine 9 deacetylase that modulates telomeric chromatin. *Nature* **452**, 492–496 (2008).
60. Liszt, G., Ford, E., Kurtev, M. & Guarente, L. Mouse Sir2 homolog Sirt6 is a nuclear ADP-ribosyltransferase. *J. Biol. Chem.* **280**, 21313–21320 (2005).
61. Ford, E. *et al.* Mammalian Sir2 homolog SIRT7 is an activator of RNA polymerase I transcription. *Genes Dev.* **20**, 1075–1080 (2006).
62. Vaquero, A. *et al.* Human SirT1 interacts with histone H1 and promotes formation of facultative heterochromatin. *Mol. Cell* **16**, 93–105 (2004).
63. Vaquero, A., Sternglanz, R. & Reinberg, D. NAD⁺-dependent deacetylation of H4 lysine 16 by class III HDACs. *Oncogene* **26**, 5505–5520 (2007).
64. Dang, W. *et al.* Histone H4 lysine 16 acetylation regulates cellular lifespan. *Nature* **459**, 802–807 (2009).
65. Nakahata, Y. *et al.* The NAD⁺-dependent deacetylase SIRT1 modulates CLOCK-mediated chromatin remodeling and circadian control. *Cell* **134**, 329–340 (2008).
66. Picard, F. *et al.* Sirt1 promotes fat mobilization in white adipocytes by repressing PPAR- γ . *Nature* **429**, 771–776 (2004).

67. Rodgers, J. T. *et al.* Nutrient control of glucose homeostasis through a complex of PGC-1 α and SIRT1. *Nature* **434**, 113–118 (2005).
68. Cantó, C. & Auwerx, J. PGC-1 α , SIRT1 and AMPK, an energy sensing network that controls energy expenditure. *Curr. Opin. Lipidol.* **20**, 98–105 (2009).
69. Brunet, A. *et al.* Stress-dependent regulation of FOXO transcription factors by the SIRT1 deacetylase. *Science (80-.)*. **303**, 2111–2115 (2004).
70. Kobayashi, Y. *et al.* SIRT1 is critical regulator of FOXO-mediated transcription in response to oxidative stress. *Int. J. Mol. Med.* **16**, 237–243 (2005).
71. Morris, B. J. Seven sirtuins for seven deadly diseases of aging. *Free Radic. Biol. Med.* **56**, 133–171 (2013).
72. Bhullar, K. S. & Hubbard, B. P. Lifespan and healthspan extension by resveratrol. *Biochim. Biophys. Acta - Mol. Basis Dis.* **1852**, 1209–1218 (2015).
73. Bonkowski, M. S. & Sinclair, D. A. Slowing ageing by design: The rise of NAD⁺ and sirtuin-activating compounds. *Nat. Rev. Mol. Cell Biol.* **17**, 679–690 (2016).
74. Guarente, L. Calorie restriction and sirtuins revisited. *Genes Dev.* **27**, 2072–2085 (2013).
75. Moniot, S., Weyand, M. & Steegborn, C. Structures, substrates, and regulators of mammalian Sirtuins - opportunities and challenges for drug development. *Front. Pharmacol.* **3**, 1–5 (2012).
76. Pan, M., Yuan, H., Brent, M., Ding, E. C. & Marmorstein, R. SIRT1 contains N- and C-terminal regions that potentiate deacetylase activity. *J. Biol. Chem.* **287**, 2468–2476 (2012).
77. Berman, H. M. *et al.* The protein data bank. *Nucleic Acids Res.* **28**, 235–242 (2000).
78. Zhao, X. *et al.* The 2.5 Å crystal structure of the SIRT1 catalytic domain bound to nicotinamide adenine dinucleotide (NAD⁺) and an indole (EX527 analog) reveals a novel mechanism of histone deacetylase inhibition. *J. Med. Chem.* (2013). doi:10.1021/jm301431y
79. Davenport, A. M., Huber, F. M. & Hoelz, A. Structural and functional analysis of human SIRT1. *J. Mol. Biol.* **426**, 526–541 (2014).
80. Dai, H. *et al.* Crystallographic structure of a small molecule SIRT1 activator-enzyme complex. *Nat. Commun.* **6**, 1–10 (2015).
81. Cao, D. *et al.* Structural basis for allosteric, substrate-dependent stimulation of SIRT1 activity by resveratrol. *Genes Dev.* **29**, 1316–1325 (2015).
82. Finnin, M. S., Donigian, J. R. & Pavletich, N. P. Structure of the histone deacetylase SIRT2. *Nat. Struct. Biol.* **8**, 621–625 (2001).
83. Jin, L. *et al.* Crystal structures of human SIRT3 displaying substrate-induced conformational changes. *J. Biol. Chem.* **284**, 24394–24405 (2009).
84. Pan, P. W. *et al.* Structure and biochemical functions of SIRT6. *J. Biol. Chem.* **286**, 14575–14587 (2011).
85. Sanders, B. D., Jackson, B. & Marmorstein, R. Structural basis for sirtuin function: What we know and what we don't. *Biochim. Biophys. Acta - Proteins Proteomics* **1804**, 1604–1616 (2010).
86. Sanders, B. D., Zhao, K., Slama, J. T. & Marmorstein, R. Structural basis for nicotinamide inhibition and base exchange in Sir2 enzymes. *Mol. Cell* **25**, 463–472 (2007).
87. Wolberger, C. Identification of a new nicotinamide binding site in a Sirtuin: A reassessment. *Mol. Cell* **28**, 1102–1103 (2007).
88. Rauh, D. *et al.* An acetylome peptide microarray reveals specificities and deacetylation substrates for all human sirtuin isoforms. *Nat. Commun.* **4**, 1–10 (2013).
89. Bheda, P., Jing, H., Wolberger, C. & Lin, H. The substrate specificity of Sirtuins. *Annu. Rev. Biochem.* **85**, 405–429 (2016).

References

90. Anderson, K. A., Green, M. F., Huynh, F. K., Wagner, G. R. & Hirschey, M. D. SnapShot: Mammalian sirtuins. *Cell* **159**, 956e1-956.e1 (2014).
91. Ghisays, F. *et al.* The N-terminal domain of SIRT1 is a positive regulator of endogenous SIRT1-dependent deacetylation and transcriptional outputs. *CellReports* **10**, 1665–1673 (2015).
92. Deota, S. *et al.* Identification of a tissue-restricted isoform of SIRT1 defines a regulatory domain that encodes specificity. *Cell Rep.* **18**, 3069–3077 (2017).
93. Kang, H. *et al.* Peptide switch is essential for Sirt1 deacetylase activity. *Mol. Cell* **44**, 203–213 (2011).
94. Kim, J. E., Chen, J. & Lou, Z. DBC1 is a negative regulator of SIRT1. *Nature* **451**, 583–586 (2008).
95. Zhao, W. *et al.* Negative regulation of the deacetylase SIRT1 by DBC1. *Nature* **451**, 587–590 (2008).
96. Kang, H., Jung, J. W., Kim, M. K. & Chung, J. H. CK2 is the regulator of SIRT1 substrate-binding affinity, deacetylase activity and cellular response to DNA-damage. *PLoS One* **4**, 1–9 (2009).
97. Hubbard, B. P. *et al.* Evidence for a common mechanism of SIRT1 regulation by allosteric activators. *Science (80-.)*. **339**, 1216–1219 (2013).
98. Malik, R. *et al.* Comparative deacetylase activity of wild type and mutants of SIRT1. *Biochem. Biophys. Res. Commun.* **391**, 739–743 (2010).
99. Feldman, J. L., Dittenhafer-Reed, K. E. & Denu, J. M. Sirtuin catalysis and regulation. *J. Biol. Chem.* **287**, 42419–42427 (2012).
100. Sauve, A. A. & Youn, D. Y. Sirtuins: NAD⁺-dependent deacetylase mechanism and regulation. *Curr. Opin. Chem. Biol.* **16**, 535–543 (2012).
101. Cen, Y. & Sauve, A. A. Transition state of ADP-ribosylation of acetyllysine catalyzed by *Archaeoglobus fulgidus* Sir2 determined by kinetic isotope effects and computational approaches. *J. Am. Chem. Soc.* **132**, 12286–12298 (2010).
102. Revollo, J. R. & Li, X. The ways and means that fine tune Sirt1 activity. *Trends Biochem. Sci.* **38**, 160–167 (2013).
103. Lavu, S., Boss, O., Elliott, P. J. & Lambert, P. D. Sirtuins - Novel therapeutic targets to treat age-associated diseases. *Nat. Rev. Drug Discov.* **7**, 841–853 (2008).
104. Taylor, D. M., Maxwell, M. M., Luthi-Carter, R. & Kazantsev, A. G. Biological and potential therapeutic roles of sirtuin deacetylases. *Cell. Mol. Life Sci.* **65**, 4000–4018 (2008).
105. Alcendor, R. R. *et al.* Sirt1 regulates aging and resistance to oxidative stress in the heart. *Circ. Res.* **100**, 1512–1521 (2007).
106. Kim, D. *et al.* SIRT1 deacetylase protects against neurodegeneration in models for Alzheimer's disease and amyotrophic lateral sclerosis. *EMBO J.* **26**, 3169–3179 (2007).
107. Parker, J. A. *et al.* Resveratrol rescues mutant polyglutamine cytotoxicity in nematode and mammalian neurons. *Nat. Genet.* **37**, 349–350 (2005).
108. Cen, Y. Sirtuin inhibitors: The approach to affinity and selectivity. *Biochim. Biophys. Acta - Proteins Proteomics* **1804**, 1635–1644 (2010).
109. Yi, J. & Luo, J. SIRT1 and p53, effect on cancer, senescence and beyond. *Biochim. Biophys. Acta - Proteins Proteomics* **1804**, 1684–1689 (2010).
110. Outeiro, T. F. *et al.* Sirtuin 2 inhibitors rescue alpha-synuclein-mediated toxicity in models of Parkinson's disease. *Science (80-.)*. **317**, 516–519 (2007).
111. Nakagawa, T. & Guarente, L. SnapShot: Sirtuins, NAD, and aging. *Cell Metab.* **20**, 192-192.e1 (2014).
112. Mostoslavsky, R. *et al.* Genomic instability and aging-like phenotype in the absence of mammalian SIRT6. *Cell* **124**, 315–329 (2006).

113. Vakhrusheva, O. *et al.* Sirt7 increases stress resistance of cardiomyocytes and prevents apoptosis and inflammatory cardiomyopathy in mice. *Circ. Res.* **102**, 703–710 (2008).
114. Imai, S. A possibility of nutraceuticals as an anti-aging intervention: Activation of sirtuins by promoting mammalian NAD biosynthesis. *Pharmacol. Res.* **62**, 42–47 (2010).
115. Houtkooper, R. H., Pirinen, E. & Auwerx, J. Sirtuins as regulators of metabolism and healthspan. *Nat. Rev. Mol. Cell Biol.* **13**, 225–238 (2012).
116. Bai, P. *et al.* PARP-1 inhibition increases mitochondrial metabolism through SIRT1 activation. *Cell Metab.* **13**, 461–468 (2011).
117. Milne, J. C. & Denu, J. M. The Sirtuin family: therapeutic targets to treat diseases of aging. *Curr. Opin. Chem. Biol.* **12**, 11–17 (2008).
118. Alcaín, F. J. & Villalba, J. M. Sirtuin inhibitors. *Expert Opin. Ther. Pat.* **19**, 283–294 (2009).
119. Heltweg, B. *et al.* Antitumor activity of a small-molecule inhibitor of human silent information regulator 2 enzymes. *Cancer Res.* **66**, 4368–4377 (2006).
120. Medda, F. *et al.* Novel cambinol analogs as sirtuin inhibitors: Synthesis, biological evaluation, and rationalization of activity. *J. Med. Chem.* **52**, 2673–2682 (2009).
121. Vergnes, B., Vanhille, L., Ouaiissi, A. & Sereno, D. Stage-specific antileishmanial activity of an inhibitor of SIR2 histone deacetylase. *Acta Trop.* **94**, 107–115 (2005).
122. Lara, E. *et al.* Salermide, a Sirtuin inhibitor with a strong cancer-specific proapoptotic effect. *Oncogene* **28**, 781–791 (2009).
123. Lain, S. *et al.* Discovery, in vivo activity, and mechanism of action of a small-molecule p53 activator. *Cancer Cell* **13**, 454–463 (2008).
124. Hirao, M. *et al.* Identification of selective inhibitors of NAD⁺-dependent deacetylases using phenotypic screens in yeast. *J. Biol. Chem.* **278**, 52773–52782 (2003).
125. Pagans, S. *et al.* SIRT1 regulates HIV transcription via Tat deacetylation. *PLoS Biol.* **3**, 0210–0220 (2005).
126. Gertz, M. *et al.* Ex-527 inhibits Sirtuins by exploiting their unique NAD⁺-dependent deacetylation mechanism. *Proc. Natl. Acad. Sci.* **110**, E2772–E2781 (2013).
127. Smith, B. C. & Denu, J. M. Mechanism-based inhibition of Sir2 deacetylases by thioacetyl-lysine peptide. *Biochemistry* **46**, 14478–14486 (2007).
128. Kiviranta, P. H. *et al.* N ϵ -thioacetyl-lysine-containing tri-, tetra-, and pentapeptides as SIRT1 and SIRT2 inhibitors. *J. Med. Chem.* **52**, 2153–2156 (2009).
129. Dai, H. *et al.* SIRT1 activation by small molecules: Kinetic and biophysical evidence for direct interaction of enzyme and activator. *J. Biol. Chem.* **285**, 32695–32703 (2010).
130. Alcaín, F. J. & Villalba, J. M. Sirtuin activators. *Expert Opin. Ther. Pat.* **19**, 403–414 (2009).
131. Beher, D. *et al.* Resveratrol is not a direct activator of sirt1 enzyme activity. *Chem. Biol. Drug Des.* **74**, 619–624 (2009).
132. Pacholec, M. *et al.* SRT1720, SRT2183, SRT1460, and resveratrol are not direct activators of SIRT1. *J. Biol. Chem.* **285**, 8340–8351 (2010).
133. Borra, M. T., Smith, B. C. & Denu, J. M. Mechanism of human SIRT1 activation by resveratrol. *J. Biol. Chem.* **280**, 17187–17195 (2005).
134. Kaeberlein, M. *et al.* Substrate-specific activation of sirtuins by resveratrol. *J. Biol. Chem.* **280**, 17038–17045 (2005).
135. Lakshminarasimhan, M., Rauh, D., Schutkowski, M. & Steegborn, C. Sirt1 activation by resveratrol is substrate sequence-selective. *Aging (Albany, NY)*. **5**, 151–154 (2013).

References

136. Gertz, M. *et al.* A molecular mechanism for direct Sirtuin activation by resveratrol. *PLoS One* **7**, 1–12 (2012).
137. Kumar, A. & Chauhan, S. How much successful are the medicinal chemists in modulation of SIRT1: A critical review. *Eur. J. Med. Chem.* **119**, 45–69 (2016).
138. Trapp, J. *et al.* Adenosine mimetics as inhibitors of NAD⁺-dependent histone deacetylases, from kinase to sirtuin inhibition. *J. Med. Chem.* **49**, 7307–7316 (2006).
139. Rahnasto-Rilla, M., Kokkola, T., Jarho, E., Lahtela-Kakkonen, M. & Moaddel, R. N-acylethanolamines bind to SIRT6. *ChemBioChem* **17**, 77–81 (2016).
140. Kim, J. *et al.* The natural phytochemical dehydroabiatic acid is an anti-aging reagent that mediates the direct activation of SIRT1. *Mol. Cell. Endocrinol.* **412**, 216–225 (2015).
141. You, W. *et al.* Structural basis of Sirtuin 6 activation by synthetic small molecules. *Angew. Chemie - Int. Ed.* **56**, 1007–1011 (2017).
142. Sauve, A. A., Moir, R. D., Schramm, V. L. & Willis, I. M. Chemical activation of Sir2-dependent silencing by relief of nicotinamide inhibition. *Mol. Cell* **17**, 595–601 (2005).
143. Sinclair, D. A. & Hubbard, B. P. Small molecule modulators of sirtuins. *Exp. Med. Chapter 5 - Methodol. Control. aging Longev.* **31**, (2013).
144. Mai, A. *et al.* Study of 1,4-dihydropyridine structural scaffold: Discovery of novel sirtuin activators and inhibitors. *J. Med. Chem.* **52**, 5496–5504 (2009).
145. Smith, J. J. *et al.* Small molecule activators of SIRT1 replicate signaling pathways triggered by calorie restriction in vivo. *BMC Syst. Biol.* **3**, 1–14 (2009).
146. Sirtris, A GSK Company, 200 Technology Square, Cambridge, MA 01239, U. Development of STACs.
147. Sasaki, T. *et al.* Phosphorylation regulates SIRT1 function. *PLoS One* **3**, (2008).
148. Yang, Y. *et al.* SIRT1 sumoylation regulates its deacetylase activity and cellular response to genotoxic stress. *Nat. Cell Biol.* **9**, 1253–1262 (2007).
149. Kwon, H. S. & Ott, M. The ups and downs of SIRT1. *Trends Biochem. Sci.* **33**, 517–525 (2008).
150. Kim, E. J., Kho, J. H., Kang, M. R. & Um, S. J. Active Regulator of SIRT1 cooperates with SIRT1 and facilitates suppression of p53 activity. *Mol. Cell* **28**, 277–290 (2007).
151. Maeda, N., Toku, S., Kenmochi, N. & Tanaka, T. A novel nucleolar protein interacts with ribosomal protein S19. *Biochem. Biophys. Res. Commun.* **339**, 41–46 (2006).
152. Knight, J. R. P., Willis, A. E. & Milner, J. Active regulator of SIRT1 is required for ribosome biogenesis and function. *Nucleic Acids Res.* **41**, 4185–4197 (2013).
153. Verdin, E. AROuSing SIRT1: Identification of a novel endogenous SIRT1 activator. *Mol. Cell* **28**, 354–356 (2007).
154. Knight, J. R. P., Allison, S. J. & Milner, J. Active regulator of SIRT1 is required for cancer cell survival but not for SIRT1 activity. *Open Biol.* **3**, (2013).
155. Lakshminarasimhan, M. *et al.* Molecular architecture of the human protein deacetylase Sirt1 and its regulation by AROS and resveratrol. *Biosci. Rep.* **33**, 395–404 (2013).
156. Kokkola, T. *et al.* AROS has a context-dependent effect on SIRT1. *FEBS Lett.* **588**, 1523–1528 (2014).
157. Conrad, E. *et al.* HIPK2 restricts SIRT1 activity upon severe DNA damage by a phosphorylation-controlled mechanism. *Cell Death Differ.* **23**, 110–122 (2016).
158. Hamaguchi, M. *et al.* DBC2, a candidate for a tumor suppressor gene involved in breast cancer. *Proc. Natl. Acad. Sci.* **99**, 13647–13652 (2002).
159. Sung, J. Y., Kim, R., Kim, J. E. & Lee, J. Balance between SIRT1 and DBC1 expression is lost in breast cancer. *Cancer Sci.* **101**, 1738–1744 (2010).

160. Close, P. *et al.* DBIRD complex integrates alternative mRNA splicing with RNA polymerase II transcript elongation. *Nature* **484**, 386–389 (2012).
161. Zheng, H. *et al.* hMOF acetylation of DBC1/CCAR2 prevents binding and inhibition of SirT1. *Mol. Cell. Biol.* **33**, 4960–4970 (2013).
162. Bateman, A. *et al.* UniProt: the universal protein knowledgebase. *Nucleic Acids Res.* **45**, D158–D169 (2017).
163. Joshi, P., Quach, O. L., Giguere, S. S. B. & Cristea, I. M. A functional proteomics perspective of DBC1 as a regulator of transcription. *J. Proteomics Bioinform.* **509**, 385–388 (2014).
164. Anantharaman, V. & Aravind, L. Analysis of DBC1 and its homologs suggests a potential mechanism for regulation of sirtuin domain deacetylases by NAD metabolites. *Cell Cycle* **7**, 1467–1472 (2008).
165. Li, J. *et al.* A conserved NAD⁺ binding pocket that regulates protein-protein interactions during aging. *Science (80-.)*. **355**, 1312–1317 (2017).
166. Yuan, J., Luo, K., Liu, T. & Lou, Z. Regulation of SIRT1 activity by genotoxic stress. *Genes Dev.* **26**, 791–796 (2012).
167. Zannini, L., Buscemi, G., Kim, J., Fontanella, E. & Delia, D. DBC1 phosphorylation by ATM/ATR inhibits SIRT1 deacetylase in response to DNA damage. *J. Mol. Cell Biol.* 294–303 (2012). doi:10.1093/jmcb/mjs035
168. Park, J. H. *et al.* Modification of DBC1 by SUMO2/3 is crucial for p53-mediated apoptosis in response to DNA damage. *Nat. Commun.* **5**, 1–12 (2014).
169. Li, Z. *et al.* Inhibition of SUV39H1 methyltransferase activity by DBC1. *J. Biol. Chem.* **284**, 10361–10366 (2009).
170. Hubbard, B. P. *et al.* Carboxamide SIRT1 inhibitors block DBC1 binding via an acetylation-independent mechanism. *Cell Cycle* **12**, 2233–2240 (2013).
171. Menssen, A. *et al.* The c-MYC oncoprotein, the NAMPT enzyme, the SIRT1-inhibitor DBC1, and the SIRT1 deacetylase form a positive feedback loop. *Proc. Natl. Acad. Sci.* **109**, E187–E196 (2012).
172. Rood, B. R., Zhang, H., Weitman, D. M. & Cogen, P. H. Hypermethylation of HIC-1 and 17p allelic loss in medulloblastoma. *Cancer Res.* **62**, 3794–3797 (2002).
173. Fujii, H. *et al.* Methylation of the HIC-1 candidate tumor suppressor gene in human breast cancer. *Oncogene* **16**, 2159–2164 (1998).
174. Kanai, Y. *et al.* DNA hypermethylation at the D17S5 locus is associated with gastric carcinogenesis. *Cancer Lett.* **122**, 135–141 (1998).
175. Konishi, H. *et al.* Detailed deletion mapping suggests the involvement of a tumor suppressor gene at 17p13.3, distal to p53, in the pathogenesis of lung cancers. *Oncogene* **17**, 2095–2100 (1998).
176. Tseng, R. C., Lee, C. C., Hsu, H. S., Tzao, C. & Wang, Y. C. Distinct HIC1-SIRT1-p53 loop deregulation in lung squamous carcinoma and adenocarcinoma patients. *Neoplasia* **11**, 763–W11 (2009).
177. Pinte, S. *et al.* The tumor suppressor gene HIC1 (hypermethylated in cancer 1) is a sequence-specific transcriptional repressor: Definition of its consensus binding sequence and analysis of its DNA binding and repressive properties. *J. Biol. Chem.* **279**, 38313–38324 (2004).
178. Guerardel, C. *et al.* Identification in the human candidate tumor suppressor gene HIC-1 of a new major alternative TATA-less promoter positively regulated by p53. *J. Biol. Chem.* **276**, 3078–3089 (2001).
179. Makos-Wales, M. *et al.* P53 activates expression of Hic-1, a new candidate tumour suppressor gene on 17p13.3. *Nat. Med.* **1**, 570 (1995).
180. Fleuriel, C. *et al.* HIC1 (Hypermethylated in cancer 1) epigenetic silencing in tumors. *Int. J. Biochem. Cell Biol.* **41**, 26–33 (2009).
181. Rood, B. R. & Leprince, D. Deciphering HIC1 control pathways to reveal new avenues in cancer therapeutics. *Expert Opin. Ther. Targets* **17**, 811–827 (2013).

References

182. Perez-Torrado, R., Yamada, D. & Defossez, P. A. Born to bind: The BTB protein-protein interaction domain. *BioEssays* **28**, 1194–1202 (2006).
183. Deltour, S., Guerardel, C. & Leprince, D. Recruitment of SMRT/N-CoR-mSin3A-HDAC-repressing complexes is not a general mechanism for BTB/POZ transcriptional repressors: the case of Hic-1 and gamma-FBP-B. *Proc. Natl. Acad. Sci.* **96**, 14831–14836 (1999).
184. Chen, W. Y. *et al.* Tumor suppressor HIC1 directly regulates SIRT1 to modulate p53-dependent DNA-damage responses. *Cell* **123**, 437–448 (2005).
185. Dehennaut, V., Loison, I., Pinte, S. & Leprince, D. Molecular dissection of the interaction between HIC1 and SIRT1. *Biochem. Biophys. Res. Commun.* **421**, 384–388 (2012).
186. Le Douce, V. *et al.* HIC1 controls cellular- and HIV-1-gene transcription via interactions with CTIP2 and HMGA1. *Sci. Rep.* **6**, 1–12 (2016).
187. Deltour, S., Pinte, S., Guerardel, C., Wasyluk, B. & Leprince, D. The human candidate tumor suppressor gene HIC1 recruits CtBP through a degenerate GLDLSKK motif. *Mol. Cell. Biol.* **22**, 4890–901 (2002).
188. Stankovic-Valentin, N. *et al.* An acetylation/deacetylation-SUMOylation switch through a phylogenetically conserved KXEP motif in the tumor suppressor HIC1 regulates transcriptional repression activity. *Mol. Cell. Biol.* **27**, 2661–2675 (2007).
189. Paget, S. *et al.* HIC1 (hypermethylated in cancer 1) SUMOylation is dispensable for DNA repair but is essential for the apoptotic DNA damage response (DDR) to irreparable DNA double-strand breaks (DSBs). *Oncotarget* **8**, 2916–2935 (2017).
190. Ariumi, Y., Kaida, A., Hatanaka, M. & Shimotohno, K. Functional cross-talk of HIV-1 Tat with p53 through its C-terminal domain. *Biochem. Biophys. Res. Commun.* **287**, 556–561 (2001).
191. Mousseau, G. & Valente, S. Strategies to block HIV transcription: Focus on small molecule Tat inhibitors. *Biology (Basel)*. **1**, 668–697 (2012).
192. Mbonye, U. & Karn, J. Control of HIV latency by epigenetic and non-epigenetic mechanisms. *Curr. HIV Res.* **9**, 554–567 (2011).
193. Le Douce, V. *et al.* Improving combination antiretroviral therapy by targeting HIV-1 gene transcription. *Expert Opin. Ther. Targets* **20**, 1311–1324 (2016).
194. Jiang, Y., Chai, L., Fasae, M. B. & Bai, Y. The role of HIV Tat protein in HIV-related cardiovascular diseases. *J. Transl. Med.* **16**, 1–7 (2018).
195. Romani, B., Engelbrecht, S. & Glashoff, R. H. Functions of Tat: the versatile protein of human immunodeficiency virus type 1. *J. Gen. Virol.* **91**, 1–12 (2010).
196. Churcher, M. J. *et al.* High affinity binding of TAR RNA by the human immunodeficiency virus type-1 Tat protein requires base-pairs in the RNA stem and amino acid residues flanking the basic region. *Journal of Molecular Biology* **230**, 90–110 (1993).
197. Smith, K. M., Himiari, Z., Tsimbalyuk, S. & Forwood, J. K. Structural basis for importin- α binding of the human immunodeficiency virus Tat. *Sci. Rep.* **7**, 1–11 (2017).
198. Brake, D. A., Debouck, C. & Biesecker, G. Identification of an Arg-Gly-Asp (RGD) cell adhesion site in human immunodeficiency virus type I transactivation protein Tat. *J. Cell Biol.* **111**, 1275–1281 (1990).
199. Bayer, P. *et al.* Structural studies of HIV-1 Tat protein. *J. Mol. Biol.* **247**, 529–535 (1995).
200. Tahirov, T. H. *et al.* Crystal structure of HIV-1 Tat complexed with human P-TEFb. *Nature* **465**, 747–751 (2010).
201. Blazek, D. & Peterlin, B. M. Tat-SIRT1 Tango. *Mol. Cell* **29**, 539–540 (2008).
202. Ivanov, A. *et al.* HIV-1 Tat phosphorylation on Ser-16 residue modulates HIV-1 transcription. *Retrovirology* **15**, 1–23 (2018).
203. Zhang, L. *et al.* Modulation of the stability and activities of HIV-1 Tat by its ubiquitination and carboxyl-terminal region. *Cell Biosci.* **4**, 1–11 (2014).

204. Kwon, H. *et al.* Human immunodeficiency virus type 1 Tat protein inhibits the Sirt1 deacetylase and induces T-cell hyperactivation. *Cell Host Microbe* **13**, 158–167 (2008).
205. Thakur, B. K., Chandra, A., Dittrich, T., Welte, K. & Chandra, P. Inhibition of SIRT1 by HIV-1 viral protein Tat results in activation of p53 pathway. *Biochem. Biophys. Res. Commun.* **424**, 245–250 (2012).
206. Chang, H.-K., Gallo, R. C. & Ensoli, B. Regulation of cellular gene expression and function by the human immunodeficiency virus type I Tat protein. *J Biomed Sci* **2**, 189–202 (1995).
207. Zhang, H. S., Zhou, Y., Wu, M. R., Zhou, H. Sen & Xu, F. Resveratrol inhibited Tat-induced HIV-1 LTR transactivation via NAD⁺-dependent SIRT1 activity. *Life Sci.* **85**, 484–489 (2009).
208. Rogosnitzky, M., Danks, R. & Kardash, E. Therapeutic potential of tranilast, an anti-allergy drug, in proliferative disorders. *Anticancer Res.* **32**, 2471–2478 (2012).
209. Boehm, M., Sticht, H., Seidel, G. & Roesch, P. Solution structure of HIV-1 Tat protein. *TO BE Publ.* (1998). doi:10.2210/PDB1TAC/PDB
210. Gasteiger, E. *et al.* Protein identification and analysis tools on the ExPASy server. in *The Proteomics Protocols Handbook* 571–607 (Humana Press, 2005). doi:10.1385/1-59259-890-0:571
211. Reinhard, L., Mayerhofer, H., Geerlof, A., Mueller-Dieckmann, J. & Weiss, M. S. Optimization of protein buffer cocktails using Thermofluor. *Acta Crystallogr. Sect. F Struct. Biol. Cryst. Commun.* **69**, 209–214 (2013).
212. Smith, B. C., Hallows, W. C. & Denu, J. M. A continuous microplate assay for Sirtuins and Nicotinamide producing enzymes. *Anal. Biochem.* **394**, 101–109 (2009).
213. Michaelis, L. & Menten, M. L. Die Kinetik der Invertinwirkung. *Biochem Z* **49**, 333–369 (1913).
214. Schutkowski, M., Fischer, F., Roessler, C. & Steegborn, C. New assays and approaches for discovery and design of Sirtuin modulators. *Expert Opin. Drug Discov.* **9**, 183–99 (2014).
215. Enzo Life Sciences. SIRT1 Fluorimetric Drug Discovery Kit* - AK-555. 1–8 (2001).
216. Fischer, F. *et al.* Sirt5 deacylation activities show differential sensitivities to nicotinamide inhibition. *PLoS One* **7**, e45098 (2012).
217. Kao, A. *et al.* Development of a novel cross-linking strategy for fast and accurate identification of cross-linked peptides of protein complexes. *Mol. Cell. Proteomics* **10**, M110.002212 (2011).
218. Wienken, C. J., Baaske, P., Rothbauer, U., Braun, D. & Duhr, S. Protein-binding assays in biological liquids using microscale thermophoresis. *Nat. Commun.* **1**, 100 (2010).
219. Jerabek-Willemsen, M., Wienken, C. J., Braun, D., Baaske, P. & Duhr, S. Molecular interaction studies using microscale thermophoresis. *Assay Drug Dev. Technol.* **9**, 342–353 (2011).
220. Nanotemper Technologies Inc. User manual for the Monolith NT.115. in *SpringerReference* 1–10 (Springer-Verlag, 2007). doi:10.1007/SpringerReference_28001
221. Ranjbar, B. & Gill, P. Circular dichroism techniques: Biomolecular and nanostructural analyses - A review. *Chem. Biol. Drug Des.* **74**, 101–120 (2009).
222. Chemes, B., Alonso, L. G., Noval, G. & Prat-gay, G. De. *Circular dichroism techniques for the analysis of intrinsically disordered proteins and domains.* **895**, (Humana Press, 2012).
223. Jasanoff, A. & Fersht, A. R. Quantitative determination of helical propensities from trifluoroethanol titration curves. *Biochemistry* **33**, 2129–2135 (1994).
224. Gerlach, M., Mueller, U. & Weiss, M. S. The MX Beamlines BL14.1-3 at BESSY II. *J. large-scale Res. Facil. JLSRF* **2**, A47 (2016).
225. Batty, T. G. G., Kontogiannis, L., Johnson, O., Powell, H. R. & Leslie, A. G. W. iMOSFLM: a new graphical interface for diffraction-image processing with MOSFLM. *Acta Crystallogr. Sect. D Biol. Crystallogr.* **67**, 271–281 (2011).
226. Paul Scherrer Institut (PSI). Available at: <https://www.psi.ch/sls/pxiii/>. (Accessed: 14th September 2018)

References

227. Sparta, K. M., Krug, M., Heinemann, U., Mueller, U. & Weiss, M. S. XDSAPP2.0. *J. Appl. Crystallogr.* **49**, 1085–1092 (2016).
228. Kabsch, W. XDS. *Acta Crystallogr. Sect. D Biol. Crystallogr.* **66**, 125–132 (2010).
229. Evans, P. Scaling and assessment of data quality. *Acta Crystallogr. Sect. D Biol. Crystallogr.* **62**, 72–82 (2006).
230. Evans, P. R. An introduction to data reduction: Space-group determination, scaling and intensity statistics. *Acta Crystallogr. Sect. D Biol. Crystallogr.* **67**, 282–292 (2011).
231. Winn, M. D. *et al.* Overview of the CCP4 suite and current developments. *Acta Crystallogr. Sect. D Biol. Crystallogr.* **67**, 235–242 (2011).
232. Zwart, P. H., Grosse-Kunstleve, R. W. & Adams, P. D. Xtriage and Fest: automatic assessment of X-ray data and substructure structure factor estimation. *CCP4 Newsl.* **43**, 27–35 (2005).
233. Winter, G. *et al.* DIALS: implementation and evaluation of a new integration package. *Acta Crystallogr. Sect. D Struct. Biol.* **74**, 85–97 (2018).
234. Gildea, R. J. *et al.* New methods for indexing multi-lattice diffraction data. *Acta Crystallogr. Sect. D Biol. Crystallogr.* **70**, 2652–2666 (2014).
235. French, B. Y. S. & Wilson, K. On the treatment of negative intensity observations. *Acta Crystallogr. Sect. A* **34**, 517–525 (1978).
236. Brunger, A. T. Free R value: a novel statistical quantity for assessing the accuracy of crystal structures. *Lett. to Nat.* **355**, 472–475 (1992).
237. Karplus, A. P. & Diederichs, K. Linking crystallographic model and data quality. *Science (80-.)*. **336**, 1030–1033 (2012).
238. Karplus, A. P. & Diederichs, K. Assessing and maximizing data quality in crystallography. *Curr. Opin. Struct. Biol.* **34**, 60–68 (2015).
239. Vagin, A. & Teplyakov, A. MOLREP: An automated program for molecular replacement. *J. Appl. Crystallogr.* **30**, 1022–1025 (1997).
240. McCoy, A. J. *et al.* Phaser crystallographic software. *J. Appl. Crystallogr.* **40**, 658–674 (2007).
241. Adams, P. D. *et al.* PHENIX: A comprehensive Python-based system for macromolecular structure solution. *Acta Crystallogr. Sect. D Biol. Crystallogr.* **66**, 213–221 (2010).
242. Vagin, A. & Lebedev, A. MoRDa, an automatic molecular replacement pipeline. *Acta Crystallogr. Sect. A Found. Adv.* **71**, s19–s19 (2015).
243. Murshudov, G. N. *et al.* REFMAC5 for the refinement of macromolecular crystal structures. *Acta Crystallogr. Sect. D Biol. Crystallogr.* **67**, 355–367 (2011).
244. Afonine, P. V. *et al.* Towards automated crystallographic structure refinement with phenix.refine. *Acta Crystallogr. Sect. D Biol. Crystallogr.* **68**, 352–367 (2012).
245. Emsley, P. & Cowtan, K. Coot: Model-building tools for molecular graphics. *Acta Crystallogr. Sect. D Biol. Crystallogr.* **60**, 2126–2132 (2004).
246. Nicholls, R. A., Long, F. & Murshudov, G. N. Low-resolution refinement tools in REFMAC5. *Acta Crystallogr. Sect. D Biol. Crystallogr.* **68**, 404–417 (2012).
247. Joosten, R. P., Long, F., Murshudov, G. N. & Perrakis, A. The PDB_REDO server for macromolecular structure model optimization. *IUCrJ* **1**, 213–220 (2014).
248. Chen, V. B. *et al.* MolProbity: All-atom structure validation for macromolecular crystallography. *Acta Crystallogr. Sect. D Biol. Crystallogr.* **66**, 12–21 (2010).
249. Schrödinger, L. *The PyMOL Molecular Graphics System, Version 1.8.* (2015).

250. Terwilliger, T. C. *et al.* Iterative-build OMIT maps: map improvement by iterative model building and refinement without model bias. *Acta Crystallogr. Sect. D Biol. Crystallogr.* **64**, 515–524 (2008).
251. Afonine, P. V. *et al.* FEM: Feature-enhanced map. *Acta Crystallogr. Sect. D Biol. Crystallogr.* **71**, 646–666 (2015).
252. Laskowski, R. A. & Swindells, M. B. LigPlot+: Multiple ligand-protein interaction diagrams for drug discovery. *J. Chem. Inf. Model.* **51**, 2778–2786 (2011).
253. Cowtan, K. Recent developments in classical density modification. *Acta Crystallogr. Sect. D Biol. Crystallogr.* **66**, 470–478 (2010).
254. Sievers, F. *et al.* Fast, scalable generation of high-quality protein multiple sequence alignments using Clustal Omega. *Mol. Syst. Biol.* **7**, (2011).
255. ChemAxon. ChemAxon - Software Solutions and Services for Chemistry and Biology. *MarvinSketch, Version 16.10.31* (2016).
256. Kelley, L. A. & Sternberg, M. J. E. Protein structure prediction on the web: A case study using the phyre server. *Nat. Protoc.* **4**, 363–373 (2009).
257. Mézáros, B., Erdős, G. & Dosztányi, Z. IUPred2A: Context-dependent prediction of protein disorder as a function of redox state and protein binding. *Nucleic Acids Res.* **46**, W329–W337 (2018).
258. Lakshminarasimhan, M. Biochemical and structural characterization of Sirtuins from mammals and *Thermotoga maritima*. *PhD thesis* (University of Bayreuth, Germany, 2012).
259. Adolph, R. Charakterisierung der Regulation von humanem Sirtuin 1 und Charakterisierung von cAMP-bindenden universellen Stressproteinen aus Mykobakterien. *Master thesis* (University of Bayreuth, Germany, 2014).
260. Kelley, L. A., Mezulis, S., Yates, C. M., Wass, M. N. & Sternberg, M. J. E. The Phyre2 web portal for protein modeling, prediction and analysis. *Nat. Protoc.* **10**, 845–858 (2015).
261. Stogios, P. J., Cuesta-Seijo, J. A., Chen, L., Pomroy, N. C. & Privé, G. G. Insights into strand exchange in BTB domain dimers from the crystal structures of FAZF and Miz1. *J. Mol. Biol.* **400**, 983–997 (2010).
262. Krissinel, E. & Henrick, K. Inference of macromolecular assemblies from crystalline state. *J. Mol. Biol.* **372**, 774–797 (2007).
263. Stogios, P. J., Downs, G. S., Jauhal, J. J. S., Nandra, S. K. & Privé, G. G. Sequence and structural analysis of BTB domain proteins. *Genome Biol.* **6**, 1–18 (2005).
264. Rumpf, T. *et al.* Selective Sirt2 inhibition by ligand-induced rearrangement of the active site. *Nat. Commun.* **6**, (2015).
265. Jenny, R. J., Mann, K. G. & Lundblad, R. L. A critical review of the methods for cleavage of fusion proteins with thrombin and factor Xa. *Protein Expr. Purif.* **31**, 1–11 (2003).
266. Oldfield, C. J. & Dunker, A. K. Intrinsically disordered proteins and intrinsically disordered protein regions. *Annu. Rev. Biochem.* **83**, 553–584 (2014).
267. Hazy, E. & Tompa, P. Limitations of induced folding in molecular recognition by intrinsically disordered proteins. *ChemPhysChem* **10**, 1415–1419 (2009).
268. Guskov, A. & Slotboom, D. J. Chapter 6: Size exclusion chromatography with multi-angle laser light scattering (SEC-MALLS) to determine protein oligomeric states. in *From Molecules to Living Organisms: An Interplay between Biology and Physics*. 169–183 (2016).
269. Lebowitz, J., Lewis, M. S. & Schuck, P. Modern analytical ultracentrifugation in protein science: A tutorial review. *Protein Sci.* **11**, 2067–2079 (2002).
270. Bernadó, P., Akerud, T., Garcia de la Torre, J., Akke, M. & Pons, M. Combined use of NMR relaxation measurements and hydrodynamic calculations to study protein Association. Evidence for tetramers of low molecular weight protein tyrosine phosphatase in solution. *J. Am. Chem. Soc.* **125**, 916–923 (2003).

References

271. Katsani, K. R., Hajibagheri, M. A. N. & Verrijzer, C. P. Co-operative DNA binding by GAGA transcription factor requires the conserved BTB/POZ domain and reorganizes promoter topology. *EMBO J.* **18**, 698–708 (1999).
272. Mattson, G. *et al.* A practical approach to crosslinking. *Mol. Biol. Rep.* **17**, 167–183 (1993).
273. Sauter, N. K., Grosse-Kunstleve, R. W. & Adams, P. D. Robust indexing for automatic data collection. *J. Appl. Crystallogr.* **37**, 399–409 (2004).
274. Ahmad, K. F. *et al.* Mechanism of SMRT corepressor recruitment by the BCL6 BTB domain. *Mol. Cell* **12**, 1551–1564 (2003).
275. McCoull, W. *et al.* Development of a novel B-cell lymphoma 6 (BCL6) PROTAC to provide insight into small molecule targeting of BCL6. *ACS Chem. Biol.* **13**, 3131–3141 (2018).
276. Kamada, Y. *et al.* Discovery of a B-Cell Lymphoma 6 Protein-Protein Interaction Inhibitor by a Biophysics-Driven Fragment-Based Approach. *J. Med. Chem.* **60**, 4358–4368 (2017).
277. Shojania, S. & D. O’Neil, J. Intrinsic disorder and function of the HIV-1 Tat protein. *Protein Pept. Lett.* **17**, 999–1011 (2010).
278. To, V., Dzananovic, E., McKenna, S. A. & O’Neil, J. The dynamic landscape of the full-length HIV-1 transactivator of transcription. *Biochemistry* **55**, 1314–1325 (2016).
279. Péloponèse, J. M. *et al.* ¹H-¹³C nuclear magnetic resonance assignment and structural characterization of HIV-1 Tat protein. *Comptes Rendus l’Academie des Sci. - Ser. III* **323**, 883–894 (2000).
280. Grégoire, C. *et al.* Homonuclear ¹H-NMR assignment and structural characterization of human immunodeficiency virus type 1 Tat Mal protein. *Biopolym. - Biospectroscopy Sect.* **62**, 324–335 (2001).
281. Mujtaba, S. *et al.* Structural basis of lysine-acetylated HIV-1 Tat recognition by PCAF bromodomain. *Mol. Cell* **9**, 575–586 (2002).
282. Thi Tuyet Nguyen, G., Schaefer, S., Gertz, M., Weyand, M. & Steegborn, C. Crystal structures of human Sirtuin 3 complexes with ADP-ribose and with carba-NAD⁺ and SRT1720 - binding details and inhibition mechanism. *Acta Crystallogr. Sect. D, Biol. Crystallogr.* **49**, (2013).

7. Supplementary

7.1 Additional materials

Table 7.1: Characteristics of other peptides used in this study. Peptides were dissolved in 20 mM buffer with pH adjusted to 7 or in 100% (v/v) DMSO (pH not adjusted) unless stated differently. Substrate peptides were synthesized and HPLC purified by GL Biochem, Shanghai, China. *FdL-1* and myrTNF α were synthesized by the group of Prof. Dr. Mike Schutkowski (University of Halle-Wittenberg, Germany). ESA peptides were synthesized by the group of Prof. Dr. Antonello Mai (Sapienza University of Rome, Italy).

Peptide	Sequence (N \rightarrow C)	MW (g/mol)	Purity (%)	Solvent
ESA peptides				
1	<i>acetyl-QYLFVPPN-NH₂</i>	1018.14	> 95	DMSO
2	<i>acetyl-YLFVPPNR-NH₂</i>	1046.19	> 95	DMSO
3	<i>acetyl-LFVPPNRY-NH₂</i>	1046.19	> 95	DMSO
4	<i>acetyl-FVPPNRYI-NH₂</i>	1046.19	> 95	DMSO
5	<i>acetyl-VPPNRYIF-NH₂</i>	1046.19	> 95	DMSO
6	<i>acetyl-PPNRYIFH-NH₂</i>	1084.20	> 95	DMSO
7	<i>acetyl-PNRYIFHG-NH₂</i>	1044.14	> 95	DMSO
8	<i>acetyl-NRYIFHGA-NH₂</i>	1018.10	> 95	DMSO
9	<i>acetyl-RYIFHGAE-NH₂</i>	1033.11	> 95	DMSO
10	<i>acetyl-YIFHGAEV-NH₂</i>	976.06	> 95	DMSO
11	<i>acetyl-IFHGAEVY-NH₂</i>	976.06	> 95	DMSO
12	<i>acetyl-FHGAEVYS-NH₂</i>	949.97	> 95	DMSO
13	<i>acetyl-HGAEVYSD-NH₂</i>	917.88	> 95	DMSO
14	<i>acetyl-GAEVYSDS-NH₂</i>	867.82	> 95	DMSO
15	<i>acetyl-AEVYSDSE-NH₂</i>	939.89	> 95	DMSO
16	<i>acetyl-EVYSDSED-NH₂</i>	983.90	> 95	DMSO
17	<i>acetyl-VYSDSEDD-NH₂</i>	969.87	> 95	DMSO
18	<i>acetyl-YSDESDDV-NH₂</i>	969.87	> 95	DMSO
19	<i>acetyl-QYLFVPPNRYIFHGAEVYSDSEDDV-NH₂</i>	3002.22	> 95	DMSO
20	<i>QYLFVPPNRYIFHGAEVYSDSEDDV-NH₂</i>	2960.22	> 95	DMSO
21	<i>NRYIFH-NH₂</i>	849.97	> 95	DMSO
22	<i>acetyl-NRYIFH-NH₂</i>	889.97	> 95	DMSO
23	<i>acetyl-QYLFVPPNRYIFHG-NH₂</i>	1792.04	> 95	DMSO
24	<i>acetyl-NRYIFHGAEVYSDS-NH₂</i>	1698.77	> 95	DMSO
25	<i>acetyl-HGAEVYSDSEDDV-NH₂</i>	1463.39	> 95	DMSO
26	<i>NRYIF-NH₂</i>	710.83	> 95	DMSO
27	<i>RYIFH-NH₂</i>	733.86	> 95	DMSO
28	<i>NRYI-NH₂</i>	563.65	> 95	DMSO
29	<i>YIFH-NH₂</i>	577.67	> 95	DMSO
30	<i>RYIF-NH₂</i>	596.72	> 95	DMSO
31	<i>RYI-NH₂</i>	449.54	> 95	DMSO
32	<i>YIF-NH₂</i>	440.53	> 95	DMSO

Continuation on next page

Continuation of Table 7.1:

Peptide	Sequence (N → C)	MW (g/mol)	Purity (%)	Solvent
Substrate peptides				
p53short	RHK-(<i>acetyl</i> -K)-LMFK	1129.45	99.3	Tris/HCl
α -Tubulin	MPSD-(<i>acetyl</i> -K)-TIG	890.03	98.0	NaH ₂ PO ₄
ACS2.3	TRSG-(<i>acetyl</i> -K)-VMR	976.17	98.0	Tris/HCl
succCPS1short	RGVL-(<i>succinyl</i> -K)-EYGV	1120.28	97.2	Tris/HCl
myrTNF α	EALPK-(<i>myristoyl</i> -K)-TGG	1151.46	> 95	DMSO
<i>FdL-1</i>	RHK-(<i>acetyl</i> -K) -7-amino-4-methylcoumarin	808.90	> 95	*
ac-Tat_46-54	SYGR-(<i>acetyl</i> -K)-KRRQ	1220.41	98.1	Tris/HCl

* buffer for *FdL-1*: 50 mM Tris/HCl, pH 8.0, 137 mM NaCl, 2.7 mM KCl, 1 mM MgCl₂

Table 7.2: Characteristics of oligonucleotides used in this study. Oligonucleotides were ordered from Sigma (salt-free) or Eurofins Genomics in HPSF (high purity salt-free) quality and dissolved in ddH₂O to reach a stock concentration of 100 µM.

Oligonucleotide	Sequence (5' → 3')	Position	Mutation	Stop-codon	Restriction	Direction
Cloning of mini-Sirt1 and mutants						
Sirt1_3'505GGGS2	GCTTCCACCGCCGCTGCCTCC ACCTACAGGGTTACAGCAAAG TT	505	no	no	no	reverse
Sirt1_5'641GGGS2	GGTGGAGGCAGCGCGGTGGA AGCCAGTATCTGTTTTTGCCA CCAAAT	641	no	no	no	forward
Sirt1-5XhoI183	TATACTCGAGGGTCCATATAC TTTTGTTTCAGCAACATC	183	no	no	XhoI	forward
Sirt1-3BamHI665stop	TATAGGATCCCTAGACGTCAT CTTCAGAGTCTGAATA	665	no	665	BamHI	reverse
Sirt1-5XhoI214	TATACTCGAGGAGTTGGATGA TATGACACTGTGGCAG	214	no	no	XhoI	forward
Sirt1-5NdeI183	TATACATATGGGTCCATATAC TTTTGTTTCAGCAACATC	183	no	no	NdeI	forward
Sirt1-3BamHI505	TATAGGATCCCTATACAGGGT TACAGCAAAGTT	505	no	505	BamHI	reverse
S1_S659D_3st665	TATAGGATCCCTAGACGTCAT CTTCAGAGTCATCATATACCT CAGCGCC	665	S659D	665	BamHI	reverse
S1_S661D_3st665	TATAGGATCCCTAGACGTCAT CTTCATCGTCTGAATATACCT CAGC	665	S661D	665	BamHI	reverse
S1_S659D_S661D	TATAGGATCCCTAGACGTCAT CTTCATCGTCATCATATACCT CAGCGCC	665	S659D, S661D	665	BamHI	reverse
Cloning of Hic1-BTB and deletion mutants						
Hic1_5'NdeI1	TATACATATGCTGGACACGAT GGAGGCG	20	no	no	NdeI	forward
Hic1_3'BamHI135st	TATAGGATCCCTACTTGCCGT GGCGCTTGAG	154	no	154	BamHI	reverse
Hic1_3'BamHI140st	TATAGGATCCCTAGTCGGGGA TCTGCAG	140	no	140	BamHI	reverse
Hic1_3'BamHI137st	TATAGGATCCCTACTGCAGGT AGCTGGC	137	no	137	BamHI	reverse
Hic1_3'BamHI125st	TATAGGATCCCTAGCTCGGCT CAGCCCC	125	no	125	BamHI	reverse
General cloning oligonucleotides						
T7_forward	TAATACGACTCACTATAGGG	n. a.	no	no	no	forward
T7_reverse	CTAGTTATGCTCAGCGGT	n. a.	no	no	no	reverse
CMV_forward	CGCAAATGGGCGGTAGGCGTG	n. a.	no	no	no	forward
pcDNA3_forward	GGCTAACTAGAGAACCCACTG	n. a.	no	no	no	forward
pcDNA3_reverse	GGCAACTAGAAGGCACAGTC	n. a.	no	no	no	reverse

Table 7.3: Molecular weight (MW) (Da) and extinction coefficient ϵ_{280} ($M^{-1} \text{ cm}^{-1}$) for the proteins used in this work. Values were calculated based on the amino acid sequence using the online tool ProtParam (ExPASy²¹⁰).

Protein	with N-terminal His ₆ -tag		without N-terminal His ₆ -tag		
	MW (Da)	ϵ_{280} ($M^{-1} \text{ cm}^{-1}$)	MW (Da)	ϵ_{280} ($M^{-1} \text{ cm}^{-1}$)	pI (pH)
fl-hSirt1	83707.2	46965	81825.1	46965	4.6
mini-Sirt1	42947.5	24130	41070.4	22640	5.3
mini-Sirt1- Δ SBD	39476.4	22640	37599.4	21150	5.4
mini-Sirt1- Δ ESA	39473.8	19660	37596.8	18170	5.7
mini-Sirt1-(S659D)	42975.5	24130	41098.4	22640	5.3
mini-Sirt1-(S661D)	42975.5	24130	41098.4	22640	5.3
mini-Sirt1-(S659D S661D)	43003.5	24130	41126.4	22640	5.2
Hic1-BTB (pET15b)	16662.2	4595	14780.2	4595	9.0
Hic1-BTB (pET15b $_{mod}$)	16904.4	6085	14693.1	4595	9.0
hAROS	17460.0	3105	15578.0	3105	10.8
Tat Cys ⁻	18470.5	19940	9673.8	8480	10.8
Tat Cys ⁻ (1-63)	15990.8	19940	7251.2	8480	11.4
Tat Cys ⁻ (21-63)	13868.4	14440	5128.9	2980	12.1

7.2 Additional results

7.2.1 Purification of human mini-Sirt1 variants

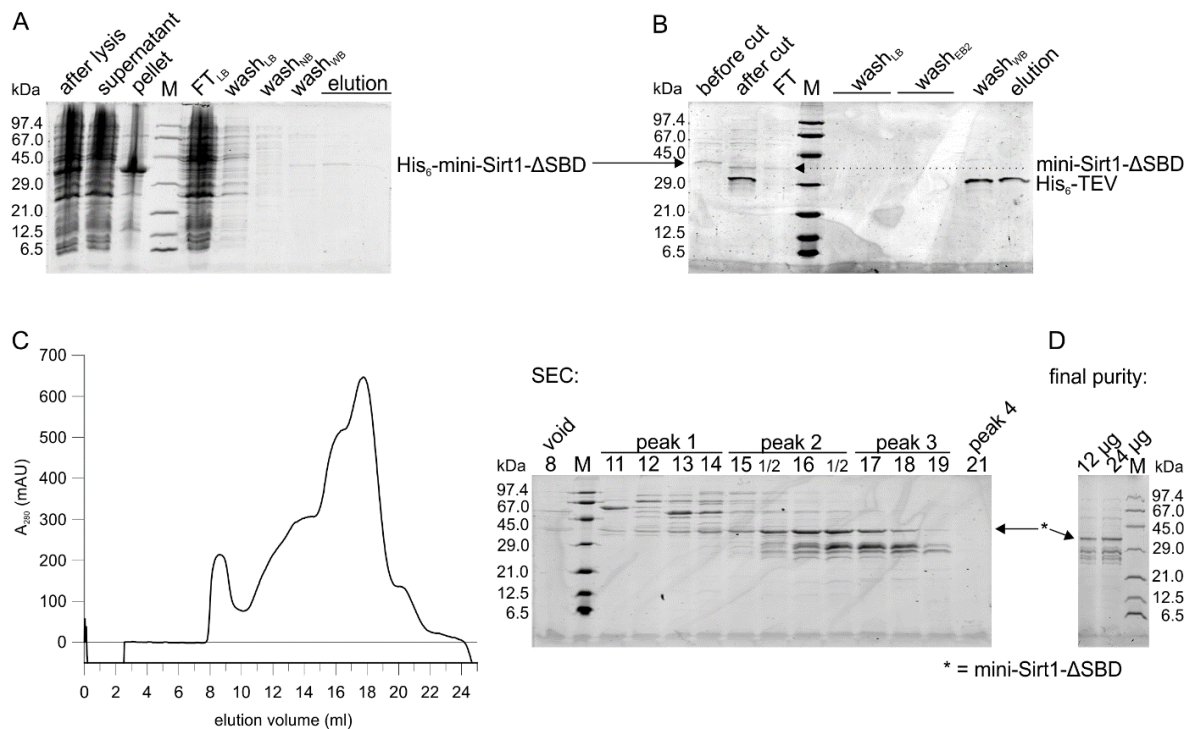


Figure 7.1: Purification of human mini-Sirt1-ΔSBD. **A** Affinity chromatography (AC) and **B** Reverse AC on Ni²⁺-immobilized beads. **C** SEC on S200 10/300 GL. Mini-Sirt1-ΔSBD elutes at 16.2 ml (peak 2). Peak 3 at 17.7 ml contains mini-Sirt1-ΔSBD and contaminants. Numbers on SDS PAGE refer to the respective elution volume from SEC. **D** Quality assessment of the purified mini-Sirt1-ΔSBD. Abbreviations: LB - lysis buffer, NB - Ni²⁺-beads equilibration buffer, WB - wash buffer, EB2 - elution buffer reverse AC.

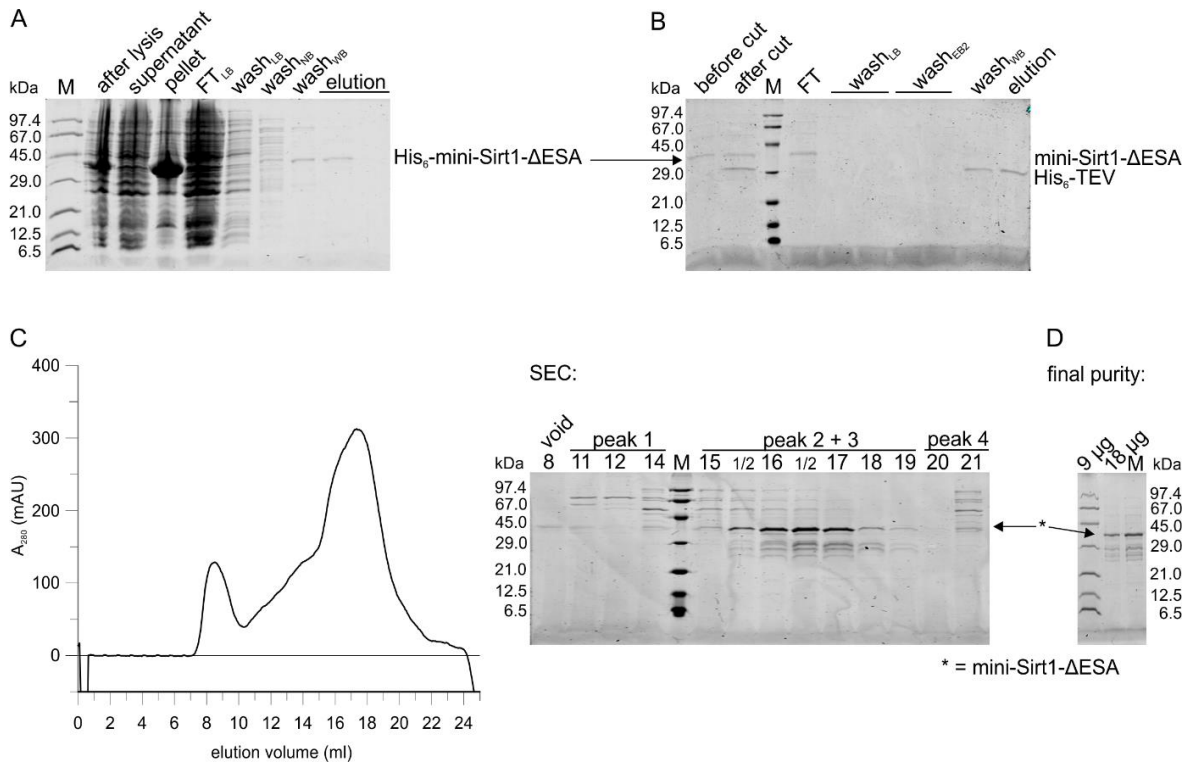


Figure 7.2: Purification of human mini-Sirt1-ΔESA. **A** Affinity chromatography and **B** Reverse AC on Ni²⁺-immobilized beads. **C** SEC on S200 10/300 GL. Mini-Sirt1-ΔESA elutes at 17.4 ml (peak 2 + 3). Numbers on SDS PAGE refer to the respective elution volume from SEC. **D** Quality assessment of the purified mini-Sirt1-ΔESA. Abbreviations: LB - lysis buffer, NB - Ni²⁺-beads equilibration buffer, WB - wash buffer, EB2 - elution buffer reverse AC.

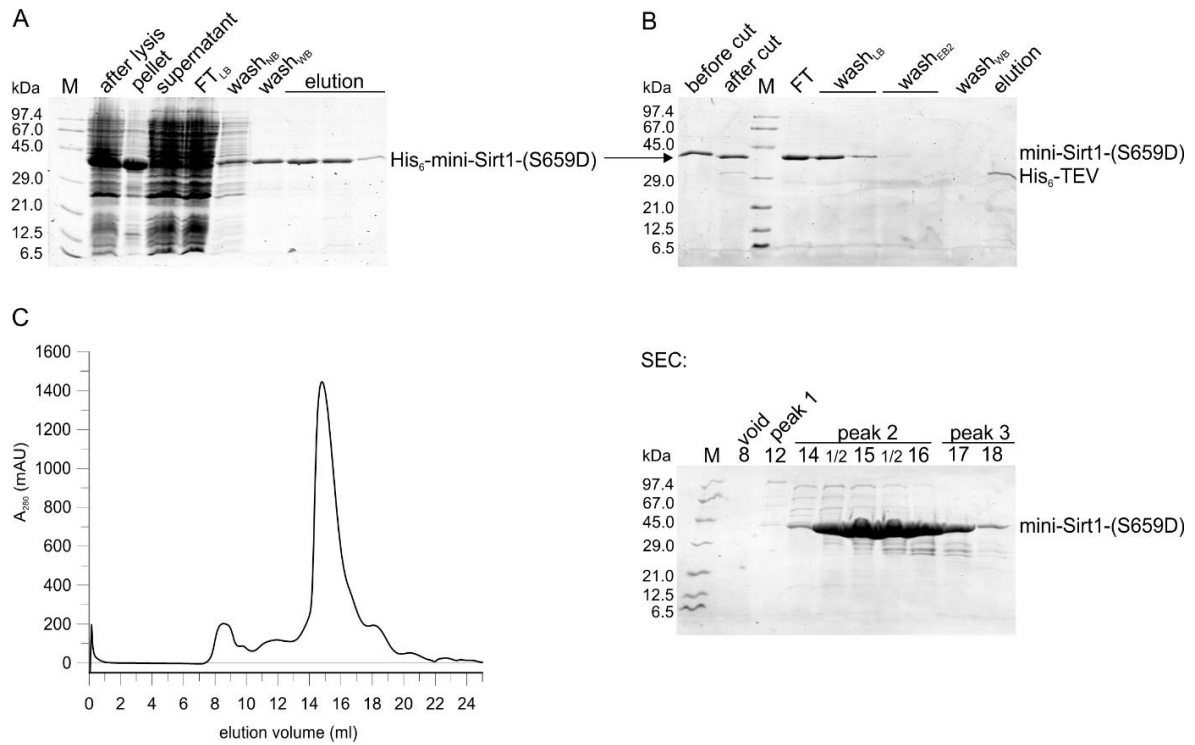


Figure 7.3: Purification of human mini-Sirt1-(S659D). **A** Affinity chromatography and **B** Reverse AC on Ni^{2+} -immobilized beads. **C** SEC on S200 10/300 GL. Mini-Sirt1-(S659D) elutes at 14.5 ml (peak 2). Numbers on SDS PAGE refer to the respective elution volume from SEC. Abbreviations: LB - lysis buffer, NB - Ni^{2+} -beads equilibration buffer, WB - wash buffer, EB2 - elution buffer reverse AC.

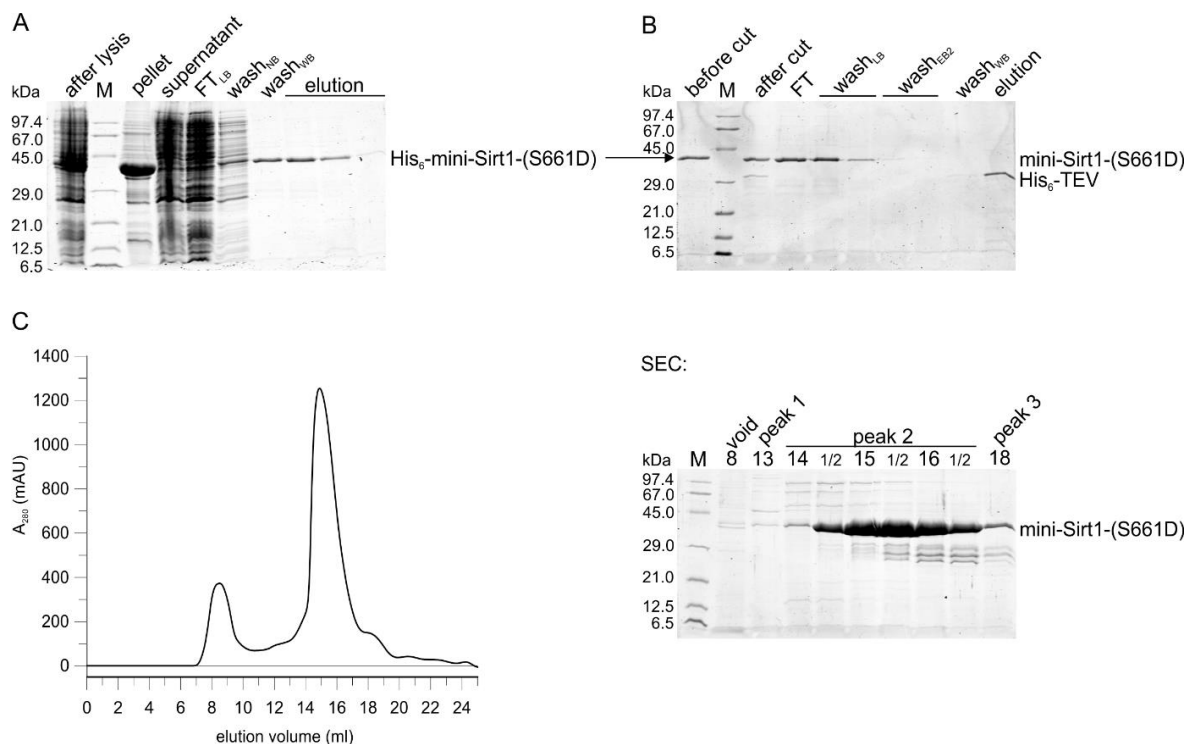


Figure 7.4: Purification of human *mini-Sirt1-(S661D)*. **A** Affinity chromatography and **B** Reverse AC on Ni²⁺-immobilized beads. **C** SEC on S200 10/300 GL. Mini-Sirt1-(S661D) elutes at 14.7 ml (peak 2). Numbers on SDS PAGE refer to the respective elution volume from SEC. Abbreviations: LB - lysis buffer, NB - Ni²⁺-beads equilibration buffer, WB - wash buffer, EB2 - elution buffer reverse AC.

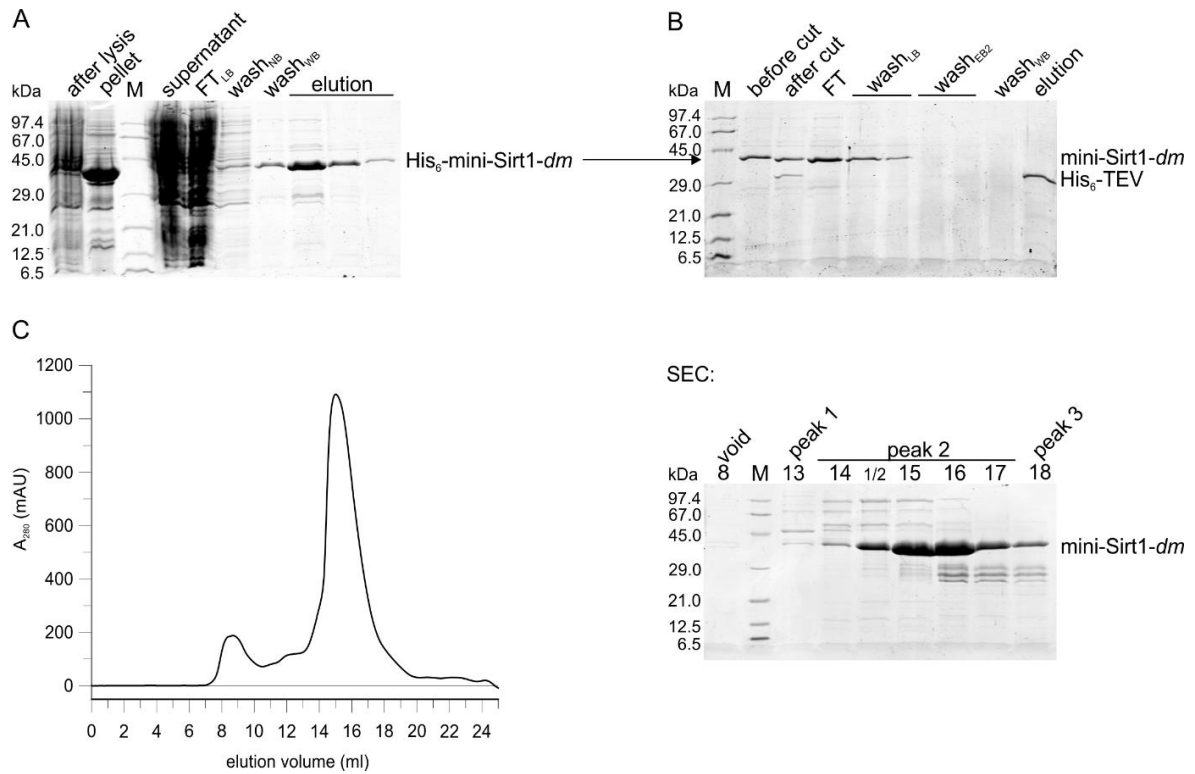


Figure 7.5: Purification of human mini-Sirt1-(S659D S661D). **A** Affinity chromatography and **B** Reverse AC on Ni²⁺-immobilized beads. **C** SEC on S200 10/300 GL. Mini-Sirt1-(S659D S661D) elutes at 15.0 ml (peak 2). Numbers on SDS PAGE refer to the respective elution volume from SEC. Abbreviations: mini-Sirt1-*dm* - mini-Sirt1 double mutant (S659D S661D), LB - lysis buffer, NB - Ni²⁺-beads equilibration buffer, WB - wash buffer, EB2 - elution buffer reverse AC.

7.2.2 Regulation of hSirt1 activity by small molecules and AROS

Table 7.4: Initial crystallization conditions for mini-Sirt1. The protein solution contained 10 mg/ml mini-Sirt1 optionally supplemented at a DMSO concentration of 6-10% (v/v) with either 1.22 mM STAC, or with 1.22 mM STAC, 1.22 mM p53short and 5 mM ADPr, or with 1.22 mM Tat₄₉₋₆₀. Crystallization conditions, which led to the successful collection of a dataset, are highlighted in bold.

Commercial screen	Crystallization condition	Comments
Dai <i>et al.</i> (2015)	0.1 M Tris/HCl, pH 8.5; 0.2 M MgCl ₂ ; 16% (w/v) PEG 4000	no crystals
JCSG Core II, A7	0.1 M bicine, pH 9.0; 10% (w/v) PEG 6000, 1 M LiCl ₂	small crystal plates/blocks for mini-Sirt1 with STAC, p53short, and ADPr
JCSG Core II, A12	0.1 M Tris/HCl, pH 8.5; 8% (w/v) PEG 8000 best condition: 0.1 M Tris/HCl, pH 8.5; 10% (w/v) PEG 8000; 0.2 M MgCl ₂	crystal growth only in combination with MgCl ₂ for mini-Sirt1/STAC (rods) or mini-Sirt1/STAC/p53short/ADPr (blocks) best diffraction at 3.7 Å resolution
JCSG Core III, A5	0.1 M CHES, pH 9.5; 50% (w/v) PEG 400; 0.2 M NaCl	crystal flowers for mini-Sirt1 with STAC, p53short, and ADPr
JCSG Core III, B5	0.1 M Tris/HCl, pH 8.5; 0.2 M MgCl ₂ ; 30% (w/v) PEG 4000	crystal rods for mini-Sirt1/STAC
JCSG Core III, D1	0.1 M imidazole, pH 8.0; 1 M sodium potassium tartrate; 0.2 M NaCl	small crystal plates/blocks for mini-Sirt1 with STAC, p53short, and ADPr
JCSG Core IV, B11	0.1 M Tris/HCl, pH 8.5; 30% (w/v) PEG 4000; 0.2 M LiSO ₄	small crystal plates/blocks for mini-Sirt1 with STAC, p53short, and ADPr
JCSG Core IV, C1	0.1 M Tris/HCl, pH 8.5; 1.5 M ammonium sulfate; 12% (v/v) glycerol	small crystal plates/blocks for mini-Sirt1 with STAC, p53short, and ADPr
JCSG Core IV, C3	0.085 M Tris/HCl, pH 8.5; 25.5% (w/v) PEG 4000; 15% (v/v) glycerol; 0.17 M sodium acetate	small crystal plates/blocks for mini-Sirt1 with STAC, p53short, and ADPr
JCSG Core IV, D2	0.1 M HEPES, pH 7.5; 1.26 M ammonium sulfate	large crystal blocks for mini-Sirt1 with STAC, p53short, and ADPr best diffraction at 4.0 Å resolution
PACT, G4	0.1 M Bis-tris propane, pH 7.5, 0.2 M potassium thiocyanate, 20% (w/v) PEG 3350 best condition: 0.1 M Bis-tris propane, pH 7.5, 0.2 M potassium thiocyanate, 20% (w/v) PEG 3350, and 10% (v/v) 2-methyl-2-propanol	large crystal blocks obtained in presence of Tat ₄₉₋₆₀ structure solved at 2.3 Å resolution revealed apo mini-Sirt1
PACT, H1	0.1 M Bis-tris propane, pH 8.5, 20% (w/v) PEG 3350, and 0.2 M sodium fluoride best condition: 0.1 M Bis-tris propane, pH 8.5, 20% (w/v) PEG 3350, and 0.2 M sodium fluoride, 10% (v/v) ethanol, and 0.01 M TCEP	large crystal plates for apo mini-Sirt1 best diffraction at 3.1 Å resolution soaking or cocrystallization with DAA, tranilast, or Tat peptides did not work

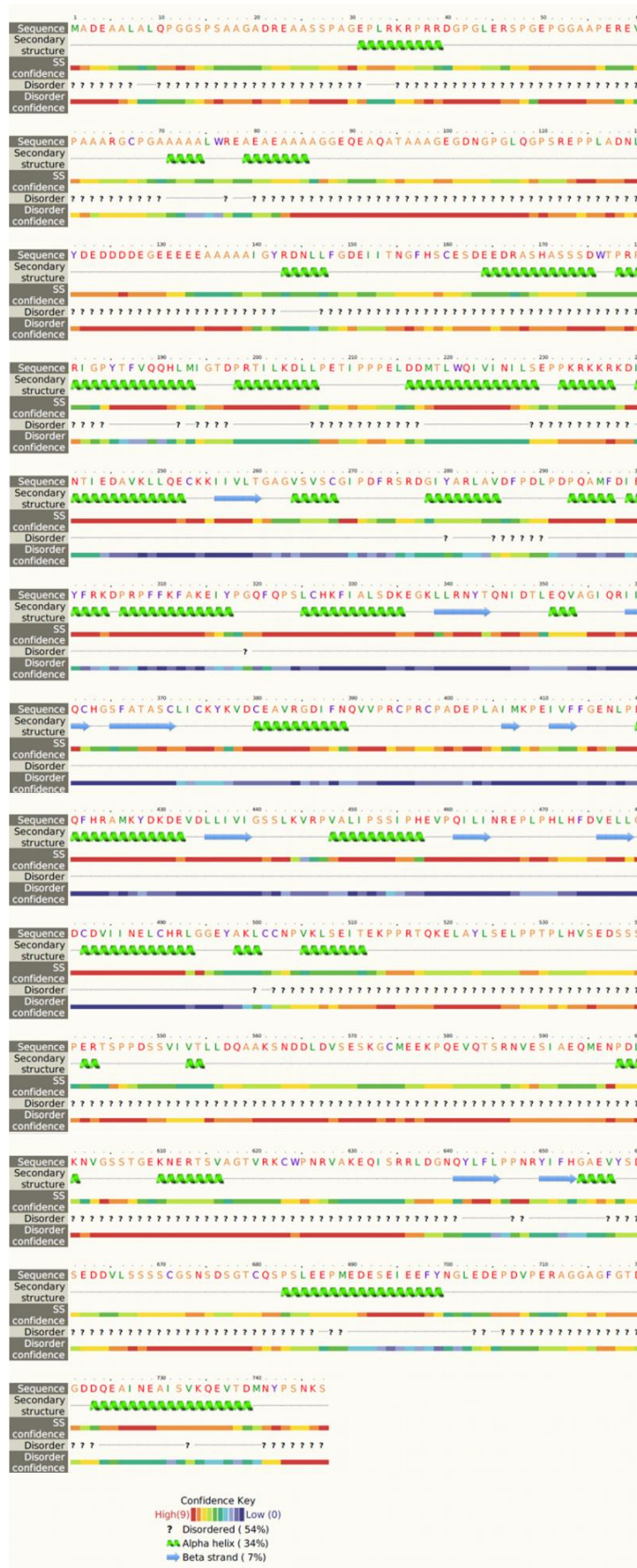


Figure 7.6: Secondary structure prediction for fl-hSirt1 using Phyre² 260 in normal mode. Secondary structure elements are depicted as α -helices (34%), β -strands (7%), or disordered regions (54%). The confidence is color-depicted from red = high to blue = low. The hSirt1 sequence was derived from Uniprot: Q96EB6.

Table 7.5: Data collection and refinement statistics for apo mini-Sirt1 (obtained after soaking with tranilast). Apo mini-Sirt1 after soaking with tranilast was refined with REFMAC5 using restrained refinement, NCS, and geometry restraints derived from PDB: 4ZZH with PROSMART. Tranilast was not observed in the structure.

Characteristic	Apo mini-Sirt1 (after soaking with tranilast)
synchrotron (detector)	BESSY, MX 14.1 (PILATUS 6M)
wavelength (Å)	0.9184
resolution range (Å)	47.7 - 3.1 (3.2 - 3.1)
space group	C222 ₁ (20)
unit cell	102.3 146.7 125.3 90.0 90.0 90.0
total reflections	73053 (6937)
unique reflections	16674 (1584)
multiplicity	4.4 (4.4)
completeness (%)	98.1 (94.7)
mean I/sigma(I)	10.4 (1.2)
Wilson B-factor (Å ²)	102.3
R _{merge}	0.111 (1.034)
R _{meas} [†]	0.126 (1.173)
R _{pim}	0.058 (0.542)
CC _{1/2} [‡]	0.997 (0.606)
CC*	0.999 (0.869)
reflections used in refinement	16663 (1582)
reflections used for R _{free}	834 (79)
R _{work}	0.237 (0.444)
R _{free} [¥]	0.323 (0.478)
CC _{work}	0.936 (0.591)
CC _{free}	0.806 (0.383)
number of non-hydrogen atoms	5645
protein atoms	5501
ligand atoms (Zn ²⁺ , PEG)	24
water molecules	120
protein residues	690
RMSD _{bonds} (Å)	0.007
RMSD _{angles} (°)	1.500
Ramachandran favored (%)	92.7
Ramachandran allowed (%)	6.2
Ramachandran outliers (%)	1.2
rotamer outliers (%)	14.4
clashscore	24.2
average B-factor	105.6
protein atoms	106.1
ligand atoms (Zn ²⁺ , PEG)	165.4
water molecules	70.9

Statistics for the highest resolution shell are shown in parentheses.

[†] R_{meas} is the redundancy independent R-factor (intensities) and was calculated from

$$R_{meas} = \frac{\sum_{hkl} \sqrt{\frac{n}{n-1}} \sum_{i=1}^n |I_i(hkl) - \bar{I}(hkl)|}{\sum_{hkl} \sum_{i=1}^n I_i(hkl)}, \text{ with } \bar{I}(hkl) = \frac{1}{n} \sum_{i=1}^n I_i(hkl).$$

[‡] CC_{1/2} is the percentage of correlation between intensities from random half-datasets.

[¥] R_{free} was calculated from 5% of measured reflections omitted from refinement.

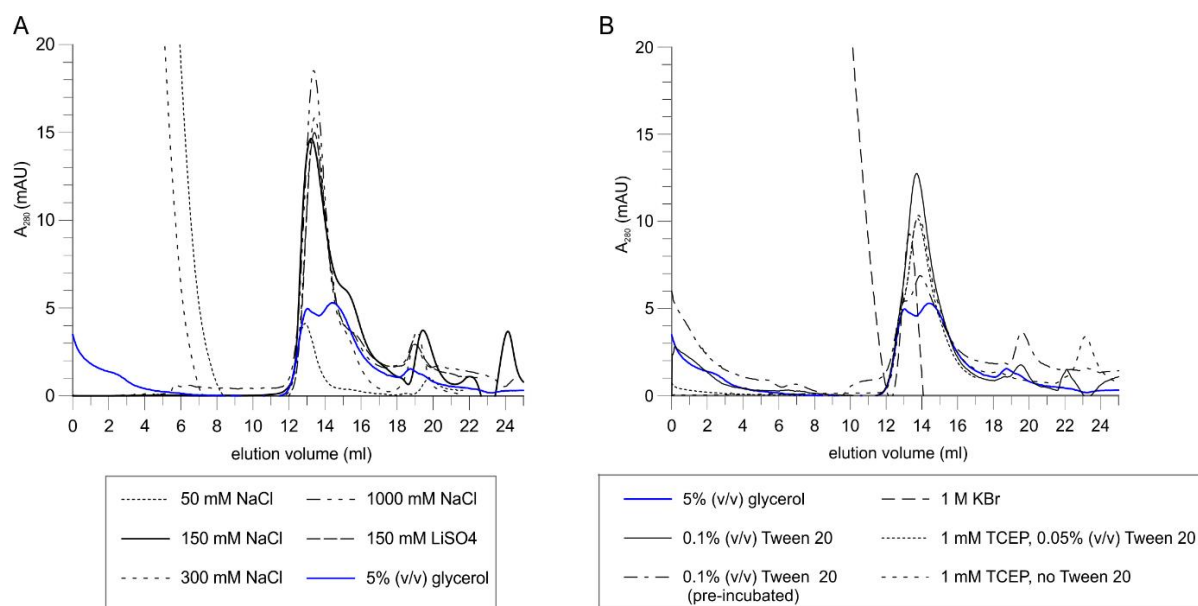


Figure 7.8: Analytical SEC of *Hic1-BTB* octamer from *pET15bmod* on *S200 10/300 GL*. **A** SEC of 500 μ g *Hic1-BTB* octamer in 150 μ l of the basis buffer 25 mM HEPES, pH 7.5, 150 mM NaCl, 10 mM DTT, 0.05% (v/v) Tween[®] 20. While salts were used instead of 150 mM NaCl, glycerol was added to the basis buffer. **B** SEC of 500 μ g *Hic1-BTB* octamer in 150 μ l of the new basis buffer 25 mM HEPES, pH 7.5, 150 mM NaCl, 10 mM DTT, 5% (v/v) glycerol, 0.05% (v/v) Tween[®] 20 (blue line). Salts, reducing agents, and detergents were used instead of their respective concentration in the basis buffer.

Table 7.6: Data collection and refinement statistics for *Hic1-BTB*. Refinement was performed with REFMAC5 in the beginning and later with Phenix.Refine using restrained refinement, overall B factors, TLS groups, and torsion-angle NCS restraints.

Characteristic	Hic1-BTB
synchrotron (detector)	BESSY, MX 14.1 (PILATUS 6M)
wavelength (Å)	0.9184
resolution range (Å)	48.7 - 2.7 (2.8 - 2.7)
space group	P2 ₁ 2 ₁ 2 ₁
unit cell	128.6 157.8 157.9 90.0 90.0 90.0
total reflections	666791 (62605)
unique reflections	88487 (8591)
multiplicity	7.5 (7.3)
completeness (%)	99.4 (97.6)
mean I/sigma(I)	5.3 (0.6)
Wilson B-factor (Å ²)	57.7
R _{merge}	0.348 (3.028)
R _{meas} [†]	0.373 (3.257)
R _{pim}	0.134 (1.182)
CC _{1/2} [‡]	0.988 (0.216)
CC*	0.997 (0.596)
reflections used in refinement	88411 (8588)
reflections used for R _{free}	2099 (203)
R _{work}	0.225 (0.393)
R _{free} [¥]	0.284 (0.423)
CC _{work}	0.953 (0.472)
CC _{free}	0.940 (0.578)
number of non-hydrogen atoms	16044
protein atoms	15538
Na ⁺	16
water molecules	490
protein residues	2057
RMSD _{bonds} (Å)	0.009
RMSD _{angles} (°)	1.040
Ramachandran favored (%)	93.1
Ramachandran allowed (%)	5.8
Ramachandran outliers (%)	1.1
rotamer outliers (%)	0.1
clashscore	8.8
average B-factor	61.7
protein atoms	61.9
Na ⁺	69.4
water molecules	53.8
number of TLS groups	16

Statistics for the highest resolution shell are shown in parentheses.

[†] R_{meas} is the redundancy independent R-factor (intensities) and was calculated from

$$R_{meas} = \frac{\sum_{hkl} \sqrt{\frac{n}{n-1}} \sum_{i=1}^n |I_i(hkl) - \bar{I}(hkl)|}{\sum_{hkl} \sum_{i=1}^n I_i(hkl)}, \text{ with } \bar{I}(hkl) = \frac{1}{n} \sum_{i=1}^n I_i(hkl).$$

[‡] CC_{1/2} is the percentage of correlation between intensities from random half-datasets.

[¥] R_{free} was calculated from 5% of measured reflections omitted from refinement.

7.2.4 Inhibition of hSirt1 by HIV1-Tat

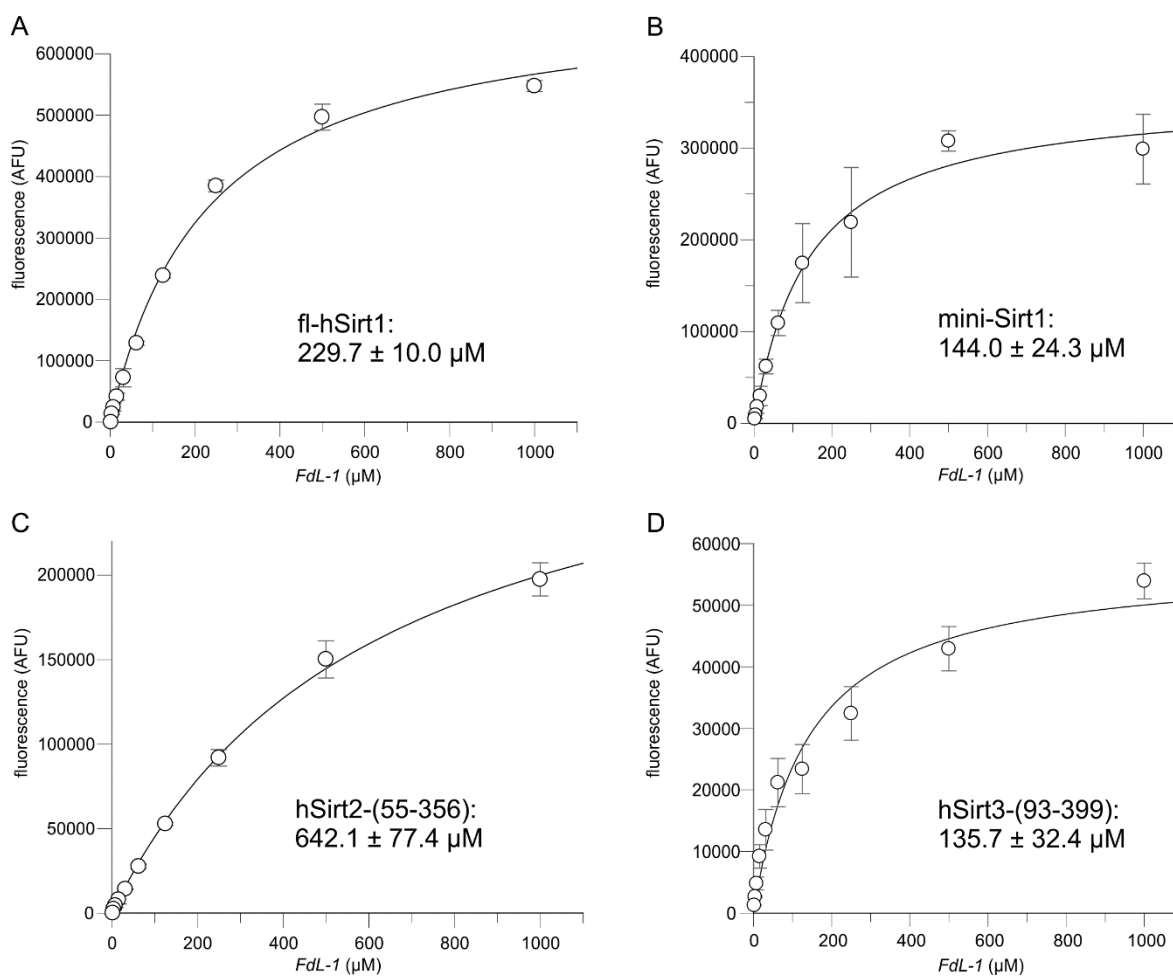


Figure 7.9: K_m determination for *FdL-1* substrate for hSirt1-3. Fluor de Lys assay with $1 \mu\text{M}$ sirtuin, 3 mM NAD^+ , and titration of *FdL-1* substrate ($n = 3$). The K_m for *FdL-1* was $229.7 \pm 10.0 \mu\text{M}$ for fl-hSirt1 (A), $144.0 \pm 24.3 \mu\text{M}$ for mini-Sirt1 (B), $642.1 \pm 77.4 \mu\text{M}$ for hSirt2-(55-356) (C), and $135.7 \pm 32.4 \mu\text{M}$ for hSirt3-(93-399) (D). For IC_{50} determinations at the respective substrate K_m , *FdL-1* was used at $230 \mu\text{M}$ for fl-hSirt1, $144 \mu\text{M}$ for mini-Sirt1, $300 \mu\text{M}$ for hSirt2-(56-356), and $135 \mu\text{M}$ for hSirt3-(93-399).

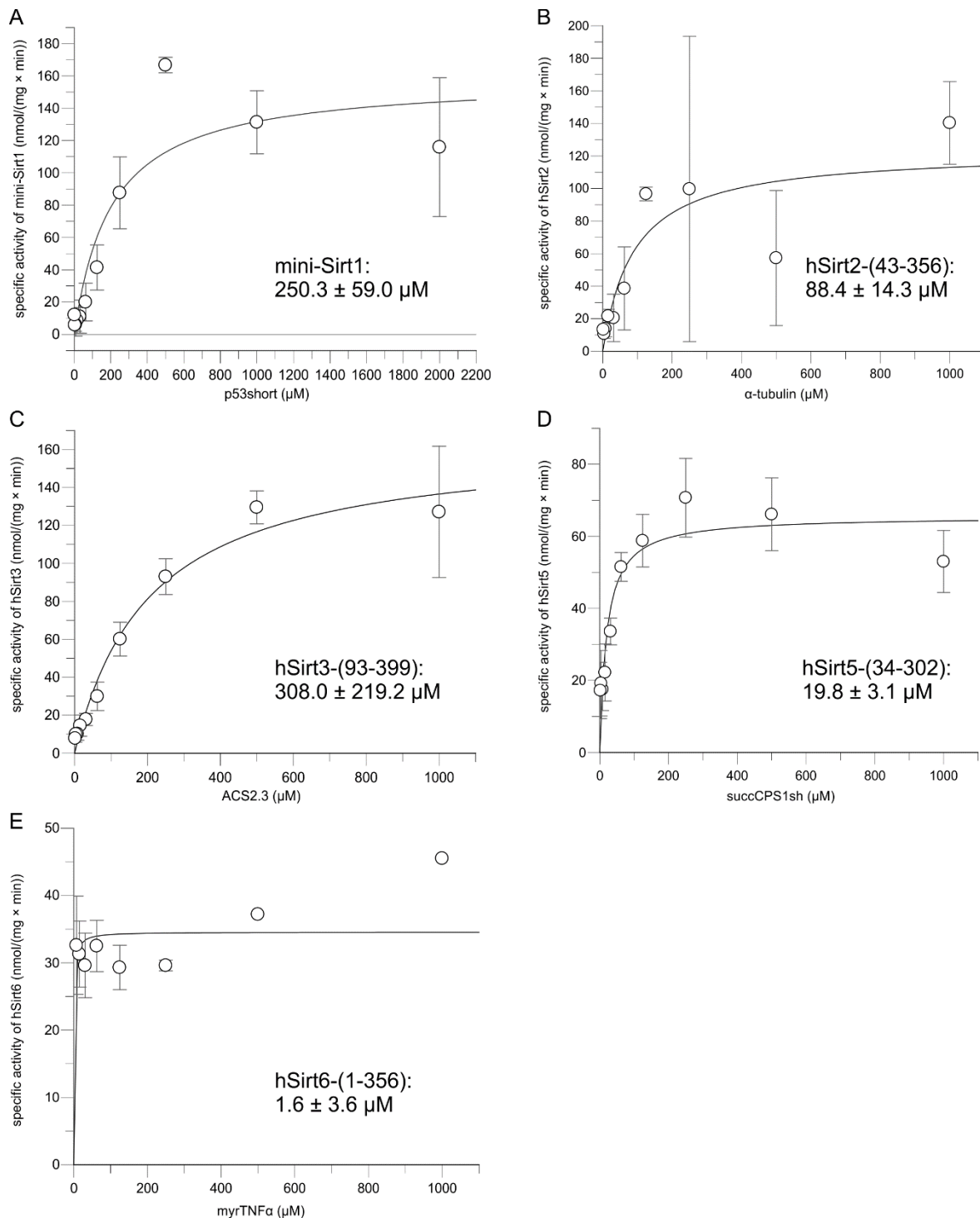


Figure 7.10: K_m determination for natural substrates for human sirtuin isoforms. Continuous coupled enzymatic assay with $1 \mu\text{M}$ sirtuin, 3 mM NAD^+ , and titration of the respective substrate ($n = 3$). The substrate K_m values were determined as follows: **A** mini-Sirt1: $250.3 \pm 59.0 \mu\text{M}$ for p53short, **B** hSirt2-(43-356): $88.4 \pm 14.3 \mu\text{M}$ for α -tubulin, **C** hSirt3-(93-399): $308.0 \pm 219.2 \mu\text{M}$ for ACS2.3, **D** hSirt5-(34-302): $19.8 \pm 3.1 \mu\text{M}$ for succCPS1short, and **E** hSirt6-(1-356): $1.6 \pm 3.6 \mu\text{M}$ for myrTNF α . For IC_{50} determinations at the respective substrate K_m , $200 \mu\text{M}$ p53short were used for mini-Sirt1, $95 \mu\text{M}$ α -tubulin for hSirt2-(43-356), $250 \mu\text{M}$ ACS2.3 for hSirt3-(39-399), $23 \mu\text{M}$ succCPS1short for hSirt5-(34-302), and $5 \mu\text{M}$ myrTNF α for hSirt6-(1-355). The K_m for p53short and hSirt2-(43-356) was estimated to $150 \mu\text{M}$ (without determination).

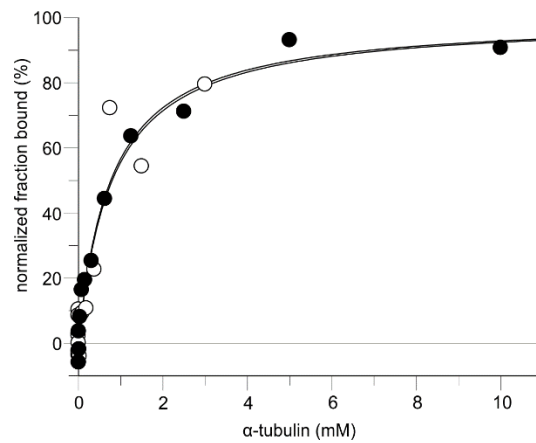


Figure 7.11: Binding affinity of α -tubulin to HIV1-Tat Cys⁻. MST with 20 nM FITC-labeled Tat Cys⁻ and titration of α -tubulin. The K_d from two individual titrations (starting from 3 mM or 10 mM) amounts to $778.3 \pm 22.4 \mu\text{M}$, calculated from thermophoresis at 25 °C, 12% LED power, and 30% MST power.

Table 7.7: Selected initial crystallization conditions for hSirt3 in complex with Tat peptides. The protein solution contained 10 mg/ml hSirt3-(118-399). Tat_46-54 and ac-Tat_46-54 were added in a final concentration of 2 mM with or without 20 mM ADPr. Inhibiting Tat peptides were added in a final concentration of 2 mM in presence of 10% (v/v) DMSO and with or without either 10 mM NAD⁺ or 20 mM ADPr as indicated. Crystallization conditions, which afforded the structures described in this thesis, are highlighted in bold and blue.

Commercial screen	Crystallization condition	Best diffraction (Å)	Space group/ Unit cell (Å)	Dataset name and comments
hSirt3/ac-Tat_46-54				
Core I, E6	0.1 M MES, pH 6, 30% (w/v) PEG 200, 5% (w/v) PEG 3000	1.65	C222 ₁ (20) 79 128 78 90 90 90	3174_E6_1 peptide visible
Core II, B7	20% (w/v) PEG 3350, 0.2 M Li ⁺ -acetate	2.24	P2 ₁ (4) 52 77 54 90 90 90	3175_B7_1 two chains of hSirt3, peptide visible in both chains to different extent
Core II, D11	0.1 M MES, pH 6.5, 12% (w/v) PEG 20000	1.98	P2 ₁ 2 ₁ 2 ₁ (19) 75 77 52 90 90 90	3175_D11_1 no peptide present
hSirt3/ac-Tat_46-54/ADPr				
Core II, B3	0.1 M imidazole, pH 8, 10% (w/v) PEG 8000, 0.2 M Ca ²⁺ -acetate	2.19	C222 ₁ (20) 78 129 78 90 90 90	3175_B3_2 peptide visible, very weak density coverage for ADPr
hSirt3/Tat_46-54				
Core II, E3	0.1 M MES, pH 6, 20% (w/v) PEG 6000, 1 M LiCl ₂	2.30	P2 ₁ (4) 86 143 95 90 116 90	3175_E3_3 no peptide present
hSirt3/Tat_49-60				
Core III, D7	0.1 M HEPES, pH 7, 20% (w/v) PEG 6000, 1 M LiCl ₂	~ 5.00	n. a.	3090_D7_1 no dataset collected due to low resolution
Core IV, E3	0.1 M Tris/HCl, pH 7, 40% (v/v) MPD, 0.2 M ammonium sulfate	~ 4.70	n. a.	3091_E3_1 no dataset collected due to low resolution
hSirt3/Tat_37-59				
Core I, A1	0.1 M CHES, pH 9, 20% (w/v) PEG 8000	1.95	P2 ₁ (4) 55 78 77 90 96 90	3088_A1_3 peptide visible
Core I, A2	0.1 M bicine, pH 8.5, 20% (w/v) PEG 6000	1.95 (incomplete)	P2 ₁ (4) 54 78 77 90 96 90	3088_A2_3 peptide visible
Core II, D11	0.1 M MES, pH 6.5, 12% (w/v) PEG 20000	3.50	P3 ₂ 2 ₁ (154) 109 109 340 90 90 120	3089_D11_3 no peptide present
Core III, A9	0.1 M bicine, pH 9, 5% (w/v) PEG 6000	3.34	P2 ₁ (4) 54 78 76 90 96 90	3090_A9_3 peptide visible
Core III, A11	0.1 M Tris/HCl, pH 8.5, 20% (w/v) PEG 1000	3.50	P2 ₁ (4) 55 78 77 90 96 90	3090_A11_3 peptide visible

Continuation on next page

Continuation of Table 7.7:

Commercial screen	Crystallization condition	Best diffraction (Å)	Space group/ Unit cell (Å)	Dataset name and comments
hSirt3/Tat_37-59/NAD⁺				
Core I, E12	0.1 M MES, pH 5, 20% (w/v) PEG 6000	~ 3.20/6.00	n. a.	3070_E12_3 no dataset collected due to multiple crystal lattices
hSirt3/Tat_34-59				
Core I, A1	0.1 M CHES, pH 9, 20% (w/v) PEG 8000	3.20	P2 ₁ (4) 54 77 76 90 96 90	3088_A1_2 peptide visible
Core I, A2	0.1 M bicine, pH 8.5, 20% (w/v) PEG 6000	2.30	P2 ₁ (4) 54 78 77 90 96 90	3088_A2_2 peptide visible
Core I, D9	20% (w/v) PEG 3350, 0.2 M ammonium formate	2.15	P2 ₁ (4) 52 78 76 90 94 90	3088_D9_2 peptide visible
hSirt3/Tat_34-59/NAD⁺				
Core I, C10	0.1 M HEPES, pH 7, 20% (w/v) PEG 6000	2.90	P2 ₁ 2 ₁ 2 ₁ (19) 77 78 108 90 90 90	3172_C10_2 two chains of hSirt3, ADPr visible, peptide visible to different extent
Core II, D11	0.1 M MES, pH 6.5, 12% (w/v) PEG 20000	2.30	P2 ₁ 2 ₁ 2 ₁ (19) 78 78 108 90 90 90	3173_D11_2 two chains of hSirt3, ADPr visible, peptide visible to different extent

Table 7.8: Data collection and refinement statistics for hSirt3 in complex with ac-Tat_46-54. The hSirt3-(118-399)/ac-Tat_46-54 complex was processed with XDSAPP and refined with Phenix.Refine using restrained refinement, individual B factors, and in later cycles also optimized xray/stereochemistry weight.

Characteristic	HSirt3-(118-399)/ac-Tat_46-54
synchrotron (detector)	BESSY, MX 14.1 (PILATUS 6M)
wavelength (Å)	0.9184
resolution range (Å)	49.31 - 1.65 (1.71 - 1.65)
space group	C222 ₁
unit cell	78.7 127.8 77.6 90.0 90.0 90.0
total reflections	528620 (51960)
unique reflections	47383 (4669)
multiplicity	11.2 (11.1)
completeness (%)	99.9 (99.5)
mean I/sigma(I)	13.9 (0.9)
Wilson B-factor (Å ²)	31.5
R _{merge}	0.091 (2.162)
R _{meas} [†]	0.095 (2.265)
R _{pim}	0.028 (0.668)
CC _{1/2} [‡]	0.999 (0.481)
CC*	1.000 (0.806)
reflections used in refinement	47368 (4666)
reflections used for R _{free}	1092 (107)
R _{work}	0.183 (0.420)
R _{free} [¥]	0.210 (0.502)
CC _{work}	0.961 (0.704)
CC _{free}	0.931 (0.657)
number of non-hydrogen atoms	2539
protein atoms	2244
ligands (Zn ²⁺)	1
water molecules	294
protein residues	283
RMSD _{bonds} (Å)	0.018
RMSD _{angles} (°)	1.430
Ramachandran favored (%)	98.6
Ramachandran allowed (%)	1.5
Ramachandran outliers (%)	0.0
rotamer outliers (%)	0.4
clashscore	2.7
average B-factor	36.6
protein atoms	35.3
ligands (Zn ²⁺)	26.8
water molecules	46.3

Statistics for the highest resolution shell are shown in parentheses.

[†] R_{meas} is the redundancy independent R-factor (intensities) and was calculated from

$$R_{meas} = \frac{\sum_{hkl} \sqrt{\frac{n}{n-1}} \sum_{i=1}^n |I_i(hkl) - \bar{I}(hkl)|}{\sum_{hkl} \sum_{i=1}^n I_i(hkl)}, \text{ with } \bar{I}(hkl) = \frac{1}{n} \sum_{i=1}^n I_i(hkl).$$

[‡] CC_{1/2} is the percentage of correlation between intensities from random half-datasets.

[¥] R_{free} was calculated from 5% of measured reflections omitted from refinement.

Table 7.9: Data collection and refinement statistics for hSirt3 structures in complex with the inhibiting peptides Tat_34-59 and Tat_37-59. Both structures were processed with DIALS and refined with Phenix. Refine using restrained refinement, individual B factors, and in later cycles also optimized xray/stereochemistry weight. For the hSirt3/Tat_34-59 complex, TLS and NCS (torsion-angle) refinement was applied in addition.

Characteristic	HSirt3-(118-399)/Tat_34-59	HSirt3-(118-399)/Tat_37-59
synchrotron (detector)	BESSY, MX 14.1 (PILATUS 6M)	BESSY, MX 14.1 (PILATUS 6M)
wavelength (Å)	0.9184	0.9184
resolution range (Å)	52.09 - 2.15 (2.23 - 2.15)	54.24 - 1.95 (2.02 - 1.95)
space group	P2 ₁	P2 ₁
unit cell	52.2 78.4 75.8 90.0 94.2 90.0	54.5 78.1 76.6 90.0 96.1 90.0
total reflections	120689 (12329)	255560 (25541)
unique reflections	32870 (3278)	46174 (4615)
multiplicity	3.7 (3.8)	5.5 (5.5)
completeness (%)	98.7 (98.7)	98.8 (98.9)
mean I/sigma(I)	11.8 (1.0)	12.0 (0.6)
Wilson B-factor (Å ²)	32.1	30.9
R _{merge}	0.173 (0.823)	0.271 (1.453)
R _{meas} [†]	0.203 (0.963)	0.299 (1.604)
R _{pim}	0.104 (0.493)	0.125 (0.670)
CC _{1/2} [‡]	0.971 (0.560)	0.949 (0.445)
CC*	0.993 (0.847)	0.987 (0.785)
reflections used in refinement	32847 (3271)	46109 (4585)
reflections used for R _{free}	1521 (169)	2335 (245)
R _{work}	0.195 (0.253)	0.221 (0.318)
R _{free} [¥]	0.240 (0.341)	0.270 (0.343)
CC _{work}	0.921 (0.768)	0.929 (0.690)
CC _{free}	0.911 (0.542)	0.918 (0.678)
number of non-hydrogen atoms	4846	5030
protein atoms	4549	4559
ligands (Zn ²⁺)	2	2
water molecules	295	469
protein residues	575	576
RMSD _{bonds} (Å)	0.004	0.002
RMSD _{angles} (°)	0.670	0.560
Ramachandran favored (%)	97.7	97.2
Ramachandran allowed (%)	2.3	2.8
Ramachandran outliers (%)	0.0	0.0
rotamer outliers (%)	0.0	0.0
clashscore	4.5	3.6
average B-factor	45.4	38.3
protein atoms	45.4	38.0
ligands (Zn ²⁺)	29.3	25.3
water molecules	44.5	41.6
TLS groups	4	0

Statistics for the highest resolution shell are shown in parentheses.

[†] R_{meas} is the redundancy independent R-factor (intensities) and was calculated from

$$R_{meas} = \frac{\sum_{hkl} \sqrt{\frac{n}{n-1}} \sum_{i=1}^n |I_i(hkl) - \bar{I}(hkl)|}{\sum_{hkl} \sum_{i=1}^n I_i(hkl)}, \text{ with } \bar{I}(hkl) = \frac{1}{n} \sum_{i=1}^n I_i(hkl).$$

[‡] CC_{1/2} is the percentage of correlation between intensities from random half-datasets.

[¥] R_{free} was calculated from 5% of measured reflections omitted from refinement.

Table 7.10: Data collection and refinement statistics for hSirt3/Tat_34-59 in complex with ADPr. For cocrystallization, NAD⁺ was added, but the structure shows ADPr. The hSirt3-(118-399)/Tat_34-59/ADPr structure was processed with DIALS and refined with Phenix.Refine using restrained refinement, individual B factors, TLS, NCS (torsion-angle) restraints, and in later cycles also optimized xray/stereochemistry weight.

Characteristic	HSirt3-(118-399)/Tat_34-59/ ADPr
synchrotron (detector)	BESSY, MX 14.1 (PILATUS 6M)
wavelength (Å)	0.9184
resolution range (Å)	53.92 - 2.30 (2.38 - 2.30)
space group	P2 ₁ 2 ₁ 2 ₁
unit cell	77.8 78.4 107.8 90.0 90.0 90.0
total reflections	300250 (20339)
unique reflections	29892 (2909)
multiplicity	10.0 (7.0)
completeness (%)	99.7 (98.7)
mean I/sigma(I)	7.4 (0.4)
Wilson B-factor (Å ²)	34.2
R _{merge}	0.425 (2.249)
R _{meas} [†]	0.447 (2.433)
R _{pim}	0.139 (0.903)
CC _{1/2} [‡]	0.930 (0.319)
CC*	0.982 (0.695)
reflections used in refinement	29843 (2897)
reflections used for R _{free}	1455 (149)
R _{work}	0.220 (0.312)
R _{free} [¥]	0.275 (0.338)
CC _{work}	0.934 (0.662)
CC _{free}	0.891 (0.535)
number of non-hydrogen atoms	4863
protein atoms	4586
ligand atoms (Zn ²⁺ , ADPr)	74
water molecules	203
protein residues	587
RMSD _{bonds} (Å)	0.004
RMSD _{angles} (°)	0.780
Ramachandran favored (%)	97.2
Ramachandran allowed (%)	2.8
Ramachandran outliers (%)	0.0
rotamer outliers (%)	0.0
clashscore	14.2
average B-factor	50.2
protein atoms	50.3
ligand atoms (Zn ²⁺ , ADPr)	60.7
water molecules	44.0
TLS groups	4

Statistics for the highest resolution shell are shown in parentheses.

[†] R_{meas} is the redundancy independent R-factor (intensities) and was calculated from

$$R_{meas} = \frac{\sum_{hkl} \sqrt{\frac{n}{n-1}} \sum_{i=1}^n |I_i(hkl) - \bar{I}(hkl)|}{\sum_{hkl} \sum_{i=1}^n I_i(hkl)}, \text{ with } \bar{I}(hkl) = \frac{1}{n} \sum_{i=1}^n I_i(hkl).$$

[‡] CC_{1/2} is the percentage of correlation between intensities from random half-datasets.

[¥] R_{free} was calculated from 5% of measured reflections omitted from refinement.

Danksagung

An dieser Stelle möchte ich mich bei allen Menschen bedanken, die mich während meiner Promotion auf verschiedene Art und Weise unterstützt haben.

Mein Dank gilt zunächst Prof. Dr. Clemens Steegborn für die Ermöglichung dieser Doktorarbeit und die spannenden Projekte. Vielen Dank für die fachlichen Diskussionen und Hilfestellungen und vor allem für die eigenverantwortliche und freie Versuchsgestaltung.

Bei Prof. Dr. Birgitta Wöhrl bedanke ich mich für die Kollaboration beim Tat-Projekt. In diesem Zusammenhang möchte ich auch Ramona Heissmann für die Aufreinigung von Tat Cys⁻ und Kristian Schweimer für die NMR-Messungen danken.

Weiterhin danke ich Prof. Dr. Antonello Mai für die Synthese der ESA/CTR-Peptide, Prof. Dr. Mike Schutkowski für die Synthese des *FdL-1*-Peptids und Dr. Dominique Leprince für die Bereitstellung des pcDNA3-Vektors mit fl-Hic1.

Bei Dr. Michael Weyand und Dr. Sébastien Moniot bedanke ich mich für die Einführung in die Röntgenkristallographie und viele hilfreiche Diskussionen. Dr. Frank Fischer, Dr. Matt Fuszard und Dr. Andrea di Fonzo danke ich für die Unterstützung in der Analyse und Etablierung massenspektrometrischer Experimente und Dr. Christian Kambach danke ich für hilfreiche Ratschläge im Bereich der Klonierung.

Mein Dank für die vielen Diskussionen zum Experimentdesign gilt besonders Dr. Weijie You, Julian Pfahler, Sooruban Shanmugaratnam, Sandra Weiß (geb. Riemer), Dr. Martin Pannek, und Dr. Sébastien Moniot.

Bei meinen Studenten Pascal Kröger und Eileen Beck möchte ich mich für die Unterstützung bei den Projekten zu Hic1 und Tat bedanken. Sabrina Wischt danke ich für den Fortschritt bei der Aufreinigung von Hic1 und Norbert Grillenbeck für die Aufreinigung diverser Sirtuine. Auch Lisa Meisel und Susanne Schäfer danke ich für ihre Unterstützung.

Allen Angehörigen der Arbeitsgruppen von Prof. Dr. Clemens Steegborn, Prof. Dr. Birte Höcker und Prof. Dr. Andreas Möglich danke ich für ein angenehmes Zusammenarbeiten, die Einführung und Benutzung diverser Geräte und viele nette gemeinsame Grillfeste.

Dr. Sébastien Moniot und Sooruban Shanmugaratnam danke ich für die konstruktive Kritik zu meiner Dissertationsschrift.

Meinen langjährigen Kollegen aus dem Wild AEROBIC, dem Studio SL one und nun dem Clever Fit Bayreuth danke ich für eine stets kurzweilige Auszeit vom Laboralltag und viele nette gemeinsame Kursstunden.

Meiner Familie und meinen Freunden danke ich für die Begleitung und moralische Unterstützung während meines Studiums und der gesamten Promotionszeit.

Zuletzt danke ich Dir, Sorro, für die vielen gemeinsamen Kaffeepausen und Dein stets offenes Ohr. Ich danke Dir von Herzen für Deine Anregungen und Ratschläge und Deine soziale und emotionale Unterstützung während der langen Endphase meiner Promotion.

(Eidesstattliche) Versicherungen und Erklärungen

Hiermit beantrage ich gem. § 8 der Promotionsordnung der Fakultät für Biologie, Chemie und Geowissenschaften vom 15. September 2017 die Zulassung zum Promotionsprüfungsverfahren.

(§ 8 Satz 2 Nr. 3 PromO)

Hiermit versichere ich eidesstattlich, dass ich die Arbeit selbstständig verfasst und keine anderen als die von mir angegebenen Quellen und Hilfsmittel benutzt habe (vgl. Art. 64 Abs. 1 Satz 6 BayHSchG).

(§ 8 Satz 2 Nr. 3 PromO)

Hiermit erkläre ich, dass ich die Dissertation nicht bereits zur Erlangung eines akademischen Grades eingereicht habe und dass ich nicht bereits diese oder eine gleichartige Doktorprüfung endgültig nicht bestanden habe.

(§ 8 Satz 2 Nr. 4 PromO)

Hiermit erkläre ich, dass ich Hilfe von gewerblichen Promotionsberatern bzw. -vermittlern oder ähnlichen Dienstleistern weder bisher in Anspruch genommen habe noch künftig in Anspruch nehmen werde.

(§ 8 Satz 2 Nr. 7 PromO)

Hiermit erkläre ich mein Einverständnis, dass die elektronische Fassung der Dissertation unter Wahrung meiner Urheberrechte und des Datenschutzes einer gesonderten Überprüfung unterzogen werden kann.

(§ 8 Satz 2 Nr. 8 PromO)

Hiermit erkläre ich mein Einverständnis, dass bei Verdacht wissenschaftlichen Fehlverhaltens Ermittlungen durch universitätsinterne Organe der wissenschaftlichen Selbstkontrolle stattfinden können.

(Ort und Datum)

(Unterschrift)